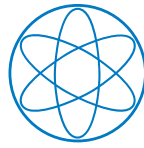PHYSIK-DEPARTMENT

Dissertation

Freed-Isobar Partial-Wave Analysis

Fabian Michael Krinner

TECHNISCHE UNIVERSITÄT MÜNCHEN

Technische Universität München

Physik-Department

Freed-Isobar Partial-Wave Analysis

Fabian Michael Krinner

ii

Abstract

The main goal of hadron spectroscopy is the identification and classification of bound states of the strong interaction. Excited hadronic states are extremely short-lived and usually decay into lighter hadrons. A common method to extrac the hadron resonances from the measured kinematic distributions of the decay products is partial-wave analysis (PWA). The conventional PWA method for decays of light mesons into multi-body final states usually relies on the isobar model, describing the decay process as a series of two-particle decays. Hereby additional intermediary hadronic states appear, called isobars. The decays of these states are described by dynamic amplitudes that have to be known beforehand and therefore may introduce a model bias. In this thesis, we develop a novel approach, in which the parametrizations for the dynamic isobar amplitudes are replaced by step-like functions to extract the dynamic amplitudes from the data, thereby greatly reducing the model dependence of the results. In this approach, which we call freed-isobar PWA, we encounter continuous mathematical ambiguities caused by exact cancellations between different amplitudes and show ways to resolve them.

We apply the freed-isobar PWA method to a data set for the process $\pi^- p \to \pi^- \pi^+ \pi^- p$, collected by the COMPASS experiment in 2008. We extract the dynamic isobar amplitudes for 24 partial waves, resolved in bins of the invariant mass of the 3π system and the four-momentum transfer between beam and target. We analyze the extracted dynamic isobar amplitudes with simple Breit-Wigner and Flatté models and obtain new insights in the interplay between the two- and three-particle dynamics of the three-pion system.

Zusammenfassung

Das Hauptziel der Hadronenspektroskopie ist die Identifikation und Klassifizierung der Bindungszustände der starken Wechselwirkung. Angeregte Hadronenzustände sind extrem kurzlebig und zerfallen typischerweise in leichtere Hadronen. Eine verbreitete Methode, um die Hadronresonanzen aus den gemessenen kinematischen Verteilungen der Zerfallsprodukte zu extrahieren, ist die Partialwellenanalyse (PWA). Die konventionelle PWA-Methode für Zerfälle leichter Hadronen in Vielteilchenendzustände beruht üblicherweise auf dem Isobarenmodell, welches den Zerfallsprozess als Kette aufeinanderfolgender Zweiteilchenzerfälle beschreibt. Hierbei treten zusätzliche hadronische Zwischenzustände auf, die man Isobare nennt. Die Zerfälle dieser Zustände werden durch dynamische Amplituden beschrieben, die von vorneherein bekannt sein müssen und so eine Modellabhängigkeit verursachen können. Diese Disseratation entwickelt eine neuartige Herangehensweise, in der die Parametrisierungen der dynamischen Isobaramplituden durch Stufenfunktionen ersetzt werden, um die dynamischen Amplituden aus den Daten zu extrahieren und so die Modellabhängigkeit stark zu reduzieren. In diesem Ansatz, den wir freiisobarische PWA nennen, stoßen wir auf kontinuierliche mathematische Ambiguitäten, da sich verschiedene Amplituden exakt wegheben können, und zeigen Wege auf, diese aufzulösen.

Wir wenden die freiisobarische PWA auf einen 2008 vom COMPASS Experiment aufgezeichneten Datensatz für den Prozess $\pi^- p \to \pi^- \pi^+ \pi^- p$ an und extrahieren die dynamischen Amplituden für 24 Partialwellen, aufgelöst in Bins der invarianten 3π Masse und des Viererimpulsübertrags zwischen Strahl- und Targetteilchen. Wir analysieren die extrahierten dynamischen Isobaramplituden mit einfachen Breit-Wigner- und Flattémodellen und erhalten so einen neuartigen Einblick in das Zusammenspiel der Zwei- und Dreiteilchendynamik dieser Dreipionensysteme.

„Habe nun, ach!"

„Faust – Der Tragödie erster Teil"
Johann Wolfgang von Goethe

Contents

Chapter 1.

Introduction

The standard model of particle physics includes three fundamental interactions. These are—after electroweak symmetry breaking—the electromagnetic, the weak and the strong interaction. Processes of the electromagnetic interaction can be calculated using an expansion in its coupling constant α and are well understood at all experimentally accessible energies. This is the case, since the coupling constant is small: $\alpha \approx \frac{1}{137} \ll 1$. Hence, contributions of higher order in α are suppressed and the series converges. Since the exchange particles of the weak interaction, the $W^\pm$ and Z^0 bosons, are massive due to electroweak symmetry breaking, effects of the weak interaction are suppressed by these large masses and can also be calculated as an expansion in the Fermi coupling G_F. The strong interaction is described by quantum chromodynamics (QCD), which is an $\mathfrak{SU}(3)$ gauge theory. The coupling constant of the strong interaction α_s becomes large ($\alpha_s \gtrsim 1$) for energy scales around or below the QCD scale $\Lambda_{\mathrm{QCD}} \approx 0.5\,\mathrm{GeV}$ due to the renormalization group behavior of the underlying $\mathfrak{SU}(3)$ gauge symmetry[a]. Since the QCD gauge bosons, the gluons, do not acquire mass through any symmetry breaking effect, perturbative approaches for QCD are only possible for energies significantly higher than Λ_{QCD}. An example are processes at energy scales of the electroweak symmetry breaking, where $\alpha_s(m_{Z^0}) = 0.1181 \pm 0.0011$. A review of the standard model of particle physics is given by the Particle Data Group (PDG) in ref. [2].

The lightest bound states of the strong interaction—the hadrons—have masses in the same order of magnitude as Λ_{QCD}, for example $m_\pi \approx 0.139\,\mathrm{GeV}/c^2$ or $m_p \approx 1\,\mathrm{GeV}/c^2$, which is more than one order of magnitude smaller than the energy scale at which QCD can be treated perturbatively. The spectrum of hadrons is characterized by rich structures, which have to be understood, on the one hand, to test QCD as the underlying theory, and on the other hand, to model the decays of other, more complicated hadronic processes like multi-body decays of excited hadrons, which will be one of the main topics in this thesis.

There are two major classes of hadrons—baryons and mesons—that differ in their quark content. In the naive quark model, baryons are bound states of three quarks with a baryon number of $B = 1$ and mesons are bound states of a quark and an antiquark with $B = 0$. In this work, we will focus on excitation spectrum of light mesons, which are composed only of up- and down-type quarks. However, within

---

[a]The exact value of Λ_{QCD} depends on the chosen renormalization scheme and can take values from $0.3\,\mathrm{GeV}$ to $1\,\mathrm{GeV}$ [1].

the scope of QCD, color-singlet states with zero baryon number cannot only be composed of a quark and an antiquark, but also of excitations of the gluonic fields. States composed of a $q\bar{q}$ pair and a gluonic excitation are called hybrids; states consisting only of gluonic excitations are called glueballs. One way to pin down possible candidates for such "spin exotic" states, which are not simply composed of a $q\bar{q}$ pair, are their spin, parity, and charge conjugation quantum numbers J^{PC}, since not all combinations are possible for simple $q\bar{q}$ states in the nonrelativistic limit[b]. Spin exotic states with such forbidden combinations of quantum numbers have been searched for in various analyses over the last decades [3–6].

Even though perturbative approaches to QCD fail at low energies, there are several non-perturbative approaches to predict the hadron spectrum, the most promising of which is lattice QCD. In this approach, the effects of QCD are simulated on a discretized space-time lattice using involved numerical Monte Carlo integration techniques to solve the corresponding path integrals. This task requires a large amount of computing power usually only available at supercomputers. Even though lattice QCD has made great progress over the last decade, its predictions of QCD bound states are mostly limited to ground states. Predictions of the excitation spectrum are currently performed at large and therefore unphysical values of the pion mass [2].

In order to be able to validate the ever improving predictions of lattice QCD, detailed experimental knowledge on the excitation spectrum of hadrons is crucial. Hadronic states can be produced via various different mechanisms. At collider experiments, these mechanisms include production in e^+e^- collisions, for example at the BES and BELLE experiments, or pp collisions at LHCb. While these current collider experiments focus mainly on the production of heavy hadrons, light hadrons are studied mainly at fixed-target experiments like the GlueX at the Jefferson National Accelerator Facility, or the COMPASS experiment at CERN. Here, other production mechanisms like photoproduction, and central and diffractive production play the main role. The main focus in this thesis will be on diffractive production, where incoming beam particles are excited into different hadronic states X via interaction with the atomic nuclei in the target, while the nuclei themselves stay intact. In this thesis, we focus on a π^- beam interacting with the protons in a liquid hydrogen target. However, diffractive production is not limited to this configuration, but is also possible for different beam particles, e.g. kaons, and target materials, e.g. lead. Since the diffractively produced hadronic states are very short-lived, they decay into lighter states, which can be detected by the experiment. A schematic view of diffractive production is shown in fig. 1.1.

Since a multitude of possibilities for the J_X^{PC} quantum numbers for X are allowed, the measured distribution of final-state particles exhibits an interference pattern of all these possibilities. The goal in an analysis of a diffractive production process is to disentangle these different contributions. To achieve this, involved

---

[b] Additional quantum numbers to characterize light hadrons are their strong isospin I and their G-parity G.
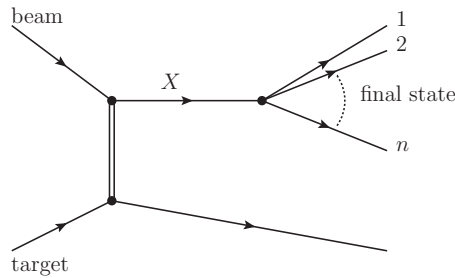
Figure 1.1.: Schematic view of the diffractive production process and the dissociation into an n-particle final state.

analysis techniques such as partial-waves analysis (PWA) are used to extract resonances and their quantum numbers from measurements of strong-interaction decays of hadrons. Similar to the quantum mechanics of a central potential, where the amplitudes can be factorized in a radial and an angular part, the latter of which is given by spherical harmonics, the amplitudes in a PWA can be factorized in a part dependent on the invariant mass m_X of the decaying state—the dynamic amplitude—and an angular part. In the textbook example for a PWA, the analysis of a decay into two spinless final-state particles, the angular part is given by spherical harmonics Y_{LM} that depend on the azimuthal and polar angles of the final-state particle momenta. The data are kinematically binned in m_X to avoid modeling the dynamic amplitude of X, since it is not given by first principles, but depends on the inner structure of X. The amplitudes factorized this way are used as basis functions for an expansion of the measured angular distributions of the final-state particles. The contributions of the basis functions to the angular distribution can then be identified with a state X with spin L and spin projection M. In such a two-body PWA, the distribution of final-state particles is described as the modulus squared of an amplitude that is a sum over all Y_{LM} multiplied with their relative strengths and phases. In theory, such an expansion is able to describe an arbitrary distribution of final-state particles exactly, if the amplitude sums up contributions for all L from zero to infinity and all M from $-L$ to L. Since any experiment is only able to collect a finite data set, it is impossible to apply such an infinite sum in any analysis of experimental data. To be able to perform a PWA, the sum over L has therefore to be truncated at a maximum value. An example for a two-body PWA is the analysis of the diffractively produced $\eta^{(\prime)}\pi^-$ system given in ref. [7], where the partial-wave expansion was truncated at $L = 6$.

However, the main focus of this thesis lies on the diffractive process $\pi^- p \to \pi^-\pi^+\pi^- p$, for which the COMPASS experiment has collected a large data set of $46 \cdot 10^6$ events in 2008. In contrast to the case of the two-particle decay, which can be described by spherical harmonics, more complicated amplitudes appear in this case. To model this three-particle decay, the isobar model is employed, which describes the process as sequence of the two two-particle decays $X \to \xi\pi^-$

and $\xi \rightarrow \pi^+\pi^-$, with another intermediary $\pi^+\pi^-$ state appearing, the isobar ξ. The decays of X and ξ can again be factorized into angular distributions and dynamic amplitudes. As in the two-particle case, the angular distributions are given from first principles and the dynamic amplitude of X can be determined by binning the data in m_X. However, this is not possible for the dynamic amplitude of the isobar, since it interferes with the whole kinematically allowed m_ξ range, and therefore has to be known and put into the analysis model beforehand. In a conventional analysis, the dynamic isobar amplitudes are modeled according to results from previous experiments, including known $\pi^+\pi^-$ resonances with different J_ξ^{PC} quantum numbers. The most prominent of these resonances is the $\rho(770)$ with $J_\xi^{PC} = 1^{--}$, others are the $f_2(1270)$ with $J_\xi^{PC} = 2^{++}$ or the $\rho_3(1690)$ with $J_\xi^{PC} = 3^{--}$. These resonances are commonly modeled using a Breit-Wigner amplitude, which is known to give a reasonable description of the dynamic isobar amplitudes, however neglecting minor features. For isobars with $J_\xi^{PC} = 0^{++}$, the picture is not as clear, since there are contributions from several possible resonances to the corresponding dynamic isobar amplitude: the $f_0(980)$, the $f_0(1370)$, the $f_0(1500)$, and a broad component, the $(\pi\pi)_S$ wave. The latter is also called $f_0(500)$ or σ, its mass and width are badly determined, and it cannot be described well by a Breit-Wigner amplitude. One common approach is the use of the $\pi\pi$ scattering amplitude, obtained in elastic scattering, to describe this dynamic isobar amplitude, but it is not a priori clear, how to parameterize the dynamic amplitude of $J_\xi^{PC} = 0^{++}$ isobars. This problem occurs in every analysis, where two pions appear in a relative S wave.

Besides the nontrivial choice of parameterization of the dynamic isobar amplitudes, another problem arises in the case of several different intermediary isobar states with identical J_ξ^{PC} quantum numbers. As already mentioned, this is the case for $J_\xi^{PC} = 0^{++}$ isobars, since there are four possible f_0 resonances. However, this may occur also for 1^{--} and 2^{++} isobars, since excited isobar resonances, like ρ' or f_2' might also contribute. F. Kaspar and F. Haas showed in refs. [8, 9], that the inclusion of multiple resonances with identical J_ξ^{PC} often leads to ambiguous models in distinct kinematic regions and that fit results for such models have a general tendency to become unstable. Also, from a theoretical point of view, the simple sum of several Breit-Wigner amplitudes overlapping in mass is problematic, since such a sum results in an amplitude description that violates unitarity. However, more elaborate parameterizations of the dynamic isobar amplitudes, that could solve this problem, are either not flexible enough, or not feasible within our analysis method, since they require free fit parameters in the dynamic isobar amplitude, that cannot be factorized out.

A first approach to these caveats of conventional PWA would be to use a model for the dynamic isobar amplitudes that has free parameters and is therefore able to adjust to the data. Even though this approach is in principle possible, it turns out to be computationally unfeasible in our case, since we use a maximum likelihood fit to the data. In such an approach, the likelihood function has to be normalized,

which requires the calculation of numerous multi-dimensional integrals. Free parameters in the model would require to recalculate these integrals for every call of the fit function, while they otherwise can be pre-calculated and stored, making the maximization much faster.

To avoid the dependence on the specification of predefined parameterizations of the dynamic isobar amplitudes without free parameters in the model, we developed an approach, called freed-isobar PWA, in which we replace the fixed dynamic isobar amplitudes by step-like functions of m_ξ. This approach—first introduced in ref. [10]—allows to infer binned approximations of the dynamic isobar amplitudes directly from the data without explicitly specifying or modeling their resonance content. It removes the model dependence on predefined parameterizations of the dynamic isobar amplitudes and allows to extract overlapping resonances without violating unitarity. The same approach has already been used to cross check the existence of newly found resonances, for example the pentaquark states found by the LHCb collaboration in ref. [11]. A first freed-isobar analysis was published by the COMPASS collaboration in ref. [12], based on a very detailed conventional PWA on the same data. However, all of these analyses only employ the freed-isobar method for single, or a very limited set of partial waves with step-like dynamic isobar amplitudes. Freed-isobar analyses with larger sets of waves, in particular with more than one wave for every J_X^{PC} combination of the decaying particle X, turned out to be unsuccessful. In this thesis, we determine the reason, why the simple extension of the freed-isobar method did not yield satisfying results in previous analyses, extend the method to an arbitrary large set of partial waves— only limited by the size of the data set—, and finally apply the method to the data collected by the COMPASS experiment for the process $\pi^- p \to \pi^- \pi^+ \pi^- p$. This way, we can not only reduce the model dependence of our PWA, but are able to extract information on the dynamic isobar amplitudes from the data.

The following text introduces this approach and is structured as follows: In chapter 2, we shortly introduce the COMPASS experiment, where the data used for the analyses of refs. [8, 9, 12–14] and for this work were recorded. In chapter 3, we give a general introduction to the conventional partial-wave analysis techniques and discuss an example of such a PWA of COMPASS data in chapter 4, especially looking at the caveats of this kind of analysis. In chapter 5, we introduce the freed-isobar PWA method in detail and discuss arising continuous mathematical ambiguities within this new approach, as well as methods to resolve them. We also demonstrate the validity of these methods in a Monte Carlo study. In chapter 6, we finally apply the freed-isobar method to COMPASS data, present the results for 24 waves obtained in various studies and compare them to results of a similar conventional PWA. In turn, we extract the resonance parameters of several $\pi^+ \pi^-$ isobar states in chapter 7 and discuss sources of systematic effects on these parameters. In chapter 8, we draw conclusions from the results of this work and give an outlook on how to proceed with the analysis given the presented results. We also propose other final states and processes, where the application of the freed-isobar method can give important insights, for example diffractive $K\pi\pi$ production at COMPASS or decays of heavy B or D mesons at B factories.

Chapter 2.

The Compass experiment

2.1. The process $\pi^- p \to \pi^- \pi^+ \pi^- p$

The focus of this work lies on the analysis of the diffractive dissociation process:

$$\pi^- p \to \pi^- \pi^+ \pi^- p, \tag{2.1}$$

for which the COMPASS experiment has collected a large data set of $46 \cdot 10^6$ exclusive events in 2008. A schematic view of the process is given in fig. 2.1. We assume the process to be dominated by Pomeron exchange, indicated by $\mathbb{P}$, which is an effective description of the underlying effects of the strong interaction. Since this process is an inelastic scattering process, it can be described by the three kinematic variables, s, t, and $m_{3\pi}$, if we do not consider the internal kinematics of the outgoing three pion system. The Mandelstam variable s is the squared center-of-mass energy of the $p\pi^-_{\text{beam}}$ system, which is fixed by the beam energy of $190\,\text{GeV}$. The second kinematic variable is the squared four-momentum transfer t between beam and target particle. Since the process is inelastic, the third variable is the invariant mass $m_{3\pi}$ of the outgoing three pion system. The target proton is assumed to stay intact. Since an inelastic process requires a minimal squared four-momentum transfer $|t|_{\text{min}}$ to excite the beam pion to an invariant mass of $m_{3\pi}$, we use the reduced four-momentum transfer squared:

$$t' = |t| - |t|_{\text{min}} > 0 \tag{2.2}$$
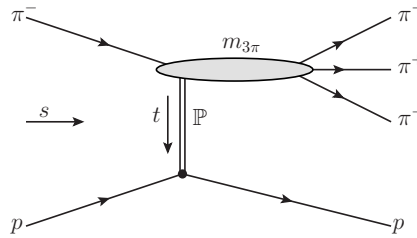
Figure 2.1.: Schematic view of the process $\pi^- p \to \pi^- \pi^+ \pi^- p$.

instead of t to describe the process throughout this work. To determine $|t|_{\mathrm{min}}$, we use the definition of t as the square of the four-momentum transferred from the beam pion to the target proton:

$$t = \left(p_{\mathrm{beam}}^{\mu} - p_{3\pi}^{\mu}\right)^2 = m_{\pi}^2 + m_{3\pi}^2 - 2p_{\mathrm{beam}}^{\mu}p_{3\pi,\mu}, \qquad (2.3)$$

where $p_{3\pi}^{\mu}$ is the total four-momentum of the three outgoing pions. We can rewrite this equation in the laboratory frame as:

$$t = m_{\pi}^2 + m_{3\pi}^2 - 2\left(E_{\mathrm{beam}}^{\mathrm{Lab}} E_{3\pi}^{\mathrm{Lab}} - \left|\vec{p}_{\mathrm{beam}}^{\mathrm{Lab}}\right|\left|\vec{p}_{3\pi}^{\mathrm{Lab}}\right|\cos\theta^{\mathrm{Lab}}\right). \qquad (2.4)$$

For known absolute values of the three-momenta and invariant masses, the energies are also fully determined and the only degree of freedom in the above equation is θ^{Lab}, the scattering angle between the direction of the beam pion and that of the outgoing three-pion system. Since t is always negative, we have to maximize the above expression to determine $|t|_{\mathrm{min}}$. This is achieved by setting $\cos\theta^{\mathrm{Lab}} = 1$, which corresponds to forward scattering:

$$|t|_{\mathrm{min}} = 2\left(E_{\mathrm{beam}}^{\mathrm{Lab}} E_{3\pi}^{\mathrm{Lab}} - \left|\vec{p}_{\mathrm{beam}}^{\mathrm{Lab}}\right|\left|\vec{p}_{3\pi}^{\mathrm{Lab}}\right|\right) - m_{\pi}^2 - m_{3\pi}^2. \qquad (2.5)$$

However, for the analyzed kinematic region of $0.1 < t' < 1.0\,(\mathrm{GeV}/c)^2$, $|t|_{\mathrm{min}}$ is negligible, so that $t' \approx |t|$.

2.2. Experimental setup

The analyzed data have been collected in 2008 by the Compass experiment, which is located at the North Area of CERN. The multi-purpose fixed-target spectrometer is able to measure various physics processes with a large acceptance over a wide kinematic range using different target and beam configurations. In this chapter, we only briefly introduce the basic features of the spectrometer, more detailed information can be found in ref. [15].

To produce diffractive events, we use a secondary negative hadron beam which is produced by a primary proton beam with an energy of $400\,\mathrm{GeV}$, which is provided by the Super Proton Synchrotron. The proton beam hits a beryllium production target thereby producing a vast amount of secondary hadrons. Particles with the desired energy and charge are selected and guided to the experiment by the magnets of the beam line. For the data analyzed here, a negatively charged hadron beam with an energy of $190\,\mathrm{GeV}$ was chosen, consisting of 96.8% negative pions at the position of the Compass target. The rest of the hadrons are negative kaons (2.4%) and antiprotons (0.6%). The beam-momentum spread is smaller than 1% [15]. Two CEDAR[a] detectors in the beam line identify the incoming beam particles.

The secondary hadron beam produced this way hits a $40\,\mathrm{cm}$ long liquid-hydrogen target, that is located inside the barrel-shaped Recoil-Proton Detector (RPD). This

---

[a]ChErenkov Differential counter with Achromatic Ring focus, for the identification of beam particles.

detector consists of two layers of scintillation detectors, divided in 12 and 24 segments, respectively. The RPD is used to ensure the exclusivity of the measurement by detecting the recoil protons that are knocked out of the target by the interactions with the beam pions. The minimum squared four-momentum transfer to the proton, that can still be detected by the RPD, is $t' \approx 0.07 \,(\mathrm{GeV}/c)^2$. This limits the acceptance for events with small t'.

Since in this work, we only consider peripheral interactions with $t' < 1.0 \,(\mathrm{GeV}/c)^2$, all final-state particles except the recoil proton are emitted in forward direction and are measured by the two-staged COMPASS spectrometer. This setup is equipped with two dipole magnets with bending powers of $1.0 \,\mathrm{Tm}$ and $4.4 \,\mathrm{Tm}$, respectively [16]. The tracks of charged particles are measured by a variety of tracking detectors. This includes silicon-microstrip detectors up- and downstream of the target, MicroMega[b] and GEM[c] detectors in the vicinity of the beam, as well as multi-wire proportional, straw-tube, and drift chambers for the large-area tracking—i.e. for particles emitted under large angles. At the end of each of the two stages, hadronic and electromagnetic calorimeters are positioned. They are not used in the present analysis, since the process in eq. (2.1) has only charged final-state particles. In the first spectrometer stage, a RICH[d] detector is able to identify final-state particles.

To pre-select data, the diffractive DT0 trigger was used. This trigger was configured to introduce minimal bias on the acceptance and to identify candidates for diffractive events. The DT0 trigger requires a coincidence of three independent trigger signals: (*i*) the beam trigger that requires an incoming beam particle, (*ii*) the recoil-proton trigger that requires a proton signal in the RPD, and (*iii*) no signal from the veto system. The veto rejects beam particles with tracks far from the nominal trajectory, final-state particles outside the geometric acceptance of the spectrometer, and signals from non-interacting beam particles. Reference [15] gives a more detailed description of this trigger. In the data-taking period of 2008, COMPASS has recorded $6.4 \cdot 10^9$ DT0 events.

2.3. Data selection

To obtain a clean exclusive sample for the process $\pi^- p \to \pi^- \pi^+ \pi^- p$, the pre-selected DT0 events are filtered further. In this work, we use the same data selection criteria as in refs. [8, 12] and only give a short overview over the selection, more details are described by F. Haas in ref. [8]. To be accepted into the final data set, an event has to fulfill several selection criteria:

- existence of an interaction vertex that is formed by the beam track and the three forward-going charged tracks and that lays within the target volume,

---

[b]Micromesh Gaseous Structure.

[c]Gas Electron Multiplier, using a stack of three amplifier foils.

[d]Ring Imaging CHerenkov detector for final-state particle identification.

Figure 2.2.: Schematic view of the COMPASS hadron-beam setup used in 2008 taken from ref. [15].

- charge conservation in the vertex and a total charge of -1 in the outgoing, three-particle system,

- detection of exactly one recoil proton in the RPD, which has to balance the transverse momentum of the three forward-going charged tracks,

- neither the beam particle nor one of the final-state particles has been identified as a kaon or (anti) proton—particles that are not identified otherwise are assumed to be pions—by the CEDARs or the RICH, respectively, and

- the reconstructed energy of the beam particle is within two standard deviations of the nominal beam energy of $191.5\,\text{GeV}$. This corresponds to a window of $\pm 3.78\,\text{GeV}$.

All events, that match these criteria are assumed to be good candidates for the process $\pi^- p \to \pi^- \pi^+ \pi^- p$. In addition, the analysis is limited to the kinematic range $0.5\,\text{GeV}/c^2 < m_{3\pi} < 2.5\,\text{GeV}/c^2$ and $0.1\,(\text{GeV}/c)^2 < t' < 1.0\,(\text{GeV}/c)^2$.

After applying all the above selection criteria, a set of $46 \cdot 10^6$ exclusive events remains, which we will analyze in the following chapters. Figure 2.3 shows kinematic distributions for the selected events. The t' spectrum exhibits an approximate exponential behavior. The drop at $t' < 0.1\,(\text{GeV}/c)^2$ is the result of the limited
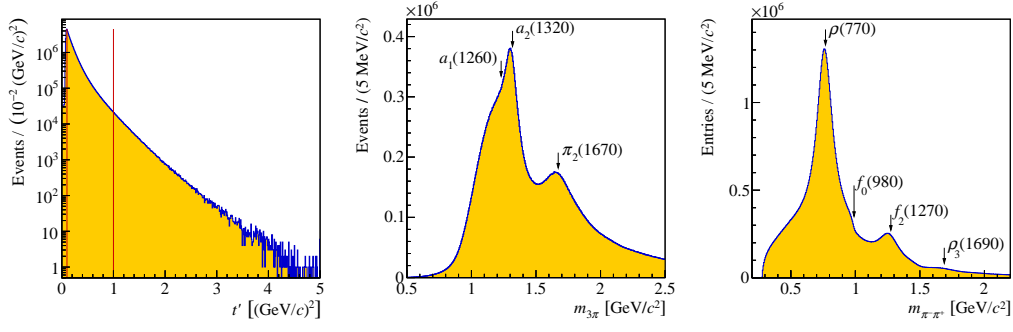
Figure 2.3.: Kinematic distributions of the $\pi^- p \to \pi^- \pi^+ \pi^- p$ data set after selection cuts. The red lines in the t' spectrum indicate the analyzed range. Features in the $m_{3\pi}$ and $m_{2\pi}$ spectra are labeled according to the intermediary resonances they correspond to. The pictures are taken from ref. [12].

acceptance of the RPD in this region. The 3π and $\pi^+\pi^-$ mass spectra show several peaks indicating the presence of intermediary states in the corresponding three- and two-particle systems. Arrows indicate masses of known states.

Chapter 3.

Amplitude Analysis method

To analyze the data set introduced in the previous chapter, we employ amplitude analysis techniques, which we first introduce in a general way, before applying them to a specific channel.

3.1. Decay processes

We discuss the analysis of the decay of an initial-state particle X into a set of n final-state particles:

$$X \to 1 + 2 + \ldots + n. \tag{3.1}$$

Such processes can be described using the four momenta of the final-state particles, which have to fulfill four-momentum conservation:

$$P_X^\mu = \sum_{i=1}^n p_i^\mu, \tag{3.2}$$

where P_X^μ is the four momentum of the decaying particle and p_i^μ are the four-momenta of the final-state particles. The invariant mass of the decaying particle is m_X.

In many cases, however, it turns out to be more suitable for an analysis, to chose different, but equally valid, sets of phase-space variables to describe decay processes. Without any specific choice, we call such a set of phase-space variables $\vec{\tau}$.

3.2. Amplitude decomposition and extended likelihood

The probability of an event in a decay process to happen at a particular point in phase-space $\vec{\tau}$ is given by the probability distribution function $\Im(\vec{\tau})$ of the intensity in an infinitesimal phase-space volume $\mathrm{d}\Phi_n$:

$$\Im(\vec{\tau}) \, \mathrm{d}\Phi_n = |\mathfrak{A}(\vec{\tau})|^2 \, \varrho(\vec{\tau}) \, \mathrm{d}\vec{\tau} \tag{3.3}$$

The function $\varrho(\vec{\tau})$ describes the phase space of the process for the particular choice of phase-space variables $\vec{\tau}$ and is defined as:

$$\varrho(\vec{\tau}) \, \mathrm{d}\vec{\tau} = \mathrm{d}\Phi_n, \tag{3.4}$$

where $\mathrm{d}\Phi_n$ is the differential Lorentz invariant phase-space element for an n-body decay of a particle with four-momentum P_X^μ into n final-state particles with four-momenta p_i^μ:

$$\mathrm{d}\Phi_n = \delta^{(4)}\left(P^\mu - \sum_{i=1}^n p_i^\mu\right)\prod_{i=1}^n \frac{\mathrm{d}^3 p_i}{(2\pi)^3\, 2E_i}. \tag{3.5}$$

The overall amplitude $\mathfrak{A}(\vec{\tau})$ for the decay is a complex-valued function, that can be expanded as a coherent superposition of decay amplitudes:

$$\mathfrak{A}(\vec{\tau}) = \sum_i \mathcal{T}_i \mathcal{A}_i(\vec{\tau}), \tag{3.6}$$

where the complex-valued decay amplitudes $\mathcal{A}_i(\vec{\tau})$ describe the dependence of the basis amplitudes on the kinematic variables and the complex-valued production amplitudes $\mathcal{T}_i$ encode the intensities and phases with which the single decay amplitudes contribute to the total process. Note, that only their relative phases carry meaning, since a global phase rotation of the total amplitude $\mathfrak{A}(\vec{\tau})$ leaves the intensity given in eq. (3.3) unchanged. The index i runs over a given set of basis amplitudes, which we call *wave set*.

With this model for the intensity, we formulate an extended likelihood function, that describes the probability to measure the data set $\mathbb{E}$, consisting of N events, given the model $\mathfrak{I}(\vec{\tau})$ for the intensity:

$$\mathcal{L}\left(\vec{\mathcal{T}}; \mathbb{E}\right) = \frac{e^{-\bar{N}}\bar{N}^N}{N!}\prod_{\text{event}\in\mathbb{E}}\frac{\mathfrak{I}(\vec{\tau}_{\text{event}})}{\bar{N}}. \tag{3.7}$$

The first term is a Poissonian factor for the probability to measure N events, with an expectation value of $\bar{N}$ events. The second factor is the product of the probabilities to measure the individual events. It is given by the model intensity evaluated at the respective point $\vec{\tau}_{\text{event}}$ in phase space normalized to the expected total number of measured events $\bar{N}$.

The expectation value $\bar{N}$ for the total number of measured events is given as the integral of the intensity weighted by the over all detection efficiency $\eta(\vec{\tau})$ over the whole phase space volume:

$$\bar{N} = \int \varrho(\vec{\tau})\,\mathrm{d}\vec{\tau}\,\mathfrak{I}(\vec{\tau})\,\eta(\vec{\tau}). \tag{3.8}$$

The overall detection efficiency is the product of the detector acceptance and the reconstruction efficiency. With the intensity given in eq. (3.3), we rewrite eq. (3.8) to see the dependence of $\bar{N}$ on the production amplitudes explicitly:

$$\bar{N} = \sum_{i,j\in\text{waves}} \mathcal{T}_i^* \tilde{\mathbf{I}}_{ij} \mathcal{T}_j, \tag{3.9}$$

where we define the acceptance-weighted integral matrix to be:

$$\tilde{\mathbf{I}}_{ij} = \int \varrho(\vec{\tau})\,\mathrm{d}\vec{\tau}\,\mathcal{A}_i^*(\vec{\tau})\,\mathcal{A}_j(\vec{\tau})\,\eta(\vec{\tau}). \tag{3.10}$$

Since there is no analytic expression for $\eta(\vec{\tau})$, we replace the integral in eq. (3.10) by a sum over a Monte Carlo data set $\mathbb{E}_{\mathrm{MC}}$ containing N_{MC} events. The Monte Carlo events are randomly drawn according to the phase-space distribution $\varrho(\vec{\tau})$, which therefore does not appear in the sum:

$$\tilde{\mathbf{I}}_{ij} = \frac{V_{\mathrm{PS}}}{N_{\mathrm{MC}}} \sum_{\mathrm{event} \in \mathbb{E}_{\mathrm{MC}}} \mathcal{A}_i^*(\vec{\tau}_{\mathrm{event}}) \mathcal{A}_j(\vec{\tau}_{\mathrm{event}}) \eta_{\mathrm{MC}}(\vec{\tau}_{\mathrm{event}}). \tag{3.11}$$

The Monte Carlo events are passed through the detector simulation and the event selection. The overall acceptance can therefore be replaced by $\eta_{\mathrm{MC}}(\vec{\tau})$, which takes the values 1 or 0, depending on whether the corresponding event is reconstructed and accepted or not. V_{PS} is the total phase-space volume:

$$V_{\mathrm{PS}} = \int \varrho(\vec{\tau}) \,\mathrm{d}\vec{\tau}. \tag{3.12}$$

Alongside with the acceptance-weighted integral matrix, we define the phase-space integral matrix:

$$\mathbf{I}_{ij} = \int \varrho(\vec{\tau}) \,\mathrm{d}\vec{\tau} \mathcal{A}_i^*(\vec{\tau}) \mathcal{A}_j = \frac{V_{\mathrm{PS}}}{N_{\mathrm{MC}}} \sum_{\mathrm{event} \in \mathbb{E}_{\mathrm{MC}}} \mathcal{A}_i^*(\vec{\tau}_{\mathrm{event}}) \mathcal{A}_j(\vec{\tau}_{\mathrm{event}}). \tag{3.13}$$

With this definition, we require the basis amplitudes $\mathcal{A}_i(\vec{\tau})$ to fulfill the normalization condition:

$$\mathbf{I}_{ii} = 1, \tag{3.14}$$

so that V_{PS} drops out everywhere. A consequence of this normalization and of using an extended likelihood function is, that the unit of $\mathcal{T}_i$ is square-root of number of events and that the expected number of events $\hat{N}$[a] for a perfect detector with unit detection efficiency $\eta(\vec{\tau})$ is given by:

$$\hat{N} = \int \varrho(\vec{\tau}) \,\mathrm{d}\vec{\tau} \mathfrak{I}(\vec{\tau}) = \sum_{i,j} \mathcal{T}_i^* \mathbf{I}_{ij} \mathcal{T}_j. \tag{3.15}$$

To perform an analysis, we adjust all production amplitudes to maximize the likelihood function defined in eq. (3.7) and therefore get the best description of the measured intensity distribution within our model. For numerical stability of the maximization, we switch for all applications from maximizing the likelihood function to maximizing its logarithm:

$$\ln \mathcal{L}\left(\vec{\mathcal{T}}; \mathbb{E}\right) = \sum_{\mathrm{event} \in \mathbb{E}} \ln\left(\mathfrak{I}(\vec{\tau}_{\mathrm{event}})\right) - \bar{N} - \ln(N!). \tag{3.16}$$

To make the dependence of the log-likelihood function on $\vec{\mathcal{T}}$ explicit, we write:

$$\ln \mathcal{L}\left(\vec{\mathcal{T}}; \mathbb{E}\right) = \sum_{\mathrm{event} \in \mathbb{E}} \ln \left| \sum_i \mathcal{T}_i \mathcal{A}_i(\vec{\tau})_{\mathrm{event}} \right|^2$$
$$- \sum_{i,j} \mathcal{T}_i^* \tilde{\mathbf{I}}_{ij} \mathcal{T}_j - \ln(N!) + \sum_{\mathrm{event} \in \mathbb{E}} \ln\left(\varrho(\vec{\tau}_{\mathrm{event}})\right). \tag{3.17}$$

---

[a]Not to be confused with the expected number of measured events $\bar{N}$, defined in eq. (3.9).

Since we are only interested in the position of the maximum of the log-likelihood function, we can drop all additive constants independent of the parameters $\vec{\mathcal{T}}$. Hence the function we maximize in a fit is:

$$\ln \hat{\mathcal{L}} \left(\vec{\mathcal{T}}; \mathbb{E} \right) = \sum_{\text{event} \in \mathbb{E}} \ln \left| \sum_i \mathcal{T}_i \mathcal{A}_i \left(\vec{\tau} \right)_{\text{event}} \right|^2 - \sum_{i,j} \mathcal{T}_i^* \tilde{\mathbf{I}}_{ij} \mathcal{T}_j. \qquad (3.18)$$

The key feature of this kind of analysis is, that the production amplitudes $\mathcal{T}_i$ are the only degrees of freedom in the model, while the decay amplitudes $\mathcal{A}_i \left(\vec{\tau} \right)$ do not have any free parameters. Therefore, we can precalculate the acceptance-weighted integral matrix $\tilde{\mathbf{I}}_{ij}$ and the decay amplitudes $\mathcal{A}_i \left(\vec{\tau}_{\text{event}} \right)$ for the measured events, which makes the analysis procedure computationally much less expensive.

All the formulas presented in this section describe the case of a single coherent process. In many cases, however, the measured process is the sum of several incoherent subprocesses p:

$$\mathfrak{I} \left(\vec{\tau} \right) = \sum_p \mathfrak{I}_p \left(\vec{\tau} \right). \qquad (3.19)$$

In this case, eq. (3.16) sightly changes to:

$$\ln \hat{\mathcal{L}} \left(\vec{\mathcal{T}}; \mathbb{E} \right) = \sum_{\text{event} \in \mathbb{E}} \ln \left(\sum_p \mathfrak{I}_p \left(\vec{\tau}_{\text{event}} \right) \right) - \sum_p \bar{N}_p. \qquad (3.20)$$

However, the advantage of having a low computational effort remains valid also in the case of several incoherent subprocesses. One example for such an incoherent subprocess, is the use of a so-called *flat-wave*, which has a constant decay-amplitude with respect to all phase space variables $\vec{\tau}$, is added incoherently to the rest of the model, and describes uncorrelated events.

3.3. Partial Waves and isobars

After the definition of the likelihood function, we consider in particular 3-body decay processes of the type:

$$X \rightarrow a + b + c. \qquad (3.21)$$

For these processes, we have to formulate a set of decay amplitudes $\mathcal{A}_i \left(\vec{\tau} \right)$, for which we employ the isobar model. In this model, we assume that the decay of X happens via a chain of sequential two-particle decays:

$$X \rightarrow \xi + c; \quad \xi \rightarrow a + b, \qquad (3.22)$$

with an additional intermediate state ξ, called the isobar, that has well-defined quantum-numbers. We now factorize the decay amplitudes in the following way:

$$\mathcal{A}_i \left(\vec{\tau} \right) = \mathcal{N}_i \Psi_i \left(\vec{\tau} \right) \Delta_i \left(m_{ab} \right). \qquad (3.23)$$

The dynamic isobar amplitudes $\Delta_i(m_{ab})$ describe solely[b] the dependence of the decay amplitudes on the invariant mass of the two-particle system (ab) that forms the intermediary state. The spin amplitudes $\Psi_i(\vec{\tau})$ are fully determined by the spin quantum numbers J^{PC} of X and ξ, the spin projection M^ε of X, and the orbital angular momentum L between ξ and the final-state particle c, which is called *bachelor particle*. The quantum numbers J^{PC} are defined as follows: J is the spin of a state and P and C are its eigenvalues under parity transformation and generalized charge conjugation. M^ε is the spin projection of X in the reflectivity basis, in which the spin-projection quantum number, $M \geq 0$, and the reflectivity quantum number, $\varepsilon = \pm 1$, are used to describe the spin projection [17]. This is in contrast to the more common case, where the spin projection can take values from $-J$ to J. The reflectivity corresponds to the eigenvalue of a partial-wave amplitude under reflection through the production plane of X, which is defined in section 4.1.2. Since in the high-energy limit, the reflectivity corresponds to the naturality of the exchange particle and the scattering process is dominated by Pomeron exchange, most waves in the model will have positive reflectivity [17].

In this work, we only consider spinless final-state particles, a, b, c. A combination of J_X^{PC}, M^ε, J_ξ^{PC}, L and a specific dynamic isobar amplitude, $\Delta(m_{ab})$ will be called partial wave amplitude from hereon. The factor $\mathcal{N}_i$ is a real-valued constant that ensures the normalization of the amplitudes according to eq. (3.14). Since the isobar is formed by the two-particle system (ab), the invariant mass of this system equals the mass of the isobar: $m_{ab} = m_\xi$.

The spin amplitudes depend on the chosen spin formalism. In this work, we will employ the covariant tensor [18, 19], the non-relativistic tensor [20, 21], and the helicity formalism [22, 23]. The choice of a formalism fully determines the spin amplitudes from first principles. This, in contrast, is not true for the dynamic isobar amplitudes, which we have to specify according to knowledge from previous experiments or based on models.

Depending on the spin formalism, the resonance amplitudes $\hat{\Delta}_i(m_\xi)$ are equal to the dynamic isobar amplitudes $\Delta_i(m_\xi)$, or they have to be dressed with, so-called barrier factors $F_L(q)$ [24] to give the amplitude the correct limiting behavior on the two-body breakup momentum q. For a state with mass m_{ab} decaying into two states with masses m_a and m_b the breakup momentum is defined by:

$$q(m_{ab}, m_a, m_b) = \frac{\sqrt{m_{ab}^4 + m_a^4 + m_b^4 - 2m_{ab}^2 m_a^2 - 2m_{ab}^2 m_b^2 - 2m_a^2 m_b^2}}{2m_{ab}}. \quad (3.24)$$

The breakup momentum corresponds to the magnitude of the three-momenta of a and b in the (ab) rest system. The barrier factors depend on the relative orbital angular momentum L between a and b and are listed up to $L = 4$ in ref. [25]. Note, that the barrier factors require a momentum scale q_R, which corresponds

---

[b]It also depends on the appearing angular momentum quantum numbers and the masses of initial- and final-state particles. These variables, however, are not within set of kinematic variables $\vec{\tau}$ and therefore these dependences are treated differently.
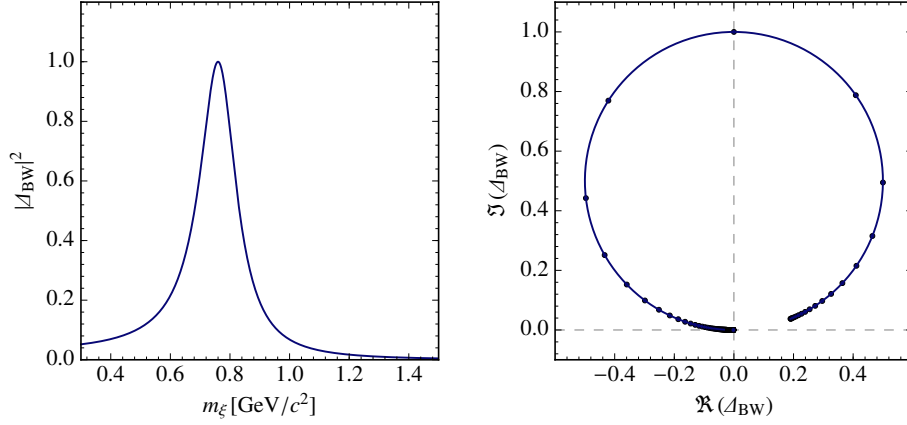
Figure 3.1.: Intensity distribution and Argand diagram of a simple Breit-Wigner resonance parameterization as given in eq. (3.26) with $m_0 = 0.76\,\text{GeV}/c^2$ and $\Gamma_0 = 0.15\,\text{GeV}/c^2$. The intensity is given by the modulus squared of the dynamic amplitude, while the Argand diagram shows the real part of the dynamic amplitude on the x-axis and its imaginary part on the y-axis. In this plot the dots on the Argand-diagram indicate points of equal spacing in m_ξ. The amplitude is normalized such, that $\hat{\Delta}^{\text{BW}}(m_\xi = m_0) = i$.

to the range of the interaction. If not explicitly stated otherwise, we will use $q_R = 0.1973$ GeV/c, which corresponds to an interaction radius of 1 fm. With these functions, the pure resonance amplitude is modified:

$$\Delta_i(m_\xi) = F_{L_i}\Big(q(m_X, m_\xi, m_c)\Big) F_{J_{\xi_i}}\Big(q(m_\xi, m_a, m_b)\Big)\hat{\Delta}_i(m_\xi), \qquad (3.25)$$

for a given value of m_X to give the full dynamic isobar amplitude.

The resonance amplitudes $\hat{\Delta}_i(m_\xi)$ encode the resonance behavior of the isobar. The simplest example for a resonance amplitude is the fixed-width Breit-Wigner resonance shape with known mass, m_0, and width, Γ_0, of the isobar state $\hat{\Delta}^{\text{BW}}(m_\xi)$; it is depicted in fig. 3.1 and is commonly used to describe isolated resonances, for example the $\rho(770)$:

$$\hat{\Delta}^{\text{BW}}(m_\xi) = \frac{m_0\Gamma_0}{m_0^2 - m_\xi^2 - im_0\Gamma_0}. \qquad (3.26)$$

For other cases, more sophisticated parameterizations are available, which often are modifications of eq. (3.26), but nevertheless external knowledge about this function is a necessary model-input.

Chapter 4.

Conventional Partial-Wave Analysis of Compass data

In chapter 5 we will introduce an extension to conventional PWA and apply it to the data set introduced in chapter 2. This analysis will be based on a conventional PWA on the same data, presented in refs. [8, 12], which we introduce in here to later compare our results from the extended analysis to the results from the conventional one.

4.1. Parameterization of the 3π decay amplitudes

To perform a partial-wave analysis of the type introduced in chapter 3 on the data set selected in chapter 2 we have to chose a formalism to formulate the spin amplitudes defined in eq. (3.23). For the analysis in refs. [8, 12] the helicity formalism is used, which we therefore use here as well for an analysis as defined in section 3.2.

4.1.1. Quantum numbers and isobars

First we specify the quantum numbers, in which the partial-wave expansion is performed. The appearing angular momentum quantum numbers are as specified in section 3.3. Since all appearing particles are hadronic states, we additionally have to specify their strong isospin I and their eigenvalue under G-parity G of the intermediary states. Since Pomeron exchange does not alter any quantum numbers other than spin and parity (and momentum), I_X of all X is 1 and G_X, is -1.

In addition, we have to specify the isobar resonance ξ, into which X decays. With this specification, also the quantum numbers $I_\xi^G J_\xi^{PC}$ are fixed. A list of all isobars used in the conventional PWA of refs. [8, 12] is given in table 4.1. Dominant isobars can also be seen as peaks in the $m_{2\pi}$ spectrum in fig. 2.3. Together with the relative orbital angular momentum L between bachelor pion and isobar, partial waves are fully defined. We will use the following naming scheme for partial waves:

$$i = I_X^G J_X^{PC} M^\varepsilon \xi \pi L, \tag{4.1}$$

where i is the partial wave index, as defined in eq. (3.6)[a]. It is a short notation

---

[a] Note, that the reflectivity ε has to be summed incoherently.

Table 4.1.: List of isobars in the conventional PWA of refs. [8, 12]

Name	I_ξ^G	J_ξ^{PC}
$(\pi\pi)_{\mathrm{S}}$	0^+	0^{++}
$f_0(980)$	0^+	0^{++}
$f_0(1500)$	0^+	0^{++}
$\rho(770)$	1^+	1^{--}
$f_2(1270)$	0^+	2^{++}
$\rho_3(1690)$	1^+	3^{--}

for all information about the corresponding partial wave. The π in the wave name indicates the bachelor pion, which is same for all partial waves appearing in this work. Since I_X and G_X of X are the same for all waves ($I_X^G = 1^-$), we omit them from hereon in the wave names.

4.1.2. Kinematic variables

Next, we have to specify the kinematic variables, in which we perform our analysis. To do this, we split the process in two parts, the production $\pi^- p \to Xp$ and the decay $X \to \pi^-\pi^+\pi^-$ of the intermediary state X.

The production is an elastic scattering process, which can be described by three the kinematic production variables s, t', and $m_{3\pi}$. The center of mass energy s is fixed by the energy of the beam, which leaves the two production variables t' and $m_{3\pi}$ free. They have already been introduced in section 2.1. We do not model the dependence of the process on the two production variables that are not determined by the beam energy, but perform the analysis independently in narrow bins of $m_{3\pi}$ and t'. This way, the $m_{3\pi}$ and t' dependences are inferred from the data in a rather model-independent way.

The second step is the decay of X into three pions. In principle, such a process has twelve degrees of freedom, one for each entry in the four momenta of the final-state particles. Since the masses of all particles are known, three degrees of freedom drop out and energy and momentum conservation removes another four degrees of freedom. Thus, in the end we can describe the process using five decay variables:

$$\vec{\tau} = \{\phi_{\mathrm{TY}}, \theta_{\mathrm{GJ}}, m_{2\pi}, \phi_{\mathrm{HF}}, \theta_{\mathrm{HF}}\}\,. \tag{4.2}$$

To specify the five decay variables, we have to select the two pion subsystem, that constitutes the isobar. To do this, we label the appearing final-state particles from the X decay as follows:

$$X \to \pi_1^- \pi_2^+ \pi_3^- \tag{4.3}$$

and take the (12) system to form the isobar, therefore the following definitions are for $\vec{\tau}_{12}$. For the Bose-symmetrized counterpart, $\vec{\tau}_{23}$, the particles π_1^- and π_3^- have to be interchanged.

The $X \to \xi\pi_3^-$ decay is described in the so-called Gottfried-Jackson (GJ) reference frame [26]. This is the rest frame of X, where the z_{GJ} axis lies in the direction of the beam-particle: $\hat{e}_z^{\text{GJ}} \propto \vec{p}_{\text{beam}}$. The y_{GJ} axis is orthogonal to the production plane, spanned by $\vec{p}_{\text{beam}}$ and $\vec{p}_{\text{recoil}}$: $\hat{e}_y^{\text{GJ}} \propto \vec{p}_{\text{recoil}} \times \vec{p}_{\text{beam}}$. The three-momenta $\vec{p}_{\text{beam}}$ and $\vec{p}_{\text{recoil}}$ are defined in an arbitrary rest system of X. To form an orthonormal right-handed coordinate system, the third basis vector is given by: $\hat{e}_x^{\text{GJ}} = \hat{e}_y^{\text{GJ}} \times \hat{e}_z^{\text{GJ}}$. In the Gottfried-Jackson frame, the two angular variables ϕ_{TY}, the so-called Treiman-Yang angle, and θ_{GJ} are defined as the azimuthal and polar angle of the three-momentum of the isobar $\vec{p}_\xi^{\,\text{GJ}} = \vec{p}_1^{\,\text{GJ}} + \vec{p}_2^{\,\text{GJ}}$. The variable $m_{2\pi}$ is the invariant mass of the isobar and as such Lorentz invariant. The isobar decay $\xi \to \pi^+\pi^-$ is described in the helicity frame. This is the rest frame of ξ, where the z_{HF} axis is in direction of the isobar momentum in the Gottfried-Jackson frame. The y_{HF} axis is given by $\hat{e}_y^{\text{HF}} \propto \hat{e}_z^{\text{GJ}} \times \hat{e}_z^{\text{HF}}$ and the x_{HF} axis completes the right-handed coordinate system: $\hat{e}_x^{\text{HF}} = \hat{e}_y^{\text{HF}} \times \hat{e}_z^{\text{HF}}$. The angular variables ϕ_{HF} and θ_{HF} are the azimuthal and polar angle of the momentum of the π_1^- stemming from the isobar decay.

4.1.3. Helicity amplitudes

For the analysis performed in refs. [8, 12] the helicity formalism was used [22, 23, 27]. In this formalism, the quantization axis for the spin of the isobar is its direction of motion, as defined in section 4.1.2. The isobar states are therefore helicity states, with a spin projection λ along the direction of the isobar momentum, which is equivalent to the z projection quantum number in this reference frame.

With the definitions made above, we are able to formulate the Bose-symmetrized decay amplitude $\mathcal{A}_i(\vec{\tau})$ for a $m_{3\pi}$ bin for a wave i, as defined in eq. (3.6):

$$\mathcal{A}_i(\vec{\tau}) = \frac{1}{\sqrt{2}} \left[\hat{\mathcal{A}}_i(\vec{\tau}_{12}) + \hat{\mathcal{A}}_i(\vec{\tau}_{23}) \right], \tag{4.4}$$

where $\hat{\mathcal{A}}_i(\vec{\tau})$ is the non-Bose-symmetrized decay amplitude from eq. (3.23):

$$\hat{\mathcal{A}}_i(\vec{\tau}) = \mathcal{N}_i \Psi_i(\vec{\tau}) \Delta_i(m_\xi), \tag{4.5}$$

and the spin amplitude $\Psi_i(\vec{\tau})$ is given by

$$\Psi_i(\phi_{\text{TY}}, \theta_{\text{GJ}}, \phi_{\text{HF}}, \theta_{\text{HF}}) =$$

$$\sum_{\lambda=-J_\xi}^{J_\xi} \sqrt{2L+1}\sqrt{2J_\xi+1}\,(L,0,J_\xi,\lambda|J_X,\lambda)\, D_{M_X\lambda}^{J_X*}(\phi_{\text{TY}}, \theta_{\text{GJ}}, 0)\, D_{\lambda 0}^{J_\xi*}(\phi_{\text{HF}}, \theta_{\text{HF}}, 0).$$

$$\tag{4.6}$$

The appearing sum runs over all possible helicity states λ of the isobar, from $-J_\xi$ to J_ξ. The $D_{m_1 m_2}^J(\alpha, \beta, \gamma)$ are the Wigner D-functions[b] that encode the angular

---

[b]Note, that complex conjugated Wigner D-functions appear in eq. (4.6), which perform active rather than passive rotations.

distributions of the two-body decays $X \to \xi \pi_3^-$ and $\xi \to \pi_1^- \pi_3^+$; they are tabulated in ref. [28]. The factor $(L, 0, J_\xi, \lambda | J_X, \lambda)$ is the Clebsch-Gordan coefficient, for the coupling of the orbital angular momentum L with spin projection of zero and the spin J_ξ of the isobar with spin projection λ to the total spin J_X which also has a spin projection of λ. The spin projections of J_X and J_ξ have to be equal, since the spin projection of L vanishes, because the quantization axis for angular momenta in the helicity frame is the direction of the isobar momentum and the orbital angular momentum is always orthogonal to the direction of motion; this is a specific feature of the helicity formalism.

Note, that within the helicity formalism, the resonance amplitudes of the isobars $\hat{\Delta}_i(m_\xi)$ in eq. (4.5) has to be modified with barrier factors, according to eq. (3.25), to obtain dynamic isobar amplitudes $\Delta_i(m_\xi)$ that have the correct dependence on the breakup momenta, since the spin amplitudes themselves do not include this dependence in the helicity formalism.

4.2. Conventional analysis of Compass data

With these prerequisites, a partial-wave analysis on the data set introduced in section 2.3 was performed, which is described in detail in refs. [8, 12]. In the following, we will give a short overview of this analysis.

As mentioned in section 4.1.2, the PWA was done in narrow bins of $m_{3\pi}$ and t' to infer the dependence of the partial-wave amplitudes on these variables from the data in a rather model-independent way. The $m_{3\pi}$ bins have a width of $20\,\mathrm{MeV}/c^2$ and span the whole analyzed range $0.5 < m_{3\pi} < 2.5\,\mathrm{GeV}/c^2$, resulting in 100 bins in the three-pion mass. The analyzed t' range, from 0.1 to $1.0(\mathrm{GeV}/c)^2$, was subdivided into ten non-equidistant bins, such that the number of events is roughly equal all bins. To achieve a better resolution, the highest t' bin was split into two, resulting in eleven t' bins. In total, the analysis consists of 1100 independent fits in every single $(m_{3\pi}, t')$ bin.

In principle, partial waves with arbitrarily high spins can contribute to process in 2.1, but the finite size of the data set and the finite amount of computing time require to chose a finite wave set. The wave set used in this analysis and the process of obtaining it are described in detail in ref. [8]. The wave-set consists of 88 partial waves, as listed in table 6.1: 80 waves with positive reflectivity, 7 with negative reflectivity, and a flat wave, as introduced in section 3.2. All waves employ the isobars and corresponding parameterizations of the resonance amplitudes listed in table 4.2. Note, that the two different reflectivity sectors are treated as incoherent sub-processes and that the negative reflectivity sector has

rank two[c]. Therefore, the model for the intensity has four incoherent contributions and eq. (3.19) becomes:

$$\Im\left(\vec{\tau}\right) = \Im_{\varepsilon=+1}\left(\vec{\tau}\right) + \Im_{\varepsilon=-1}^{r=1}\left(\vec{\tau}\right) + \Im_{\varepsilon=-1}^{r=2}\left(\vec{\tau}\right) + \Im_{\text{flat}}\left(\vec{\tau}\right), \tag{4.7}$$

where r denotes the rank of the negative-reflectivity sector.

For the parameterization of the resonance amplitudes, several variations of the fixed-width Breit-Wigner formula in eq. (3.26) are used. One common modification, is the use of a mass dependent width:

$$\hat{\Delta}_{\text{BW}}^{\text{rel}}\left(m_\xi\right) = \frac{m_0\Gamma_0}{m_0^2 - m_\xi^2 - \mathrm{i}m_0\Gamma(m_\xi)}, \tag{4.8}$$

where the width $\Gamma(m_\xi)$ is a real-valued function of the isobar mass [29]:

$$\Gamma(m_\xi) = \Gamma_0 \frac{m_0}{m_\xi} \frac{q\left(m_\xi, m_\pi, m_\pi\right)}{q\left(m_0, m_\pi, m_\pi\right)} \frac{F_{J_\xi}^2\left(q\left(m_\xi, m_\pi, m_\pi\right)\right)}{F_{J_\xi}^2\left(q\left(m_0, m_\pi, m_\pi\right)\right)}. \tag{4.9}$$

For the $\rho(770)$ resonance, a different parameterization of the mass-dependent width was used:

$$\Gamma(m_\xi) = \Gamma_0 \frac{q\left(m_\xi, m_\pi, m_\pi\right)}{q\left(m_0, m_\pi, m_\pi\right)} \frac{F_{J_\xi}^2\left(q\left(m_\xi, m_\pi, m_\pi\right)\right)}{F_{J_\xi}^2\left(q\left(m_0, m_\pi, m_\pi\right)\right)}. \tag{4.10}$$

For the $\rho_3(1690)$ resonance, another modification of fixed-width the Breit-Wigner formula in eq. (3.26) was used:

$$\hat{\Delta}_{\rho_3}\left(m_\xi\right) = \frac{\sqrt{m_\xi m_0}\Gamma_0}{m_0^2 - m_\xi^2 - \mathrm{i}m_0\Gamma_0}. \tag{4.11}$$

Since the mass of the $f_0(980)$ is close to the $K\bar{K}$ threshold, the Flatté formula [30, 31] is used to describe its resonance amplitude:

$$\hat{\Delta}^{\text{Flatté}}\left(m_\xi\right) = \frac{1}{m_0^2 - m_\xi^2 - \mathrm{i}\left(\phi_\pi g_\pi + \phi_{\text{K}} g_{\text{K}}\right)}, \tag{4.12}$$

where g_π and g_{K} are the couplings of the resonance to the $\pi\pi$ and KK decay channel—the parameter values are taken from ref. [30]—and $\phi_{\pi,\text{K}}$ are given as [30, 31]:

$$\phi_{\pi,\text{K}} = \frac{2q\left(m_\xi, m_{\pi,\text{K}}, m_{\pi,\text{K}}\right)}{m_\xi}. \tag{4.13}$$

---

[c] In the PWA of refs. [8, 12] the spin density matrix $\varrho_{ij} = \mathcal{T}_i^*\mathcal{T}_j$ is constructed. Using only one production amplitude per wave, this matrix has a rank of one. However, if r sets of incoherent production amplitudes are used for one sector, the resulting spin-density matrix has rank r. For a more detailed discussion on the rank consult ref. [12].

Table 4.2.: Isobars and the parameterizations used for their resonance amplitudes as in refs. [8, 12].

Resonance	Parameterization	Parameters
$(\pi\pi)_{\mathrm{S}}$[d]	M-solution	-
$\mathrm{f}_0(980)$	Flatté formula (eq. (4.12))	$m_0 = 965\,\mathrm{MeV}/c^2$ $g_\pi = 0.165(\mathrm{GeV}/c^2)^2$ $g_\pi/g_{\mathrm{K}} = 4.21$
$\mathrm{f}_0(1500)$	Breit-Wigner (eq. (3.26))	$m_0 = 1507\,\mathrm{MeV}/c^2$ $\Gamma_0 = 109\,\mathrm{MeV}/c^2$
$\rho(770)$	Breit-Wigner (eqs. (4.8) and (4.10))	$m_0 = 768.5\,\mathrm{MeV}/c^2$ $\Gamma_0 = 150.7\,\mathrm{MeV}/c^2$
$\mathrm{f}_2(1270)$	Breit-Wigner (eqs. (4.8) and (4.9))	$m_0 = 1275.4\,\mathrm{MeV}/c^2$ $\Gamma_0 = 185.2\,\mathrm{MeV}/c^2$
ρ_3	Breit-Wigner (eq. (4.11))	$m_0 = 1690\,\mathrm{MeV}/c^2$ $\Gamma_0 = 190\,\mathrm{MeV}/c^2$

Since the $(\pi\pi)_{\mathrm{S}}$ is known to have a very broad mass shape, the modified M-solution taken from ref. [32] was used as parameterization for the resonance amplitude, which is not a modification of the Breit-Wigner formula. Since the $\mathrm{f}_0(980)$ is used as separate isobar and its corresponding contributions have been subtracted from the resonance amplitude of the $(\pi\pi)_{\mathrm{S}}$.

With these parameterizations of the resonance amplitudes of all included isobars, a detailed PWA of the Compass data was performed in refs. [8, 12]. However, since the used parameterizations of the resonance amplitudes are not the only possible choices. F. Haas performed several studies on the effect of different parameterizations of the resonance amplitudes in ref. [8]:

- replacing the Flatté by a relativistic Breit-Wigner for the $\mathrm{f}_0(980)$,

- replacing the $\mathrm{f}_0(500)$ and the $\mathrm{f}_0(980)$ by a combined parameterization, the K_1-solution, also taken from ref. [32], and

- replacing the relativistic Breit-Wigner for the $\rho(770)$ resonance by a $(\pi\pi)_{\mathrm{P}}$-wave, taken from ref. [33].

These studies showed, that at least for some partial waves the results can depend strongly on the used parameterizations for the resonance amplitudes of the isobars. Figure 4.1 shows, as an example, some of the observed strong effects: a change of the $\mathrm{f}_0(980)$ parameterization strongly influences height of the peak in the $\pi(1800)$

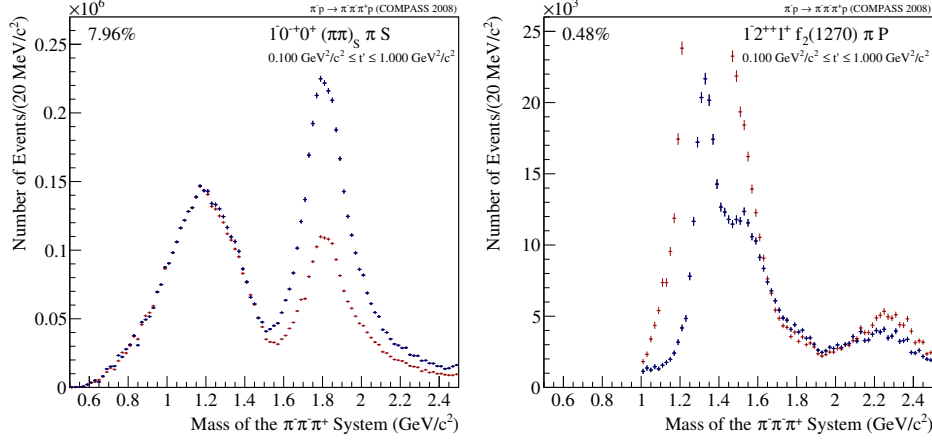[d]Also known as $\mathrm{f}_0(500)$ or σ.

Figure 4.1.: Comparison of partial-wave intensities obtained from a PWA using the resonance amplitudes listed in table 4.2 (blue) with those using alternative resonance amplitudes (red). In the left study, the Flatté form of the $f_0(980)$ was replaced by a relativistic Breit-Wigner amplitude and in the right study, the relativistic Breit-Wigner amplitude for the $\rho(770)$ was replaced by a parameterization for the $(\pi\pi)_P$-wave, taken from ref. [33]. Both pictures are taken from ref. [8].

region in the $0^{-+}0^+ (\pi\pi)_S \pi S$ wave. A change in the parameterization of the $\rho(770)$ strongly changes the extracted $2^{++}1^+ f_2(1270) \pi P$ amplitude. This influence of the choice of a particular parameterizations for dynamic isobar amplitudes on the PWA results on waves employing this parameterization, as well as on waves that do not, is one of the major caveats of a PWA with predefined resonance amplitudes.

4.3. Problems of conventional PWA

In section 4.2 we have seen the strong dependence of partial-wave amplitudes obtained by conventional PWA on the choice of parameterizations for the resonance amplitudes of the isobars. However, for a PWA model, the resonance content of the isobars has to be specified as well. Dominating resonances can easily be seen in kinematic distributions, like in the 2π spectrum in fig. 2.3. Smaller signals, for example stemming from excited resonances or from states with higher spins can not be identified this way. Since in some cases there are several disputed states, is not clear, which of them to include in the model (see ref. [2]).

A first solution to this problem, that comes to mind, would be the addition of several isobar resonances to the model. However, it turns out that this approach has some caveats due to the fact, that there is no reliable way to determine, whether a resonance is actually present in the data. One way to compare different models is the resulting value of the likelihood function, but such a comparison only carries meaning for nested models, since additional free fit parameters always increase the
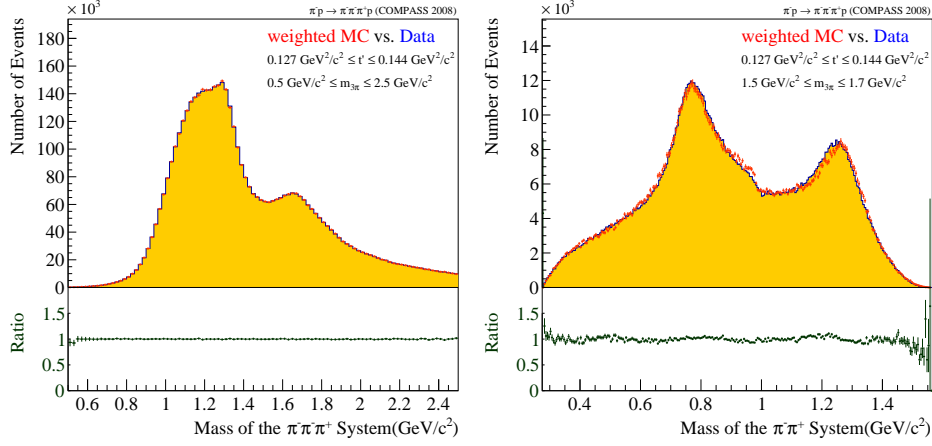
Figure 4.2.: Comparison between weighted Monte Carlo and real data of $m_{3\pi}$ and $m_{2\pi}$ spectra. Both pictures are taken from ref. [8].

value of the likelihood function and thus this value cannot be used for a reliable model selection procedure. A second approach to judge the goodness of PWA models is to generate weighted Monte Carlo data sets according to corresponding fit results and compare the resulting kinematic distributions to the input data. Such a comparison is shown in fig. 4.2. However, also this approach fails, if the corresponding signals are several orders of magnitude smaller, than dominating isobars.

A more elaborate approach to model selection has been developed by K. Bicker in ref. [13], where he develops an automated prior-based model selection method. This method was applied to the diffractive three pion production by O. Drotleff and F. Kaspar and in refs. [9, 14]. But even for this elaborate method, it turns out to be difficult to determine, whether excited isobar resonances contribute to the data, since especially at low $m_{3\pi}$ waves that differ only in their respective dynamic isobar amplitudes become indistinguishable.

In addition to these problems, a simple summation of several waves, that differ only in their respective resonance amplitudes, violates unitarity—a fundamental requirement of S matrix theory. One possible approach would be, to employ resonance amplitudes with free parameters in the fit, to directly determine these parameters from the data. However, the analysis method introduced in section 3.2 does not allow for free parameters in the decay amplitudes, since they do not enter the fit model linearly and therefore would require a recalculation of the normalization integrals and the decay amplitudes for all events in every fit iteration and thus increase the necessary computational effort for such analyses by several orders of magnitude.

26

Chapter 5.

Freed-isobar Partial-Wave Analysis

In section 4.3 we have seen, that in a conventional PWA the choice of the most suitable parameterization for the dynamic isobar amplitudes and the reliable determination of appearing isobar resonances, that contribute only weakly to the process, is difficult. Due to technical reasons, a direct fit of the dynamic isobar amplitudes is impractical, and could also lead to other problems like multi-modality and increased model bias, as seen in refs. [34, 35] in a related analysis, where the systematic uncertainties due to model building are an order of magnitude larger than the statistical ones. Therefore, we propose a different approach, that aims for a more model-independent extraction of dynamic isobar amplitudes.

5.1. The basic idea of freed-isobar PWA

To circumvent the strong dependence of PWA results on the predefined parameterizations of isobar dynamic amplitudes, seen in section 4.2, and to be able to extract small contributions directly from the data, we explore a method, first presented in ref. [10] and described in detail in ref. [36]. Here the necessity for prior knowledge on the dynamic isobar amplitudes is circumvented by replacing the fixed parameterizations in eq. (3.23) with sets indicator functions $\Delta_{\mathrm{bin}}^{\sqcap}\left(m_\xi\right)$ such that:

$$\Delta_i\left(m_\xi\right) = \sum_{\mathrm{bin}} \alpha_i^{\mathrm{bin}} \Delta_{\mathrm{bin},i}^{\sqcap}\left(m_\xi\right), \tag{5.1}$$

where the sum runs over n_{bins} contiguous regions in m_ξ that span the whole kinematically allowed range. The parameters α_i^{bin} are complex-valued constants that represent the dynamic amplitude of the partial wave labeled with index i at a given bin of the isobar mass. The dynamic amplitude is approximated as constant over the narrow mass range of the m_ξ bins. The indicator functions are given by:

$$\Delta_{\mathrm{bin}}^{\sqcap}\left(m_\xi\right) = \left\{ \begin{array}{l} 1 \text{ if } m_\xi \in \mathrm{bin}, \\ 0 \text{ otherwise.} \end{array} \right. \tag{5.2}$$

With this replacement, the total amplitude in eq. (3.6) becomes:

$$\mathfrak{A}\left(\vec{\tau}\right) = \sum_i \mathcal{N}_i \mathcal{T}_i \Psi_i\left(\vec{\tau}\right) \sum_{\mathrm{bins}} \alpha_i^{\mathrm{bin}} \Delta_{\mathrm{bin},i}^{\sqcap}\left(m_\xi\right). \tag{5.3}$$

We can now define:

$$\mathcal{T}_i^{\text{bin}} = \mathcal{N}_i/\mathcal{N}_i^{\text{bin}} \mathcal{T}_i \alpha_i^{\text{bin}} \text{ and } \mathcal{A}_i^{\text{bin}}(\vec{\tau}) = \mathcal{N}_i^{\text{bin}} \Psi_i(\vec{\tau}) \Delta_{\text{bin},i}^{\square}(m_\xi), \qquad (5.4)$$

to obtain:

$$\mathfrak{A}(\vec{\tau}) = \sum_i \sum_{\text{bins}} \mathcal{T}_i^{\text{bin}} \mathcal{A}_i^{\text{bin}}(\vec{\tau}). \qquad (5.5)$$

This expression is of the same structure as eq. (3.6), where each amplitude for an m_ξ bin appears like an independent partial wave. We therefore can employ the same maximum likelihood approach layed out in section 3.2. The factor $\mathcal{N}_i^{\text{bin}}$ ensures proper normalization of every m_ξ bin in every wave.

Since the number of free parameters increases by $2(n_{\text{bins}} - 1)$ for every dynamic amplitude that is replaced according to eq. (5.1), this approach is only suitable for large data sets. However, when applicable, this method allows for the binned extraction of isobar dynamic amplitudes directly from the data with a resolution of the chosen bin width.

If a fixed isobar parameterization is replaced in the way described above, we will refer to it as *freed* isobar; isobars with fixed dynamic amplitudes will be called *fixed*. Note, that not all waves in a wave set have to be freed and every model combining any number of waves with fixed and freed isobars is possible within this approach:

$$\mathfrak{A}(\vec{\tau}) = \sum_i \sum_{\text{bins}} \mathcal{T}_i^{\text{bin}} \mathcal{A}_i^{\text{bin}}(\vec{\tau}) + \sum_j \mathcal{T}_j \mathcal{A}_j, \qquad (5.6)$$

where the index i runs over all waves with freed isobars and j runs over all waves with fixed isobars.

Since the $\mathcal{T}_i^{\text{bin}}$ are in units of square root of number of events, their magnitude does not only depend on the dynamic amplitude of the isobar, but also on the width of the isobar mass bin, since in a narrower bin lie less events. Since in our analysis we want to have a variable bin width, we introduce the normalized production amplitudes $\mathcal{B}_i^{\text{bin}}$:

$$\mathcal{B}_i^{\text{bin}} = \frac{\mathcal{T}_i^{\text{bin}}}{\sqrt{\text{bin width}}}. \qquad (5.7)$$

This quantity is useful to plot the results of a freed isobar analysis, since discontinuities due to a changing bin width are removed.

5.2. Ambiguities in freed-isobar PWA

Since the replacement of fixed isobars by freed ones drastically increases the freedom in the PWA model, the question arises, if such a model is still able to describe the data unambiguously. To study this, we look at the simple example case:

$$\pi(1800) \to \pi_1^- \pi_2^+ \pi_3^-. \qquad (5.8)$$

In this process, all initial- and final-state particles have the quantum numbers $J^{PC} = 0^{-+}$, thus every particle is a scalar and there are no external angles due to polarizations to take into account, so only two kinematic variables suffice to describe the process. We chose them to be m_{12} and m_{23}, which are the invariant masses of the two-particle systems (12) and (23). Since in the final state two identical π^- appear, eq. (3.23) has to be slightly modified, as in eq. (4.4), to ensure the required Bose symmetry:

$$\mathcal{A}_i\left(m_{12}, m_{23}\right) = \Psi_i\left(m_{12}, m_{23}\right)\Delta_i\left(m_{12}\right) + \Psi_i\left(m_{23}, m_{12}\right)\Delta_i\left(m_{23}\right). \qquad (5.9)$$

For simplicity, we leave out the normalization factors of eq. (3.23) in this chapter, but all results stay valid with the proper normalization defined in eq. (3.14).

For the process specified in eq. (5.8), we have to chose a wave set. For simplicity, we restrict ourselves to two waves, one for the decay via a $(\pi^+\pi^-)$ isobar with $J^{PC} = 0^{++}$ and one via a $J^{PC} = 1^{--}$ isobar. Since the spin of the $\pi(1800)$ is zero, the orbital angular momentum between the bachelor π^- and the isobar has to be equal to the spin of the latter. Hence, the decay into the spin-zero isobar proceeds via an S-wave and that into the spin-one isobar via a P-wave. For this example, we label the two waves S and P.

With this at hand, the total amplitude in this model is:

$$\begin{aligned}\mathfrak{A}\left(m_{12}, m_{23}\right) =& \mathcal{T}_{\mathrm{S}}\left(\Psi_{\mathrm{S}}\left(m_{12}, m_{23}\right)\Delta_{\mathrm{S}}\left(m_{12}\right) + \Psi_{\mathrm{S}}\left(m_{23}, m_{12}\right)\Delta_{\mathrm{S}}\left(m_{23}\right)\right)\\ &\mathcal{T}_{\mathrm{P}}\left(\Psi_{\mathrm{P}}\left(m_{12}, m_{23}\right)\Delta_{\mathrm{P}}\left(m_{12}\right) + \Psi_{\mathrm{P}}\left(m_{23}, m_{12}\right)\Delta_{\mathrm{P}}\left(m_{23}\right)\right).\end{aligned} \qquad (5.10)$$

We now consider completely arbitrary dynamic isobar amplitudes in the S and P waves, which would correspond to freed dynamic isobar amplitudes with an infinite number of bins and therefore a vanishing bin width. With this complete freedom, we construct parameterizations for the dynamic isobar amplitudes, $\Delta_{\mathrm{S}}^0\left(m_\xi\right)$ and $\Delta_{\mathrm{P}}^0\left(m_\xi\right)$, that cause the total amplitude in eq. (5.10) to vanish:

$$\begin{aligned}&\Psi_{\mathrm{S}}\left(m_{12}, m_{23}\right)\Delta_{\mathrm{S}}^0\left(m_{12}\right) + \Psi_{\mathrm{S}}\left(m_{23}, m_{12}\right)\Delta_{\mathrm{S}}^0\left(m_{23}\right) +\\ &\Psi_{\mathrm{P}}\left(m_{12}, m_{23}\right)\Delta_{\mathrm{P}}^0\left(m_{12}\right) + \Psi_{\mathrm{P}}\left(m_{23}, m_{12}\right)\Delta_{\mathrm{P}}^0\left(m_{23}\right) = 0.\end{aligned} \qquad (5.11)$$

Note, that for simplicity, we left out the production amplitudes $\mathcal{T}_{\mathrm{S/P}}$, since they are constant prefactors to the arbitrary dynamic amplitudes and can be absorbed therein.

If we find a pair of functions $\Delta_{\mathrm{S}}^0\left(m_\xi\right)$ and $\Delta_{\mathrm{P}}^0\left(m_\xi\right)$, that fulfill eq. (5.11), we can add them with an arbitrary complex-valued coefficient $\mathcal{C}$ to eq. (5.10) and obtain:

$$\begin{aligned}\mathfrak{A}\left(m_{12}, m_{23}\right) = \ &\Psi_{\mathrm{S}}\left(m_{12}, m_{23}\right)\left(\mathcal{T}_{\mathrm{S}}\Delta_{\mathrm{S}}\left(m_{12}\right) + \mathcal{C}\Delta_{\mathrm{S}}^0\left(m_{12}\right)\right)\\ &+\Psi_{\mathrm{S}}\left(m_{23}, m_{12}\right)\left(\mathcal{T}_{\mathrm{S}}\Delta_{\mathrm{S}}\left(m_{23}\right) + \mathcal{C}\Delta_{\mathrm{S}}^0\left(m_{23}\right)\right)\\ &+\Psi_{\mathrm{P}}\left(m_{12}, m_{23}\right)\left(\mathcal{T}_{\mathrm{P}}\Delta_{\mathrm{P}}\left(m_{12}\right) + \mathcal{C}\Delta_{\mathrm{P}}^0\left(m_{12}\right)\right)\\ &+\Psi_{\mathrm{P}}\left(m_{23}, m_{12}\right)\left(\mathcal{T}_{\mathrm{P}}\Delta_{\mathrm{P}}\left(m_{23}\right) + \mathcal{C}\Delta_{\mathrm{P}}^0\left(m_{23}\right)\right).\end{aligned} \qquad (5.12)$$

We see, that since $\Delta_{\mathrm{S/P}}^0\left(m_\xi\right)$ fulfill eq. (5.11), the total amplitude described in eq. (5.12) is independent of $\mathcal{C}$, and in turn the intensity and the likelihood are

as well. Therefore, two descriptions of the amplitude differing by the value of $\mathcal{C}$ cannot be distinguished in a log likelihood fit.

In a conventional PWA this does not pose a problem, since there the dynamic amplitudes are fixed and different values of $\mathcal{C}$, which would result in different dynamic amplitudes for S and P wave, are not within the scope of the model. However, in a freed isobar analysis[a], different dynamic amplitudes and therefore different values of $\mathcal{C}$ are possible within the model. Therefore, $\mathcal{C}$ represents a continuous ambiguity in the freed isobar model.

We will call such a combination of dynamic amplitudes, that fulfill eq. (5.10) *zero mode* from hereon. The exact shape of these dynamic amplitudes depends om the chosen spin formalism. In the following, we will discuss them for several cases and for two different spin formalisms: the non-relativistic tensor formalism and the covariant tensor formalism, taken from refs. [18–21] and shortly layed out in appendix A[b].

5.2.1. Non-relativistic tensor formalism

As first formalism to determine the dynamic amplitudes of the zero mode in the examples case of section 5.2, we use the non-relativistic tensor formalism [20, 21], in which quantities of spin s are represented as symmetric, traceless three-dimensional tensors of rank s. We chose this formalism first, since it is commonly used in various analyses and was numerically tested to be equivalent to the helicity formalism introduced in section 4.1.3, if the range of the interaction $1/q_R$, introduced in section 3.3, is set to zero.

Since in the S-wave, all appearing spin quantum-numbers are zero, the spin amplitude for this wave is trivial:

$$\Psi_{\mathrm{S}}^{\mathrm{Zem}}(m_{12}, m_{23}) = 1. \tag{5.13}$$

The P-wave spin amplitude is:

$$\Psi_{\mathrm{P}}^{\mathrm{Zem}}(m_{12}, m_{23}) = \vec{p}_3 \cdot \vec{p}_1\,' = -(\vec{p}_1 + \vec{p}_2) \cdot \vec{p}_1\,', \tag{5.14}$$

where $\vec{p}_1$, $\vec{p}_2$ and $\vec{p}_3$ are the three-momenta of the final-state particles in the $\pi(1800)$ rest frame, thus:

$$\vec{p}_1 + \vec{p}_2 + \vec{p}_3 = \vec{0}. \tag{5.15}$$

---

[a]At the moment, we still consider the case of an infinitesimal bin width. The effects of finite binning will be discussed in section 5.2.5.

[b]In these both formalisms, the resonance amplitudes are equal to the dynamic isobar amplitudes. Therefore, we will use $\Delta_i(m_\xi) \equiv \hat{\Delta}_i(m_\xi)$ throughout his chapter.

The vector $\vec{p}_1'$ is the three-momentum of π_1 in the rest system of the isobar ξ. To boost from the rest frame of $\pi(1800)$ to the rest frame of ξ, we need the four-momentum of ξ, which is given by:

$$p_{12}^\mu = p_1^\mu + p_2^\mu = \begin{pmatrix} \sqrt{m_{12}^2 + p_3} \\ 0 \\ 0 \\ -p_3 \end{pmatrix}, \qquad (5.16)$$

where we chose our coordinate system such, that $\vec{p}_3$ is in z direction $\hat{e}_z$. With these definitions, we can apply the Lorentz transformation into the ξ rest frame to p_1^μ:

$$p_1'^\mu = \begin{pmatrix} \frac{\sqrt{m_{12}^2+p_3^2}}{m_{12}} & 0 & 0 & \frac{p_3}{m_{12}} \\ 0 & 1 & 0 & 0 \\ 0 & 0 & 1 & 0 \\ \frac{p_3}{m_{12}} & 0 & 0 & \frac{\sqrt{m_{12}^2+p_3^2}}{m_{12}} \end{pmatrix} \begin{pmatrix} \sqrt{m_\pi^2 + |\vec{p}_1|^2} \\ p_{1x} \\ p_{1y} \\ p_{1z} \end{pmatrix}. \qquad (5.17)$$

The full spin amplitude is then given by:

$$\Psi_{\mathrm{P}}^{\mathrm{Zem}}(m_{12}, m_{23}) = p_{1z}'p_3 = \left(\frac{p_3}{m_{12}} \sqrt{m_\pi^2 + |\vec{p}_1|^2} + \frac{\sqrt{m_{12}^2 + p_3^2}}{m_{12}} p_{1z} \right) p_3, \qquad (5.18)$$

where we have made use of the fact, that $\vec{p}_3$ points in z direction. With the kinematical identities:

$$p_{1z} = \frac{\vec{p}_1 \cdot \vec{p}_3}{p_3}; \quad \vec{p}_1 \cdot \vec{p}_3 = \frac{1}{2} \left(|\vec{p}_2|^2 - |\vec{p}_1|^2 - |\vec{p}_3| \right); \quad |\vec{p}_i| = \sqrt{E_i^2 - m_\pi^2}, \qquad (5.19)$$

and the expressions for the energies of the final-state particles in the rest frame of $\pi(1800)$:

$$E_1 = \frac{m_{\pi(1800)}^2 - m_{23}^2 + m_\pi^2}{2m_{\pi(1800)}}; \quad E_2 = \frac{m_{12}^2 + m_{23}^2 - 2m_\pi^2}{2m_{\pi(1800)}}; \quad E_3 = \frac{m_{\pi(1800)}^2 - m_{12}^2 + m_\pi^2}{2m_{\pi(1800)}}, \qquad (5.20)$$

eq. (5.18) simplifies to:

$$\Psi_{\mathrm{P}}^{\mathrm{Zem}}(m_{12}, m_{23}) = \frac{m_{12}}{4m_{\pi(1800)}} \left(m_{\pi(1800)}^2 - m_{12}^2 - 2m_{23}^2 + 3m_\pi^2 \right). \qquad (5.21)$$

With this expression we find, that the following parameterizations for the dynamic amplitudes fulfill eq. (5.11) at every point in phase space and therefore constitute the zero mode:

$$\Delta_{\mathrm{S}}^{\mathrm{0Zem}}(m_\xi) = -\frac{1}{8} \left(m_{\pi(1800)}^2 - 3m_{\xi^2} + 3m_\pi^2 \right), \qquad (5.22)$$

$$\Delta_{\mathrm{P}}^{\mathrm{0Zem}}(m_\xi) = \frac{m_{\pi(1800)}}{m_\xi}. \qquad (5.23)$$

5.2.2. Covariant tensor formalism

Since the formalism discussed in section 5.2.1 is non-relativistic, we explore a second formalism, which is fully covariant: the covariant tensor formalism taken from refs. [18, 19] which we shortly introduce in appendix A.3. Since in the S-wave all spin quantum-numbers are zero, the corresponding spin-amplitude is the same as in the non-relativistic tensor formalism:

$$\Psi_{\mathrm{S}}^{\mathrm{Cov}}\left(m_{12}, m_{23}\right) = 1. \tag{5.24}$$

For the P-wave L and J_ξ take the value of one. Those two quantities are represented by two tensors of rank one: X_L^μ and X_ξ^μ, given in eq. (A.40). The spin amplitude is then:

$$\Psi_{\mathrm{P}}^{\mathrm{Cov}}\left(m_{12}, m_{23}\right) = X_L^\mu X_{\xi\mu}. \tag{5.25}$$

Keep in mind, that throughout this work we employ the Einstein sum convention. With the kinematic definitions:

$$p_\xi^\mu = p_1^\mu + p_2^\mu; \qquad\qquad k_\xi^\mu = \frac{1}{2}\left(p_1^\mu - p_2^\mu\right) \tag{5.26}$$

$$P^\mu = p_\xi^\mu + p_3^\mu; \qquad\qquad K^\mu = \frac{1}{2}\left(p_\xi^\mu - p_3^\mu\right), \tag{5.27}$$

the tensor corresponding to the decay of X with an orbital angular momentum of 1 becomes:

$$X_L^\mu = \left(g^\mu{}_\nu - \frac{P^\mu P_\nu}{m_{\pi(1800)}^2}\right) K^\nu. \tag{5.28}$$

The tensor for the isobar decay is:

$$X_\xi^\mu = \left(g^\mu{}_\nu - \frac{p_\xi^\mu p_{\xi\nu}}{m_\xi^2}\right) k_\xi^\nu = \frac{1}{2}\left(p_1^\mu - p_2^\mu\right). \tag{5.29}$$

With these definitions, the spin amplitude for the P-wave can be formulated in terms of m_{12} and m_{23}, using eq. (A.46):

$$\Psi_{\mathrm{P}}^{\mathrm{Cov}}\left(m_{12}, m_{23}\right) = X_L^\mu X_{\xi\mu} = \frac{1}{8m_{\pi(1800)}^2}\left(m_{\pi(1800)}^2 + m_{12}^2 - m_\pi^2\right)$$
$$\left(m_{\pi(1800)}^2 - m_{12}^2 - 2m_{23}^2 + 3m_\pi^2\right). \tag{5.30}$$

In the calculation above, we use the following identities for the appearing scalar products:

$$p_1^\mu p_{2\mu} = \frac{1}{2}\left(m_{12}^2 - 2m_\pi^2\right), \tag{5.31}$$

$$p_2^\mu p_{3\mu} = \frac{1}{2}\left(m_{23}^2 - 2m_\pi^2\right), \tag{5.32}$$

$$p_1^\mu p_{3\mu} = \frac{1}{2}\left(m_{\pi(1800)}^2 - m_{12}^2 - m_{23}^2 + m_\pi^2\right). \tag{5.33}$$

Compared with eq. (5.30) we find, that the P-wave spin amplitude in the non-relativistic tensor formalism differs only by a factor γ from the covariant tensor formalism:

$$\Psi_{\mathrm{P}}^{\mathrm{Cov}}\left(m_{12}, m_{23}\right) = \gamma \Psi_{\mathrm{P}}^{\mathrm{Zem}}\left(m_{12}, m_{23}\right), \tag{5.34}$$

where γ is the Lorentz factor of the isobar in the $\pi(1800)$ rest-system:

$$\gamma = \frac{E_{12}}{m_{12}} = \frac{\sqrt{m_{12}^2 + p_3^2}}{m_{12}} = \frac{m_{\pi(1800)}^2 + m_{12}^2 - m_\pi^2}{m_{\pi(1800)} m_{12}}. \tag{5.35}$$

Since $\Psi_{\mathrm{S}}\left(m_{12}, m_{23}\right)$ is equal in both formalisms and γ only depends on m_{12}, we can modify the dynamic amplitudes of the zero mode accordingly:

$$\Delta_{\mathrm{S}}^{0\mathrm{Cov}}\left(m_\xi\right) = \Delta_{\mathrm{S}}^{0\mathrm{Zem}}\left(m_\xi\right) = -\frac{1}{8}\left(m_{\pi(1800)}^2 - 3m_{\xi^2} + 3m_\pi^2\right), \tag{5.36}$$

$$\Delta_{\mathrm{P}}^{0\mathrm{Cov}}\left(m_\xi\right) = \frac{\Delta_{\mathrm{P}}^{0\mathrm{Zem}}\left(m_\xi\right)}{\gamma} = \frac{m_{\pi(1800)}^2}{m_{\pi(1800)}^2 + m_\xi^2 - m_\pi^2}, \tag{5.37}$$

and find, that these fulfill eq. (5.11) in case of the covariant tensor formalism, therefore the existence of the zero mode is not a consequence of a specific formalism, but appears in both of them.

5.2.3. Ambiguities for spin 1 three-body states

Above, we have shown the existence of a zero mode in the decay of a $\pi(1800)$ with $J^{PC} = 0^{-+}$ into three pions. We now consider the decay of a particle with $J^{PC} = 1^{++}$, for example an $a_1(1260)$, into the same final state.

We again use two isobars with $J^{PC} = 0^{++}$ and 1^{--} but since the overall spin is now one, the spinless isobar is in a relative P-wave with the bachelor pion, and the isobar with spin-one is in a relative S-wave. For these waves, the spin amplitudes in the covariant tensor formalism are given in eq. (A.48):

$$\Psi_{\mathrm{S}}^\mu\left(\vec{\tau}\right) = O^\mu{}_\nu X_{(12)\xi}^\nu, \tag{5.38}$$

$$\Psi_{\mathrm{P}}^\mu\left(\vec{\tau}\right) = O^\mu{}_\nu X_{(12)L}^\nu, \tag{5.39}$$

where the same tensor structures $X_{(12)L}^\mu$ and $X_{(12)\xi}^\mu$ as defined in eq. (5.28) and eq. (5.29) appear. We explicitly label them here with the particle content of the isobar, since we will need also their Bose symmetrized counterparts $X_{(23)L}^\mu$ and $X_{(23)\xi}^\mu$, where particles 1 and 3 are interchanged. Since the amplitudes represent spin 1 quantities they still carry a Lorentz-index, that corresponds to the three possible values for the spin-projection M. The fourth degree of freedom is removed by the projection operator $O^\mu{}_\nu$ given in eq. (A.50):

$$O^\mu{}_\nu = g^\mu{}_\nu + \frac{P^\mu P_\nu}{m_{a_1}^2}, \tag{5.40}$$

where is P^μ defined in eq. (5.26).

With this definition, we find:

$$O^\mu_{\ \nu} P^\nu = \left(g^\mu_{\ \nu} - \frac{P^\mu P_\nu}{m_{a_1}^2} \right) P^\nu = 0. \tag{5.41}$$

Using these definitions, we can write the total amplitude:

$$\mathfrak{A}^\mu_{a_1} (\vec{\tau}) = O^\mu_{\ \nu} \mathbb{X}^\nu, \tag{5.42}$$

where $\mathbb{X}^\mu$ is a linear combination of X^μ_L and X^μ_ξ:

$$\begin{aligned} \mathbb{X}^\mu =\ & X^\mu_{(12)L} \Delta_S (m_{12}) + X^\mu_{(12)\xi} \Delta_P (m_{12}) \\ & + X^\mu_{(12)L} \Delta_S (m_{23}) + X^\mu_{(23)\xi} \Delta_P (m_{23}) \\ =\ & c_1 p_1^\mu + c_2 p_2^\mu + c_3 p_3^\mu, \end{aligned} \tag{5.43}$$

where we can write the last equality, since the three four-momenta of the final-state particles are the only available four-vectors. With the definitions of the tensor structures, we can collect the coefficients c_1, c_2, and c_3:

$$\begin{aligned} c_1 = \frac{1}{2} \Bigg[& -\Delta_S^{a_1} (m_{12}) + \left(1 - \frac{m_{12}^2 - m_\pi^2}{m_{a_1}^2} \right) \Delta_P^{a_1} (m_{12}) \\ & - \left(1 + \frac{m_{23}^2 - m_\pi^2}{m_{a_1}^2} \right) \Delta_P^{a_1} (m_{23}) \Bigg] \end{aligned} \tag{5.44}$$

$$\begin{aligned} c_2 = \frac{1}{2} \Bigg[& \Delta_S^{a_1} (m_{12}) + \left(1 - \frac{m_{12}^2 - m_\pi^2}{m_{a_1}^2} \right) \Delta_P^{a_1} (m_{12}) \\ & + \Delta_S^{a_1} (m_{23}) + \left(1 - \frac{m_{23}^2 - m_\pi^2}{m_{a_1}^2} \right) \Delta_P^{a_1} (m_{23}) \Bigg] \end{aligned} \tag{5.45}$$

$$\begin{aligned} c_3 = \frac{1}{2} \Bigg[& - \left(1 + \frac{m_{12}^2 - m_\pi^2}{m_{a_1}^2} \right) \Delta_P^{a_1} (m_{12}) \\ & - \Delta_S^{a_1} (m_{23}) + \left(1 - \frac{m_{23}^2 - m_\pi^2}{m_{a_1}^2} \right) \Delta_P^{a_1} (m_{23}) \Bigg]. \end{aligned} \tag{5.46}$$

If we find dynamic amplitudes $\Delta_S^{0a_1} (m_\xi)$ and $\Delta_P^{0a_1} (m_\xi)$ such, that:

$$c_1 = c_2 = c_3, \tag{5.47}$$

the linear combination $\mathbb{X}^\mu$ is proportional to P^μ and the total amplitude $\mathfrak{A}^\mu (m_{12}, m_{23})$ vanishes due to eq. (5.41). This is true, if both dynamic amplitudes are constant with the fixed ratio of:

$$\Delta_S^{0a_1} (m_\xi) = -\frac{2}{3} \Delta_P^{0a_1} (m_\xi). \tag{5.48}$$

Thus we have identified a zero mode in the decay of a spin one particle.

Another peculiar process is the decay of a spin-exotic $J^{PC} = 1^{-+}$ state, e.g. a π_1, into the same 3π final state. We only consider the decay via a $J^{PC} = 1^{--}$ isobar, which has to be in a relative P-wave with respect to the bachelor pion to render the parity of the system to be -1. Using the known tensors for a spin one isobar X^μ_ξ and a P-wave decay X^μ_L, the spin amplitude for this process is given according to eq. (A.47) as:

$$\Psi^\mu_{\pi_1}(\vec{\tau}) = O^\mu{}_\nu \epsilon^{\nu\rho\sigma\tau} P_\rho X_{L\sigma} X_{\xi\tau}, \tag{5.49}$$

where $\epsilon^{\mu\nu\rho\sigma}$ is the totally antisymmetric tensor. Since P^μ, X^μ_L, and X^μ_ξ are linear combinations of p^μ_1, p^μ_2 and, p^μ_3 and the contraction of two indices of the antisymmetric tensor with identical vectors vanishes, the spin amplitude simplifies to:

$$\Psi^\mu_{\pi_1}(\vec{\tau}) = -O^\mu{}_\nu \epsilon^{\nu\rho\sigma\tau} p_{1\rho} p_{2\sigma} p_{3\tau}. \tag{5.50}$$

Since in this example, we only have one wave, the Bose symmetrized amplitude has to vanish to fulfill eq. (5.11) and constitute a zero mode:

$$0 = \Psi^\mu_{\pi_1}(\vec{\tau}) \Delta^0_{\pi_1}(m_{12}) + \Psi^\mu_{\pi_1}(\vec{\tau}) \Delta^0_{\pi_1}(m_{23}). \tag{5.51}$$

Making use of the antisymmetry of the ϵ-tensor, we arrive at:

$$0 = O^\mu{}_\nu \epsilon^{\nu\rho\sigma\tau} p_{1\rho} p_{2\sigma} p_{3\tau} \left(\Delta^0_{\pi_1}(m_{23}) - \Delta^0_{\pi_1}(m_{12}) \right), \tag{5.52}$$

which is fulfilled, if $\Delta^0_{\pi_1}(m_\xi)$ is constant. A change of the dynamic isobar amplitude of this wave by a constant does not change the overall amplitude. This result shows, that it is possible to find a zero mode within a single wave.

5.2.4. General pseudoscalar decays

Up to now, all zero modes originated from the Bose symmetrization of freed-isobar waves. However, ambiguities may arise also in cases without Bose symmetrization. To show this, we consider the decay of a pseudoscalar particle X into three different pseudoscalars a, b, and c.

Since we consider the most general case, we allow for all possible particle combinations to form the isobar: (ab), (ac) and (bc). We start by considering $J^{PC}_\xi = 0^{++}$ isobars. Since in this case, the isobar has to be in a relative S-wave with respect to the bachelor particle, we can write for the total amplitude:

$$\mathfrak{A}^{\mathrm{S}}_{abc}(m_{ab}, m_{bc}) = \mathcal{T}^{\mathrm{S}}_{ab}\Delta^{\mathrm{S}}_{ab}(m_{ab}) + \mathcal{T}^{\mathrm{S}}_{ac}\Delta^{\mathrm{S}}_{ac}(m_{ac}) + \mathcal{T}^{\mathrm{S}}_{bc}\Delta^{\mathrm{S}}_{bc}(m_{bc}), \tag{5.53}$$

since the spin amplitudes are all constant. For every two-particle combination we allow for a completely independent dynamic amplitude. Note, that the third invariant mass m_{ac} is not an additional phase-space variable, since it is fully determined by:

$$m^2_{ab} + m^2_{ac} + m^2_{bc} = m^2_X + m^2_a + m^2_b + m^2_c. \tag{5.54}$$

Looking at equation eq. (5.53), we already find two zero modes in this model, with constant shape in each dynamic amplitude:

$$
\begin{aligned}
\mathfrak{A}^{\mathrm{S}}_{abc}\left(m_{ab}, m_{bc}\right) =& \mathcal{T}^{\mathrm{S}}_{ab}\Delta^{\mathrm{S}}_{ab}\left(m_{ab}\right) + \mathcal{C}^{\mathrm{S}}_1 \\
& + \mathcal{T}^{\mathrm{S}}_{ac}\Delta^{\mathrm{S}}_{ac}\left(m_{ac}\right) + \mathcal{C}^{\mathrm{S}}_2 \\
& + \mathcal{T}^{\mathrm{S}}_{bc}\Delta^{\mathrm{S}}_{bc}\left(m_{bc}\right) - \mathcal{C}^{\mathrm{S}}_1 - \mathcal{C}^{\mathrm{S}}_2.
\end{aligned}
\tag{5.55}
$$

This amplitude sum is completely independent of $\mathcal{C}^{\mathrm{S}}_1$ and $\mathcal{C}^{\mathrm{S}}_2$, but the way they are grouped in eq. (5.55) indicates, how they can be absorbed in the respective dynamic isobar amplitudes. If only two S-waves are free, one zero mode remains. With just a single free S-wave, no zero modes remain, even if this amplitude is Bose-symmetrized, since eq. (5.55) requires opposite sign in the coefficients, while Bose symmetry requires equality.

We now consider isobars with quantum numbers $J^{PC}_\xi = 1^{--}$, which therefore have to be in a relative P-wave with respect to the bachelor particle. Since the masses of the final-state particles may be different, the P-wave amplitude differs from the first example case in section 5.2.1. In the non-relativistic tensor formalism, it is given by:

$$
\Psi^{\mathrm{P}}_{ab}\left(m_{ab}, m_{bc}\right) = \frac{m_{ab}}{4m_X}\left(m_{bc}^2 - m_{ac}^2 - \left(m_X^2 - m_c^2\right)\frac{m_a^2 - m_b^2}{m_{ab}^2}\right),
\tag{5.56}
$$

where the isobar is formed by (ab). For the other two possible combinations, (bc) and (ac), cyclic permutations of the particle content in eq. (5.56) are performed.

With this formula, the total amplitude of all P-waves combined is:

$$
\begin{aligned}
\mathfrak{A}^{\mathrm{P}}_{abc}\left(m_{ab}, m_{bc}\right) =& \Psi_{ab}\left(m_{ab}, m_{bc}\right)\left(\mathcal{T}^{\mathrm{P}}_{ab}\Delta^{\mathrm{P}}_{ab}\left(m_{ab}\right) + \mathcal{C}^{\mathrm{P}}\Delta^{0}_{\mathrm{P}}\left(m_{ab}\right)\right) \\
& + \Psi_{bc}\left(m_{ab}, m_{bc}\right)\left(\mathcal{T}^{\mathrm{P}}_{bc}\Delta^{\mathrm{P}}_{bc}\left(m_{bc}\right) + \mathcal{C}^{\mathrm{P}}\Delta^{0}_{\mathrm{P}}\left(m_{bc}\right)\right) \\
& + \Psi_{ac}\left(m_{ab}, m_{bc}\right)\left(\mathcal{T}^{\mathrm{P}}_{ac}\Delta^{\mathrm{P}}_{ac}\left(m_{ac}\right) + \mathcal{C}^{\mathrm{P}}\Delta^{0}_{\mathrm{P}}\left(m_{ac}\right)\right).
\end{aligned}
\tag{5.57}
$$

This total amplitude is independent of $\mathcal{C}^{\mathrm{P}}$, if we use:

$$
\Delta^{0}_{\mathrm{P}}\left(m_\xi\right) = m_\xi,
\tag{5.58}
$$

which therefore constitutes another zero mode in this process, which is only present if all three possible particle combinations employ freed dynamic amplitudes for spin-one isobars.

If we allow for S- and P-waves to have freed dynamic amplitudes for the isobars simultaneously, we encounter three additional zero modes—one for each particle combination—that connect both spin amplitudes:

$$
\begin{aligned}
\mathfrak{A}_{abc}\left(m_{ab}, m_{bc}\right) =& \mathfrak{A}^{\mathrm{S}}_{abc}\left(m_{ab}, m_{bc}\right) + \mathfrak{A}^{\mathrm{P}}_{abc}\left(m_{ab}, m_{bc}\right) \\
=& \sum_{\mathrm{cycl.}}\Bigg[\mathcal{T}^{\mathrm{S}}_{ab}\Delta^{\mathrm{S}}_{ab}\left(m_{ab}\right) + \left(\mathcal{C}^{\mathrm{SP}}_{bc} - \mathcal{C}^{\mathrm{SP}}_{ac}\right)m_{ab}^2 + \mathcal{C}^{\mathrm{SP}}_{ab}\left(m_X^2 - m_c^2\right)\frac{m_a^2 - m_b^2}{m_{ab}^2} \\
& + \Psi^{\mathrm{P}}_{ab}\left(m_{ab}, m_{bc}\right)\left(\mathcal{T}^{\mathrm{P}}_{ab}\Delta^{\mathrm{P}}_{ab}\left(m_{ab}\right) + \mathcal{C}^{\mathrm{SP}}_{ab}\frac{4m_X}{m_{ab}}\right)\Bigg],
\end{aligned}
\tag{5.59}
$$

where the sum runs over all cyclic permutations of the particles a, b, and c. The three zero mode amplitudes are encoded by $\mathcal{C}_{ab}^{\mathrm{SP}}$, $\mathcal{C}_{ac}^{\mathrm{SP}}$, and $\mathcal{C}_{bc}^{\mathrm{SP}}$.

If we use freed free S- and P-wave dynamic amplitudes for only two of the possible three combinations of final-state particles, that form the isobar system, one zero mode remains. If we use freed dynamic amplitudes for only one combination, no zero mode remains.

In total, we find seven zero modes in the case of freed S- and P-waves in all three possible combinations of final state particles to form the isobar: three connecting the S-waves, encoded with $\mathcal{C}_i^{\mathrm{S}}$ in eq. (5.55); one connecting the P-waves, encoded by $\mathcal{C}^{\mathrm{P}}$ in eq. (5.57); and three connecting S- and P-waves, encoded by $\mathcal{C}_{ij}^{\mathrm{SP}}$ in eq. (5.59).

5.2.5. Identifying zero modes numerically

In the previous chapters, we have performed various analytic calculations to identify zero modes in several cases and in different formalisms. In all cases, the appearing spin quantum numbers were either zero or one. In general, also waves with higher spins can exhibit ambiguities. For these waves, as well as for cases with more than two waves contributing, analytical calculations become very time consuming, thus we use a numerical method to identify zero modes, that is suitable for freed-isobar analyses.

Since in a freed isobar analysis, the dynamic amplitudes have an arbitrary shape up to the bin width of the step functions, they can approximate the continuous shapes of the zero modes. As a result, the total amplitude, and therefore the intensity of a zero mode approximated by step functions will not vanish completely[c], but will be very small compared to different shapes, for example an approximated Breit-Winger amplitude.

To find the shapes of freed-isobar waves, that describe such an unusually small intensity, we look at the phase-space integral matrix $\mathbf{I}_{ij}$ defined in eq. (3.11), that gives the total intensity described by a set of production amplitudes $\vec{\mathcal{T}}$ as:

$$\mathfrak{I} = \sum_{i,j} \mathcal{T}_i^* \mathbf{I}_{ij} \mathcal{T}_j; \tag{5.60}$$

the sum runs over the set of selected partial waves. It is useful to keep in mind, that all eigenvalues of $\mathbf{I}_{ij}$ are real and non-negative, since it is a hermitian positive semi-definite matrix. If we restrict the sum in eq. (5.60) to the single step functions of the waves with freed isobars, we can write the condition to have a small intensity as:

$$\sum_i \sum_{\mathrm{bins}} \sum_{i'} \sum_{\mathrm{bins}'} \mathcal{T}_{\mathrm{bin},i}^{0*} \mathbf{I}_{i,i'}^{\mathrm{bin},\mathrm{bin}'} \mathcal{T}_{\mathrm{bin}',i'}^0 \ll 1, \tag{5.61}$$

where the set of production amplitudes $\vec{\mathcal{T}}^0$ corresponds to the shape of the zero mode approximated by steplike functions normalized to one: $|\vec{\mathcal{T}}^0|^2 = 1$. Since the

---

[c]If the shape of a zero mode is constant with m_ξ, the step functions can describe it exactly and the intensity will vanish completely in this special case.
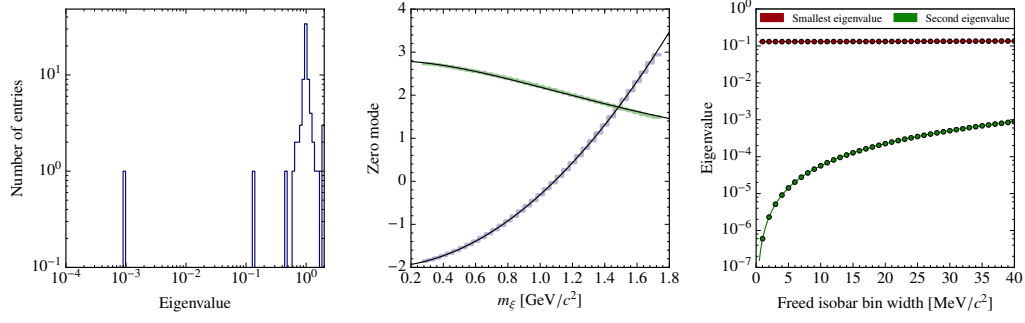
Figure 5.1.: Left: eigenvalue spectrum of the example model $\pi(1800) \to [\pi\pi]_\mathrm{S}\,\pi^-$ and $[\pi\pi]_\mathrm{P}\,\pi^-$ specified in section 5.2.5. Center: binned shapes of the zero mode for the S-wave in blue and P-wave in green. The corresponding black lines show the continuous shapes given in eq. (5.36) and eq. (5.37). Right: Dependence of the two smallest eigenvalues of the phase-space integral matrix on the freed-isobar bin width.

phase-space integral matrix is a Gramian matrix, the expectation value for the intensity described by a set of production amplitudes $\vec{\mathcal{T}}$, with $|\vec{\mathcal{T}}|^2 = 1$, is one.

In order to identify an approximated zero mode $\vec{\mathcal{T}}^0$ from the integral matrix, we look at the eigendecomposition of $\mathbf{I}_{ij}$. Here $\vec{\mathcal{T}}^0$ represents an eigenvector corresponding to an eigenvalue of:

$$\lambda^0 \ll 1. \tag{5.62}$$

As an example case, we employ the same model as in section 5.2.2: a $\pi(1800)$ decaying into three pions via S- and P-wave isobars, using again the covariant tensor formalism for the spin amplitudes. For both isobars, we use bin widths of $40\,\mathrm{MeV}/c^2$, starting from threshold $m_\xi = 2m_\pi$ and spanning the whole kinematic range. This results in 37 bins in the isobar mass and thus 74 complex-valued degrees of freedom in the model. With this definition, we construct the phase-space integral matrix according to eq. (3.13) and perform an eigenvector decomposition of it. The resulting eigenvalue spectrum is shown in the left plot of fig. 5.1, where the smallest eigenvalue corresponds to λ^0. Since we are able to identify the zero mode in this spectrum, we can compare the resulting shape from the numerical calculation with the shapes obtained in section 5.2.2 via an analytic calculation. The center plot of fig. 5.1 shows that we find a nice agreement of both approaches. Since for a larger number of waves with freed isobars, the number of zero modes might not be known a priory and the spectrum of eigenvalues might also not suffice to tell, whether an eigenvalue qualifies as small, we need some criteria on how to identify an eigenvalue corresponding to a zero mode.

One way to do this, is to create artificial zero modes and use their eigenvalues as comparison. We do this by introducing waves with a fixed dynamic amplitude and waves with a freed dynamic amplitude, that have matching angular momentum quantum numbers. Therefore, the freed dynamic amplitude can approximate the

fixed one with an opposite sign, so that fixed and freed amplitudes cancel up to the finite bin width and therefore create an artificial zero mode. By performing an eigendecomposition of the corresponding phase-space integral matrix including fixed and freed waves, we can identify the eigenvalue that corresponds to this cancellation and therefore has to be small. Doing this for our example case, we find eigenvalues of $\lambda_\mathrm{S} = 3.36 \cdot 10^{-3}$ and $\lambda_\mathrm{P} = 3.43 \cdot 10^{-3}$ for these artificial zero modes in both waves and see, that they are in the same order of magnitude as the eigenvalue corresponding to the real zero mode $\lambda_0 = 9.01 \cdot 10^{-4}$ as defined in eq. (5.62).

Another way to identify eigenvalues, that correspond to zero modes in a numerical approach, is to study the dependence of the smallest eigenvalues on the bin width of the freed isobar waves. Since a smaller bin width in the isobar masses results in a smaller subdivision of the two-dimensional plane spanned by the isobar masses m_{12} and m_{23}, as defined in section 5.2 for our example case, eigenvalues corresponding to a zero mode exhibit a quadratic behavior with respect to the bin width. This can be seen in the right plot of fig. 5.1, where the smallest eigenvalue vanishes quadratically with the freed-isobar bin width, as indicated by the continuous line, while the second smallest converges to a finite value.

5.2.6. Consequences for Partial-Wave Analysis

The existence of zero modes has nontrivial consequences for freed-isobar partial-wave analyses. With the coefficient $\mathcal{C}$ in eq. (5.10) we have identified a complex-valued degree of freedom, that leaves the total amplitudes—and hence the intensity and the likelihood function—unchanged. Therefore, we cannot fix this degree of freedom by a fit to the intensity.

In analyses with fixed isobar shapes, this does not pose a problem, since the fixed dynamic amplitudes do not have any degree of freedom, but in freed-isobar analyses this may affect the fit results, since the dynamic amplitudes of the isobars are allowed to take any shape. In such cases, we can rewrite eq. (5.10) as:

$$
\begin{aligned}
\mathfrak{A}\left(m_{12}, m_{23}\right) =&\, \Psi_\mathrm{S}\left(m_{12}, m_{23}\right) \sum_\mathrm{bin} \Delta_\mathrm{bin}^{\sqcap}\left(m_{12}\right)\left(\mathcal{T}_\mathrm{S,bin} + \mathcal{C}\mathcal{T}_\mathrm{S,bin}^0\right) \\
&+ \Psi_\mathrm{S}\left(m_{23}, m_{12}\right) \sum_\mathrm{bin} \Delta_\mathrm{bin}^{\sqcap}\left(m_{23}\right)\left(\mathcal{T}_\mathrm{S,bin} + \mathcal{C}\mathcal{T}_\mathrm{S,bin}^0\right) \\
&+ \Psi_\mathrm{P}\left(m_{12}, m_{23}\right) \sum_\mathrm{bin} \Delta_\mathrm{bin}^{\sqcap}\left(m_{12}\right)\left(\mathcal{T}_\mathrm{P,bin} + \mathcal{C}\mathcal{T}_\mathrm{P,bin}^0\right) \\
&+ \Psi_\mathrm{P}\left(m_{23}, m_{12}\right) \sum_\mathrm{bin} \Delta_\mathrm{bin}^{\sqcap}\left(m_{23}\right)\left(\mathcal{T}_\mathrm{P,bin} + \mathcal{C}\mathcal{T}_\mathrm{P,bin}^0\right),
\end{aligned}
\tag{5.63}
$$

where $\mathcal{T}_\mathrm{S/P,bin}^0$ is the corresponding component of $\vec{\mathcal{T}}^0$ determined by the eigenvalue decomposition introduced in the previous section for the particular wave and bin. The resulting amplitude is not completely independent of $\mathcal{C}$, since the corresponding eigenvalue λ_0 is small but finite, but varies slowly with this parameter, while the described dynamic amplitudes for the S- and P-wave may change drastically.

We can write the connection between a fit result and the physical dynamic amplitudes as:

$$\mathcal{T}^{\text{fit}}_{\text{S/P,bin}} = \mathcal{T}^{\text{phys}}_{\text{S/P,bin}} - \mathcal{C}^{\text{fit}}\mathcal{T}^{0}_{\text{S/P,bin}}, \tag{5.64}$$

where $\mathcal{T}^{\text{phys}}_{\text{S/P,bin}}$ are the physical values of the dynamic amplitudes in the corresponding isobar mass-bins and $\mathcal{T}^{\text{fit}}_{\text{S/P,bin}}$ are the values determined by the maximization of the likelihood function. They may be shifted by an amount $\mathcal{C}^{\text{fit}}$ away from the physical values in the direction of the zero mode $\mathcal{T}^{0}_{\text{S/P,bin}}$.

If we perform a maximum likelihood fit with such a model, the fitting algorithm will find some value of $\mathcal{C}^{\text{fit}}$, which due to numerical effects and the small dependence of the likelihood on this parameter, can be away from the physical value. To account for this, we have to perform a second step using additional knowledge on the dynamic amplitudes to fix $\mathcal{C}$ to the correct value. In section 5.3, we will explore this second step using Monte Carlo data.

5.3. Monte-Carlo study

To study the consequences of a zero mode in our example case, given in section 5.2.5, we generate a Monte Carlo data set with 10^5 events, using simple Breit-Wigner shapes $\Delta^{\text{BW}}_{\text{S/P}}(m_\xi)$ for the S- and P-wave isobars. For this simple example, we use a mass of $980\,\text{MeV}/c^2$ and a width of $100\,\text{MeV}/c^2$ for the $J^{PC}_\xi = 0^{++}$ isobar, roughly resembling the $f_0(980)$ resonance, and mass of $770\,\text{MeV}/c^2$ and a width of $160\,\text{MeV}/c^2$ for the $J^{PC}_\xi = 1^{--}$ isobar, roughly resembling the $\rho(770)$ resonance. We then analyze the generated data set with a freed-isobar model.

The fit result $\vec{\mathcal{T}}^{\text{fit}}$ for the dynamic amplitudes does not match the input shapes, since the fit was performed to the intensity distribution, which is nearly invariant under a change of the parameter $\mathcal{C}$ in eq. (5.63). To correct for this we have to use additional knowledge on the physical dynamic amplitudes to be able to counteract the nearly arbitrary value of $\mathcal{C}^{\text{fit}}$ in eq. (5.64). We do this, by shifting the fit result in the direction $\vec{\mathcal{T}}^0$ of the zero mode in such a way, that the resulting dynamic amplitudes resemble the dynamic amplitude used to generate the Monte Carlo data set as good as possible, i.e. by minimizing the following quantity:

$$\chi^2\left(\mathcal{C}, \mathcal{F}\right) = \sum_{i,j} \delta_i\left(\mathcal{C}, \mathcal{F}\right) \mathbf{C}^{-1}_{ij} \delta_j\left(\mathcal{C}, \mathcal{F}\right), \tag{5.65}$$

where $\mathbf{C}_{ij}$ is the covariance matrix of the production amplitudes $\vec{\mathcal{T}}^{\text{fit}}$. The indices i and j represent combined indices, that encode, the wave, the mass bin, and whether the corresponding quantity is the real or imaginary part of the corresponding complex-valued dynamic amplitude, since the fitting algorithm only deals with real-valued parameters and therefore the covariance matrix describes real-valued parameters:

$$i = \left\{\{\text{S}, \text{P}\}, \{\text{bin}\}, \{\Re, \Im\}\right\}. \tag{5.66}$$

The functions $\delta_i\left(\mathcal{C}, \mathcal{F}\right)$ are given by:

$$\delta_i\left(\mathcal{C}, \mathcal{F}\right) = \left\{ \begin{matrix} \Re \\ \Im \end{matrix} \right\} \left(\mathcal{T}_i^{\mathrm{fit}} + \mathcal{C}\mathcal{T}_i^0 - \mathcal{F}\Delta_i^{\mathrm{BW}}\right), \qquad (5.67)$$

where $\mathcal{F}$ is a complex-valued parameter used to fix the normalization and global phase of the reference shapes Δ_i^{BW}. The reference shapes Δ_i^{BW} are given by the Monte Carlo input shape for the particular wave evaluated at the center of mass of the corresponding isobar mass bin. With this minimization, we are able to reproduce the dynamic amplitudes used as input in the model, as shown in fig. 5.2.
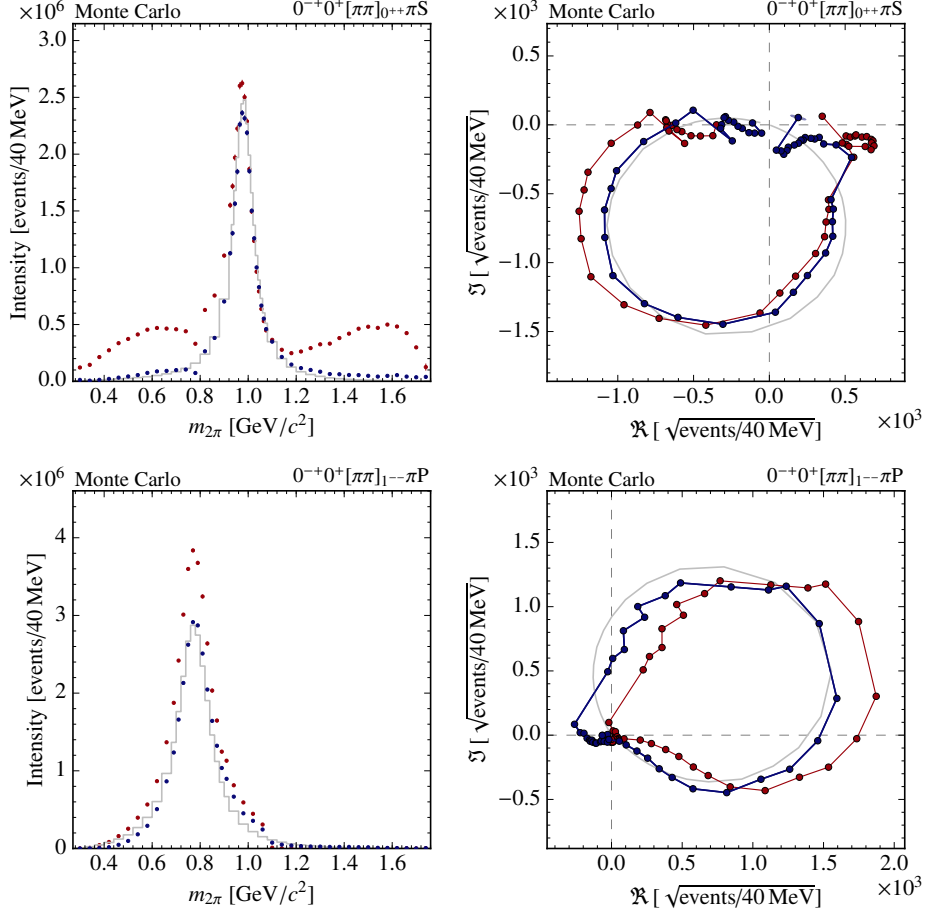
Figure 5.2.: Result of the freed-isobar fit to the Monte Carlo data set as described in section 5.3. In plots of this kind, red points show the result obtained from the freed-isobar fit. Blue points show the dynamic amplitudes after correcting for the zero mode. The dynamic amplitude used to generate the Monte Carlo data is shown in gray. The left plots show the intensity distribution $|\mathcal{B}|^2$ of the dynamic amplitudes, defined in eq. (5.7), and the right plots show the corresponding Argand diagrams of $\mathcal{B}$. In this Figure, the upper row depicts the results for the $0^{-+}0^{+}$ $[\pi\pi]_{0^{++}} \pi$S-wave and the lower row for the $0^{-+}0^{+} [\pi\pi]_{1^{--}} \pi$P wave. The zero mode correction was performed by minimizing eq. (5.65). Note, that for reasons of clarity, we removed the direction of a global phase rotation from the covariance matrix, according to appendix C, when determining the uncertainties used in the Argand diagram. For the intensity distributions, a phase rotation has no effect on the uncertainties.

Chapter 6.

Extensive Freed-isobar Partial-Wave Analysis

In this chapter, we analyze the data set introduced in section 2.3 and analyzed with the fixed-isobar method in refs. [8, 12] again, now using freed-isobar PWA introduced in chapter 5. A first freed-isobar PWA of this data was already published in ref. [12] alongside with the fixed-isobar PWA, using the following three freed-isobar waves[a]:

$$0^{-+}0^+ \, [\pi\pi]_{0^{++}} \, \pi\text{S}; \quad 1^{++}0^+ \, [\pi\pi]_{0^{++}} \, \pi\text{P}; \quad 2^{-+}0^+ \, [\pi\pi]_{0^{++}} \, \pi\text{D}. \qquad (6.1)$$

Since there is only one freed wave in each $J_X^{PC} M^\varepsilon$ sector, no zero modes were present in this analysis. Some results of this first freed-isobar PWA are shown in section 6.3.7 Due to the success of this first freed-isobar PWA, we develop an extended freed-isobar model, based on the fixed-isobar wave set of refs. [8, 12] and introduced in chapter 4 and applied it to the same data set.

In section 6.1, we will first introduce this extended freed-isobar wave set and show the validity of the model and the method to resolve zero-mode ambiguities on a Monte-Carlo data set in section 6.2. In section 6.3 we apply the freed-isobar model to the data set introduced in section 2.3 and discuss the results for the individual waves, followed by the discussion of several extended studies with further enlarged freed-isobar wave sets in section 6.4. In the end we extract resonance parameters for isobar resonances from the results of the freed-isobar PWA in chapter 7.

Table 6.1.: Quantum numbers and isobars of all waves in the fixed-isobar PWA of refs. [8, 12]. The fourth column indicates, in which studies waves are freed, the single studies are explained in the text. The fifth column gives the relative intensities, as defined in eq. (6.2) and taken from ref. [12].

$J^{PC}M^\varepsilon$	Isobar	L		[%]	$J^{PC}M^\varepsilon$	Isobar	L		[%]
$0^{-+}0^+$	$(\pi\pi)_{\text{S}}$	S		8.0	$3^{++}0^+$	$f_2(1270)$	P	H	0.4
$0^{-+}0^+$	$f_0(980)$	S	} 11	2.4	$3^{++}0^+$	$\rho_3(1690)$	S	H	0.4
$0^{-+}0^+$	$f_0(1500)$	S		0.1	$3^{++}0^+$	$\rho_3(1690)$	I		<0.1
$0^{-+}0^+$	$\rho(770)$	P	11	3.5	$3^{++}1^+$	$(\pi\pi)_{\text{S}}$	F		0.3

[a]The naming scheme of freed-isobar waves is explained in eq. (6.4).

Table 6.1 Continued from previous page

$J^{PC}M^\varepsilon$	Isobar	L		[%]
$0^{-+}0^+$	$f_2(1270)$	D		0.2
$1^{++}0^+$	$(\pi\pi)_\mathrm{S}$	P	$\left.\right\}11$	4.1
$1^{++}0^+$	$f_0(980)$	P		0.3
$1^{++}0^+$	$\rho(770)$	S	11	32.7
$1^{++}0^+$	$\rho(770)$	D	D	0.9
$1^{++}0^+$	$f_2(1270)$	P	D	0.4
$1^{++}0^+$	$f_2(1270)$	F		0.1
$1^{++}0^+$	$\rho_3(1690)$	D		0.1
$1^{++}0^+$	$\rho_3(1690)$	G		<0.1
$1^{++}1^+$	$(\pi\pi)_\mathrm{S}$	P		0.2
$1^{++}1^+$	$f_0(980)$	P		0.1
$1^{++}1^+$	$\rho(770)$	S	11	4.1
$1^{++}1^+$	$\rho(770)$	D		0.6
$1^{++}1^+$	$f_2(1270)$	P		0.5
$1^{-+}1^+$	$\rho(770)$	P	E	0.8
$2^{++}1^+$	$\rho(770)$	D	11	7.7
$2^{++}1^+$	$f_2(1270)$	P	F	0.5
$2^{++}1^+$	$\rho_3(1690)$	D		<0.1
$2^{++}2^+$	$\rho(770)$	D		0.3
$2^{++}2^+$	$f_2(1270)$	P		<0.1
$2^{-+}0^+$	$(\pi\pi)_\mathrm{S}$	D	$\left.\right\}11$	3.0
$2^{-+}0^+$	$f_0(980)$	D		0.6
$2^{-+}0^+$	$\rho(770)$	P	11	3.8
$2^{-+}0^+$	$\rho(770)$	F	11	2.2
$2^{-+}0^+$	$f_2(1270)$	S	11	6.7
$2^{-+}0^+$	$f_2(1270)$	D	G	0.9
$2^{-+}0^+$	$f_2(1270)$	G		0.1
$2^{-+}0^+$	$\rho_3(1690)$	P		0.2
$2^{-+}1^+$	$(\pi\pi)_\mathrm{S}$	D		0.4
$2^{-+}1^+$	$\rho(770)$	P	11	3.3
$2^{-+}1^+$	$\rho(770)$	F		0.1
$2^{-+}1^+$	$f_2(1270)$	S	G	0.9
$2^{-+}1^+$	$f_2(1270)$	D		0.1
$2^{-+}1^+$	$\rho_3(1690)$	P		0.1
$2^{-+}2^+$	$\rho(770)$	P		0.2
$2^{-+}2^+$	$f_2(1270)$	S		0.1
$2^{-+}2^+$	$f_2(1270)$	D		0.1
$3^{++}0^+$	$(\pi\pi)_\mathrm{S}$	F		0.2
$3^{++}0^+$	$\rho(770)$	D	H	0.9
$3^{++}0^+$	$\rho(770)$	G		0.4
$3^{++}1^+$	$\rho(770)$	D		1.0
$3^{++}1^+$	$\rho(770)$	G		0.1
$3^{++}1^+$	$f_2(1270)$	P		0.4
$3^{++}1^+$	$\rho_3(1690)$	S		0.1
$3^{-+}1^+$	$\rho(770)$	F		0.1
$3^{-+}1^+$	$f_2(1270)$	D		<0.1
$4^{++}1^+$	$\rho(770)$	G	I	0.8
$4^{++}1^+$	$f_2(1270)$	F	I	0.2
$4^{++}1^+$	$\rho_3(1690)$	D		<0.1
$4^{++}2^+$	$\rho(770)$	G		<0.1
$4^{++}2^+$	$f_2(1270)$	F		<0.1
$4^{-+}0^+$	$(\pi\pi)_\mathrm{S}$	G		0.3
$4^{-+}0^+$	$\rho(770)$	F	J	1.0
$4^{-+}0^+$	$f_2(1270)$	D		0.3
$4^{-+}0^+$	$f_2(1270)$	G		<0.1
$4^{-+}1^+$	$\rho(770)$	F		0.4
$4^{-+}1^+$	$f_2(1270)$	D		0.1
$5^{++}0^+$	$(\pi\pi)_\mathrm{S}$	H		0.1
$5^{++}0^+$	$\rho(770)$	G		0.3
$5^{++}0^+$	$f_2(1270)$	F		0.1
$5^{++}0^+$	$f_2(1270)$	H		<0.1
$5^{++}0^+$	$\rho_3(1690)$	D		<0.1
$5^{++}1^+$	$(\pi\pi)_\mathrm{S}$	H		0.1
$5^{++}1^+$	$f_2(1270)$	F		0.1
$6^{++}1^+$	$\rho(770)$	I		<0.1
$6^{++}1^+$	$f_2(1270)$	H		<0.1
$6^{-+}0^+$	$(\pi\pi)_\mathrm{S}$	I		0.1
$6^{-+}0^+$	$\rho(770)$	H	K	0.7
$6^{-+}0^+$	$f_2(1270)$	G		0.1
$6^{-+}0^+$	$\rho_3(1690)$	F		<0.1
$6^{-+}1^+$	$(\pi\pi)_\mathrm{S}$	I		0.1
$6^{-+}1^+$	$\rho(770)$	H		0.1
$1^{++}1^-$	$\rho(770)$	S		0.3
$1^{-+}0^-$	$\rho(770)$	P		0.3
$1^{-+}1^-$	$\rho(770)$	P		0.7
$2^{++}0^-$	$\rho(770)$	D		0.3
$2^{++}0^-$	$f_2(1270)$	P		0.2
$2^{++}1^-$	$f_2(1270)$	P		0.3
$2^{-+}1^-$	$f_2(1270)$	S		0.2
FLAT				

6.1. Freed-isobar wave set

Based on the PWA of the reaction $\pi^- p \to \pi^- \pi^+ \pi^- p$, presented in refs. [8, 12] and introduced in section 4.2, we apply the freed-isobar PWA method to the same channel.

To be able to compare both analyses, we employ the helicity formalism, introduced in section 4.1.3, as well and use the same wave set. However, since the number of waves in the fixed-isobar model is 87, listed in table 6.1, freeing all dynamic isobars amplitudes would result in over 2000 complex-valued free parameters in the fit assuming a width of $40\,\mathrm{MeV}/c^2$ for the $m_{2\pi}$ intervals; the exact number depends on the kinematically allowed range for the isobar mass and therefore on the $m_{3\pi}$ bin (see fig. 6.1). Therefore, we free only a subset of selected waves and leave the remaining waves with predefined fixed dynamic isobar amplitudes. Any combination of waves with freed and with fixed dynamic isobar amplitudes is possible within the freed-isobar approach.

Even though we cannot use freed isobar dynamic amplitudes in all waves of the model, we want to minimize model-dependence of our PWA results as good as possible. Since improper parameterizations in waves with fixed dynamic isobar amplitudes might influence the results for freed-isobar waves, we want to minimize this effect known as leakage. Therefore, we chose the freed waves such, that they have the biggest contribution in the PWA results of refs. [8, 12], since the effects of improper parameterizations in "small" waves on "big" waves are expected to be negligible. As a measure for the size of a wave, we use its relative intensity, defined as:

$$\mathfrak{I}_i = \sum_{\substack{t \in \{t' \text{ bins}\} \\ m \in \{m_{3\pi} \text{ bins}\}}} \frac{\left| \mathcal{T}_i^{m,t} \right|^2 \tilde{\mathbf{I}}_{ii}}{\bar{N}}, \tag{6.2}$$

with $\bar{N}$ and $\tilde{\mathbf{I}}_{ii}$ defined in eq. (3.8) and eq. (3.10). The relative intensities for the waves in the fixed-isobar PWA are listed in table 6.1. Since interference effects are not taken into account in eq. (6.2), the relative intensities of all waves do not have to add up to 1; in the fixed-isobar PWA of refs. [8, 12], they add up to 1.05.

Using the results of refs. [8, 12], we find that a good choice for a set of freed-isobar waves are the 11 waves with the highest relative intensities, since their relative intensities sum up to over 75%, they are the only waves with a relative intensity above 1%, and the only waves with a relative intensity higher than the flat wave. The set of freed waves is indicated in table 6.1. Along with the basic set of 11 freed waves, several further studies were performed, which are also indicated in table 6.1. These studies are:

- "C": The basis set of 11 freed waves consisting of the waves with the largest relative intensities. These waves are also free in all other studies,

- "E": Addition of the $1^{-+}1^+ [\pi\pi]_{1^{--}} \pi P$ wave to the basis set of study "C",

- "D": Addition of two additional freed waves with $J_X^{PC} M^\varepsilon = 1^{++}0^+$ to the basis set of study "C",

- "G": Addition of two additional freed waves with $J_X^{PC} = 2^{-+}$ to the basis set of study "C",

- "F": Addition of the freed $2^{++}1^+$ $[\pi\pi]_{2^{++}}$ πS wave to the basis set of study "C",

- "H": Addition of three $J_X^{PC} M^\varepsilon = 3^{++}0^+$ waves to he basis set of study "C",

- "I": Addition of two $J_X^{PC} M^\varepsilon = 4^{++}1^+$ waves to he basis set of study "C",

- "J": Addition of the freed $4^{-+}0^+$ $[\pi\pi]_{1^{--}}$ πF wave to he basis set of study "C", and

- "K": Addition of the freed $6^{-+}0^+$ $[\pi\pi]_{1^{--}}$ πH wave to he basis set of study "C".

Within this set of the 11 waves with the highest relative intensities are the three waves, that were freed in the freed-isobar isobar PWA in ref. [12] and are listed in eq. (6.1). Since a freed-isobar wave replaces all fixed-isobar waves with matching J_ξ^{PC} quantum numbers in the fixed-isobar PWA and three different isobars with $J_\xi^{PC} = 0^{++}$ were included, the set of 11 fixed-isobar waves replaces 15 fixed-isobar waves. This is indicated by brackets in table 6.1.

As $m_{2\pi}$ intervals, we use in general a bin width of $40\,\mathrm{MeV}/c^2$. The lowest bin, however, starts at $2m_\pi$ and ends at $320\,\mathrm{MeV}/c^2$, which corresponds to a slightly larger width. In $m_{2\pi}$ regions with known dominating resonances, we use smaller bin widths to be able to better resolve the resonance structures. The $m_{2\pi}$ range of this finer binning depends on the quantum numbers of the corresponding isobar:

- for waves with $J_\xi^{PC} = 0^{++}$, we use a bin width of $10\,\mathrm{MeV}/c^2$ in the region of the $f_0(980)$ resonance, in the range from 920 to $1080\,\mathrm{MeV}/c^2$,

- for waves with $J_\xi^{PC} = 1^{--}$, we use a bin width of $20\,\mathrm{MeV}/c^2$ in the region of the $\rho(770)$ resonance, in the range from 640 to $920\,\mathrm{MeV}/c^2$,

- for waves with $J_\xi^{PC} = 2^{++}$, we use a bin width of $20\,\mathrm{MeV}/c^2$ in the region of the $f_2(1270)$ resonance, in the range from 1180 to $1400\,\mathrm{MeV}/c^2$, and

- for waves with $J_\xi^{PC} = 3^{--}$, we use a bin width of $20\,\mathrm{MeV}/c^2$ in the region of the $\rho_3(1690)$ resonance, in the range 1500–$1700\,\mathrm{MeV}/c^2$.

Since we use the same data set as refs. [8, 12], but our model has much more free parameters, shown in fig. 6.1 as a function of $m_{3\pi}$, we use a coarser binning in $m_{3\pi}$ and t' to reduce the statistical uncertainties on our results. In $m_{3\pi}$, we use a bin width of $40\,\mathrm{MeV}/c^2$, which is twice the bin width as in the fixed-isobar PWA,
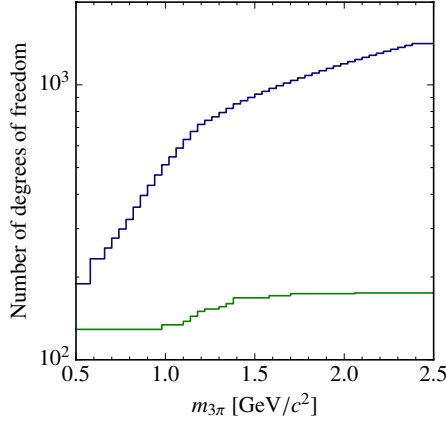
Figure 6.1.: Number of free parameters in the freed-isobar PWA model (blue) and the fixed-isobar model (green) as a function of $m_{3\pi}$.

over the whole range from 0.5 to $2.5\,\text{GeV}/c^2$, which corresponds to 50 independent $m_{3\pi}$ bins. In t' we also use a non-equidistant binning which yields similar numbers of events in every t' bin, but we subdivide the data in only four bins with the following bin borders:

$$\{0.100, 0.141, 0.194, 0.326, 1.000\}\,(\text{GeV}/c)^2\,. \tag{6.3}$$

This way, we end up with a total of 200 $(m_{3\pi},\ t')$ bins[b], that are analyzed independently. In addition, there are two small differences between the two PWA models:

- all resonance amplitudes with the exception of $(\pi\pi)_\text{S}$ are described by a relativistic Breit-Wigner parameterization given in eq. (4.8) and using eq. (4.9) for the mass dependent width. The corresponding resonance parameters are listed in table 6.2,

- the sector with negative reflectivity $\varepsilon = -1$ has only rank one. We therefore have only three incoherent sectors: waves with positive reflectivity, waves with negative reflectivity and the flat wave. The rank of a PWA model was shortly introduced in section 4.2, a more detailed discussion can be found in ref. [12].

For waves with freed isobars, we slightly modify the naming scheme for waves, which was defined in eq. (4.1). A wave with a freed isobar with quantum numbers J_ξ^{PC} is represented by:

$$J_X^{PC} M^\varepsilon\, [\pi\pi]_{J_\xi^{PC}}\, \pi L. \tag{6.4}$$

[b]The fixed-isobar PWA of refs. [8, 12] had 1100 independent $(m_{3\pi}, t')$ bins.

Table 6.2.: Resonance parameters for fixed resonance amplitudes used in the freed-isobar PWA.

	$m_0 \, [\text{MeV}/c^2]$	$\Gamma_0 \, [\text{MeV}/c^2]$
$f_0(980)$	990	70
$f_0(1500)$	1505	109
$\rho(770)$	769	150.9
$f_2(1270)$	1275.1	185.1
$\rho_3(1690)$	1688.8	161

Since in the context of a PWA only the relative phases between the individual waves carry meaning, we have to define a reference wave, whose production amplitude has a phase of zero. Throughout this chapter, we use the $4^{-+}0^+\rho(770)\,\pi\text{F}$ wave as reference. The only exception is one study in section 6.4.7, where this wave is freed. In this study, the $6^{-+}0^+\rho(770)\,\pi\text{H}$ wave is used as reference instead.

6.2. Monte Carlo study

Since the freed-isobar model formulated in section 6.1 results in a very involved PWA with a very large number of free parameters—the exact number depends on the $m_{3\pi}$ bin, as shown in fig. 6.1—we test this PWA method first on a Monte Carlo data set and check, if we are able to reproduce known dynamic isobar amplitudes.

To generate the Monte Carlo data set, we want to use a model that is as close to real data as possible. Therefore we use fixed-isobar results from refs. [8, 12] as input. However, since the production amplitudes for several waves tend to jump with $m_{3\pi}$ bins, we use a model to smoothly describe their $m_{3\pi}$ dependence. For 14 waves we use the model developed by S Wallner in ref. [35]. For the other 73 waves, where such a model is not available, we describe the $m_{3\pi}$ dependence of the production amplitudes by the best fitting complex-valued parabola to the results of the fixed-isobar PWA. We based this model on the third t' bin of the fixed-isobar PWA, ranging from 0.127 to 0.144 $(\text{GeV}/c)^2$. However, for the freed-isobar fit, this value is unimportant, since the decay amplitudes are independent of t'. We neglect contributions from the flat wave.

With this model for the $m_{3\pi}$ dependence of the production amplitudes of the individual waves, we generate a total of $12.5 \cdot 10^6$ events—this number roughly corresponds to the number of events in one of the four t' bins of real data—distributed over the $m_{3\pi}$ bins according to the intensity distribution of the model for the production amplitudes[c].

We then perform a freed-isobar PWA of this Monte Carlo data set with the model specified in section 6.1, using 50 sets of random start values for all free fit parameters for every independent $m_{3\pi}$ bin. In the following, we present the result

---

[c]Since the data are generated independently for every $m_{3\pi}$ bin, this is not automatically fulfilled.

this PWA for every freed $J_X^{PC} M^\varepsilon$ sector separately, starting with waves without zero modes, followed by waves with zero modes, for which we will also discuss various methods to resolve the arising ambiguities.

6.2.1. Waves without zero modes

The freed-isobar waves in our model, that are not affected by zero modes are the $1^{++}1^+ [\pi\pi]_{1^{--}} \pi S$ wave, the $2^{-+}1^+ [\pi\pi]_{1^{--}} \pi P$ wave, and the $2^{++}1^+ [\pi\pi]_{1^{--}} \pi D$ wave, replacing the $1^{++}1^+ \rho(770) \pi S$, $2^{-+}1^+ \rho(770) \pi P$, and the $2^{++}1^+ \rho(770) \pi D$ waves of the fixed-isobar model. The results for these waves are depicted in fig. 6.2 for one bin in $m_{3\pi}$. The $m_{3\pi}$ bin was chosen from 1.5 to $1.54 \, \text{GeV}/c^2$, since it lies in the center of the analyzed range from 0.5 to $2.5 \, \text{GeV}/c^2$. For all three waves a nice agreement between the fixed parameterizations used for data generation—a relativistic Breit-Wigner describing the $\rho(770)$ resonance with resonance parameters listed in table 6.2—and the dynamic isobar amplitudes[d] extracted by the freed-isobar PWA can be seen in the intensity distributions and the Argand diagrams. This also holds for the other $m_{3\pi}$ bins, which are not depicted here for reasons of brevity. This shows, that the freed-isobar method is able to reliably extract dynamic isobar amplitudes in the absence of zero modes.

Since the dependence of the $2^{++}1^+ \rho(770) \pi D$ production amplitudes on $m_{3\pi}$ was modeled in ref. [35], we additionally depict the dependence on $m_{3\pi}$ in the left plot of fig. 6.3, where a clear isolated peak corresponding to the $a_2(1320)$ resonance is visible, that nicely matches the shape used in the generation of the Monte-Carlo data set. The right plot of fig. 6.3 show the two-dimensional intensity distribution as function of $m_{3\pi}$ and $m_{2\pi}$. Here, a nice peak corresponding to the decay $a_2(1320) \to \rho(770) \pi$ is visible, as expected. This confirms, that the freed-isobar method is able to extract the parameterizations used to generate the Monte Carlo data over all bins in $m_{3\pi}$.

6.2.2. Strategy for resolving zero-mode ambiguities

In section 6.2.1 we have discussed the three waves in the freed-isobar model, that are not affected by zero modes. The remaining eight waves, in contrast, suffer from zero modes and the corresponding ambiguities which we therefore have to resolve. To do so, we employ a similar technique, introduced in section 5.3, but we explore a number of different constraints on the dynamic isobar amplitudes, since we want to be able to apply this method to real data, where the true dynamic isobar amplitudes are unknown.

The first approach, analogous to the one introduced in section 5.3, is to use the fixed dynamic isobar amplitudes used in the generation of the Monte Carlo data set as model. We name such an approach "fix$_\text{waves}$", where the index indicates the set of waves used for this approach. With the fixed dynamic isobar amplitudes as

---

[d]Since helicity formalism was used, the dynamic isobar amplitudes include barrier factors throughout this chapter.
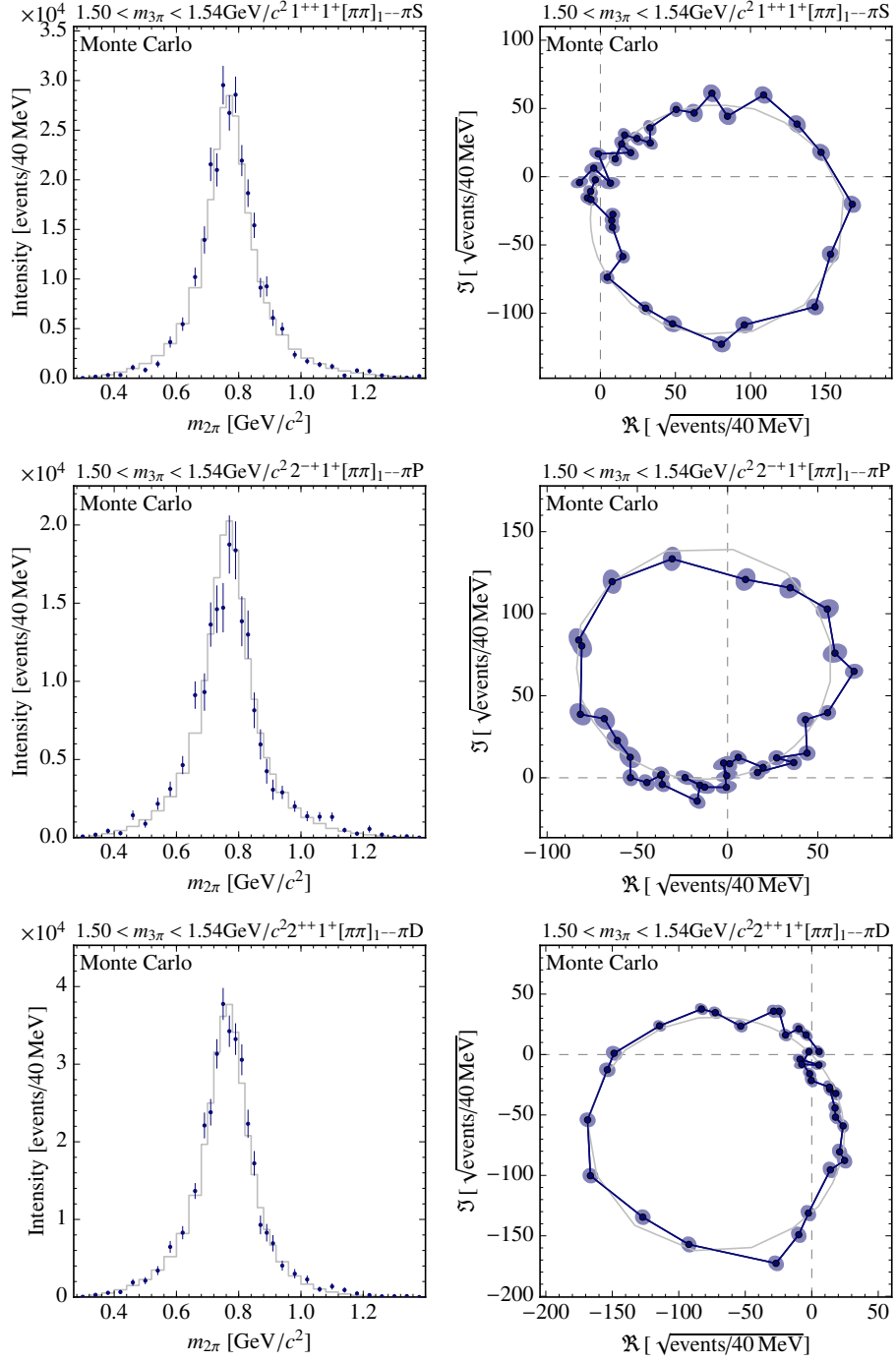
Figure 6.2.: Intensity distributions and Argand diagrams for the freed-isobar PWA on Monte Carlo data, similar to fig. 5.2. The gray lines indicate the dynamic isobar amplitudes used in the fixed-isobar PWA.
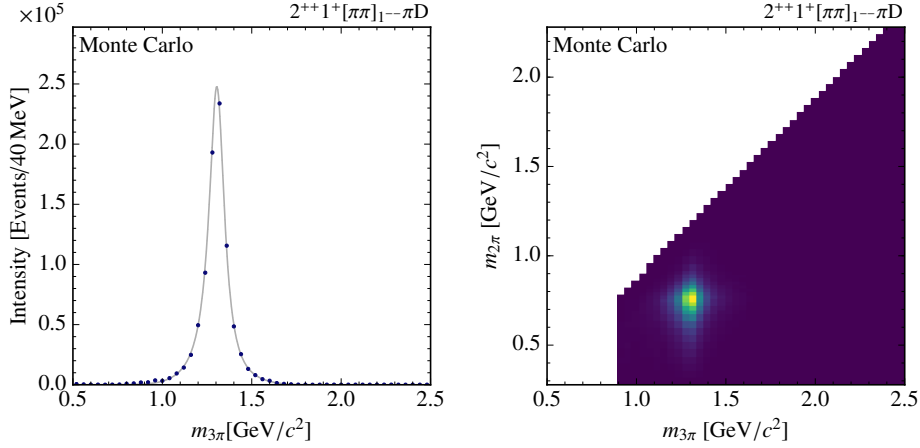
Figure 6.3.: Left: Intensity distribution as function of $m_{3\pi}$, calculated as sum over all $m_{2\pi}$ bins according to eq. (5.60) (blue), compared to the distribution used in data-generation (gray). Right: Intensity distribution $|\mathcal{B}|^2$ of the $2^{++}1^+ [\pi\pi]_{1^{--}} \pi D$ wave as a function of $m_{3\pi}$ and $m_{2\pi}$ as obtained from a freed-isobar PWA of the Monte Carlo data.

model in eq. (5.67), eq. (5.65) is minimized to obtain the zero-mode coefficients $\mathcal{C}$. Since the model employs fixed dynamic isobar amplitudes, this approach can be used independently for every $m_{3\pi}$ bin.

In a second approach we use a model for the dynamic isobar amplitudes with free parameters that are adjusted simultaneously with the zero-mode coefficients $\mathcal{C}$. In this work we use such a constraint for dynamic isobar amplitudes with $J_\xi^{PC} = 1^{--}$, 2^{++}, and 3^{--}, fitting the resonance parameters of the Breit-Wigner parameterization—eq. (4.8) with eq. (4.9)—for the $\rho(770)$, the $f_2(1270)$, and the $\rho_3(1690)$ resonance, respectively. We will call such an approach "fit$_{\text{waves}}$", where the index again gives the isobar resonance constrained with this approach. In such an approach, the model in eq. (5.67) has free parameters and therefore the corresponding χ^2 function in eq. (5.65) has two more free parameters, m_0 and Γ_0 of the Breit-Wigner parameterization, that are adjusted in the minimization. Since we aim for a consistent result over all $m_{3\pi}$ bins, the resonance parameters are the same for all $m_{3\pi}$ bins and therefore the zero-mode coefficients for all $m_{3\pi}$ bins and the resonance parameters are adjusted simultaneously. If not stated otherwise, we use the whole kinematically allowed $m_{2\pi}$ range in the fit.

Both methods introduced up to now use a model to constrain the dynamic isobar amplitudes. In addition, we explore a third approach, that does not rely on such a model, but requires smoothness neighboring $m_{3\pi}$ bins. To do this, we define the residual of two neighboring bins b and b':

$$\delta_i^b\left(\mathcal{C}^b, \mathcal{C}^{b'}\right) = \left\{ \begin{array}{c} \Re \\ \Im \end{array} \right\} \left(\mathcal{T}_i^{\text{fit},b} + \mathcal{C}^b \mathcal{T}_i^{0,b} - \mathcal{T}_i^{\text{fit},b'} - \mathcal{C}^{b'} \mathcal{T}_i^{0,b'} \right), \qquad (6.5)$$

where $\mathcal{C}^b$, $\mathcal{T}_i^{\text{fit},b}$, and $\mathcal{T}_i^{0,b}$ are the zero-mode coefficient, fit result for the production amplitudes, and the shape of the zero mode in the $m_{3\pi}$ bin b. With these, we can define a χ^2 function, that depends on all zero-mode coefficients of all $m_{3\pi}$ bins $\vec{\mathcal{C}}$:

$$\chi^2(\vec{\mathcal{C}}) = \frac{1}{2} \sum_{b=1}^{N_{3\pi}-1} \sum_{i,j} \left[\delta_i^b \left[\mathbf{C}^b\right]_{ij}^{-1} \delta_j^b + \delta_i^b \left[\mathbf{C}^{b'}\right]_{ij}^{-1} \delta_j^b \right], \qquad (6.6)$$

where $\mathbf{C}^b$ is the covariance matrix of the production amplitudes in the $m_{3\pi}$ bin b. The sum runs over all $N_{3\pi}$ bins in $m_{3\pi}$ and $b' = b+1$. For reasons of readability, we omitted the explicit dependence of δ_i^b on $\mathcal{C}^b$ and $\mathcal{C}^{b'}$ in eq. (6.6).

If we minimize eq. (6.6), we minimize the total differences δ_i^b of the dynamic isobar amplitudes in neighboring $m_{3\pi}$ bins and adjust the zero-mode coefficients in all bins simultaneously to obtain the smoothest possible result. We label this method "smooth" from hereon.

In some cases, a set of waves might be affected by more than one zero mode. In this case, one zero-mode coefficient for every zero mode has to be determined. This is done the same way, as in the case of only one zero mode, with the following substitution in eqs. (5.67) and (6.5):

$$\mathcal{T}_i^{\text{fit}} + \mathcal{C}\mathcal{T}_i^0 \to \mathcal{T}_i^{\text{fit}} + \sum_z \mathcal{C}_z \mathcal{T}_i^{z,0}, \qquad (6.7)$$

where the sum runs over all contributing zero-modes and $\mathcal{C}_z$ and $\mathcal{T}_i^{z,0}$ are the zero-mode coefficient and shape of the corresponding zero mode z.

All of the different methods defined so far offer a way to determine the values of the zero-mode coefficients. Since these values can differ for the individual methods, we need to find a way to obtain one final set of zero-mode coefficients. To do so, we define the relative consistency of a method b with a method a:

$$d_b^a = \frac{\chi_a^2(\vec{\mathcal{C}}_b) - \chi_a^2(\vec{\mathcal{C}}_a)}{\chi_a^2(\vec{\mathcal{C}}_a)}, \qquad (6.8)$$

where $\chi_a^2(\vec{\mathcal{C}})$ is the chi square function corresponding to method a and $\vec{\mathcal{C}}_a$ is the set of zero-mode coefficients for all $m_{3\pi}$ bins, that minimizes this function. The relative consistency gives the relative increase of a χ^2 function with respect to its minimum for a set of zero-mode coefficients. Note, that the definition in eq. (6.8) of this measure for consistency is not commutative: $d_a^b \neq d_b^a$. We call a set of zero-mode coefficients from a method b consistent with a method a, if $d_b^a < 1$. If a method has free parameters other than $\mathcal{C}$ in the model, for example resonance parameters, these are kept at the values found in minimization. Using the relative intensities, we define the weight w_a of a method:

$$w_a = \left(\sum_b d_a^b \right)^{-1}. \qquad (6.9)$$

We use a weighted sum of the zero-mode coefficients of all methods as our final set of zero-mode coefficients, using the weight defined in eq. (6.9). To obtain the set of zero-mode coefficients that is most consistent with all methods, the weights are calculated for every $m_{3\pi}$ bin independently, so the composition of the final zero-mode coefficients out of the different methods is allowed to change with $m_{3\pi}$. The resulting zero-mode coefficients will be labeled with "weighted".

6.2.3. The $J_X^{PC} M^\varepsilon = 0^{-+}0^+$ sector

The sector of freed waves with $J_X^{PC} M^\varepsilon = 0^{-+}0^+$ quantum numbers contains two waves: the $0^{-+}0^+ [\pi\pi]_{0^{++}} \pi S$ and the $0^{-+}0^+ [\pi\pi]_{1^{--}} \pi P$ wave. These correspond to the two waves, discussed in section 5.2.1 and section 5.3 and therefore we encounter the same zero mode. We will use the strategy introduced in section 6.2.2 to resolve the ambiguity introduced by the zero mode.

Using the labeling scheme introduced in section 6.2.2, we use the following four methods to resolve the zero-mode ambiguity: "fix$_{all}$", "fix$_{f_0}$", "fit$_\rho$", and "smooth". The fit results for the resonance parameters obtained with the "fit$_\rho$" method are:

$$m_\rho = 770.3 \pm 0.4 \, \text{MeV}/c^2 \text{ and } \quad \Gamma_\rho = 152.1 \pm 0.9 \, \text{MeV}/c^2. \quad (6.10)$$

This is in fair agreement with the parameters used in the generation of the Monte Carlo data-set ($m_\rho = 769 \, \text{MeV}/c^2$; $\Gamma_\rho = 150.9 \, \text{MeV}/c^2$). The relatively large deviation of the fit parameters from the input values in terms of standard deviations is due to the fact, that the events in this wave are distributed according to the integral of the intensity distribution of the dynamic isobar amplitude over the range of the $m_{2\pi}$ bin, while in the fit only an integral over the amplitude is possible. This effect is discussed further in appendix D.

The resulting relative consistencies defined in eq. (6.8) between all methods and summed of all $m_{3\pi}$ bins, as well as the weighted average, "weighted", and the case without zero mode correction, "uncorr", are shown in the left plot of fig. 6.4. The weighted average yield zero-mode coefficients, that are consistent with all four methods. The zero-mode coefficients obtained with the smoothness method are inconsistent with the other three methods. However, the other three methods yield zero-mode coefficients consistent with the smoothness method and therefore give reasonably smooth results. Setting all zero-mode coefficients to zero, i.e. not correcting for zero modes, is inconsistent with the majority of the constraints.

As an example, the results for one $m_{3\pi}$ bin $1.8 \, \text{GeV}/c^2$—the mass of the $\pi(1800)$ resonance—are shown in fig. 6.5. We find good agreement between the Monte-Carlo input and the resulting dynamic amplitudes after resolving the ambiguities.

6.2.4. The $J_X^{PC} M^\varepsilon = 1^{++}0^+$ sector

The sector of freed waves with $J_X^{PC} M^\varepsilon = 1^{++}0^+$ quantum numbers contains two waves: the $1^{++}0^+ [\pi\pi]_{0^{++}} \pi P$ wave and the $1^{++}0^+ [\pi\pi]_{1^{--}} \pi S$ wave. In section 5.2.3, we have shown, that this combination of freed-isobar waves has a zero

Monte Carlo — $0^{-+}0^+$

	fit$_\rho$	fix$_{f_0}$	fix$_{\text{all}}$	smooth	uncorr.	weight
smooth	0.04	0.38	0.03	0.00	0.09	0.05
fix$_{\text{all}}$	0.06	1.60	0.00	1.09	8.40	0.33
fix$_{f_0}$	1.02	0.00	2.13	7.62	0.90	0.48
fit$_\rho$	0.00	0.95	0.06	4.46	8.60	0.05

Monte Carlo — $1^{++}0^+$

	fit$_\rho$	fix$_{f_0}$	fix$_{\text{all}}$	smooth	uncorr.	weight
smooth	0.20	0.14	0.17	0.00	0.44	0.17
fix$_{\text{all}}$	1.51	7.22	0.00	78.04	79.56	0.08
fix$_{f_0}$	0.13	0.00	0.07	0.30	0.32	0.08
fit$_\rho$	0.00	9.00	0.97	56.60	47.20	0.62

Monte Carlo — $2^{-+}0^+$

	fit$_\rho^2$	fit$_{f_2}$	fix$_{f_0}$	fix$_{\text{all}}$	smooth	uncorr.	weight
smooth	0.30	0.18	0.14	0.15	0.00	0.25	0.11
fix$_{\text{all}}$	0.09	0.23	0.17	0.00	0.38	0.25	0.01
fix$_{f_0}$	0.46	0.31	0.00	0.20	0.40	0.16	0.16
fit$_{f_2}$	0.40	0.00	0.49	0.26	0.59	0.52	0.21
fit$_\rho^2$	0.00	0.45	0.52	0.12	0.60	0.56	0.14

Figure 6.4.: Relative consistencies d_b^a, as defined in eq. (6.8), of the zero-mode coefficients obtained with the method b given on the ordinance to the method a on the abscissa, summed over all $m_{3\pi}$ bins. Left for the $J_X^{PC} M^\varepsilon = 0^{-+}0^+$ sector, center for the $1^{++}0^+$ sector, and right for the $2^{-+}0^+$ sector on the right in the Monte Carlo study introduced in section 6.2. By definition, the values on the diagonal vanish.

mode if the relativistic tensor formalism is used. With the numerical approach introduced in section 5.2.5, we were able to confirm that this mode is also present in the non-relativistic helicity formalism.

Since the set of freed isobars is the same as in section 6.2.3, we employ the same four constraints here to resolve the ambiguity. The resulting relative consistencies d_b^a of the methods are shown in the center plot of fig. 6.4. The weighted average yields zero-mode coefficients consistent with all used methods. Similar to the $0^{-+}0^+$ sector (see section 6.2.3), the results of the smoothness method and not correcting for the zero modes are inconsistent with the other methods. However, all other methods yield zero-mode coefficients consistent with the smoothness method. The "fit$_\rho$ " method yields the following resonance parameters:

$$m_\rho = 770.1 \pm 0.1\,\text{MeV}/c^2 \text{ and } \Gamma_\rho = 152.9 \pm 0.2\,\text{MeV}/c^2. \qquad (6.11)$$

We find a similar deviation from the input values as for the $0^{-+}0^+$ sector (see section 6.2.3), which again is a consequence of the integration over the $m_{2\pi}$ bin width (see appendix D).

To see the effect of the zero mode from another perspective, we do not show an example $m_{3\pi}$ bin for this sector, but the two-dimensional intensity distribution before and after resolving the zero-mode ambiguities. In fig. 6.6 it can be seen, that only the corrected results have a smooth behavior over the analyzed $m_{3\pi}$ range, while the uncorrected results jump from $m_{3\pi}$ bin to $m_{3\pi}$ bin.

6.2.5. The $J_X^{PC} M^\varepsilon = 2^{-+}0^+$ sector

The sector of freed waves with $J_X^{PC} M^\varepsilon = 2^{-+}0^+$ quantum numbers contains four freed waves: $2^{-+}0^+ [\pi\pi]_{0^{++}} \pi\text{D}$, $2^{-+}0^+ [\pi\pi]_{1^{--}} \pi\text{P}$, $2^{-+}0^+ [\pi\pi]_{1^{--}} \pi\text{F}$, and $2^{-+}0^+$
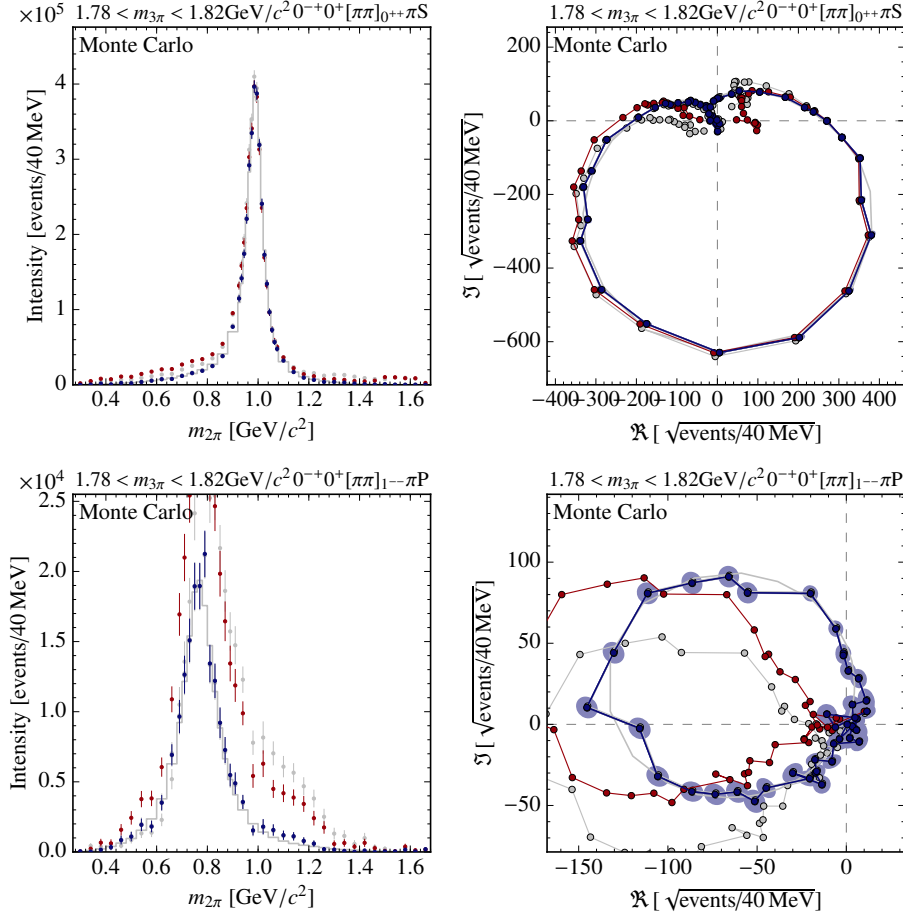
Figure 6.5.: Results for the $J_X^{PC} M^\varepsilon = 0^{-+}0^+$ waves before (red) and after (blue) resolving the zero-mode ambiguity with the weighted average of all used methods. The gray points are the results of the single methods; the gray line is the Monte-Carlo input.

$[\pi\pi]_{2^{++}} \pi S$ and is therefore the largest freed-isobar sector. With the numerical method introduced in section 5.2.5, we found two[e] zero modes in this sector, that contribute to the four waves.

Since we have more freed waves in this sector than in the previous two, we also employ more methods to resolve the arising ambiguities. In addition to "fix$_{all}$" and "fix$_{f_0}$", we use the "fit$_\rho$" method, where the $\rho(770)$ resonance is fitted in both freed waves with an $J_\xi^{PC} = 1^{--}$ isobar simultaneously. Since in this sector also a $J_\xi^{PC} = 2^{++}$ isobar is freed, we also use the "fit$_{f_2}$" method; we use this constraint only for the $m_{3\pi} > 1.38 \, \text{GeV}/c^2$ region, so that $m_{2\pi}$ can reach the nominal $f_2(1270)$ mass.

---

[e]In a dedicated study we find, there is only one exact zero mode. However, since a second eigenvector with a comparably small eigenvalue is present it has to be treated the same way.
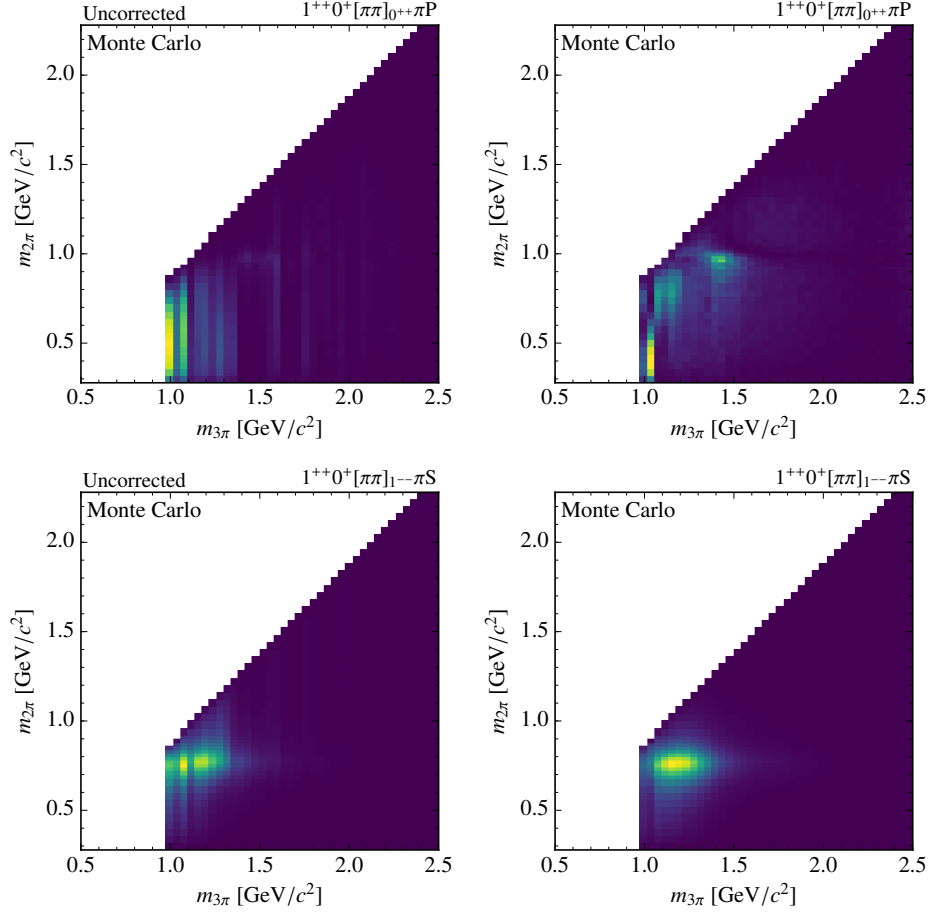
Figure 6.6.: Intensity distributions as in fig. 6.3 for the $J_X^{PC}M^\varepsilon = 1^{++}0^+$ waves before (left) and after (right) fixing the zero-mode coefficients to the weighted average weighted of the four methods discussed in the text.

The "fit$_\rho$" method gives the following values for the resonance parameters:

$$m_\rho = 768.3 \pm 0.2 \,\text{MeV}/c^2 \text{ and } \Gamma_\rho = 153.0 \pm 0.4 \,\text{MeV}/c^2, \tag{6.12}$$

which are similar to the ones found in the $0^{-+}0^+$ and the $1^{++}0^+$ sector (see sections 6.2.3 and 6.2.4). The "fit$_{f_2}$" method gives the following values $f_2(1270)$ parameters:

$$m_{f_2} = 1275.1 \pm 0.2 \,\text{MeV}/c^2 \text{ and } \Gamma_{f_2} = 184.5 \pm 0.5 \,\text{MeV}/c^2, \tag{6.13}$$

which are in good agreement with the input values of $m_{f_2} = 1275.1 \,\text{MeV}/c^2$ and $\Gamma_{f_2} = 185.1 \,\text{MeV}/c^2$.

The consistency of the individual methods is shown in the right plot of fig. 6.4. We see a better consistency between the different methods. This might be due

to the fact, that all freed waves in this sector have a similar relative intensity, in contrast to the 0^{-+} and 1^{++} sectors, and therefore the results of a single wave do not dominate the zero-mode coefficients found by the minimizer, $\mathcal{C}^{\mathrm{fit}}$ in eq. (5.64).

6.3. Freed-isobar PWA of Compass data

In section 6.2, we have shown, that the extended freed-isobar model, described in section 6.1 is able to reproduce the known dynamic isobar amplitudes in an PWA of Monte Carlo data, if the ambiguities caused by the zero modes are resolved.

We now apply the same model specified in section 6.1 to the $\pi^- p \to \pi^- \pi^+ \pi^- p$ data set, introduced in section 2.3. Since our model is based on the fixed-isobar PWA model of refs. [8, 12], we want to compare our results with the results published there. However, due to the different binnings in $m_{3\pi}$ and t', we cannot compare the two PWA results directly. Hence, we perform an additional fixed-isobar PWA with the same wave set as used in refs. [8, 12] but with the $m_{3\pi}$ and t' binnings as specified in section 6.1. The changes in the fixed dynamic isobar amplitudes and the rank of the negative reflectivity sector stated in section 6.1 are applied, as well. The results of this fixed-isobar PWA can be directly compared to the results of the freed-isobar PWA.

In the following, we present the results for the individual waves of this freed-isobar PWA in the same order as for the results of the Monte Carlo study in section 6.2. Since the set of freed-isobar waves is the same in the PWA of Monte Carlo and real data is the same, the appearing zero modes are also the same.

6.3.1. The $1^{++}1^+ [\pi\pi]_{1^{--}} \pi\mathrm{S}$ wave

The $1^{++}1^+ [\pi\pi]_{1^{--}} \pi\mathrm{S}$ wave does not have zero mode. Therefore, we can directly compare the results for this wave with the results from the fixed-isobar PWA. To do this, we coherently sum up the amplitudes of all $m_{2\pi}$ bins as described in eq. (5.60), where the sum runs over all kinematically allowed $m_{2\pi}$ bins of the $1^{++}1^+$ $[\pi\pi]_{1^{--}} \pi\mathrm{S}$ wave for the respective $m_{3\pi}$ bin. We can compare the resulting intensity of this sum over all $m_{2\pi}$ bins with the intensity of the fixed-isobar $1^{++}1^+ \rho(770) \pi\mathrm{S}$ wave.

This comparison—also incoherently summed over all four t' bins—is shown in the upper left plot of fig. 6.7. We see a qualitative agreement of the over all shapes. A closer look reveals, that the intensity from the freed-isobar PWA is a bit lower in the region of the $\mathrm{a}_1(1260)$ peak. One possible for this reason is, that the dynamic isobar amplitude in this wave is not perfectly described by the fixed Breit-Wigner parameterization in the fixed-isobar PWA. This can be seen in the lower row of fig. 6.7, where the resulting dynamic isobar amplitude for the $\rho(770)$ resonance peaks at slightly lower $m_{2\pi}$ as compared to the fixed dynamic isobar amplitude. Also, the Argand diagram of the dynamic isobar amplitude deviates slightly from a circle. This deviation cannot simply be explained by a global phase rotation. This distortion of the $\rho(770)$ shape might be due to rescattering

effects of the final-state particles or due to contributing non-resonant processes. The most prominent of such processes is the Deck effect, discussed in appendix B. However, in the upper left plot of fig. 6.7, a nice correlation of the appearing 3π and 2π resonances is observed, indicating, that this wave is dominated by the decay $a_1(1260) \rightarrow \rho(770)\,\pi$.

6.3.2. The $2^{-+}1^+\,[\pi\pi]_{1^{--}}\,\pi$P wave

In the $2^{-+}1^+\,[\pi\pi]_{1^{--}}\,\pi$P wave there is no zero mode, so we do not have to resolve any ambiguities in this wave.

Results for this wave are shown in fig. 6.8. The t'-summed intensity distribution as a function of $m_{3\pi}$ obtained with the freed-isobar PWA matches the one of the fixed-isobar PWA nicely in most $m_{3\pi}$ bins. However, the dynamic isobar amplitude, shown on the bottom row of fig. 6.8 for one bin in $m_{3\pi}$ and t', deviates from the one used in the fixed-isobar PWA. The reason for this deviation might again lay in rescattering effects or in non-resonant contributions, as mentioned in section 6.3.1. The two-dimensional intensity distribution in the upper right plot of fig. 6.8 shows a broad structure in $m_{3\pi}$, decaying into the $\rho(770)$, that cannot easily be identified with any known π_2 resonance.

6.3.3. The $2^{++}1^+\,[\pi\pi]_{1^{--}}\,\pi$D wave

The last wave in our model "C" with a freed dynamic isobar amplitude that does not suffer from zero-mode ambiguities is the $2^{++}1^+\,[\pi\pi]_{1^{--}}\,\pi$D wave. As shown in fig. 6.9, we find a good agreement of the intensity distributions from the freed-isobar PWA and those from the fixed-isobar PWA. In both analyses, a distinct peak from the $a_2(1320)$ resonance is visible. In the upper right plot of fig. 6.9, we see that this peak is strongly correlated with the $\rho(770)$ resonance, so the main decay process in this wave is $a_2(1320) \rightarrow \rho(770)\,\pi$. This process constitutes the decay with the least background contributions in the analysis. The intensity distribution of the dynamic isobar amplitude, nicely matches the parameterization used in the fixed-isobar PWA. However, in the Argand diagram, there are significant differences that can be attributed to differences in the phase motion as function of $m_{2\pi}$. They cannot be accounted for by a global phase rotation. A reason for this might be rescattering of non-resonant effects, similar to the ones mentioned in sections 6.3.1 and 6.3.2.

6.3.4. The $J_X^{PC}M^\varepsilon = 0^{-+}0^+$ sector

As in the Monte Carlo study, discussed in section 6.2.3, the first sector affected by a zero mode is $J_X^{PC}M^\varepsilon = 0^{-+}0^+$ with two freed waves in the PWA model: $0^{-+}0^+$ $[\pi\pi]_{0^{++}}\,\pi$S and $0^{-+}0^+\,[\pi\pi]_{1^{--}}\,\pi$P.

To resolve the ambiguities caused by the presence of the zero mode, we use the same constraints as in the Monte Carlo case discussed in section 6.2.3. As constraints for of the J_ξ^{PC} dynamic amplitudes, we use the same parameterization
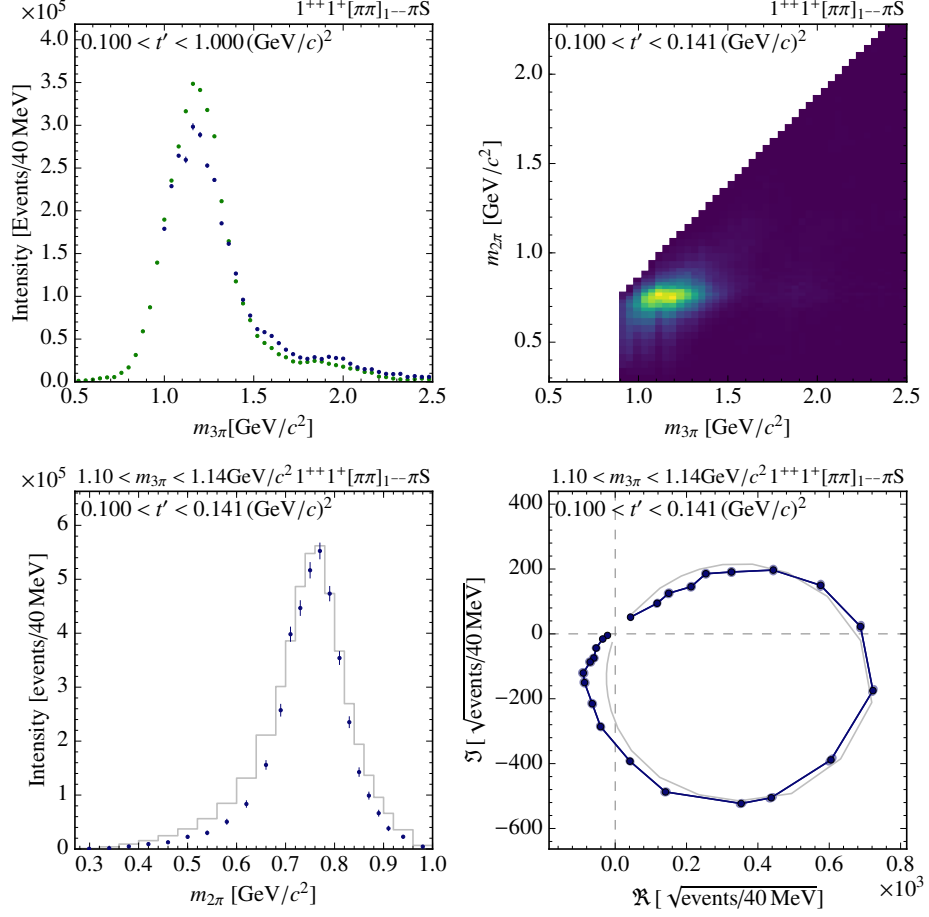
Figure 6.7.: Results for the $1^{++}1^+ [\pi\pi]_{1^{--}} \pi S$ wave. Upper left: comparison of the t'-summed intensity distributions over $m_{3\pi}$. The blue points are from the freed-isobar PWA, the green points from the fixed-isobar PWA. Upper right: intensity distribution as a function of $m_{2\pi}$ and $m_{3\pi}$ for the lowest t' bin. Lower row: dynamic isobar amplitude for a single bin in $m_{3\pi}$ and the lowest t' bin, shown as intensity distribution on the left and as Argand diagram on the right. The dynamic isobar amplitude used in the fixed-isobar PWA is shown as gray line for comparison.
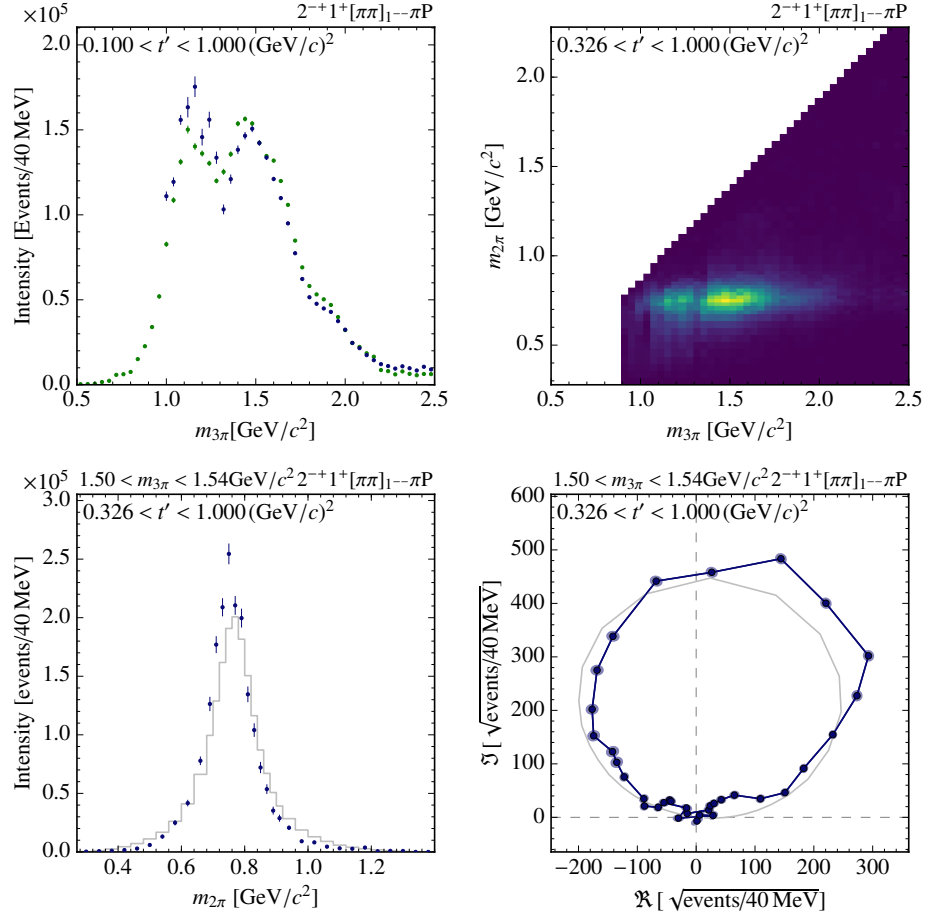
Figure 6.8.: Similar to fig. 6.7, now showing results for the $2^{-+}1^{+}\,[\pi\pi]_{1^{--}}\,\pi\mathrm{P}$ wave.

that was used in the fixed-isobar PWA. All methods to resolve the zero-mode ambiguities are performed in every t' bin independently. Using the results of all four methods, we construct the weighted average of the resulting zero-mode coefficients $\mathcal{C}$, as described in eq. (6.9). We again find, that the set of zero-mode coefficients constructed this way are consistent with all used methods (see fig. 6.10). Using these zero-mode coefficients, we compare the resulting intensity distributions with those from the fixed-isobar PWA in figs. 6.11 and 6.13. For both 0^{-+} waves, we find, that the intensity distributions match nicely. On the one hand, this indicates that the methods of resolving the zero-mode ambiguities are not only consistent with each other, but are also consistent with the fixed-isobar PWA. On the other hand, this agreement shows, that the parameterizations of the dynamic isobar amplitudes used in the fixed-isobar PWA already give a quite accurate description of the occurring physics.
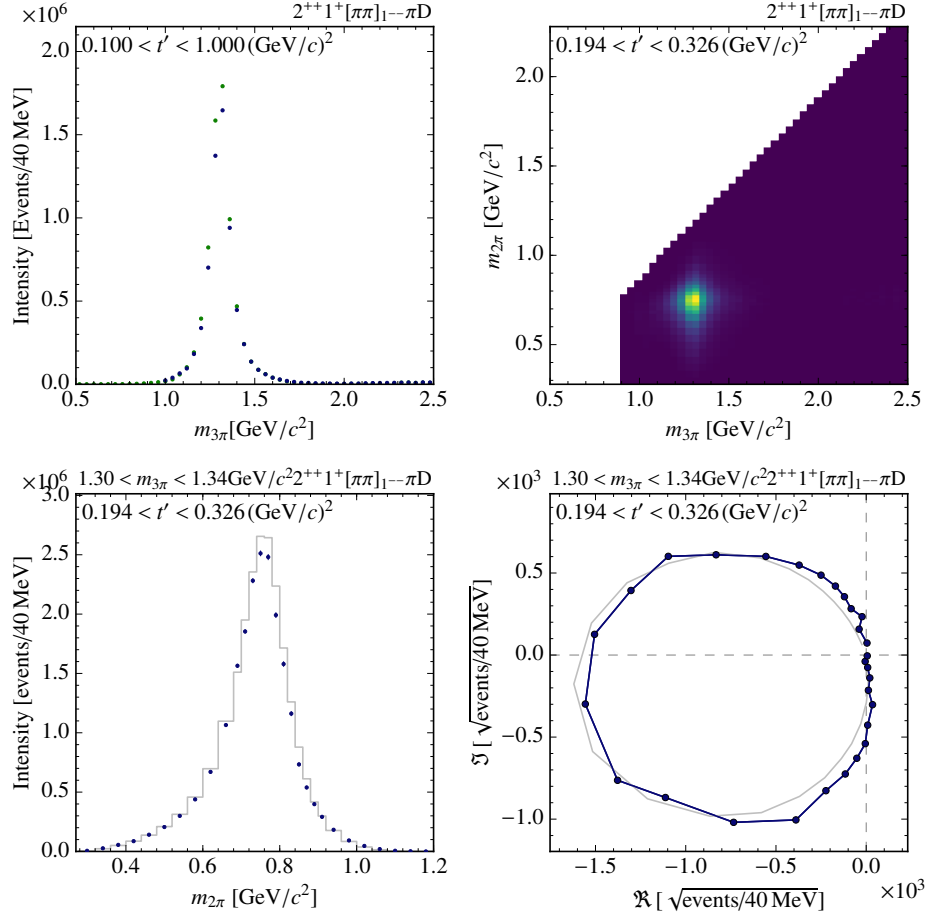
Figure 6.9.: Similar to fig. 6.7, now showing results for the $2^{++}1^+ [\pi\pi]_{1^{--}} \pi D$ wave.

The two-dimensional intensity distribution for the $0^{-+}0^+ [\pi\pi]_{0^{++}} \pi S$ wave in fig. 6.11 shows a distinct peak corresponding to the decay $\pi(1800) \rightarrow f_0(980)\,\pi$ and a smaller one for $\pi(1800) \rightarrow f_0(1500)\,\pi$, as well as broader structures at low $m_{2\pi}$ and $m_{3\pi}$. The resulting dynamic isobar amplitude for an $m_{3\pi}$ bin at the position of the $\pi(1800)$ resonance shows, that the interplay of the fixed parameterizations for $(\pi\pi)_S$, $f_0(980)$, and $f_0(1500)$ is able to describe the main features of the freed-isobar result. In the Argand diagram, two circles are visible, corresponding to the two resonances $f_0(980)$ and $f_0(1500)$. The resonance parameters of these two resonances will be determined in sections 7.0.10 and 7.0.11. In fig. 6.12, two additional Argand diagrams for $m_{3\pi}$ below and above the $\pi(1800)$ resonance are shown. We see, that the diagrams are rotated in the complex plane due to the phase motion from the $\pi(1800)$ resonance.

The two-dimensional intensity distribution for the $0^{-+}0^+ [\pi\pi]_{1^{--}} \pi P$ wave in fig. 6.13 shows a broad three-pion structure at about $1.4\,\text{GeV}/c^2$ decaying into $\rho(770)\,\pi^-$. Since we do not observe any phase motion of the coupling of the $\rho(770)$—$\mathcal{F}$ in eq. (5.67)—in any t' bin, this peak can most likely not be attributed to a resonance like the $\pi(1300)$. However, the dynamic isobar amplitude at a single $m_{3\pi}$ bin, depicted in the lower row of fig. 6.13, show a distinct intensity peak and a circle in the Argand diagram corresponding to the $\rho(770)$ resonance. For the determination of the resonance parameters of the $\rho(770)$ see section 7.0.8.

6.3.5. The $J_X^{PC} M^\varepsilon = 1^{++}0^+$ sector

The $J_X^{PC} M^\varepsilon = 1^{++}0^+$ sector contains two waves with freed $J_\xi^{PC} = 0^{++}$ and 1^{--} isobars which are connected by one zero mode. We use the same methods as in section 6.2.4 to resolve the arising ambiguities and find good consistencies of the weighted average with all methods employed.

The results for the $1^{++}0^+ [\pi\pi]_{0^{++}} \pi P$ wave are shown in fig. 6.14, where we see a good agreement of the intensity distribution with the one from the fixed-isobar PWA after correcting the former for the zero mode. The uncorrected freed-isobar results, however, differ up to an order of magnitude from the fixed-isobar results. This again shows the necessity to resolve these ambiguities. In the two-dimensional intensity distribution, we see a broad structure at low two-pion masses and a distinct peak, corresponding to the decay $a_1(1420) \rightarrow f_0(980)\,\pi$. The $a_1(1420)$ was seen first by the COMPASS experiment [37]. Since the appearance of a 1^{++} resonance at this mass is unexpected, it is important to show that the signal is not simply an artifact of the PWA method. Since the corresponding peak appears in the freed-isobar study, we can conclude, that the $a_1(1420)$ is no such artifact, stemming from possibly improper parameterizations of the $J_\xi^{PC} = 0^{++}$ dynamic isobar amplitudes. Looking at the dynamic isobar amplitudes in the bottom row of fig. 6.14, we see, that the amplitudes used in the fixed-isobar PWA deviate from the dynamic amplitudes resulting from the freed-isobar PWA. The resonance parameters of the $f_0(980)$ resonance will be determined in section 7.0.10.
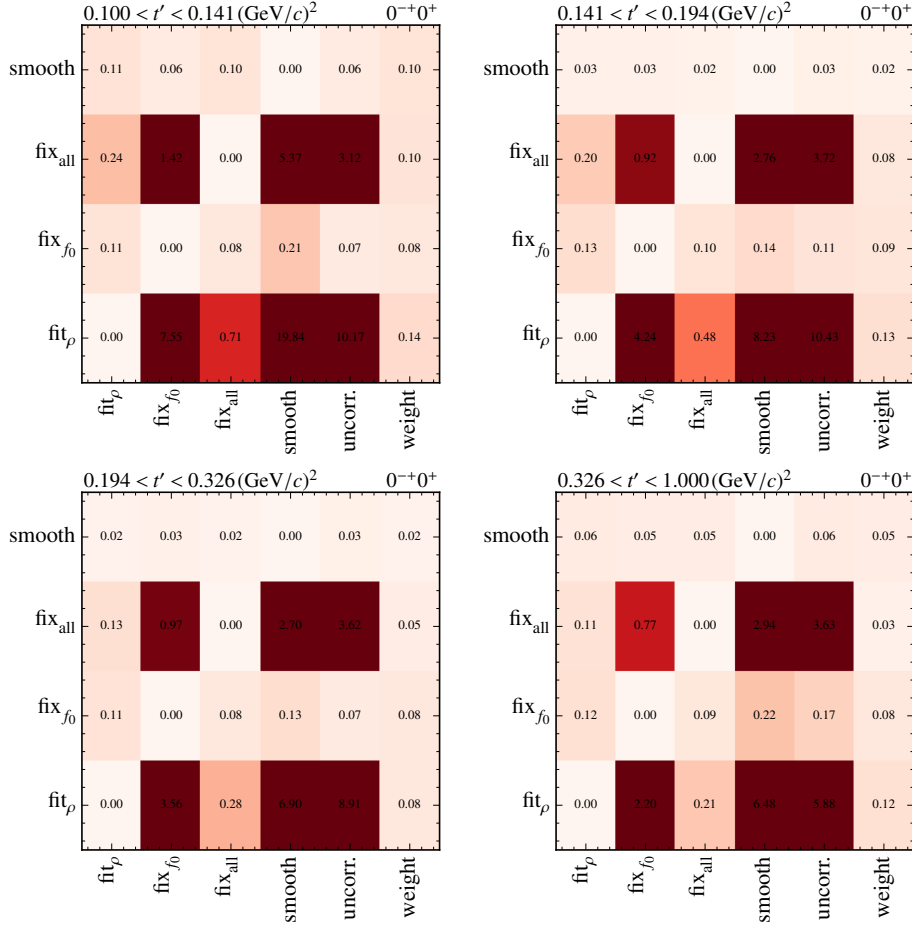
Figure 6.10.: Relative consistencies d_b^a, as defined in eq. (6.8), for the different methods to resolve the zero-mode coefficients in the $J_X^{PC} M^\varepsilon = 0^{-+}0^+$ sector for the four t' bins.

In the second wave of the sector, the $1^{++}0^+ [\pi\pi]_{1^{--}} \pi S$ wave, we also see a good agreement of the intensity distributions in $m_{3\pi}$ with that from the fixed-isobar PWA, after correcting the former for the zero-mode ambiguities. The results for this wave are shown in fig. 6.15. In the two-dimensional intensity distribution, we see a clear peak corresponding to the decay $a_1(1260) \rightarrow \rho(770)\pi$, the most dominant process in the whole PWA. In the bottom row of fig. 6.15, we see a nice agreement of the freed dynamic isobar amplitude of the $J_\xi^{PC} = 1^{--}$ isobar with the parameterization used in the fixed-isobar PWA. The determination of the resonance parameters of the $\rho(770)$ resonance parameters will be discussed in section 7.0.8.
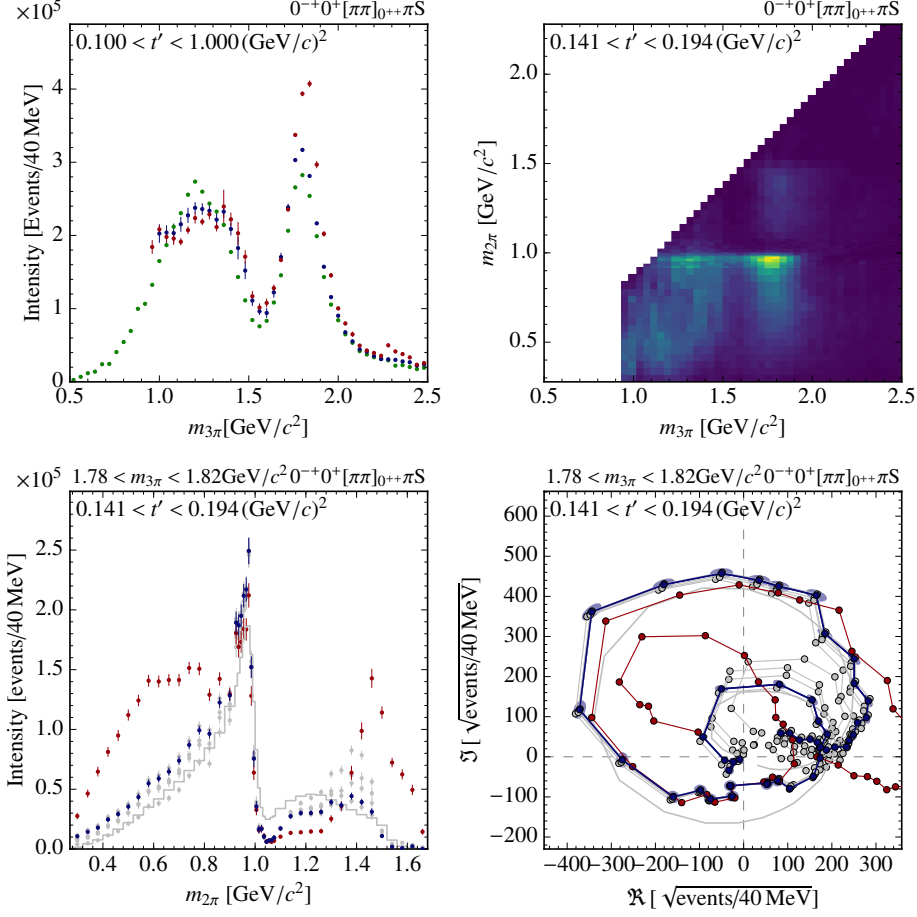
Figure 6.11.: Similar to fig. 6.7, now showing the $0^{-+}0^+ [\pi\pi]_{0^{++}} \pi S$ wave. The red points show the direct results from the freed-isobar PWA without correcting for the zero mode. The blue points show the result after correction for the zero mode with the weighted average of the individual methods. The gray points in the bottom-row plots show the results of the individual methods. The picture in the upper left shows the incoherent sum over all four t' bins; the other three pictures only show results for a single t' bin.
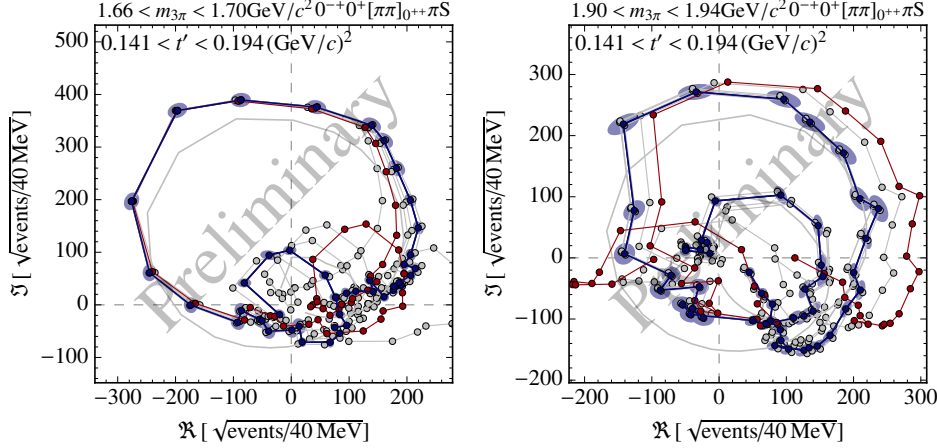
Figure 6.12.: Argand diagrams for the $0^{-+}0^+ [\pi\pi]_{0^{++}} \pi$S wave, similar to the lower right plot of fig. 6.11 for $m_{3\pi}$ bins below and above the $\pi(1800)$ resonance.

6.3.6. The $J_X^{PC} M^\varepsilon = 2^{-+}0^+$ sector

The $J^{PC} M^\varepsilon = 2^{-+}0^+$ sector contains four freed waves, which are affected by two zero modes. Again, we use the same methods as in section 6.2.5 to resolve the arising ambiguities. In fig. 6.16, we see that the different methods are not as consistent as in the other J^{PC} sectors discussed in sections 6.3.4 and 6.3.5. However, since the resulting intensity spectra qualitatively agree with those from the fixed-isobar PWA after correcting for the two zero modes (see the upper left plots of figs. 6.17 to 6.20), we still trust the weighted average introduced in eq. (6.9) to yield reliable zero-mode coefficients. We only find minor differences in the peak region of the $2^{-+}0^+ [\pi\pi]_{1^{--}} \pi$P wave. In section 7.0.9 we will see, that the fits of the $J_\xi^{PC} = 2^{++}$ isobar with a relativistic Breit-Wigner amplitude for the $f_2(1270)$ resonance exhibit a larger χ^2/ndf that comparable fit for other waves. This indicates, that the real dynamic amplitude of the 2^{++} isobar cannot be properly described with a simple Breit-Wigner amplitude, explaining the inconsistency of the "fit$_{f_2}$" with the rest of the methods.

For the $2^{-+}0^+ [\pi\pi]_{0^{++}} \pi$D wave, shown in fig. 6.17, we see broad structures at low $m_{3\pi}$ and $m_{2\pi}$ and a peak at $m_{3\pi} \approx 1.9\,\text{GeV}/c^2$ and $m_{2\pi} \approx 1\,\text{GeV}/c^2$. This corresponds to the process $\pi_2(1880) \to f_0(980)\,\pi$. In the dynamic isobar amplitude for an $m_{3\pi}$ bin at the $\pi_2(1880)$ resonance, we observe, that also the $f_0(1500)$ resonance contributes weakly. We also see, that the parameterizations for the dynamic isobar amplitudes used in the fixed-isobar PWA do not agree with those from the freed-isobar PWA.

The results for the $2^{-+}0^+ [\pi\pi]_{1^{--}} \pi$P wave are shown in fig. 6.17. In the two-dimensional intensity distribution, a broad peak, corresponding to the process
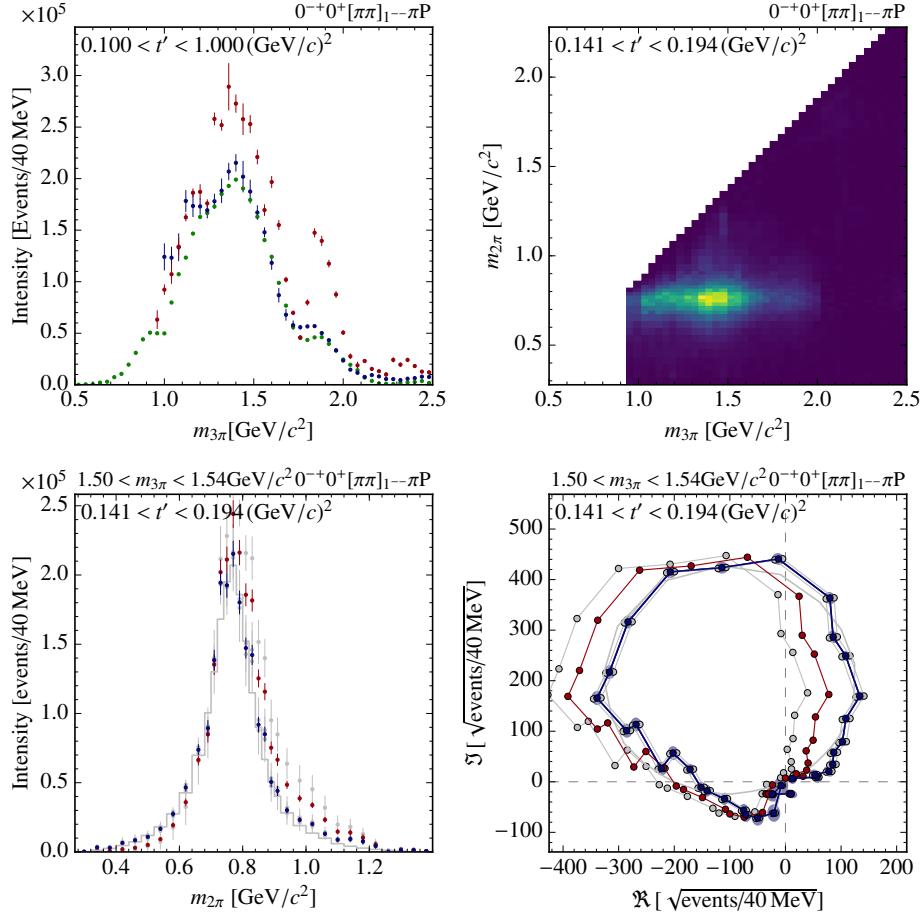
Figure 6.13.: Similar to fig. 6.11, now showing results for the $0^{-+}0^+ [\pi\pi]_{1^{--}} \pi\mathrm{P}$ wave.

$\pi_2(1670) \to \rho(770)\,\pi$ is visible. The dynamic isobar amplitude from the freed-isobar PWA matches the parameterization used for the $\rho(770)$ in the fixed-isobar PWA.

The two-dimensional intensity distribution of the $2^{-+}0^+ [\pi\pi]_{1^{--}} \pi\mathrm{F}$ wave (see fig. 6.19) is dominated by a peak corresponding to the process $\pi_2(1880) \to \rho(770)\,\pi$, but also has some contribution from $\pi_2(1670) \to \rho(770)\,\pi$. The dynamic isobar amplitude from the freed-isobar PWA matches the parameterization used for the $\rho(770)$ in the fixed-isobar PWA.

The $2^{-+}0^+ [\pi\pi]_{2^{++}} \pi\mathrm{S}$ wave is the only wave with freed $J_\xi^{PC} = 2^{++}$ dynamic isobar amplitude in model "C". In the two-dimensional intensity distribution (see fig. 6.20), we see a distinct peak corresponding to the process $\pi_2(1670) \to \mathrm{f}_2(1270)\,\pi$. The dynamic isobar amplitude from the freed-isobar PWA nicely matches that of the Breit-Wigner description of the $\mathrm{f}_2(1270)$ in the fixed-isobar PWA. The determination of resonance parameters of the $\rho(770)$ and $\mathrm{f}_2(1270)$ resonances will be discussed in chapter 7.
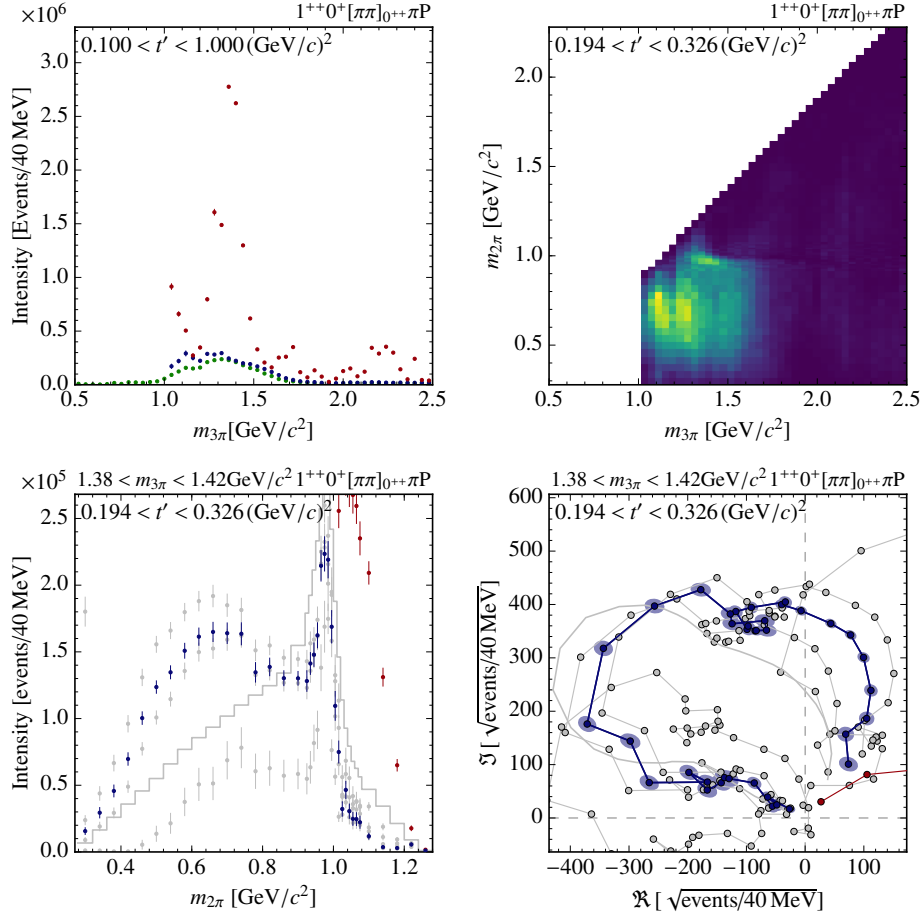
Figure 6.14.: Similar to fig. 6.11, now showing results for the $1^{++}0^+ [\pi\pi]_{0^{++}} \pi$P wave.

6.3.7. Comparison with published freed-isobar PWA

A first freed-isobar PWA on the COMPASS data set introduced in chapter 2 was published in ref. [12] alongside the fixed-isobar PWA described in chapter 4, as already mentioned at the beginning of this chapter. This freed-isobar PWA was performed in $m_{3\pi}$ bins of $40 \, \text{MeV}/c^2$ width and four t' bins. The binning in $m_{2\pi}$ is the same as in the studies presented here, but two small differences, already mentioned in section 6.1, with respect to our analysis model exist: the dynamic isobar amplitudes of the fixed-isobar waves are the ones listed in table 6.2 and the negative reflectivity sector has rank 2. In fig. 6.21 the two-dimensional intensity distributions for single t' bins are shown, which can be compared to the corresponding plots in figs. 6.11, 6.14 and 6.20. Since every J_X^{PC} sector contains only one freed wave, no zero modes are present in this model. The results of our analysis are very similar to those in ref. [12] and we again see, that our method of resolving zero mode ambiguities works.
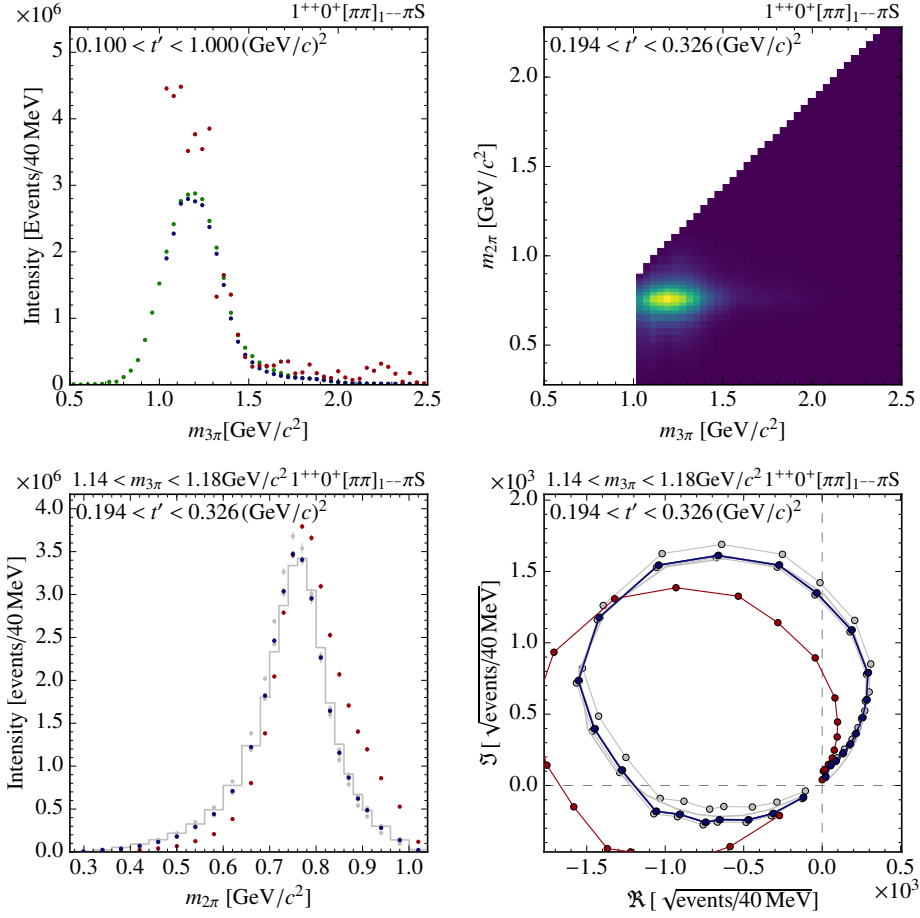
Figure 6.15.: Similar to fig. 6.11, now showing results for the $1^{++}0^+ [\pi\pi]_{1--} \pi S$ wave.

6.3.8. Waves with fixed dynamic isobar amplitudes

In addition to the 11 waves with freed dynamic isobar amplitudes, the wave set of study "C" contains 72 waves with fixed dynamic isobar amplitudes. We compare the PWA result for these waves with the PWA result for the 88-wave set with only fixed dynamic isobar amplitudes (see table 6.1). We find a good qualitative agreement for both analyses for almost all waves. Here we will only discuss waves, that exhibit systematic qualitative differences between the fixed- and the freed-isobar PWA stretching over several $m_{3\pi}$ bins. These waves are shown in fig. 6.22. With respect to the fixed-isobar PWA, the following changes are observed in the freed-isobar PWA:

- $1^{++}0^+ \rho_3(1690) \pi G$: the peak at $m_{3\pi} = 1.4 \, \text{GeV}/c^2$ vanishes;

- $2^{-+}0^+ \rho_3(1690) \pi P$: a narrow peak around $m_{3\pi} = 1.45 \, \text{GeV}/c^2$ appears;
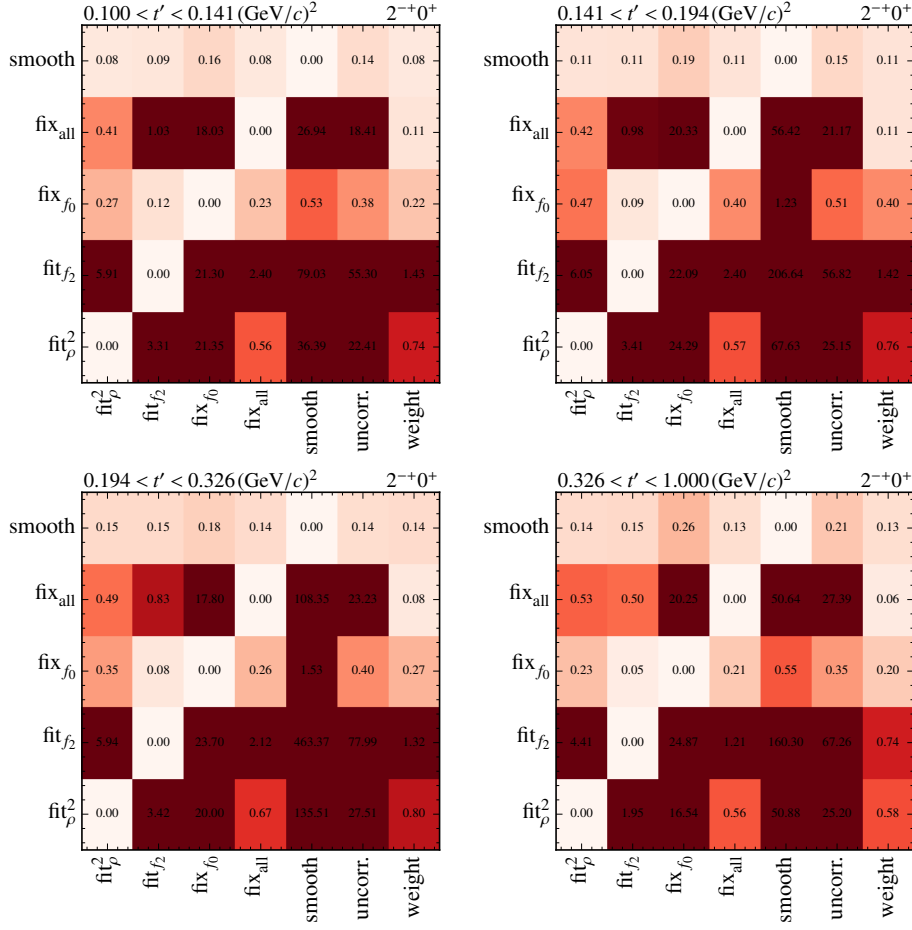
Figure 6.16.: Similar to fig. 6.10, now showing results for the $J_X^{PC}M^\varepsilon = 2^{-+}0^+$ sector.

- $2^{-+}1^+ (\pi\pi)_S \pi D$: a peak at $m_{3\pi} = 0.95\,\text{GeV}/c^2$ appears;

- $5^{++}0^+ \rho_3(1690)\,\pi D$: the intensity increases strongly for $m_{3\pi} > 2.2\,\text{GeV}/c^2$;

- $2^{-+}1^- f_2(1270)\,\pi S$: the broad structure in the 1.5 to 1.9 GeV/c^2 mass region vanishes;

- $2^{++}1^- f_2(1270)\,\pi P$: the peak around $m_{3\pi} = 1.55\,\text{GeV}/c^2$ vanishes.

These six waves all have small relative intensities, well below 1% (see table 6.1), so we do not expect leakage effects of these differences on the overall results of the PWA. The vanishing of peak-like structures in the freed-isobar PWA, like observed in the $1^{++}0^+ \rho_3(1690)\,\pi G$, the $2^{-+}1^- f_2(1270)\,\pi S$ and the $2^{++}1^- f_2(1270)\,\pi P$
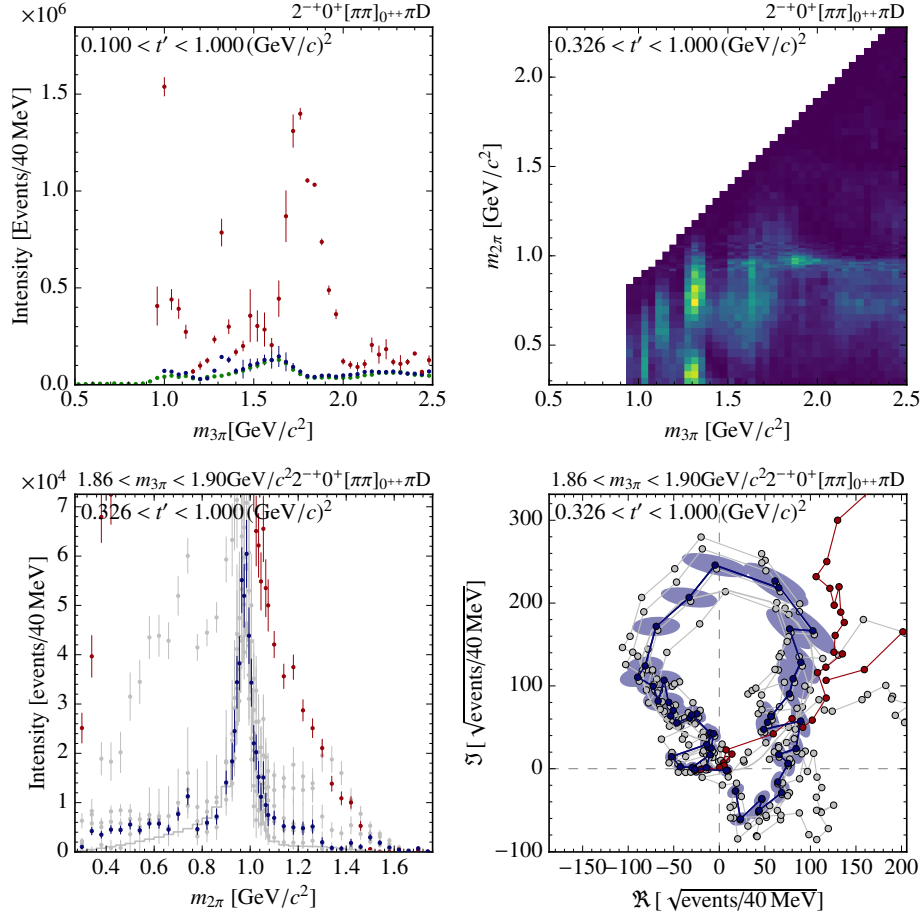
Figure 6.17.: Similar to fig. 6.11, now showing results for the $2^{-+}0^+ [\pi\pi]_{0^{++}} \pi D$ wave.

waves[f] can be explained by the drastically increased number of free parameters and the larger freedom of the freed-isobar PWA. Further studies have to show, whether these original peak-like structures are physical, and vanish due to leakage into freed-isobar waves, or they stem from imperfections in the fixed-isobar dynamic amplitudes and vanish, since the freed dynamic isobar amplitudes better resemble the physical dynamic isobar amplitudes.

The appearance of new peaking structures as in the $2^{-+}0^+ \rho_3(1690) \pi P$, the $2^{-+}1^+ (\pi\pi)_S \pi D$ and the $5^{++}0^+ \rho_3(1690) \pi D$ waves cannot be explained by leakage effects. However, we see this change in all four bins of t'. A possible reason for the appearing peak in the $2^{-+}0^+ \rho_3(1690) \pi P$ wave, that occurs in the subthreshold region, seems to be that in both models the production amplitude of

---

[f]Two of these waves have negative reflectivity $\varepsilon = -1$ and are therefore badly understood, since the process is assumed to happen via Pomeron-exchange with positive reflectivity.
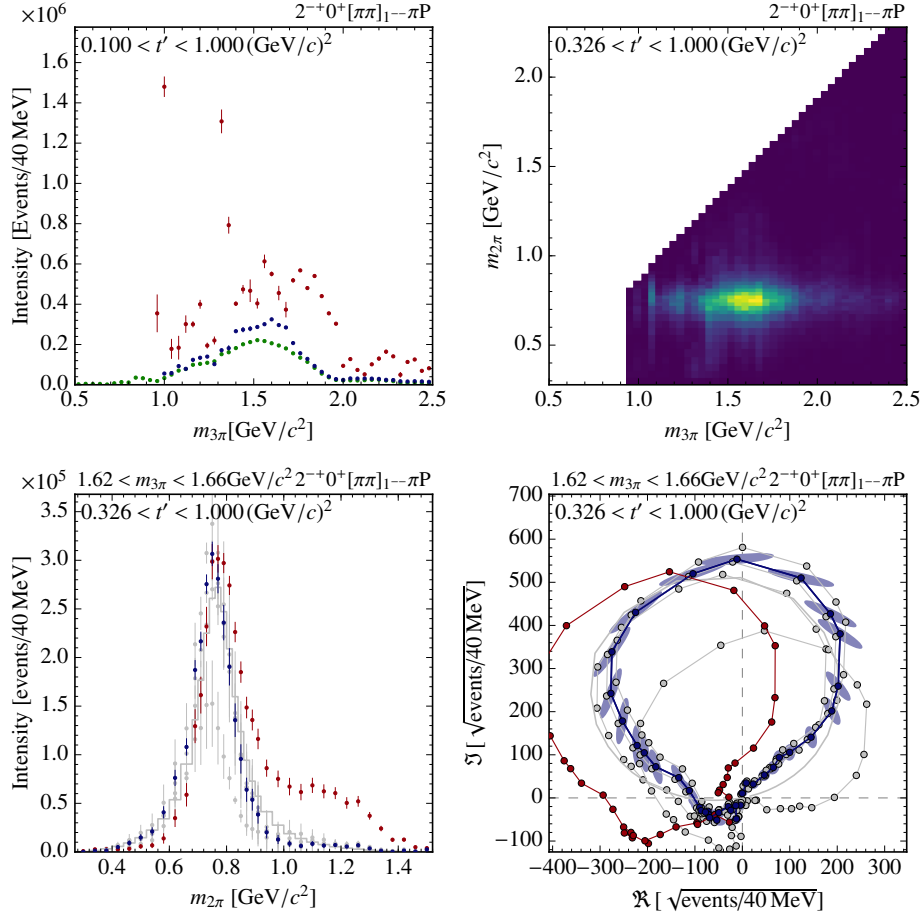
Figure 6.18.: Similar to fig. 6.11, now showing results for the $2^{-+}0^+ [\pi\pi]_{1^{--}} \pi\mathrm{P}$ wave.

the corresponding $2^{-+}1^+ \rho_3(1690) \pi\mathrm{P}$ wave is fixed to zero below $1.3\,\mathrm{GeV}/c^2$. The so-called partial-waves thresholds were originally fine-tuned by F. Haas to avoid such jumps in the 88-wave fixed-isobar model, therefore we do not see jumps in the fixed-isobar PWA [8]. Since waves with freed isobar dynamic amplitudes do not have such thresholds, the thresholds for fixed-isobar waves have to be adapted in further studies.

The arising sub-threshold peak in the $2^{-+}1^+ (\pi\pi)_\mathrm{S} \pi\mathrm{D}$ wave, however, cannot be explained by threshold effects. Since it arises around $1\,\mathrm{GeV}/c^2$ and there is no $2^{-+}1^+\mathrm{f}_0(980) \pi\mathrm{D}$ in the wave set, the peak is most likely caused by the $\mathrm{f}_0(980)$ resonance.

Neither the existence of a resonance, nor a partial-wave threshold is able to explain the structure arising in the $5^{++}0^+\rho_3(1690) \pi\mathrm{D}$. To find the origin of this deviation, more dedicated leakage studies are necessary.
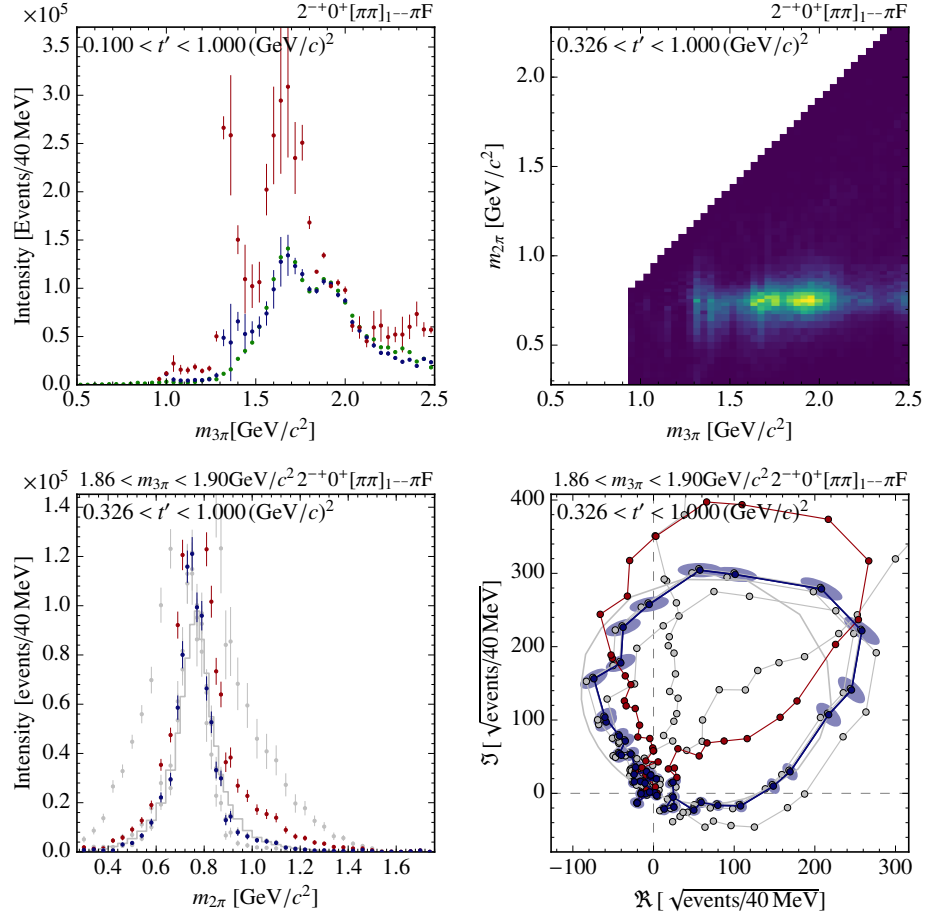
Figure 6.19.: Similar to fig. 6.11, now showing results for the $2^{-+}0^+\,[\pi\pi]_{1--}\,\pi F$ wave.

6.4. Further freed-isobar studies on Compass data

In section 6.3 we have seen, that the results of the freed-isobar PWA are qualitatively consistent with the results of the fixed-isobar PWA. Starting from the model for the 11 wave freed-isobar PWA, specified in section 6.1 and listed in table 6.1, we explore different extensions of this freed wave set and apply them to the same data set to obtain insight into the dynamic isobar amplitudes of selected interesting waves. A list of these studies has already been given in section 6.1.

6.4.1. Freeing the spin-exotic $1^{-+}1^+\,[\pi\pi]_{1--}\,\pi P$ wave

As a first extension to the freed-isobar model, study "E", specified in table 6.1, we free the dynamic isobar amplitude of the $1^{-+}1^+\rho(770)\,\pi P$ wave in addition the 11 waves of "C". This wave is of particular interest, since it has spin-exotic quantum

Figure 6.20.: Similar to fig. 6.11, now showing results for the $2^{-+}0^+ [\pi\pi]_{2^{++}} \pi S$ wave.
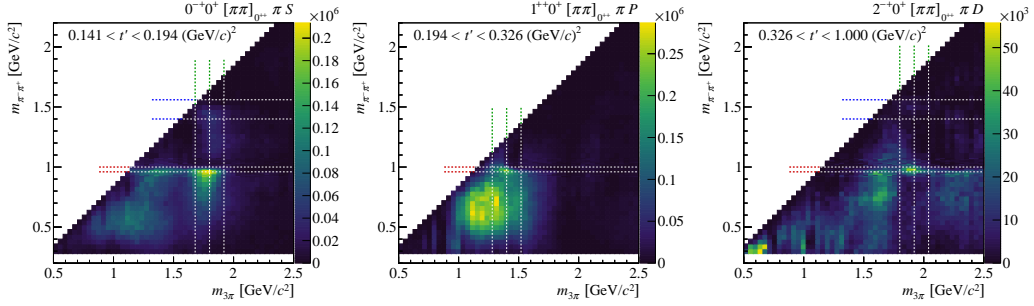
Figure 6.21.: Two dimensional intensity distribution for the $0^{-+}0^+ [\pi\pi]_{0^{++}} \pi S$ wave in the second t' bin (left), for the $1^{++}0^+ [\pi\pi]_{0^{++}} \pi P$ wave in the third t' bin (center), and the $2^{-+}0^+ [\pi\pi]_{0^{++}} \pi D$ wave in the highest t' bin (right) taken from ref. [12].
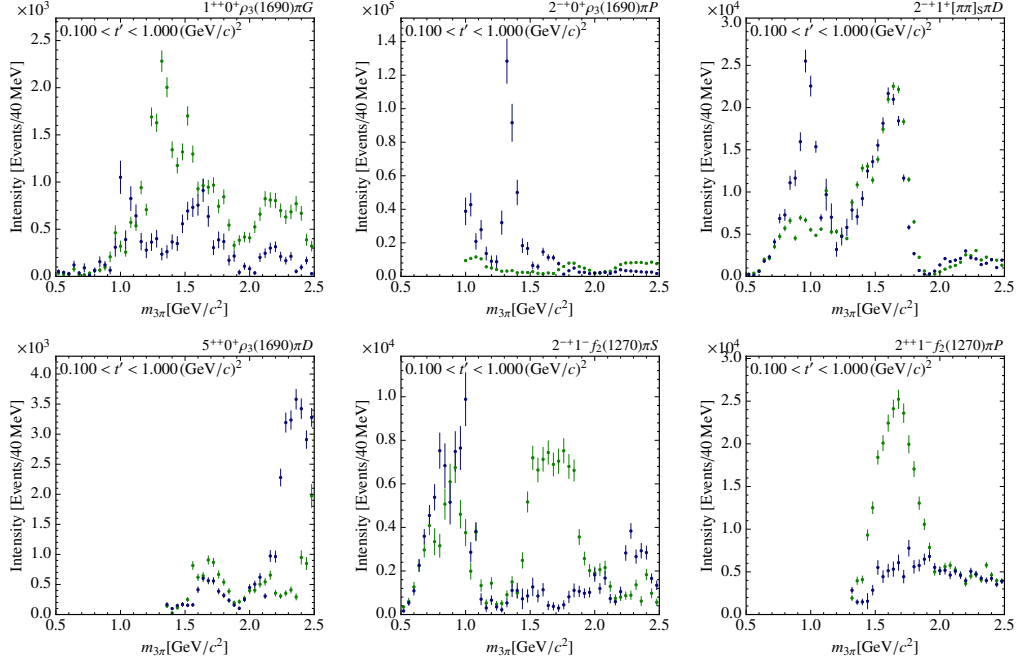
Figure 6.22.: Comparison of the PWA results using the 88-wave set with fixed isobar amplitudes and the wave set of study "C" with freed dynamic isobar amplitudes (see table 6.1). Blue points represent the freed-isobar PWA and green points the fixed-isobar PWA.

numbers, that are forbidden for a simple quark-antiquark state. Resonance signals in this wave were claimed by several analyses, for example in refs. [3–6], but yield strong model-dependence of the intensity distribution and a controversial resonance interpretation.

F. Haas was able to show in ref. [8], that the shape of the intensity distribution of the spin-exotic wave below $1.4\,\mathrm{GeV}/c^2$ exhibits a strong dependence on the chosen wave set. The results from refs. [3–6], could be reproduced using the respective wave sets and the data set collected by COMPASS. However, although the wave set for the fixed-isobar PWA was chosen to reduce discontinuities induced by thresholds, it remains difficult to pin down the resonance content of the spin-exotic wave.

To investigate the isobar content of the spin-exotic wave, we study the freed dynamic isobar amplitudes of this wave. We have seen in section 5.2.3, that a zero mode exists in this wave, that does not connect to any other wave and needs to be corrected for. The existence of a zero mode in this wave might explain the strong dependence of the spin-exotic wave on the wave set observed in earlier studies [3–6]. We use the $\rho(770)$ resonance as a constraint, once as a fixed Breit-Wigner parameterization, "fix$_\rho$", and as a Breit-Wigner parameterization with floating mass and width, "fit$_\rho$", as described in section 6.2.2. We leave out the smoothness method in
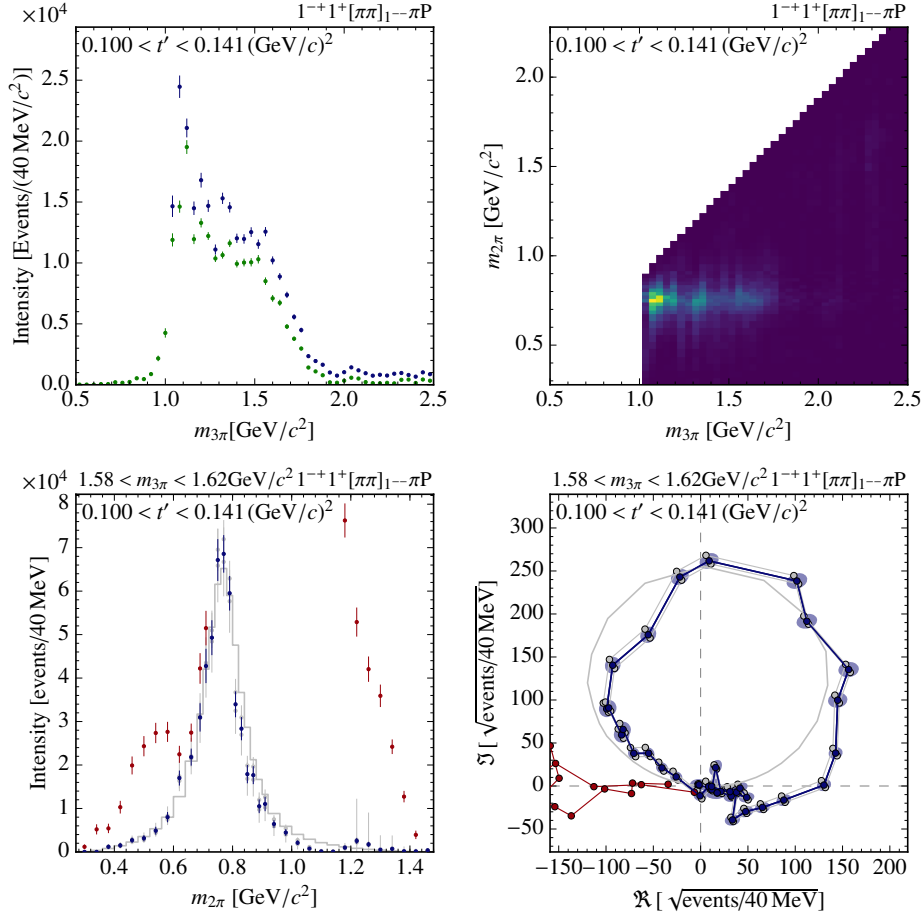
Figure 6.23.: Similar to fig. 6.11, now showing results for the $1^{-+}1^+\,[\pi\pi]_{1^{--}}\,\pi\mathrm{P}$ wave in the lowest bin in t'.

this wave, since we see for example in section 6.2.3, that it tends to give unphysical results and is not counteracted by enough other methods in this case. The results for the spin-exotic wave are shown in figs. 6.23 and 6.24 for the lowest and highest bin in t'. In both t' bins, we see an excess of the intensity distributions over the fixed-isobar PWA, while the shapes are consistent. In the two-dimensional intensity distributions we see broad structures in $m_{3\pi}$, decaying into $\rho(770)\,\pi^-$. The peak position moves to higher values of $m_{3\pi}$ in the higher t' bin and could correspond to a π_1 resonance. The extracted dynamic isobar amplitudes are dominated by the $\rho(770)$ resonance, but exhibit deviations from a simple Breit-Wigner shape.

6.4.2. Extension of the freed $J_X^{PC}M^\varepsilon = 1^{++}0^+$ sector

In study "D", we explore the $J_X^{PC}M^\varepsilon = 1^{++}0^+$ sector further, by also freeing the dynamic isobar amplitudes in the $1^{++}0^+\,\rho(770)\,\pi\mathrm{D}$ wave and the $1^{++}0^+\mathrm{f}_2(1270)\,\pi\mathrm{P}$
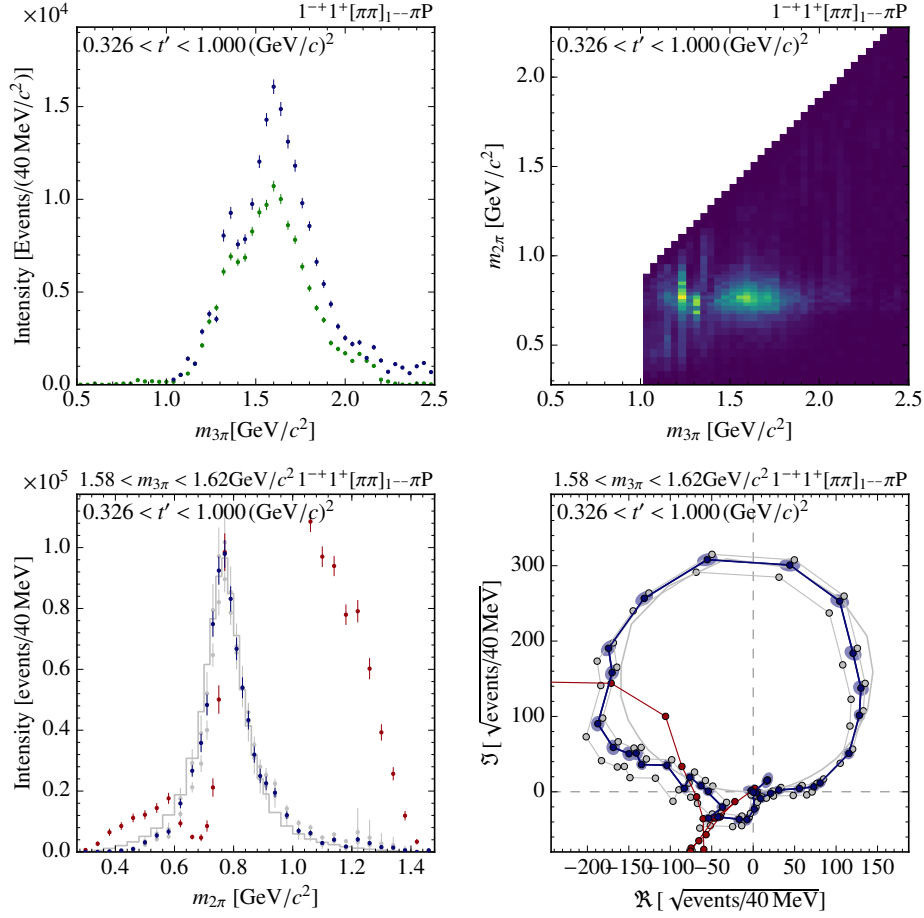
Figure 6.24.: Similar to fig. 6.11, now showing results for the $1^{-+}1^+ \left[\pi\pi\right]_{1--} \pi\mathrm{P}$ wave in the highest bin in t'.

wave in addition to the 11 freed waves of study "C" defined in table 6.1. Since there are zero modes present in the $1^{++}0^+$ sector, we have to resolve the corresponding ambiguities. We do so, by employing the same methods, as in section 6.2.5.

Among the waves with fixed dynamic isobar amplitudes, we only find significant differences to the PWA with 11 freed-isobar waves in the $1^{++}0^+\mathrm{f}_2(1270)\,\pi\mathrm{F}$ wave, as shown in fig. 6.25. This seems to be due to the fact, that the dynamic isobar amplitude of the $1^{++}0^+\mathrm{f}_2(1270)\,\pi\mathrm{P}$ is now freed. Since the $1^{++}0^+\mathrm{f}_2(1270)\,\pi\mathrm{F}$ wave contributes only 0.13% to the total intensity of the fixed-isobar PWA, we do not expect sizable effects of this leakage on other waves.

Comparing the results for the waves with freed dynamic isobar amplitudes of this study with an extended freed $1^{++}0^+$ sector to the model with 11 freed-isobar waves, we find no major differences, except for the $1^{++}0^+ \left[\pi\pi\right]_{0++} \pi\mathrm{P}$ wave, were the broad structure at low $m_{3\pi}$ and $m_{2\pi}$ has a different shape compared to the 11 freed wave model. The difference can be seen by comparing the two-dimensional
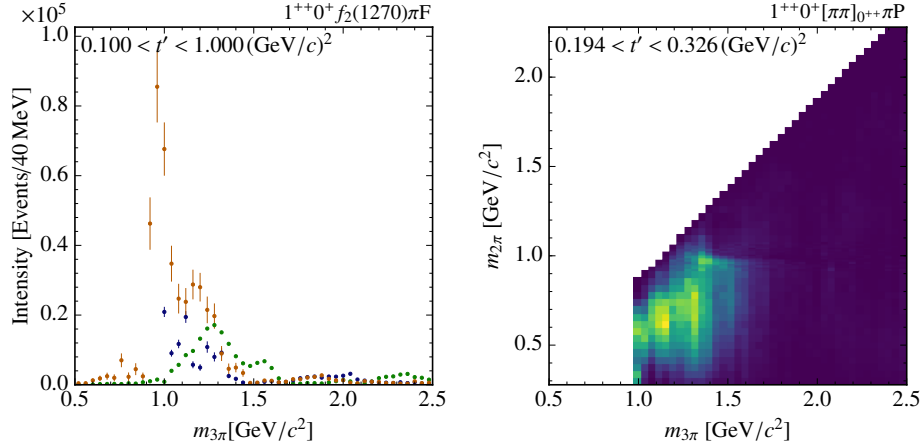
Figure 6.25.: Left: Intensity distribution for the $1^{++}0^+ f_2(1270)\,\pi F$ wave obtained in the fixed-isobar PWA (green), the freed-isobar PWA with 11 freed waves (blue) and the freed-isobar PWA with additionally freed $J_X^{PC} M^\varepsilon = 1^{++}0^+$ waves (orange). Right: Two-dimensional intensity distribution for the $1^{++}0^+ [\pi\pi]_{0^{++}}\,\pi P$ wave obtained with the extended $J_X^{PC} M^\varepsilon = 1^{++}0^+$ wave set.

intensity distribution in figs. 6.14 and 6.25 for one bin in t'; however, the picture is similar in all four t' bins.

The results for the additionally freed $1^{++}0^+ [\pi\pi]_{1^{--}}\,\pi D$ wave are shown in fig. 6.26. In the two-dimensional intensity distribution, we see a broad structure decaying into $\rho(770)\,\pi^-$ that does not correspond to any known a_1 resonance. Comparing the intensity distribution to the fixed-isobar PWA we see an excess over the fixed-isobar result. The intensity distribution has large uncertainties in the region of the $a_1(1260)$ resonance, that are caused by the presence of several zero modes and the fact, that the intensity of the $1^{++}0^+ [\pi\pi]_{1^{--}}\,\pi S$ wave is two orders of magnitudes higher. Due to the zero modes, the size of the uncertainties on the big wave reflect into the uncertainties on the small wave. The excess over the fixed-isobar PWA might be caused by the fact, that the fixed dynamic isobar amplitude used in the fixed-isobar PWA for the $1^{++}0^+ \rho(770)\,\pi D$ wave does not describe the freed-isobar dynamic amplitude, as can be seen in the Argand diagram in fig. 6.26.

The results for the additionally freed $1^{++}0^+ [\pi\pi]_{2^{++}}\,\pi P$ wave are shown in fig. 6.27. Looking at the comparison of the intensity distributions to the fixed-isobar PWA, we find a much more pronounced peak in the mass region of the $a_1(1260)$, around $1.3\,\mathrm{GeV}/c^2$. The two-dimensional intensity distribution reflects the appearance of this distinct peak. Since in this $m_{3\pi}$ region, only the low-mass tail of the $f_2(1270)$ resonance lays within the kinematically allowed region, a false description of this tail in the fixed-isobar model may lead to big changes
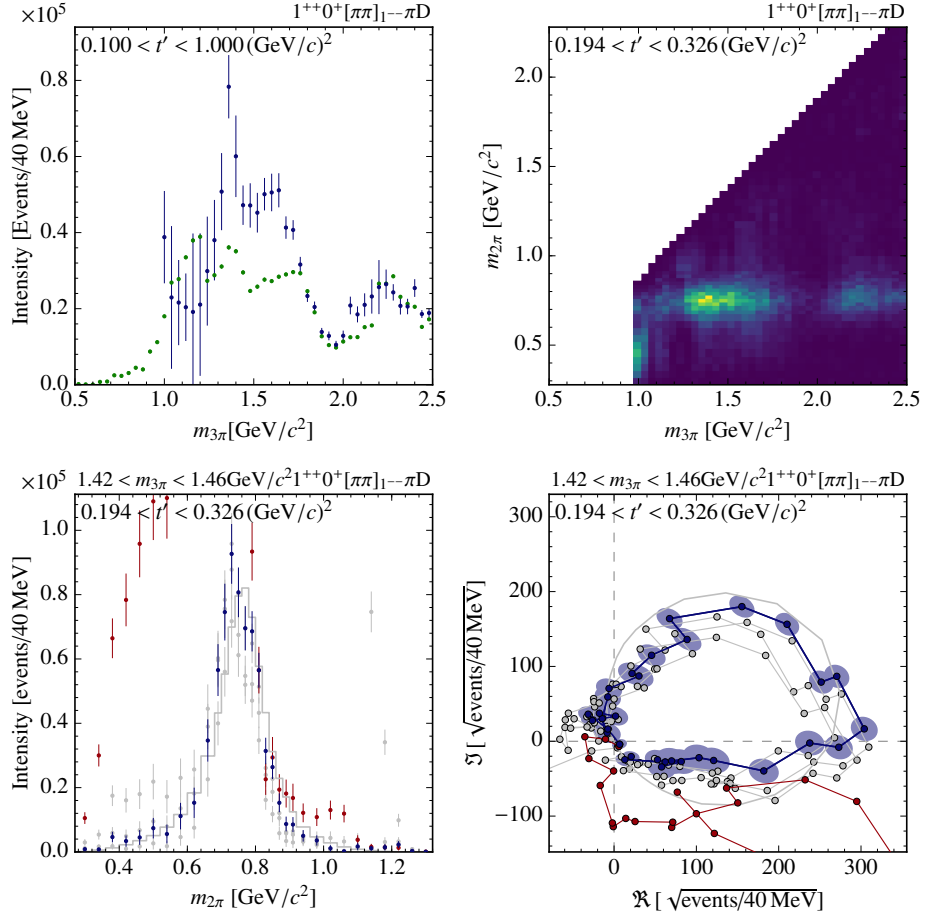
Figure 6.26.: Similar to fig. 6.11, now showing results for the $1^{++}0^+ [\pi\pi]_{1--} \pi D$ wave.

in this wave. The extracted dynamic isobar amplitudes, shown in the lower row of fig. 6.27, exhibit indeed some differences compared to the fixed-isobar dynamic amplitude that night explain this behavior.

6.4.3. Extension of the freed $J_X^{PC} M^\varepsilon = 2^{-+}0^+$ sector

In study "G", we free the $2^{-+}0^+ [\pi\pi]_{2++} \pi D$ wave and the $2^{-+}1^+ [\pi\pi]_{2++} \pi S$ wave in addition to the 11 waves of "C", resulting in a total of 13 freed-isobar waves. Comparing the results for the remaining 71 waves with fixed dynamic isobar amplitudes from this 13-freed wave model, we find a good agreement with the 11-freed wave fit and only see some differences in the $2^{-+}1^+ \rho_3(1690) \pi P$ wave.

Since there are several zero modes in the $2^{-+}0^+$ sector, we have to constrain them. We do so, by using five different methods: 1) Fixed parameterizations for all 5 free dynamic isobar amplitudes in the $2^{-+}0^+$ sector with the same parameters
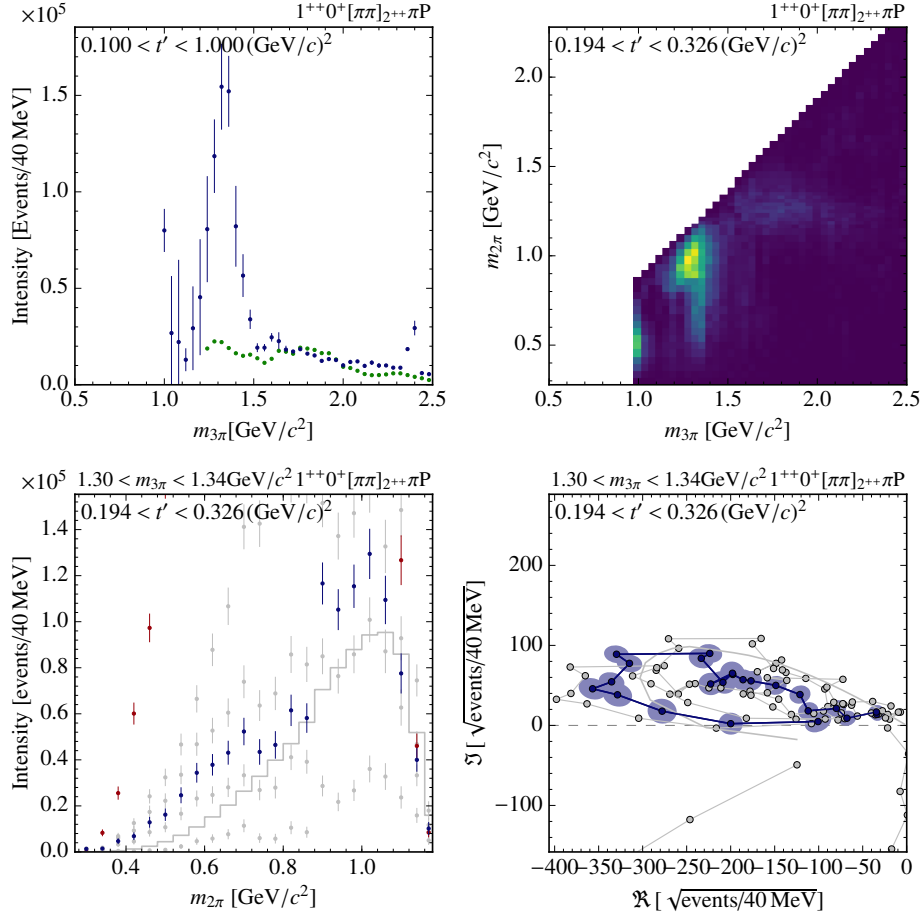
Figure 6.27.: Similar to fig. 6.11, now showing results for the $1^{++}0^+ [\pi\pi]_{2^{++}} \pi\mathrm{P}$ wave.

as used in the fixed-isobar PWA, "fix$_{\mathrm{all}}$", 2) fixed parameterizations for the $2^{-+}0^+$ $[\pi\pi]_{0^{++}} \pi\mathrm{D}$ dynamic amplitudes, "fix$_{\mathrm{f_0}}$", 3) a $\rho(770)$ Breit-Wigner parameterization with floating mass and width for the $J_\xi^{PC} = 1^{--}$ dynamic amplitudes, "fit$_\rho$", 4) a $\mathrm{f_2}(1270)$ Breit-Wigner parameterization with floating mass and width for the $J_\xi^{PC} = 2^{++}$ dynamic amplitudes, "fit$_{\mathrm{f_2}}$" and 5) the smoothness criterion "smooth". We do not find a zero mode in the $2^{-+}1^+$ sector.

If we compare the dynamic isobar amplitudes after resolving the zero modes with the results of the fit with 11 freed waves, we do not observe major differences. Results for the additionally freed $2^{-+}0^+ [\pi\pi]_{2^{++}} \pi\mathrm{D}$ wave are shown in fig. 6.28. We see a distinct peak in the two-dimensional intensity distribution, corresponding to the decay $\pi_2(1880) \rightarrow \mathrm{f_2}(1270)\,\pi$. Comparing the resulting intensity distribution to the fixed-isobar PWA, we see, that the gross features match, but that the freed-isobar PWA yields a more pronounced $\pi_2(1880)$ peak. This is due to the fact,

that the fixed dynamic isobar amplitude used to describe the $f_2(1270)$ is not able to describe all features of the freed-isobar one, as can be seen in the lower row of fig. 6.28. The shoulder at small $m_{2\pi}$ cannot be described in the fixed-isobar model, and the position of the $f_2(1270)$ resonance looks slightly shifted. These differences may be caused by additional physical structures in the $2^{-+}0^+ [\pi\pi]_{2^{++}} \pi D$ dynamic isobar amplitude, or by leakage from other waves due to the much larger number of degrees of freedom.

Nevertheless, the plots in the lower row of fig. 6.28 suggest, that the fit quality could be improved by scaling the Breit-Wigner amplitude with a constant. This turns out not to be the case, which can be seen by looking at the data in a different representation. Figure 6.29 depicts the same data, now as real and imaginary part of the dynamic isobar amplitude. It can be seen, that a simple scaling of the Breit-Wigner description does not improve the fit quality.

The results for the $2^{-+}1^+ [\pi\pi]_{2^{++}} \pi S$ wave are shown in fig. 6.30. In the two-dimensional intensity distribution we see a clear peak corresponding to the decay $\pi_2(1670) \to f_2(1270)\,\pi$. If we compare the one dimensional intensity distribution to the fixed-isobar results, we see an increase by roughly a factor of two. This higher intensity can also be seen in the corresponding dynamic isobar amplitudes, which explains this behavior and is similar in the surrounding $m_{3\pi}$ and t' bins, which are not shown for reasons of brevity. The parameterization used in the fixed-isobar PWA therefore seems to be particularly different from the physical one in this wave.

6.4.4. Extension of the freed $J_X^{PC} M^\varepsilon = 2^{++}1^+$ sector

In the 11 wave model, we have only freed one wave in the $J_X^{PC} M^\varepsilon = 2^{++}1^+$ sector, and therefore did not encounter a zero mode. In study "F", we also free the $2^{++}1^+ [\pi\pi]_{2^{++}} \pi P$ wave. Doing so, we get a zero mode, which we correct using four different methods: 1) fixed dynamic amplitudes for both waves "fix$_{all}$", using a Breit-Wigner with floating mass and width 2) for the $J_\xi^{PC} = 1^{--}$ isobar, "fit$_\rho$", or 3) for the $J_\xi^{PC} = 2^{++}$ isobar, "fit$_{f_2}$", and 4) the smoothness criterion "smooth".

Comparing the results for the $2^{++}1^+ [\pi\pi]_{1^{--}} \pi D$ wave to the 11 wave model, we do not find major differences. The results for the additionally freed $2^{++}1^+ [\pi\pi]_{2^{++}} \pi P$ wave are shown in fig. 6.31. Fixed- and freed-isobar PWA match nicely, although the uncertainties on the freed-isobar results are rather large in the $a_2(1320)$ peak region. The reason for this is, that the relative intensity of the $2^{++}1^+ [\pi\pi]_{1^{--}} \pi P$ wave is two orders of magnitude higher than for the $2^{++}1^+ [\pi\pi]_{2^{++}} \pi P$ wave. Since both waves are connected via a zero mode, the size of the uncertainties on the results of the $J_\xi^{PC} = 1^{--}$ wave projects to the much smaller $J_\xi^{PC} = 2^{++}$ wave in this $m_{3\pi}$ region.

In the lower row of fig. 6.31 we see, that the description of the resulting dynamic amplitude with a Breit-Wigner amplitude for the $f_2(1270)$ resonance matches nicely. In the two-dimensional intensity distribution, structures appear that cor-
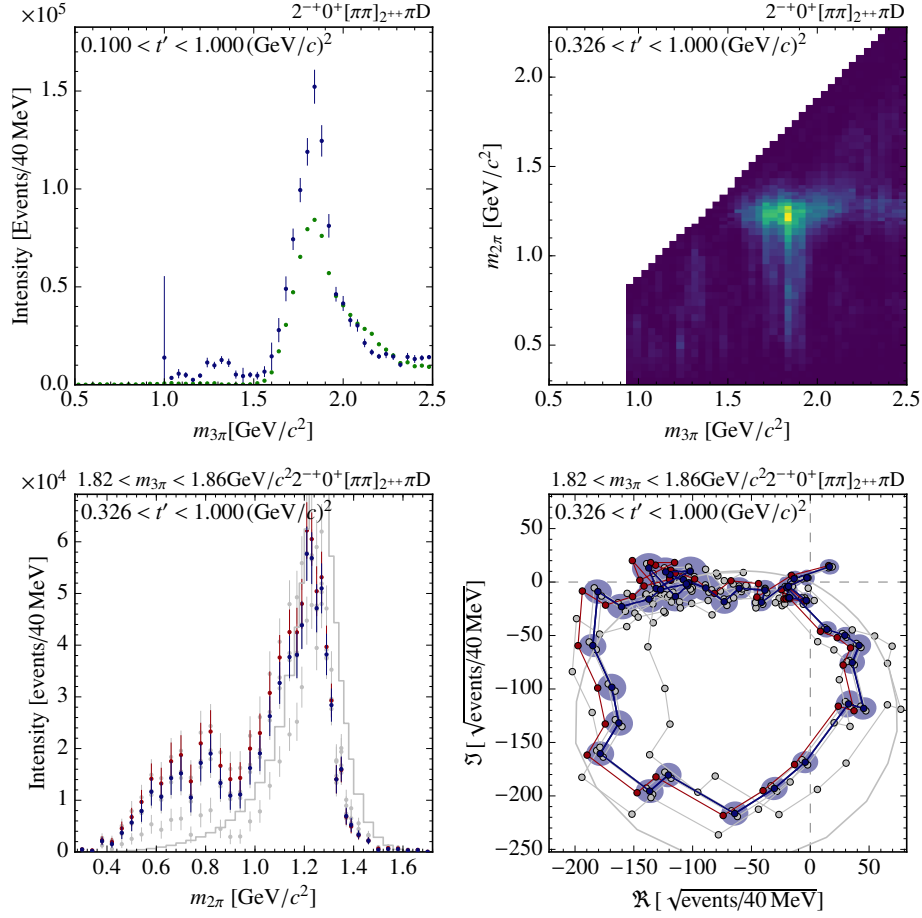
Figure 6.28.: Similar to fig. 6.11, now showing results for the $2^{-+}0^+ [\pi\pi]_{2^{++}} \pi D$ wave.

respond to the decay $a_2(1320) \to f_2(1270)\,\pi$, even though the process is a sub-threshold decay.

Most of the intensity distributions of the waves, that still employ fixed dynamic isobar amplitudes, agree well with the 11 wave model. However, a much more pronounced $a_2(1320)$ peak appears in the $2^{++}1^+\rho_3(1690)\,\pi D$ wave. This effect is shown in fig. 6.32 and is present in all four t' bins. It might appear because the additional freed wave removes tensions within the 2^{++} sector. However, since the corresponding decay $a_2(1320) \to \rho_3(1690)\,\pi$ would be far sub-threshold, we do not expect this process to happen with such a high intensity. A more likely explanation is leakage from a wave with an orbital angular momentum of 3, for example the $2^{++}1^+f_2(1270)\,\pi F$ wave, which is not included in the PWA. For this wave, the values of the spin of the isobar and of the orbital angular momentum are interchanged with the values for the $2^{++}1^+\rho_3(1690)\,\pi D$ wave. This also explains, why we see this effect only after freeing the $J^{PC}_\xi = 2^{++}$ isobar. An additional fit could resolve this question, but is outside the scope of this work.
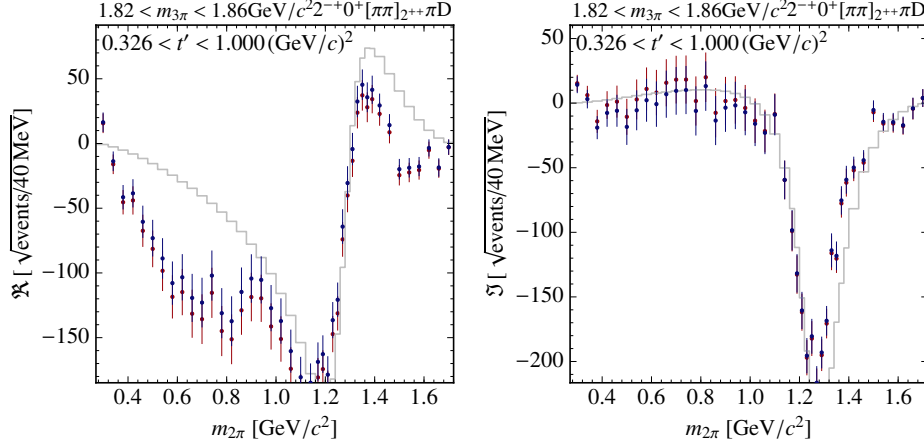
Figure 6.29.: Similar to fig. 6.28, now showing real and imaginary part of the dynamic isobar amplitude of the $2^{-+}0^+ [\pi\pi]_{2^{++}} \pi D$ wave.

6.4.5. Addition of a freed $J_X^{PC} M^\varepsilon = 3^{++}0^+$ sector

In study "H", we extend the set of 11 freed waves by three waves in the $J_X^{PC} M^\varepsilon = 3^{++}0^+$ sector: $3^{++}0^+ [\pi\pi]_{1^{--}} \pi D$, $3^{++}0^+ [\pi\pi]_{2^{++}} \pi P$, and $3^{++}0^+ [\pi\pi]_{3^{--}} \pi S$. The main goal was to study the $\rho_3(1690)$ isobar; the $3^{++}1^+ \rho_3(1690) \pi S$ wave has the highest relative intensity of all $\rho_3(1690)$ waves in the fixed-isobar model. We find, that in the $3^{++}0^+$ sector, a zero mode is present, that contributes only to the waves with $J_\xi^{PC} = 1^{--}$ and 3^{--} isobars. We correct for the corresponding ambiguity by using 4 different methods: 1) fixed dynamic amplitudes for both waves "fix$_{\text{all}}$", a Breit-Wigner dynamic amplitude with floating mass and width for 2) the $\rho(770)$ and 3) for the $\rho_3(1690)$ resonance, "fit$_\rho$" and "fit$_{\rho 3}$", and 4) the smoothness method, "smooth".

Comparing the intensity distributions of the fixed-isobar waves and the freed-isobar waves with those in the 11 wave model, we do not find any major differences. We only see small deviations in the low-mass tail of the $3^{++}0^+ \rho(770) \pi G$ wave, which is shown in fig. 6.32.

The results for the $3^{++}0^+ [\pi\pi]_{1^{--}} \pi D$ wave are shown in fig. 6.33. In the two-dimensional intensity distribution we see a broad peak, that could correspond to the decay $a_3(1875) \to \rho(770) \pi$ However, The comparison of the intensity distribution with the fixed-isobar PWA shows some differences. This can be explained by the fact, that the extracted dynamic isobar amplitudes, shown in the lower row of fig. 6.33 differ from a pure $\rho(770)$ Breit-Wigner shape.

In the $3^{++}0^+ [\pi\pi]_{2^{++}} \pi P$ wave, we also see a structure, that could correspond to the $a_3(1875)$ resonance, now decaying into $f_2(1270) \pi^-$ (see fig. 6.34). In the comparison with the fixed-isobar model, we see an excess of the freed-isobar wave over the fixed-isobar one, even though the dynamic amplitude is compatible with a Breit-Wigner description.
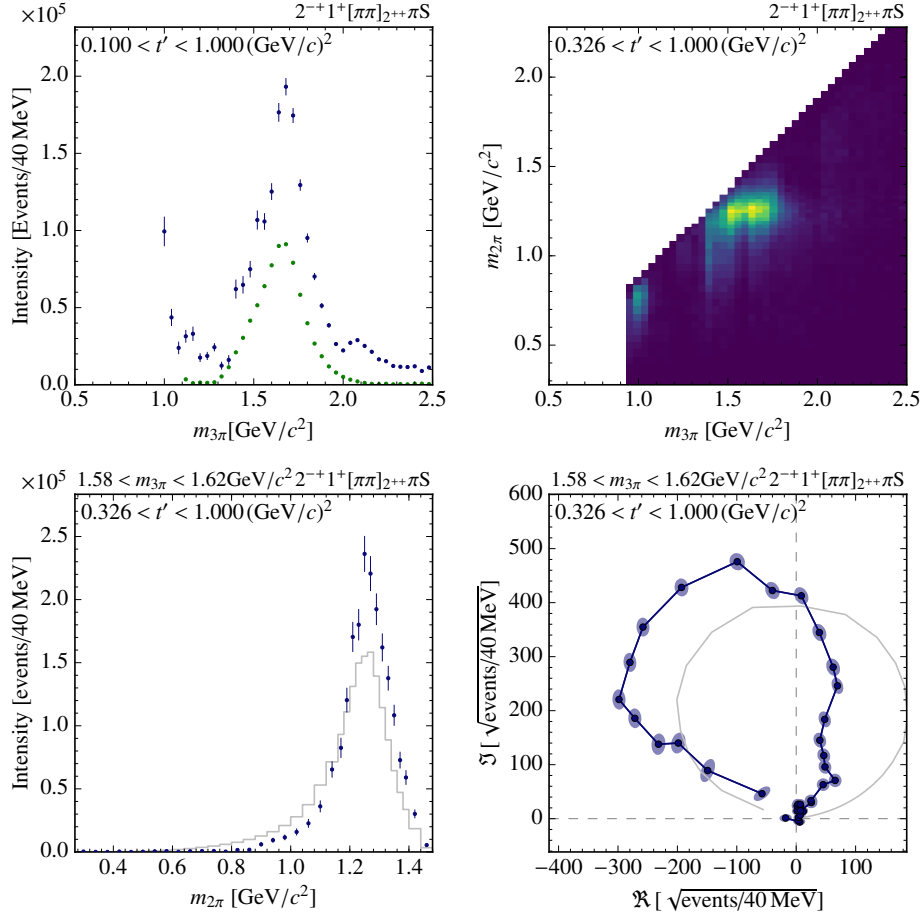
Figure 6.30.: Similar to fig. 6.11, now showing results for the $2^{-+}1^+ [\pi\pi]_{2^{++}} \pi S$ wave.

The third wave in this sector is the $3^{++}0^+ [\pi\pi]_{3^{--}} \pi S$ wave, which is shown in fig. 6.35. The two-dimensional intensity distribution again exhibits a peak compatible with the $a_3(1875)$, now decaying into $\rho_3(1690)\pi^-$. Also for this wave, the intensity distribution differs from that of the fixed-isobar PWA, which again can be attributed to the fact, that the dynamic isobar amplitudes do not have a simple $\rho_3(1690)$ Breit-Wigner shape.

However, even though we observe a peaking structure that could correspond to the $a_3(1875)$ resonance in all three freed $J_X^{PC} = 3^{++}$ waves, we have to perform an analysis of the production amplitudes of these waves in order to determine their resonance content. To determine the production amplitudes, we fit the dynamic isobar amplitudes in every $m_{3\pi}$ and t' bin separately with a Breit-Wigner parameterization, as given in eqs. (4.8) and (4.9) and extract the complex coupling $\mathcal{F}$, as in eq. (5.67), of this parameterization. Since we do not observe any phase motion of these coefficients with $m_{3\pi}$, we cannot state the existence of any resonance content in the freed $J_X^{PC} = 3^{++}$ waves, that can be described by a simple Breit-Wigner parameterization.
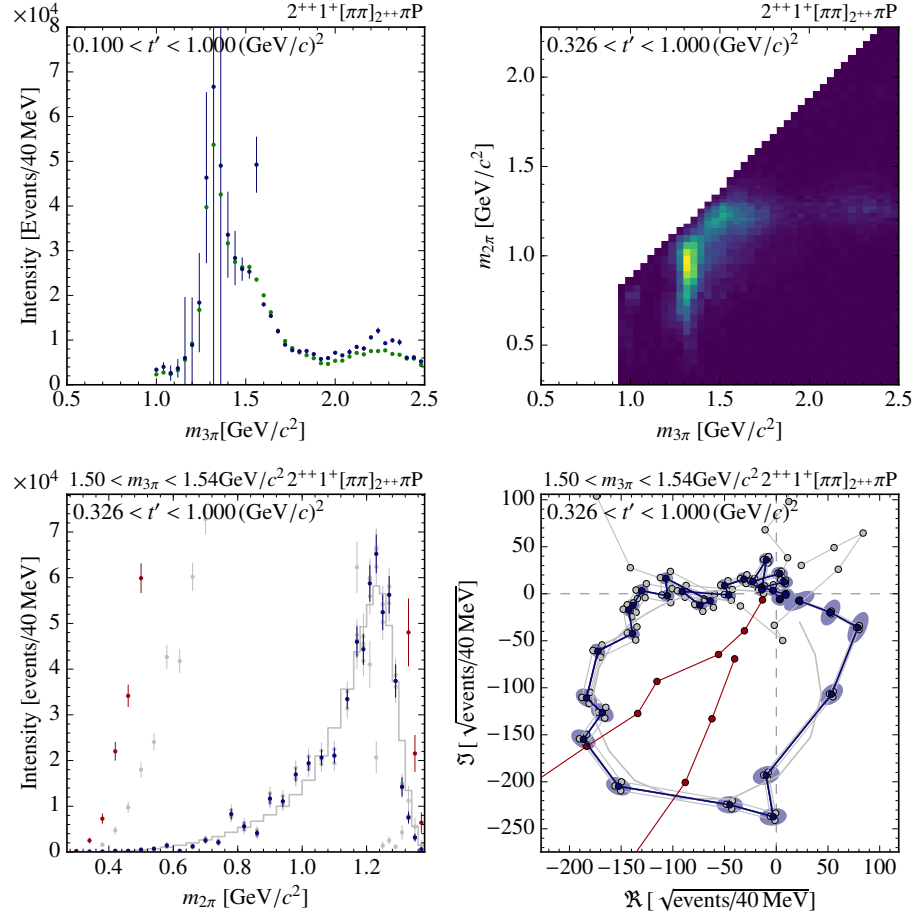
Figure 6.31.: Similar to fig. 6.11, now showing results for the $2^{++}1^+ [\pi\pi]_{2^{++}} \pi P$ wave.

A dedicated resonance model fit on the $a_3(1875)$ resonance by S. Wallner on the results of the fixed-isobar PWA, similar to the analysis described in ref. [38], did also not show any Breit-Wigner like resonance content in these three $J_X^{PC} = 3^{++}$ waves. In this study, the production amplitudes of the corresponding fixed-isobar waves, $3^{++}0^+\rho(770)\,\pi D$, $3^{++}0^+f_2(1270)\,\pi P$, and $3^{++}0^+\rho_3(1690)\,\pi S$, were fitted with a Breit-Wigner resonance model. Therefore, we can conclude, that either a more elaborate description of these peaking structures is necessary to pin down a possible $a_3(1875)$ resonance, or the peaks are not caused by a resonance at all.

6.4.6. Addition of a freed $J_X^{PC}M^\varepsilon = 4^{++}1^+$ sector

In study "I", two waves with $J_X^{PC}M^\varepsilon = 4^{++}1^+$ are freed, the $4^{++}1^+ [\pi\pi]_{1^{--}} \pi G$ wave and the $4^{++}1^+ [\pi\pi]_{2^{++}} \pi F$ wave, in addition to the waves in model "C". For the $4^{++}1^+$ sector, we do not find a zero mode. We do not find any major
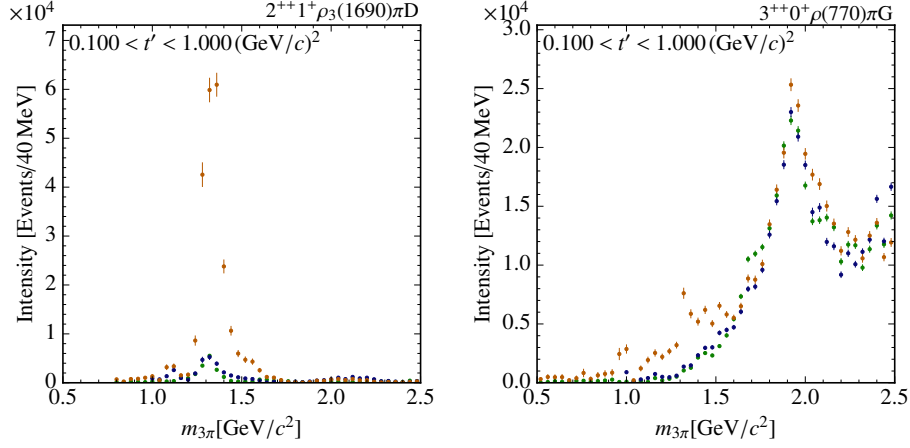
Figure 6.32.: Results for the $2^{++}1^+ \rho_3(1690)\,\pi$D and the $3^{++}0^+ \rho(770)\,\pi$G wave, for the fixed-isobar PWA (green), the 11-freed-wave model (blue), and the freed-isobar model with an additionally freed $J_X^{PC}M^\varepsilon = 2^{++}1^+$ wave or an additionally freed $J_X^{PC}M^\varepsilon = 3^{++}0^+$ sector (orange), respectively.

differences compared to the "C" freed-isobar PWA, neither for the freed- nor for the fixed-isobar waves, that appear in both models.

The results for the freed $4^{++}1^+ [\pi\pi]_{1^{--}}\,\pi$G wave are shown in fig. 6.36. In the two-dimensional intensity distribution, we see a clear peak for the decay $a_4(2040) \to \rho(770)\,\pi$. Comparing the intensity distribution with the fixed-isobar PWA, we find a very good agreement. This is in accordance with the fact, that the extracted dynamic isobar amplitude is compatible with a simple $\rho(770)$ Breit-Wigner, which can be seen in the lower row of fig. 6.36.

The second freed wave in this sector, the $4^{++}1^+ [\pi\pi]_{2^{++}}\,\pi$F wave, is shown in fig. 6.37. In the two-dimensional intensity distribution, we again see a clear peak, corresponding to the $a_4(2040)$, now decaying into $f_2(1270)\,\pi^-$. In comparison with the fixed-isobar PWA, we see an excess of the intensity in the low- and high-mass tails, while the $a_4(2040)$ peak roughly matches. The deviations in the tails are again due to the fact, that a simple $f_2(1270)$ Breit-Wigner does not suffice to describe the extracted dynamic isobar amplitude further away from the $a_4(2040)$ peak. In the low $m_{3\pi}$ region, this is due to the fact, that the dynamic isobar amplitude does not contain an $f_2(1270)$ resonance, while in the high $m_{3\pi}$ region, the $f_2(1270)$ resonance is present in the dynamic isobar amplitude, but we see additional structures at a $m_{2\pi}$ region of about $1.4\,\mathrm{GeV}/c^2$. However, these structures cannot be described by an additional Breit-Wigner like resonance, so we cannot state the presence of an excited f_2' resonance. To clarify the presence of such an excited resonance, a more advanced parameterization is necessary, which is not available at the moment.
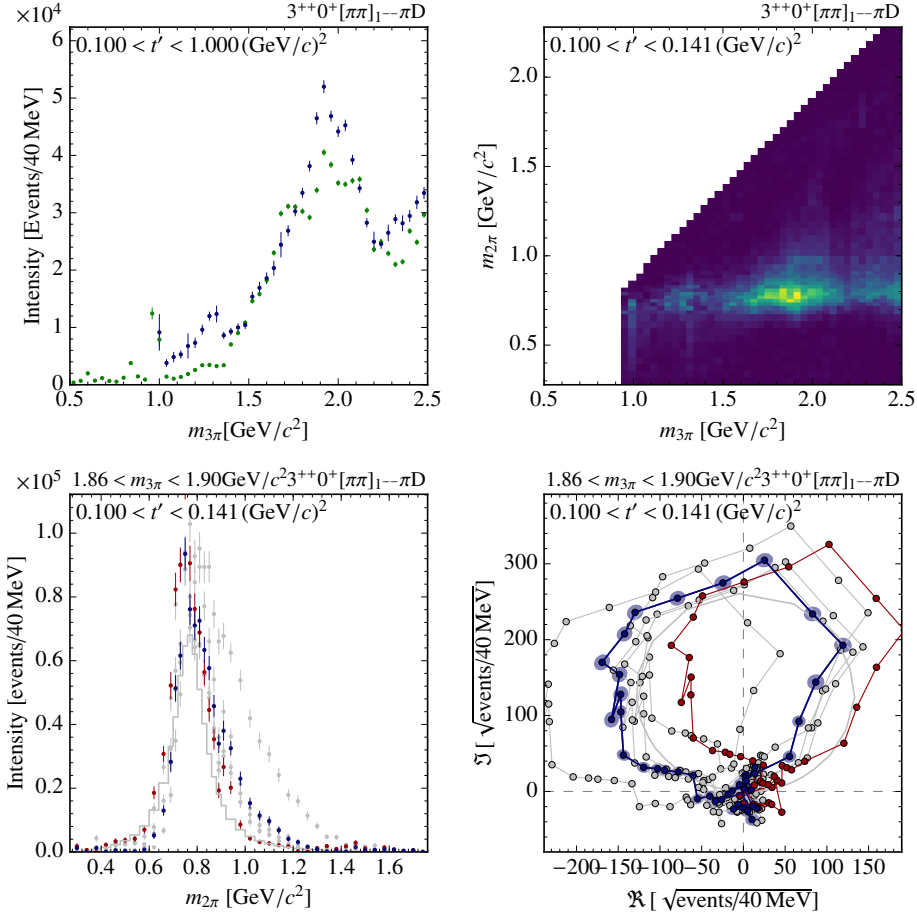
Figure 6.33.: Similar to fig. 6.11, now showing results for the $3^{++}0^+ [\pi\pi]_{1--} \pi D$ wave.

6.4.7. Additionally freed $4^{-+}0^+ [\pi\pi]_{1--} \pi F$ and $6^{-+}0^+ [\pi\pi]_{1--} \pi H$ waves

We perform two more studies—"J" and "K"—, where we added the $4^{-+}0^+ [\pi\pi]_{1--} \pi F$ or the $6^{-+}0^+ [\pi\pi]_{1--} \pi H$ wave to the set of 11 freed waves. There are no additional zero modes in these two models. In both studies, we do not find any significant differences to the PWA using the 11-freed-wave model, neither in the freed-, nor the fixed-isobar waves. The only exception are minor differences in the $4^{-+}0^+ f_2(1270) \pi G$ wave in the study with the freed $4^{-+}0^+ [\pi\pi]_{1--} \pi F$ wave.

The results for the freed $4^{-+}0^+ [\pi\pi]_{1--} \pi F$ wave are shown in fig. 6.38. In the two-dimensional intensity distribution, we see a broad structure above $m_{3\pi} > 1.6 \, \text{GeV}/c^2$, that decays into $\rho(770) \, \pi^-$. This broad structure can most likely be attributed to the Deck effect, introduced in appendix B, and not to any resonant π_4 contribution. In comparison with the fixed-isobar PWA, we see a slight excess
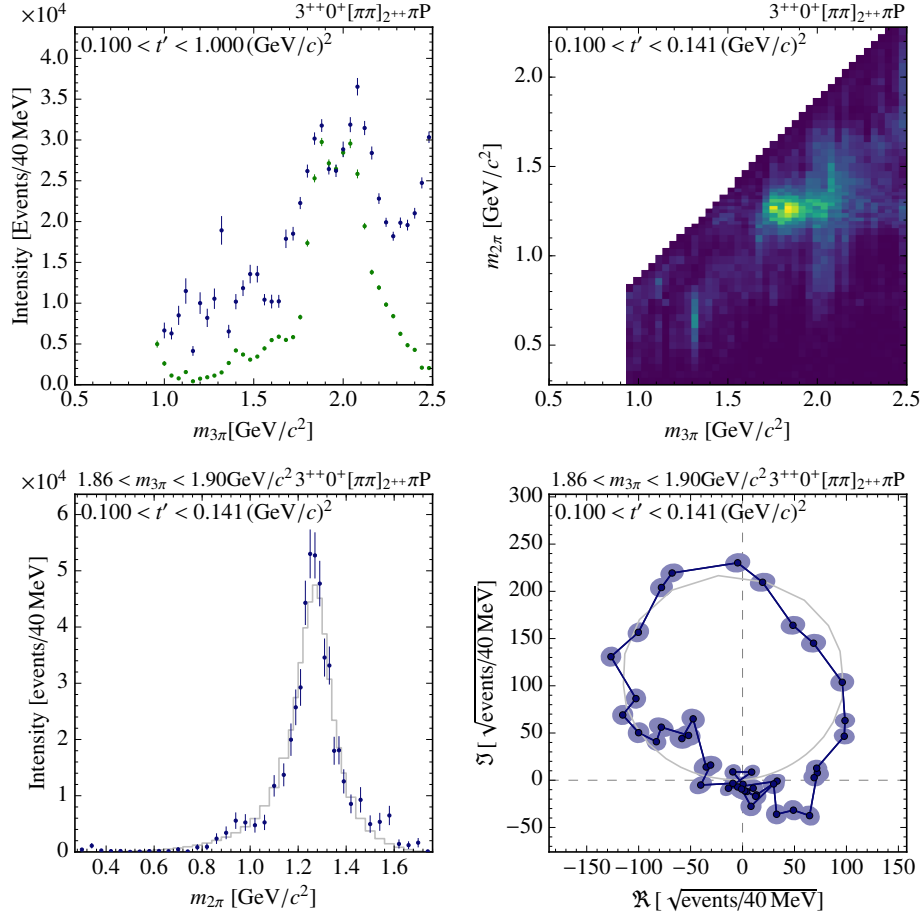
Figure 6.34.: Similar to fig. 6.11, now showing results for the $3^{++}0^+ [\pi\pi]_{2^{++}} \pi P$ wave.

in the peak of the broad structure, which may be attributed to the imperfect description of the extracted dynamic isobar amplitudes by a $\rho(770)$ Breit-Wigner shape (see fig. 6.38). Such deviations may also be a result of the Deck effect, since the study in appendix B suggests, that most of the intensity in the $4^{-+}0^+ \rho(770) \pi F$ is generated by this non-resonant contribution. The $4^{-+}0^+ \rho(770) \pi F$ wave is used as phase reference in all other studies. Since it is freed here, this is not possible and we use the $6^{-+}0^+ \rho(770) \pi H$ wave as reference instead.

The results for the $6^{-+}0^+ [\pi\pi]_{1^{--}} \pi H$ wave are shown in fig. 6.39. Similar to the 4^{-+} wave, we see a broad structure decaying to $\rho(770) \pi^-$. This structure can again be attributed to the Deck effect. The excess of the intensity distribution over the fixed-isobar PWA may be explained by the fact, that the $\rho(770)$ Breit-Wigner description does not fit the extracted dynamic isobar amplitudes. Such a deviation may also be caused by the Deck effect. The study in appendix B suggests, that most of the intensity in the $6^{-+}0^+ \rho(770) \pi H$ wave is generated by the Deck effect.
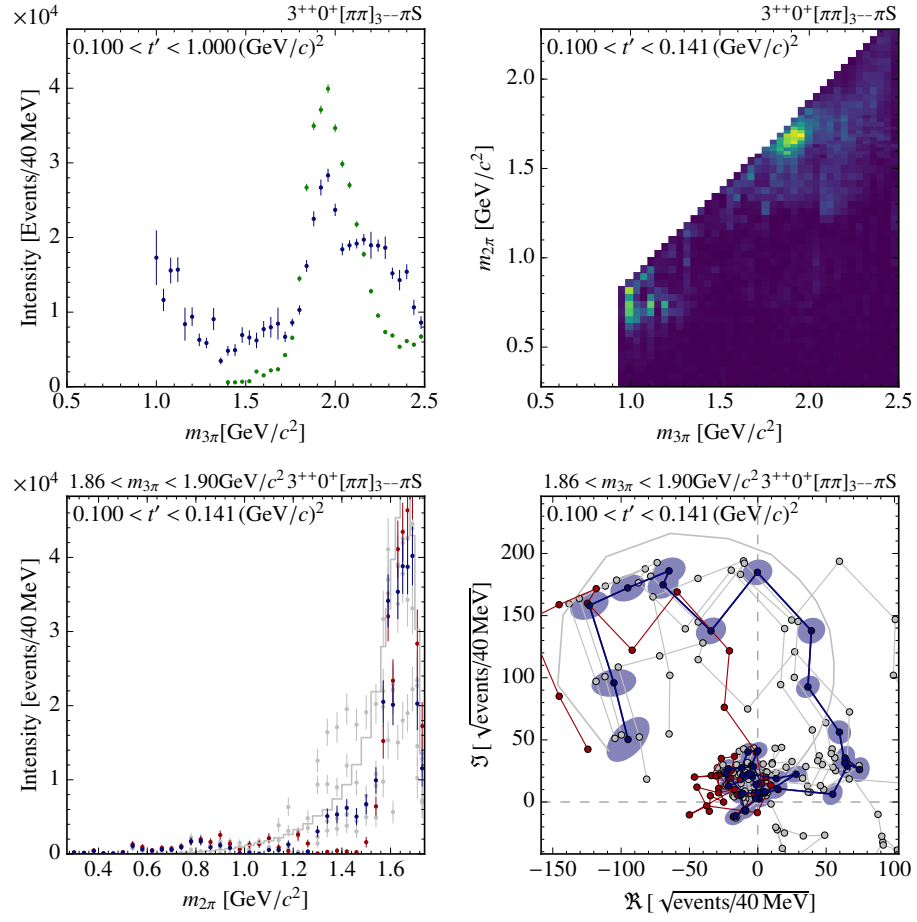
Figure 6.35.: Similar to fig. 6.11, now showing results for the $3^{++}0^+\,[\pi\pi]_{3^{--}}\,\pi S$ wave.
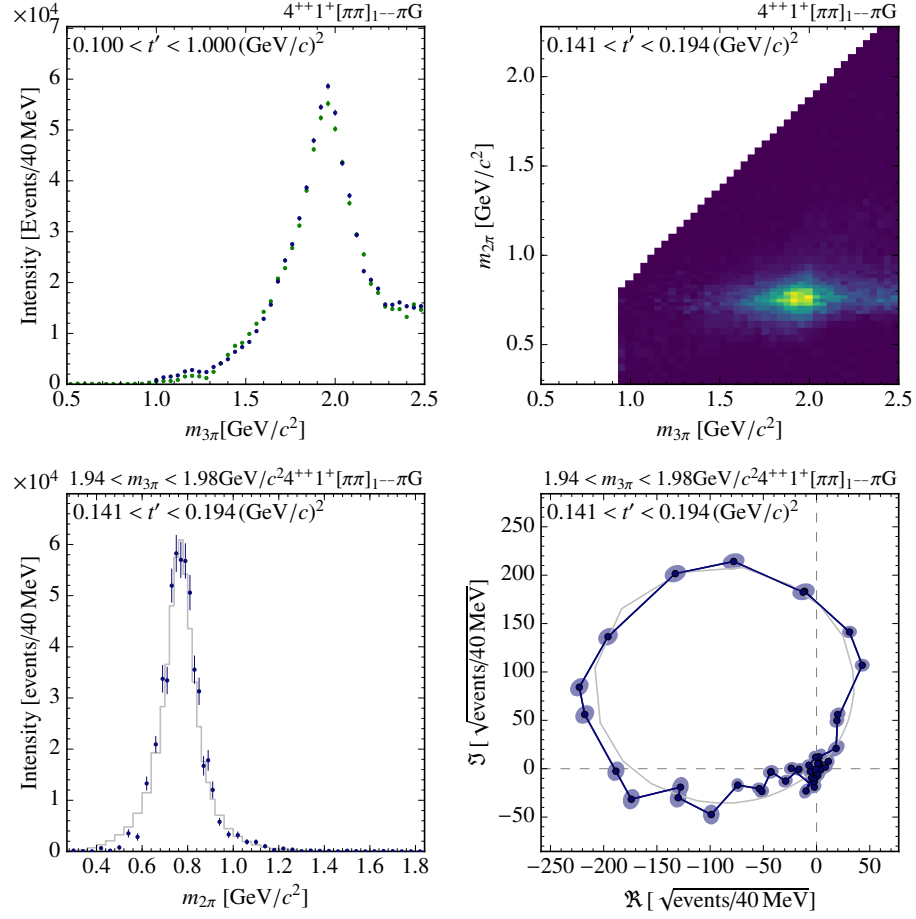
Figure 6.36.: Similar to fig. 6.11, now showing results for the $4^{++}1^+ [\pi\pi]_{1^{--}} \pi G$ wave.
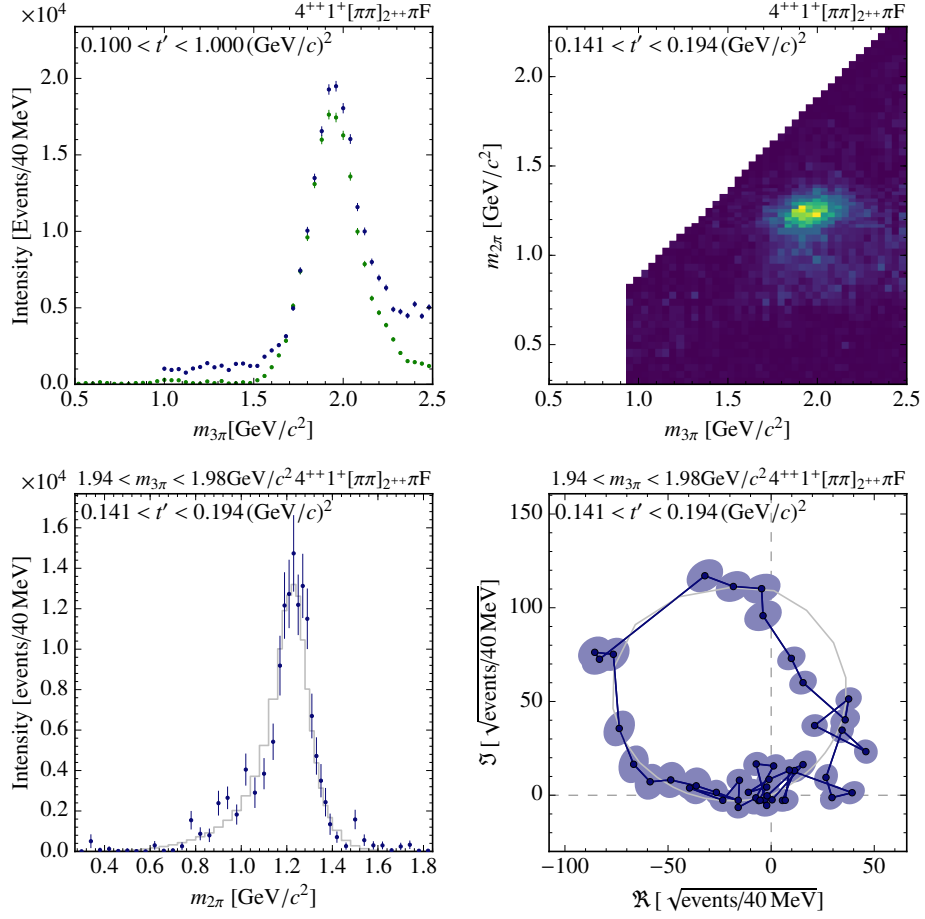
Figure 6.37.: Similar to fig. 6.11, now showing results for the $4^{++}1^+ [\pi\pi]_{2^{++}} \pi F$ wave.
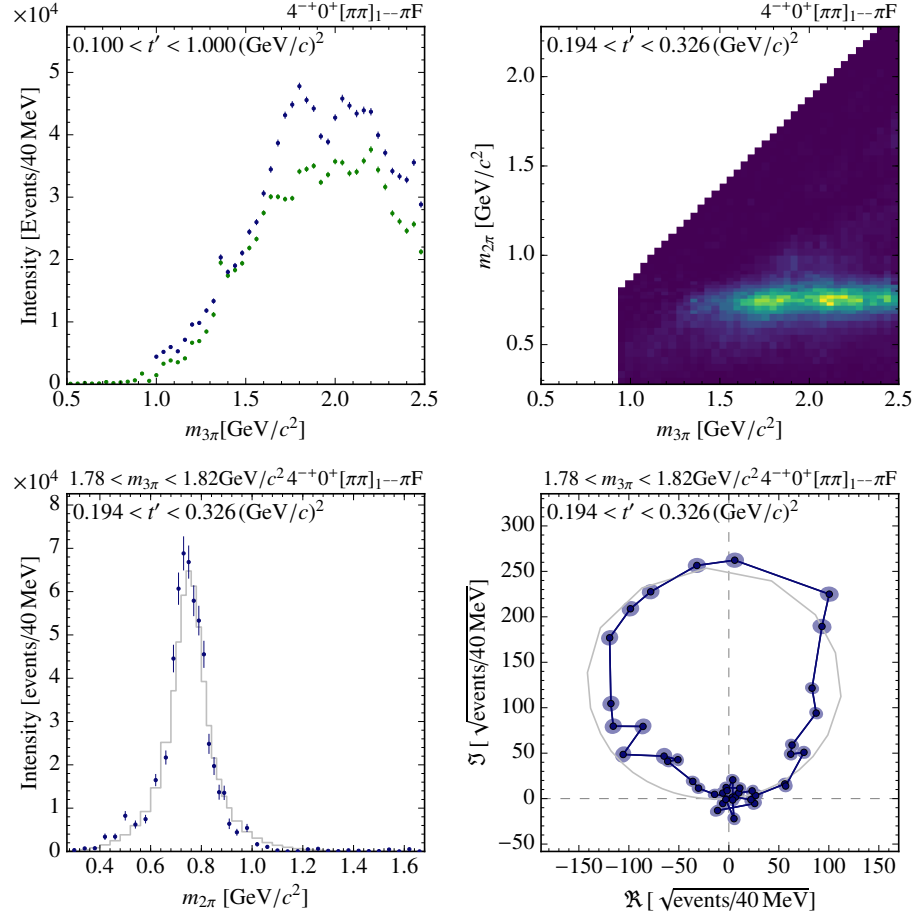
Figure 6.38.: Similar to fig. 6.11, now showing results for the $4^{-+}0^+ [\pi\pi]_{1^{--}} \pi\mathrm{F}$ wave.
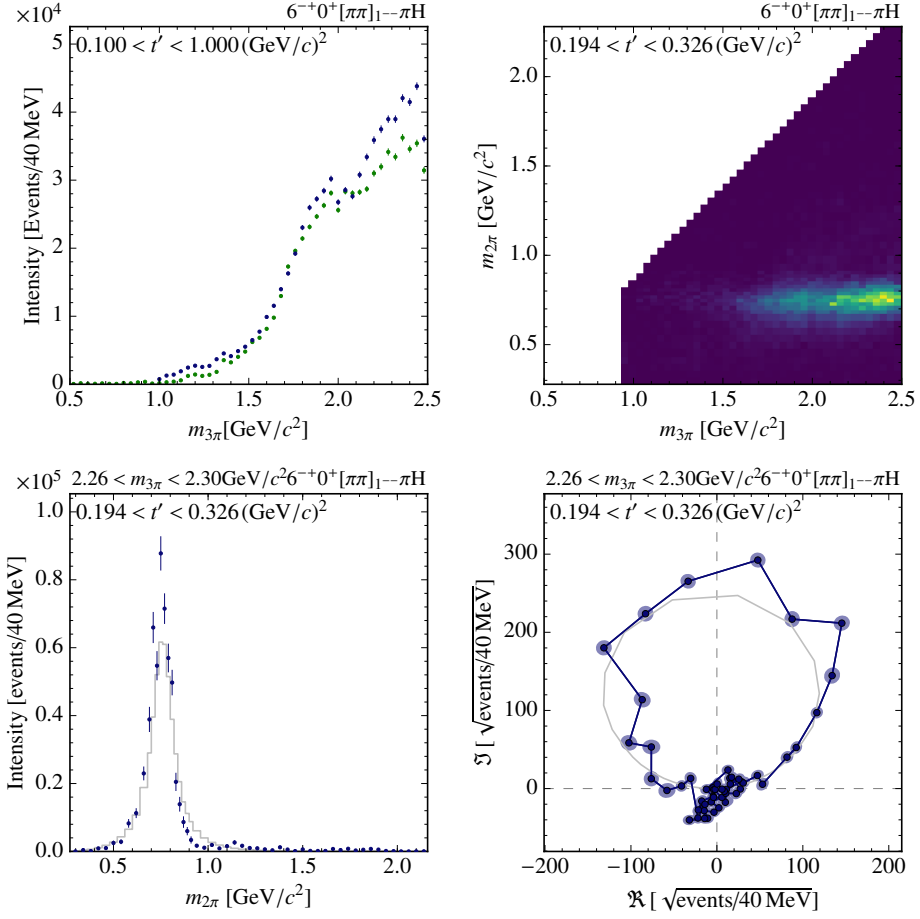
Figure 6.39.: Similar to fig. 6.11, now showing results for the $6^{-+}0^{+}\,[\pi\pi]_{1^{--}}\,\pi H$ wave.

Chapter 7.

Determination of isobar resonance parameters

Up to now, we have extracted the dynamic isobar amplitudes of the individual waves and corrected for appearing zero modes. To make further use of these data, we extract the parameters of the appearing isobar resonances by fitting the dynamic amplitudes with a resonance model.

In several of the freed waves, zero modes are present, which we have to take into account. It turns out, that leaving the zero mode coefficient and the resonance parameters free simultaneously, leads to an unstable fit in some cases. Therefore, we first fix the zero mode coefficients, as described in section 6.2.2 and then fit the resulting dynamic isobar amplitudes with the resonance model. On the results for the dynamic isobar amplitudes with resolved zero-mode ambiguities, we fit a parameterization to determine the parameters of the dominating isobar resonances. For all resonances except the $f_0(980)$ we use a Breit-Wigner parameterization, as given in eqs. (4.8) and (4.9). We perform this fit in independently in every $(m_{3\pi}, t')$ bin to see, whether the Breit-Wigner parameterization is able to describe the data consistently over the whole $m_{3\pi}$ ranage. If this is the case and the dynamic isobar amplitudes were given by a pure Breit-Wigner, we expect the extracted resonance parameters—masses and widths—to be constant over $m_{3\pi}$ and t' and the same for all waves. However, we will see that none of the appearing resonance resonance exhibits such a constant behavior, but suffer from systematic effects from non-resonant contribution and rescattering with the bachelor pion. In addition, we perform fits of the resonance parameters in every t' bin using the whole $m_{3\pi}$ range to be able to compare the resulting parameter values with those for the individual $m_{3\pi}$ bins.

7.0.8. Resonance parameters of $\rho(770)$

Combining all studies, we have a total of 13 different waves with a freed $[\pi\pi]_{1^{--}}$ isobar (see table 6.1). For all these waves, we fit the extracted dynamic isobar amplitudes for every $m_{3\pi}$ and t' bin separately with a Breit-Wigner amplitude, given in eqs. (4.8) and (4.9). Doing so, we can study the dependence of the parameters of the $\rho(770)$ resonance—mass m_ρ and width Γ_ρ—on the 3π mother wave and on $m_{3\pi}$ and t'. We performed these fits once using the full kinematically
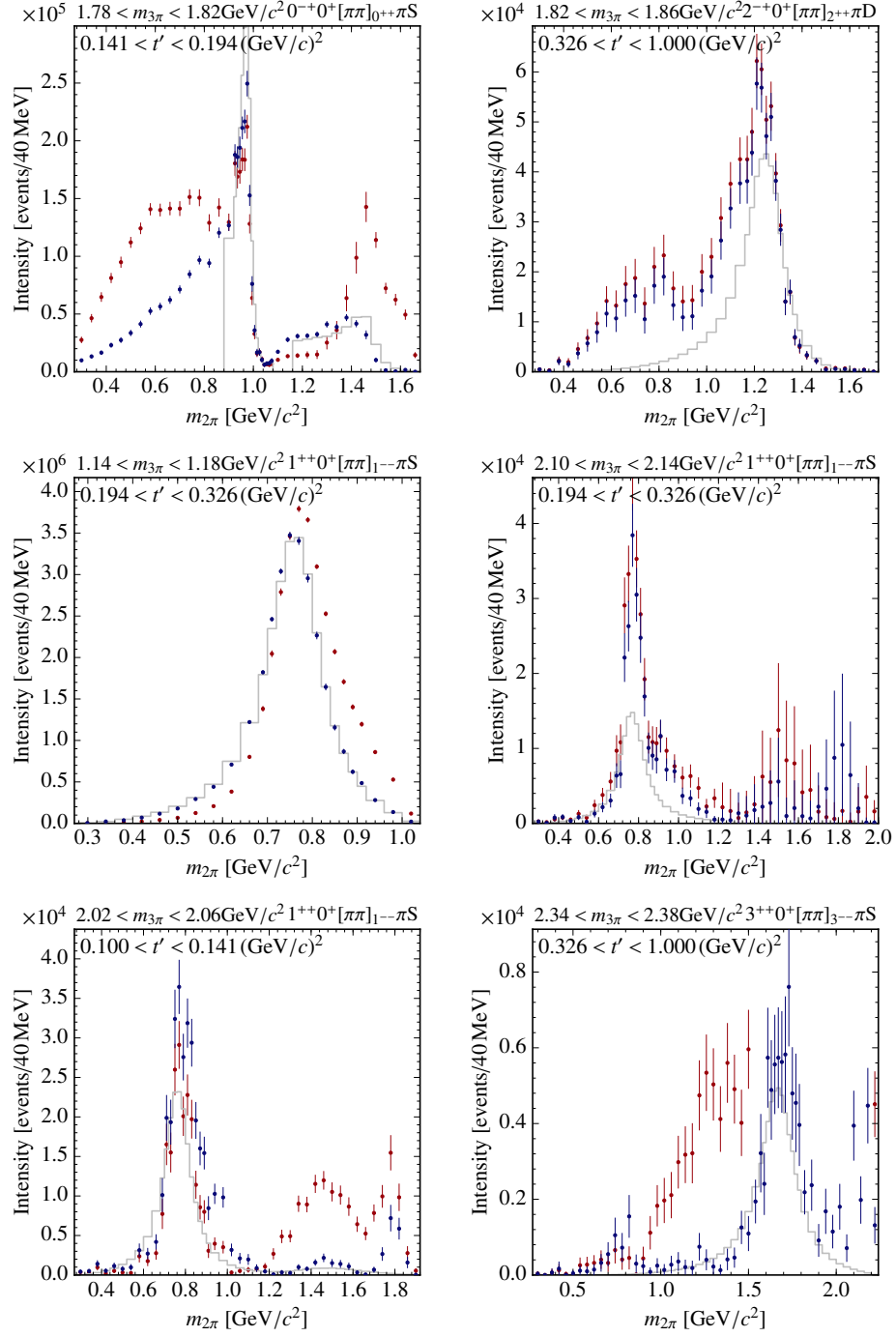
Figure 7.1.: Example results for the resonance fits for the different resonances. The plots are similar to fig. 6.11, the gray line now shows the model curve. In the upper left plot the two independent fits of the $f_0(980)$ and the $f_0(1500)$ are shown.

allowed $m_{2\pi}$ range and once restricting the range to the region $m_{2\pi} < 1.2\,\mathrm{GeV}/c^2$ to limit the influence of the high-mass tail.

Two examples for fits of $\rho(770)$ dynamic amplitudes are depicted in the middle row of fig. 7.1. The left plot shows the same data as fig. 6.15 and we see, that the Breit-Wigner with adjusted parameters fits the data points better that the fixed parameterization, as expected. The right plot shows an example $m_{3\pi}$ bin of the same t' bins, where the Breit-Wigner description is not sufficient to describe the dynamic isobar amplitude. The model curve lies systematically lower than the data points, which gives the impression that simple scaling improves the fit. However, loking at the real and imaginary part of the dynamic isobar amplitude reveals, that this is not the case, similar to the the $2^{-+}0^+\,[\pi\pi]_{2++}\,\pi\mathrm{D}$ wave, depited in fig. 6.29.

In fig. 7.2 the results for the $\rho(770)$ parameters obtained with the Breit-Wigner fit to the extracted dynamic isobar amplitudes of the $0^{-+}0^+\,[\pi\pi]_{1--}\,\pi\mathrm{P}$ wave from study "C" are shown for all four t' bins. The different colors represent the following t' bins: blue $0.100 < t' < 0.141\,(\mathrm{GeV}/c)^2$, red $0.141 < t' < 0.194\,(\mathrm{GeV}/c)^2$ green $0.194 < t' < 0.326\,(\mathrm{GeV}/c)^2$, and orange $0.326 < t' < 1.000\,(\mathrm{GeV}/c)^2$. Points with uncertainties above $150\,\mathrm{MeV}$ are not shown to obtain clearer pictures. The top row shows the values of χ^2/ndf, which are around 5—a typical value for waves analyzed this way—indicating, that a pure Breit-Wigner amplitude is not able to capture all details of the extracted dynamic isobar amplitudes. The resonance parameters m_ρ and Γ_ρ shown in the center and bottom row of fig. 7.2 exhibit no strong dependence on $m_{3\pi}$ and are similar in the different t' bins. Only in the highest t' bin the $\rho(770)$ width shows a larger variation. We do not observe strong effects due to the $m_{2\pi}$ fit range. The resulting parameters for the individual $m_{3\pi}$ bins scatter around the results for the fits using the whole $m_{3\pi}$ range simultaneously.

Figure 7.3 shows the results for the same analysis performed for the $1^{++}0^+$ $[\pi\pi]_{1--}\,\pi\mathrm{S}$ wave obtained in study "C". The typical value of χ^2/ndf is around 10, which is the largest χ^2/ndf of all analyzed $[\pi\pi]_{1--}$ waves. However, this is mostly caused by the fact, that the relative statistical uncertainties on the $1^{++}0^+$ $[\pi\pi]_{1--}\,\pi\mathrm{S}$ wave are very small, since it describes the highest relative intensity in the fit model. We also observe, that a restriction of the $m_{2\pi}$ fit range improves the fit quality for $m_{3\pi} > 1.6\,\mathrm{GeV}/c^2$, which indicates, that at high $m_{2\pi}$ additional contributions play a role in this dynamic isobar amplitude. One such contribution might stem from the presence of excited ρ' resonances, which will be studied further in section 7.0.13. The extracted $\rho(770)$ parameters, shown in the middle and bottom row of fig. 7.3, exhibit a dependence on $m_{3\pi}$, that is similar in all t' bins. This dependence only gets a bit weaker for $m_{3\pi} > 2\,\mathrm{GeV}/c^2$, if the fit range is restricted to $m_{2\pi} < 1.2\,\mathrm{GeV}/c^2$. This again hints to the presence of additional contributions to the dynamic isobar amplitude in the high-$m_{2\pi}$ range, since this range is only kinematically allowed in the high-$m_{3\pi}$ region. The results obtained by fits over the whole $m_{3\pi}$ range are only consistent with the results for the $m_{3\pi}$ region from 1.0 to 1.3 GeV/c^2. This is the mass region of the dominating $a_1(1260)$ resonance, where $1^{++}0^+\,[\pi\pi]_{1--}\,\pi\mathrm{S}$ wave has the highest intensity. The
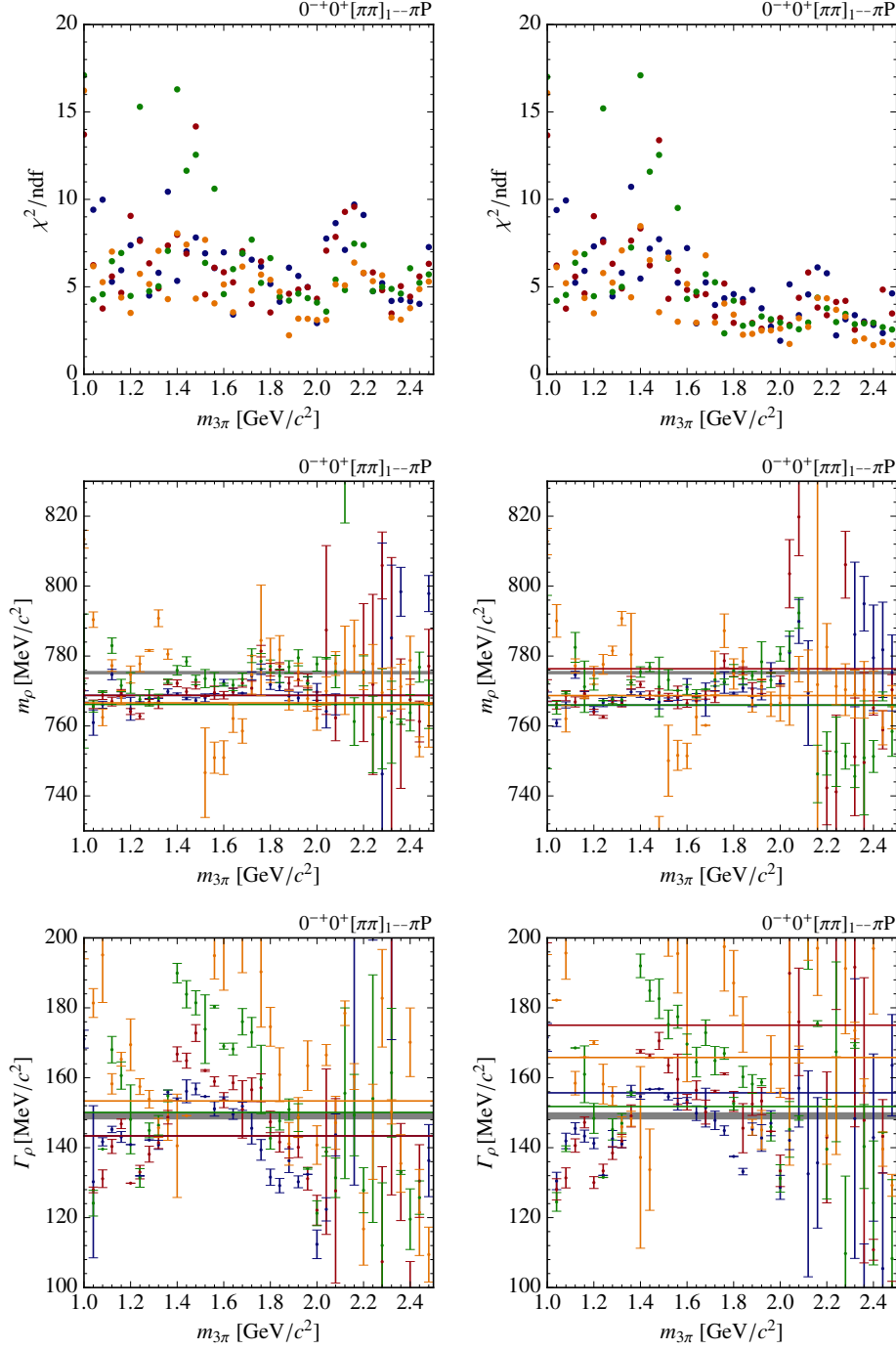
Figure 7.2.: Results of the fits in $m_{3\pi}$ and t' bis of the isobar dynamic amplitude extracted for the $0^{-+}0^{+} [\pi\pi]_{1^{--}} \pi P$ wave: The χ^2/ndf of the fits (top), the resulting $\rho(770)$ mass (center), and the resulting $\rho(770)$ width (bottom). The $m_{2\pi}$ fit range is given by kinematic limits (left) and limited to the range below $1.2\,\mathrm{GeV}/c^2$ (right). The horizontal lines indicate the result of a combined fit of the $\rho(770)$ parameters over the whole $m_{3\pi}$ range. The colors represent different t' bins (see text). The gray band indicates the corresponding value given by the PDG [2].

results in this region therefore have a very strong influence on the extracred $\rho(770)$ parameters using the whole $m_{3\pi}$ range.

Figure 7.4 shows the results of the same analysis performed for the spin-exotic $1^{-+}1^+ [\pi\pi]_{1^{--}} \pi\mathrm{P}$ wave obtained in study "E". We observe a χ^2/ndf around 5, that decreases only little when restricting the $m_{2\pi}$ range in the fits. The resulting $\rho(770)$ parameters are consistent with the fit over whole $m_{3\pi}$ range. Only in the region of $m_{3\pi} > 2\,\mathrm{GeV}/c^2$, the results begin to scatter further, since there the intensity of the $1^{-+}1^+ [\pi\pi]_{1^{--}} \pi\mathrm{P}$ wave is very small. We only observe a $m_{3\pi}$ dependence of m_ρ in the region of $m_{3\pi}$ from 1.8 to $2.0\,\mathrm{GeV}/c^2$ when the $m_{2\pi}$ fit range is not restricted. This hints to additional contributions in this dynamic isobar amplitude in the high-$m_{2\pi}$ region.

To obtain a global picture for the values of the $\rho(770)$ resonance parameters, we fit the (m_ρ, Γ_ρ) distribution obtained from all individual fits with a two-dimensional Gaussian. Since for some $m_{3\pi}$ and t' bins and waves, the fit of the Breit-Wigner does not converge, we restrict the results to be fitted to the ranges $700\,\mathrm{MeV}/c^2 < m_\rho < 850\,\mathrm{MeV}/c^2$ and $80\,\mathrm{MeV}/c^2 < \Gamma_\rho < 250\,\mathrm{MeV}/c^2$. We use the results for the $\rho(770)$ resonance parameters obtained with an unrestricted $m_{2\pi}$ range[a]. For this fit, we use the maximum likelihood method and weight the individual points by their respective $\left(\chi^2/\mathrm{ndf}\right)^{-1}$, neglecting their statistical uncertainties. We chose this procedure, since we want the bins best described by a Breit-Wigner to have the biggest impact, regardless of the intensity of the respective wave, which largely determines the size of the statistical uncertainties. Figure 7.5 shows the (m_ρ, Γ_ρ) distribution and its projections on the m_ρ and Γ_ρ axes with the result of the Gaussian fit. We see, that the Gaussian fit allows to estimate the central value and the standard deviation of the distribution. The Gaussian fit yields the following results:

$$\begin{aligned}
\mu_{m_\rho} &= 770\,\mathrm{MeV}/c^2, & \sigma_{m_\rho} &= 17\,\mathrm{MeV}/c^2, \\
\mu_{\Gamma_\rho} &= 146\,\mathrm{MeV}/c^2, & \sigma_{\Gamma_\rho} &= 28\,\mathrm{MeV}/c^2, \\
\varrho_{m_\rho \Gamma_\rho} &= 0.102,
\end{aligned} \tag{7.1}$$

where $\mu_{m,\Gamma}$ and $\sigma_{m,\Gamma}$ are the mean values and standard deviations of the respective quantities and $\varrho_{m_\rho \Gamma_\rho}$ is their correlation coefficient. The Gaussian standard deviations give an estimate for the size of systematic effects of the mother wave, $m_{3\pi}$, and t' on the fitted $\rho(770)$ parameters. Such effects may be caused for example by rescattering with the third pion or by non-resonant contributions like the Deck effect (see appendix B). Since we do not have an appropriate model for these effects, we can only estimate their size using the standard deviations of the Gaussian fit and include them in the systematic uncertainties[b]. For a model correctly describing such effects, the Gaussian standard deviations of the (m_ρ, Γ_ρ) distribution are

---

[a]A Gaussian fit to the (m_ρ, Γ_ρ) distribution obtained with a fit range of $m_{2\pi} < 1.2\,\mathrm{GeV}/c^2$ yields the same central values and slightly smaller standard deviations. We use the unrestricted range, since the resulting distribution is more similar to a Gaussian.

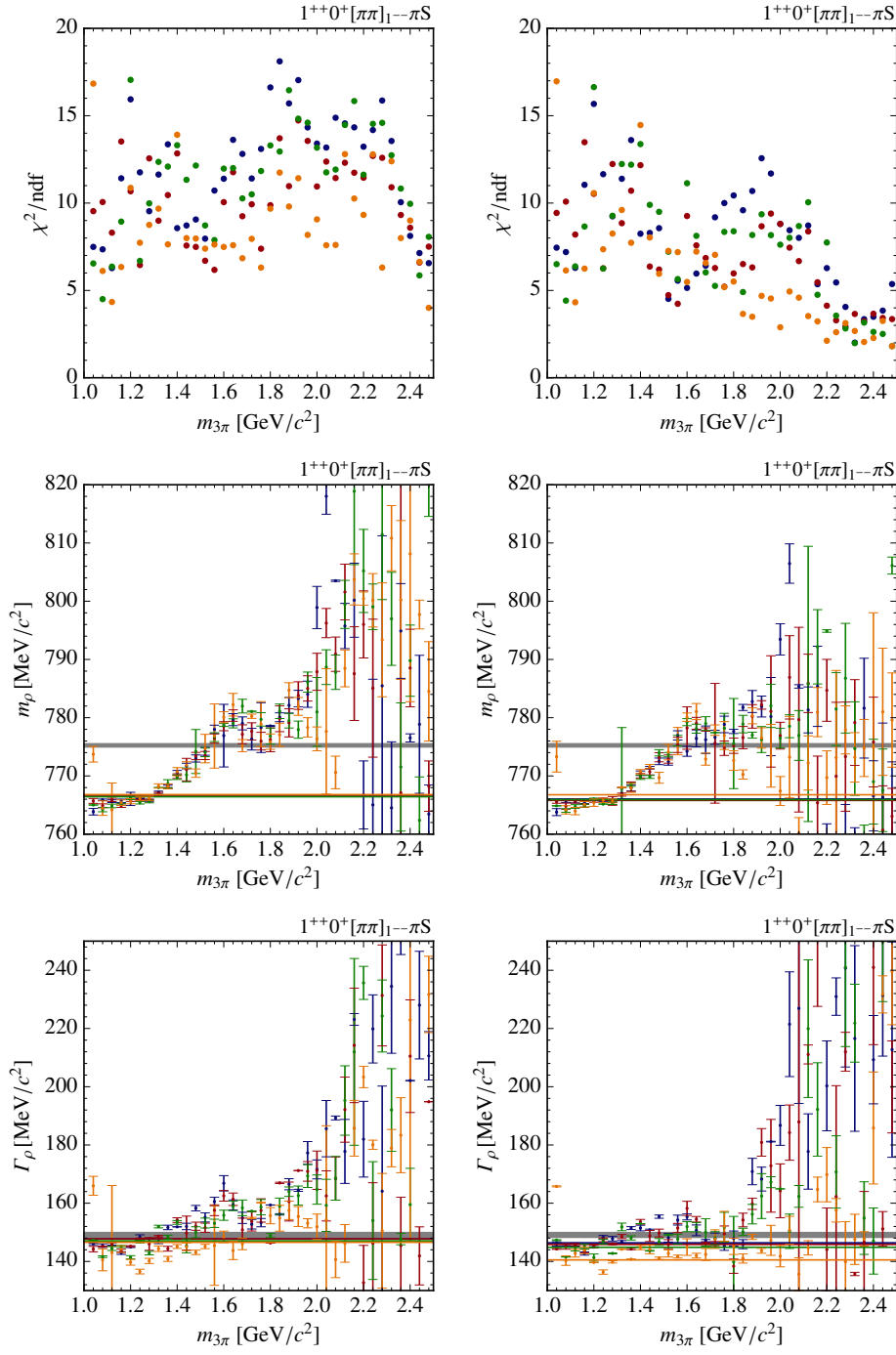[b]In this chapter, we only discuss systematic uncertainties of this kind and neglect other possible contributions.

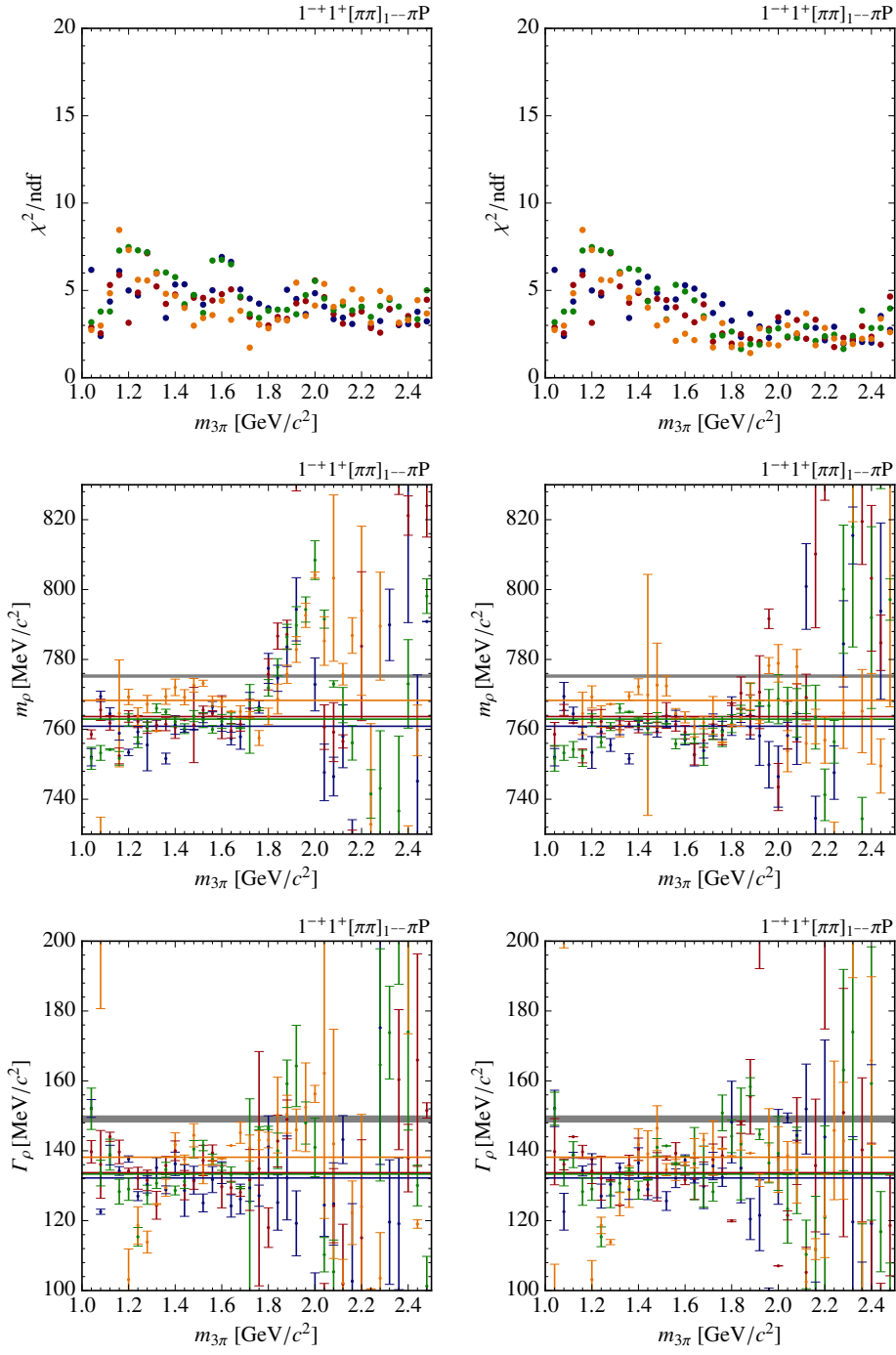Figure 7.3.: Similar to fig. 7.2, now showing results for the $1^{++}0^+ [\pi\pi]_{1^{--}} \pi S$ wave.

Figure 7.4.: Similar to fig. 7.2, now showing results for the $1^{-+}1^+\,[\pi\pi]_{1^{--}}\,\pi\mathrm{P}$ wave.
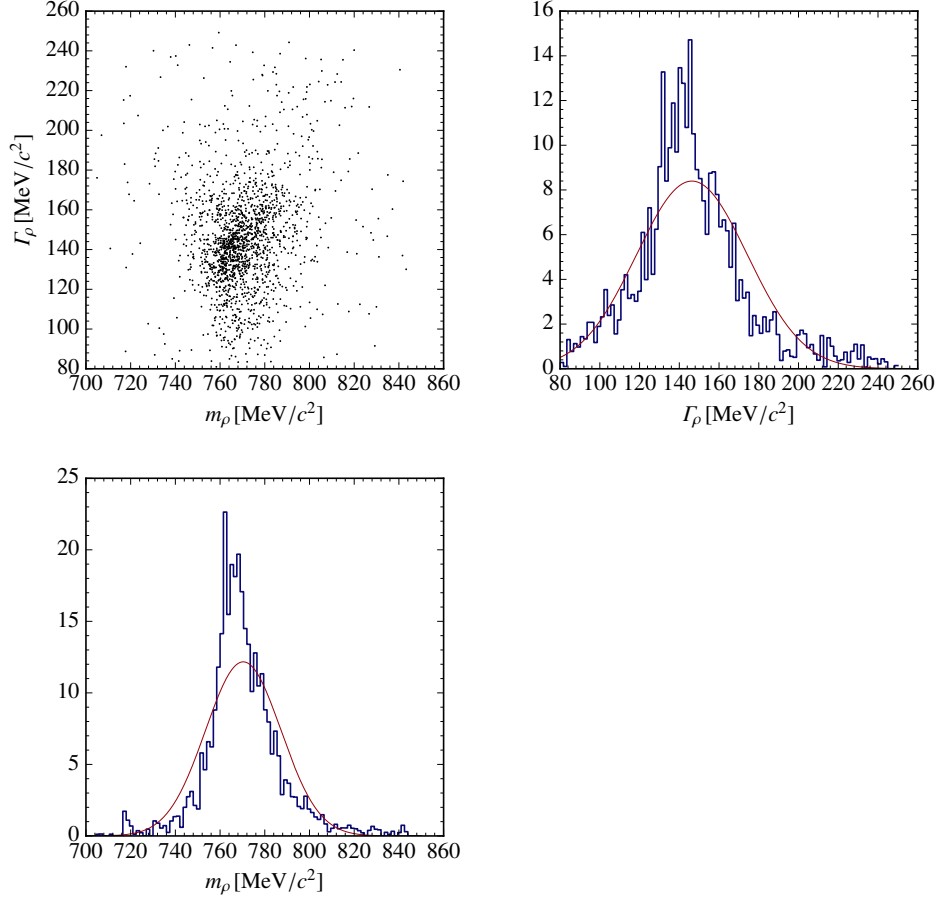
Figure 7.5.: Distribution of fit results for m_ρ and Γ_ρ and the projections on the axes. The red lines indicate the Gaussian fit.

expected to vanish. Within the ranges of these systematic uncertainties introduced due to our simple Breit-Wigner model, the central values are consistent with the ones given by the PDG [2].

7.0.9. Resonance parameters of $f_2(1270)$

Combining all performed studies, we have a total of seven waves that employ a freed $[\pi\pi]_{2^{++}}$ isobar (see table 6.1). Similar to the $\rho(770)$ in chapter 7, we fit the $f_2(1270)$ resonance in all seven waves in every $m_{3\pi}$ and t' bin separately with a Breit-Wigner parameterization, as given in eqs. (4.8) and (4.9). This way, we study the dependence of m_{f_2} and Γ_{f_2} on $m_{3\pi}$, t', and the mother wave. Since the mass of the $f_2(1270)$ resonance is much higher than that of the $\rho(770)$, we do not restrict the $m_{2\pi}$ range in these fits. However, we verified that by restricting the $m_{2\pi}$ fit range to the region below $1.8\,\text{GeV}/c^2$, which had no significant influence on the results.

An example for a fit of a Breit-Wigner for the $f_2(1270)$ resonance is shown in the upper right plot of fig. 7.1, which shows the same data as fig. 6.28. We see, that even though the adjusted Breit-Wigner describes the data slightly better than the fixed parameterization, it is not able to fully model all observed features. Even tough the intensity distribution would suggest, that a simple scaling of the Breit-Wigner description improves the fit, this is not the case for similar reasons as discussed in section 6.4.3.

As an example for the resulting parameter values, we show the results for the $2^{-+}0^+ [\pi\pi]_{2^{++}} \pi S$ wave, taken from study "C" and for the the $2^{-+}0^+ [\pi\pi]_{2^{++}} \pi D$ wave from study "G" in fig. 7.6. For both waves, we observe a rather large χ^2/ndf of around 10, indicating, that the $f_2(1270)$ resonance is not well described by a Breit-Wigner parameterization in the $J^{PC}M^\varepsilon = 2^{-+}0^+$ waves, as can be seen in the upper right plot of fig. 7.1. All other waves with a $[\pi\pi]_{2^{++}}$ isobar exhibit a typical value of 5 for χ^2/ndf in these fits. For the $2^{-+}0^+ [\pi\pi]_{2^{++}} \pi S$ wave, we observe a strong dependence of m_{f_2} on $m_{3\pi}$, which is similar in all t' bins and peaks at the position of the $\pi_2(1880)$ resonance. In the $2^{-+}0^+ [\pi\pi]_{2^{++}} \pi D$ wave, we also see such a dependence, now with a dip at the $\pi_2(1880)$ resonance. The $m_{3\pi}$ dependences of Γ_{f_2} also show a peak and dip around the mass of $\pi_2(1880)$, respectively, roughly consistent in all four t' bins. This shows, that the dynamic isobar amplitude of the $f_2(1270)$ strongly depends on the decaying mother particle.

The results for m_{f_2} and Γ_{f_2} from all waves, $m_{3\pi}$ and t' bins in the ranges $1.0 < m_{f_2} < 2.0\,\text{GeV}/c^2$ and $0.1 < \Gamma_{f_2} < 0.4\,\text{GeV}/c^2$ are fitted by a two-dimensional Gaussian similar to section 7.0.8. The resulting Gaussian parameters are:

$$
\begin{aligned}
\mu_{m_{f_2}} &= 1256\,\text{MeV}/c^2, & \sigma_{m_{f_2}} &= 50\,\text{MeV}/c^2, \\
\mu_{\Gamma_{f_2}} &= 178\,\text{MeV}/c^2, & \sigma_{\Gamma_{f_2}} &= 51\,\text{MeV}/c^2, \\
\varrho_{m_{f_2}\Gamma_{f_2}} &= 0.112.
\end{aligned}
\tag{7.2}
$$

As in the case of the $\rho(770)$, the Gaussian widths of this fit is an estimate for systematic effects of rescattering and non-resonant contributions caused by the simplicity of our Breit-Wigner model, which does not take such effects into account. Within the range of these effects, the resulting central values for m_{f_2} and Γ_{f_2} are consistent with the values given by the PDG [2]. The correlation coefficient of mass and width of 0.112 is similar to the one of the $\rho(770)$ resonance.

7.0.10. Resonance parameters of $f_0(980)$

The analysis model contains three waves that employ freed $[\pi\pi]_{0^{++}}$ isobars, all included in study "C" (see table 6.1). Unlike the $[\pi\pi]_{1^{--}}$ or the $[\pi\pi]_{2^{++}}$ isobars, the resulting 0^{++} dynamic amplitudes are not dominated by a single resonance, but are composed of contributions from the broad $(\pi\pi)_S$ wave and the resonances $f_0(980)$ and $f_0(1500)$. Since the description of the broad $(\pi\pi)_S$ component is difficult and the signal for the $f_0(1500)$ is weak, we first restrict ourselves to the determination
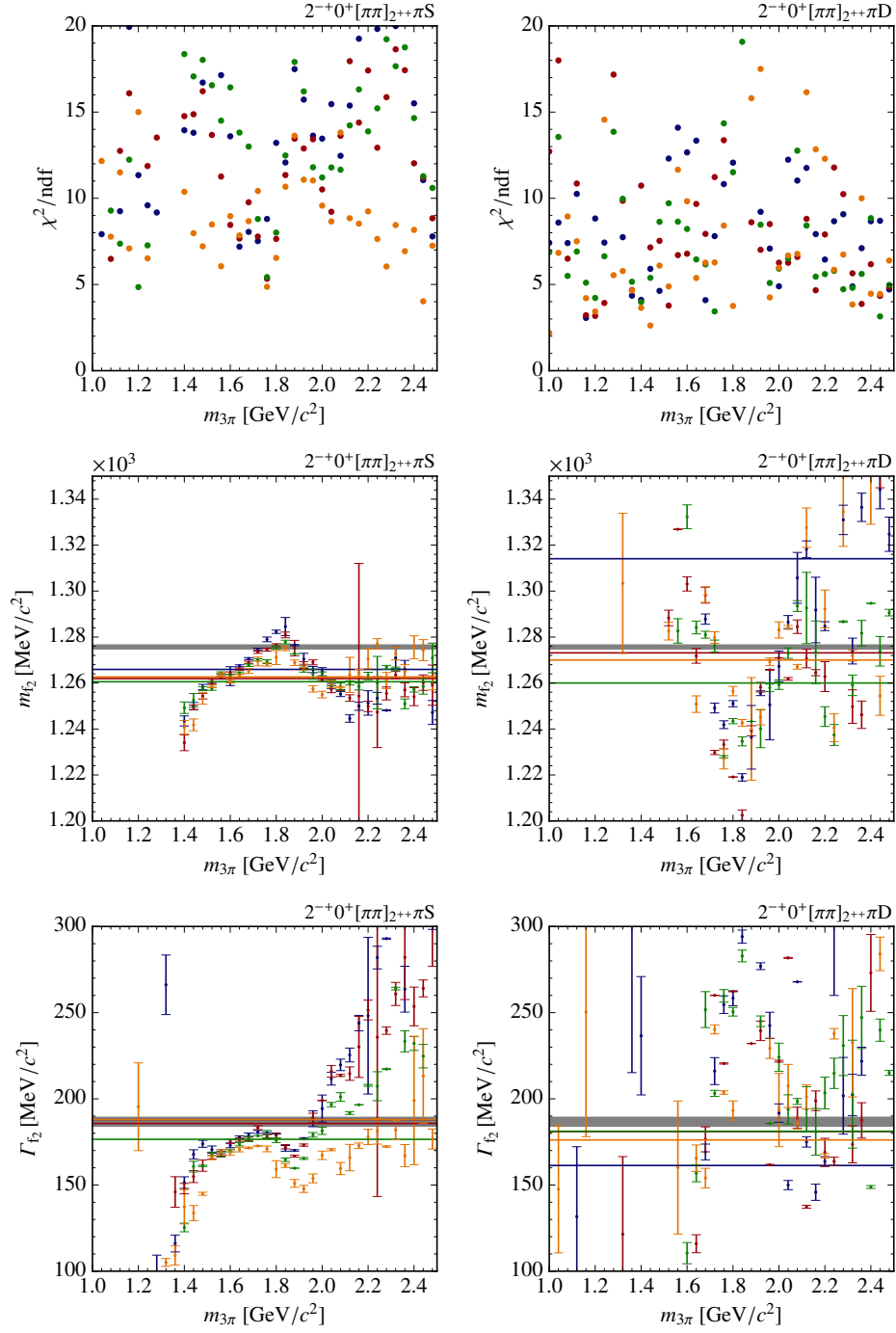
Figure 7.6.: Similar to fig. 7.2, now showing results from fits of an $f_2(1270)$ Breit-Wigner to the dynamic isobar amplitude of the $2^{-+}0^+ [\pi\pi]_{2^{++}} \pi S$ wave from study "C" (left) and the $2^{-+}0^+ [\pi\pi]_{2^{++}} \pi D$ wave from study "G" (right).

of the $f_0(980)$ parameters. Therefore, we limit the $m_{2\pi}$ fit range to a narrow window from 0.9 to $1.1\,\mathrm{GeV}/c^2$ around the $f_0(980)$ mass. We describe the contribution of the $(\pi\pi)_\mathrm{S}$ component by the parameterization used in the fixed-isobar analysis (see table 4.2). Since we only analyze a narrow $m_{2\pi}$ window and the $(\pi\pi)_\mathrm{S}$ parameterization varies only slowly, we do not expect large systematic effects from this choice. We verified this by performing a similar fit with a polynomial of first degree instead of the $(\pi\pi)_\mathrm{S}$ parameterization, which yields comparable results. We describe the $f_0(980)$ with a Flatté parameterization, as given in eq. (4.12) and fit its resonance parameters, m_{f_0}, g_π and g_K, for every $m_{3\pi}$ and t' bin in all three waves.

An example for such a fit of the $f_0(980)$ is depicted in the upper left plot fig. 7.1, alongside an independent fit of the $f_0(1500)$ resonance. The data points are the same as in fig. 6.11. We see, that the interference of the Flatté parameterization with the broad $(\pi\pi)_\mathrm{S}$ component offers a good description of the data.

As an example for the resulting $f_0(980)$ parameters, we show the results for the $0^{-+}0^+\,[\pi\pi]_{0^{++}}\,\pi\mathrm{S}$ wave in fig. 7.7. The χ^2/ndf is around 5 for the two lowest t' bins and decreases with increasing $m_{3\pi}$ to around 2. This χ^2/ndf value is lower for the two highest t' bins, indicating that non-resonant contributions may have a stronger influence at low t'. For the $m_{3\pi}$ range from 1.4 to $2.0\,\mathrm{GeV}/c^2$ the fit results for m_{f_0} yield stable results in all t' bins, while the fits become unstable for low and high $m_{3\pi}$, since in these $m_{3\pi}$ regions the wave has a small intensity. A similar effect can be seen for the results for g_π, while the results for g_K seem to be unstable over the whole $m_{3\pi}$ range. A reason for this is, that this parameter describes the $f_0(980) \to \mathrm{KK}$ decay, which is invisible in our analysis.

As in sections 7.0.8 and 7.0.9, we determine the central values and standard deviations for the resonance parameters by a Gaussian fit to the results for the three waves in the $m_{3\pi}$ and t' bins. Since the Flatté parameterization has three resonance parameters, we use a three-dimensional Gaussian in this case[c]. The resulting parameters are:

$$
\begin{aligned}
\mu_{m_{f_0}} &= 980\,\mathrm{MeV}/c^2, & \sigma_{m_{f_0}} &= 12\,\mathrm{MeV}/c^2, \\
\mu_{g_\pi} &= 0.067\,\left(\mathrm{GeV}/c^2\right)^2, & \sigma_{g_\pi} &= 0.029\,\left(\mathrm{GeV}/c^2\right)^2, \\
\mu_{g_\mathrm{K}} &= 0.071\,\left(\mathrm{GeV}/c^2\right)^2, & \sigma_{g_\mathrm{K}} &= 0.131\,\left(\mathrm{GeV}/c^2\right)^2, & (7.3) \\
\varrho_{m_{f_2},g_\pi} &= -0.156, & \varrho_{m_{f_2},g_\mathrm{K}} &= 0.436 \\
\varrho_{g_\pi,g_\mathrm{K}} &= 0.383.
\end{aligned}
$$

The central value of the $f_0(980)$ resonance mass is compatible with the value quoted by the PDG [2] and with the value used in the fixed-isobar analysis of refs. [8, 12] which were taken from ref. [30]. In contrast, the central value for g_π is inconsistent with the value in ref. [30]. Due to the large systematic uncertainties and the high

---

[c]Similar to section 7.0.8, we restrict the fit results to $800 < m_{f_0} < 1200\,\mathrm{MeV}/c^2$, $0 < g_\pi < 0.2\,\left(\mathrm{GeV}/c^2\right)^2$, and $-0.2 < g_\mathrm{K} < 0.5\,\left(\mathrm{GeV}/c^2\right)^2$.
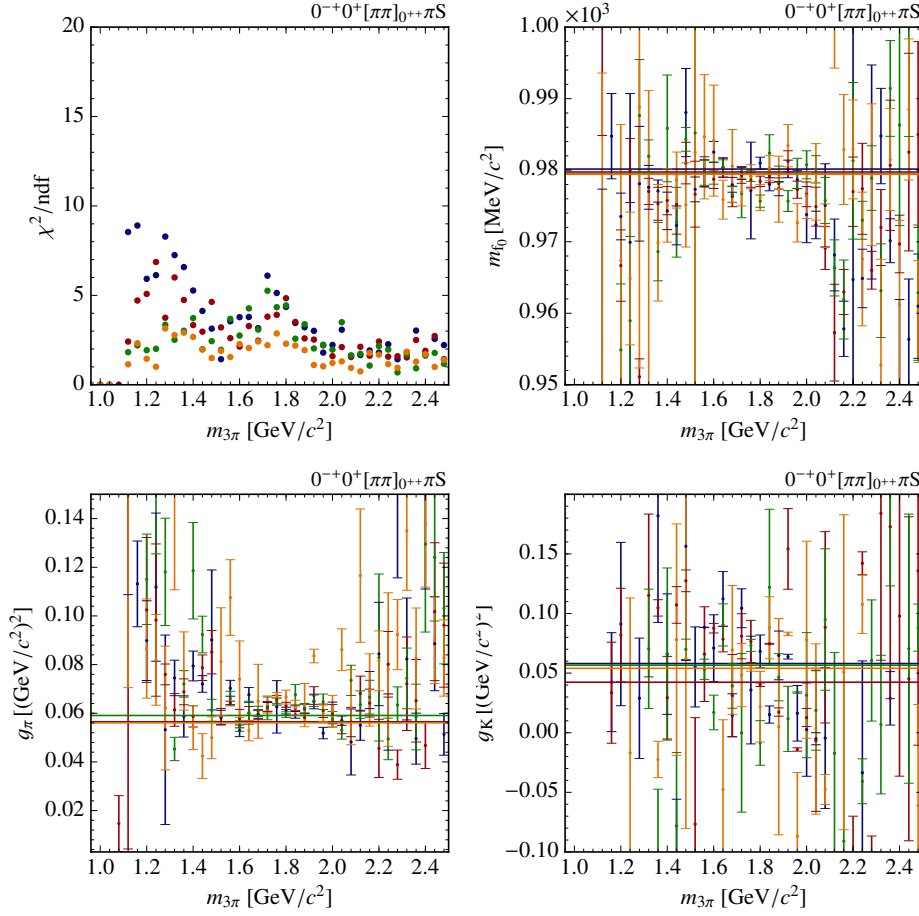
Figure 7.7.: Similar to fig. 7.2, now showing results for the $f_0(980)$ Flatté parameters, m_{f_0}, g_π and g_K, in the $0^{-+}0^+ [\pi\pi]_{0^{++}} \pi S$ wave from study "C".

correlations of g_K with the other two resonance parameters, we cannot make any statement on the consistency of this parameter, which is very weakly determined in our studies.

7.0.11. Resonance parameters of $f_0(1500)$

Since $[\pi\pi]_{0^{++}}$ isobars also contain the $f_0(1500)$ resonance, we try to extract its resonance parameters similarly to section 7.0.10, now using an $m_{2\pi}$ mass window from 1.25 to 1.72 GeV/c^2. As parameterization, we use a Breit-Wigner amplitude as given in eqs. (4.8) and (4.9). We employ the same description for the broad $(\pi\pi)_S$ component as in section 7.0.10. Since the mass of the $f_0(1500)$ is rather high, we perform this analysis only for $m_{3\pi}$ bins above 1.5 GeV/c^2.

An example for such a fit of the $f_0(1500)$ is depicted in the upper left plot fig. 7.1, alongside an independent fit of the $f_0(980)$ resonance. The data points are the same as in fig. 6.11. We see, that the interference of the Breit-Wigner parameterization with the broad $(\pi\pi)_S$ component offers a good description of the data.

The results of the $f_0(1500)$ parameters are shown in fig. 7.8, for the $0^{-+}0^+$ $[\pi\pi]_{0^{++}}\pi S$ wave (left) and the $2^{-+}0^+ [\pi\pi]_{0^{++}}\pi D$ wave (right). For both waves, we obtain good χ^2/ndf values of around 2.5. Except for the high-$m_{3\pi}$ region of the $2^{-+}0^+ [\pi\pi]_{0^{++}}\pi D$ wave, the results for $m_{f_0(1500)}$ and $\Gamma_{f_0(1500)}$ are stable over $m_{3\pi}$ and t'. Fits of the $f_0(1500)$ resonance in the $1^{++}0^+ [\pi\pi]_{0^{++}}\pi P$ wave turned out to be unstable, so we excluded this wave from the fit, since there seems to be no contribution from this isobar resonance.

We fit a two-dimensional Gaussian to the distribution of the $f_0(1500)$ parameters[d], resulting in the following Gaussian parameters:

$$
\begin{aligned}
\mu_{m_{f_0(1500)}} &= 1494\,\mathrm{MeV}/c^2, & \sigma_{m_{f_0(1500)}} &= 68\,\mathrm{MeV}/c^2, \\
\mu_{\Gamma_{f_0(1500)}} &= 109\,\mathrm{MeV}/c^2, & \sigma_{\Gamma_{f_0(1500)}} &= 30\,\mathrm{MeV}/c^2, \\
\varrho_{m_{f_0(1500)}\Gamma_{f_0(1500)}} &= 0.161.
\end{aligned}
\tag{7.4}
$$

The central values are close to the values given by the PDG [2]. Using a polynomial of first degree to model the $(\pi\pi)_S$ background instead of the parameterization given in table 4.2, the resulting central values are $\mu_{m_{f_0(1500)}} = 1473\,\mathrm{MeV}/c^2$ and $\mu_{\Gamma_{f_0(1500)}} = 130\,\mathrm{MeV}/c^2$.

7.0.12. Resonance parameters of $\rho_3(1690)$

The only wave employing a freed $[\pi\pi]_{3^{--}}$ isobar is the $3^{++}0^+ [\pi\pi]_{3^{--}}\pi S$ wave in study "H". We fit the resulting dynamic isobar amplitudes for every $m_{3\pi}$ and t' bin with a Breit-Wigner parameterization for the $\rho_3(1690)$ resonance. An example for such a fit of the $\rho_3(1690)$ is shown in the lower right plot of fig. 7.1, where we see, that the Breit-Wigner parameterization offers a good description of the $\rho_3(1690)$ peak region, but is not able to model the features at lower and higher $m_{2\pi}$. The resulting resonance parameters are shown in the left column of fig. 7.9. The χ^2/ndf values are around 5. The resonance mass of the $\rho_3(1690)$ mass rises between $m_{3\pi} = 1.6\,\mathrm{GeV}/c^2$ and $1.8\,\mathrm{GeV}/c^2$, where the $\rho_3(1690)$ mass is below threshold, and then approximates a constant. This dependence is consistent in all four t' bins. The rise can be explained with the opening of the 2π phase space for the $\rho_3(1690)$ resonance in this $m_{3\pi}$ region. The $\rho_3(1690)$ width rises with $m_{3\pi}$ and

---

[d]Similar to section 7.0.8, we restrict the fit results to $1200 < m_{f_0(1500)} < 1800\,\mathrm{MeV}/c^2$ and $50 < \Gamma_{f_0(1500)} < 200\,\mathrm{MeV}/c^2$.
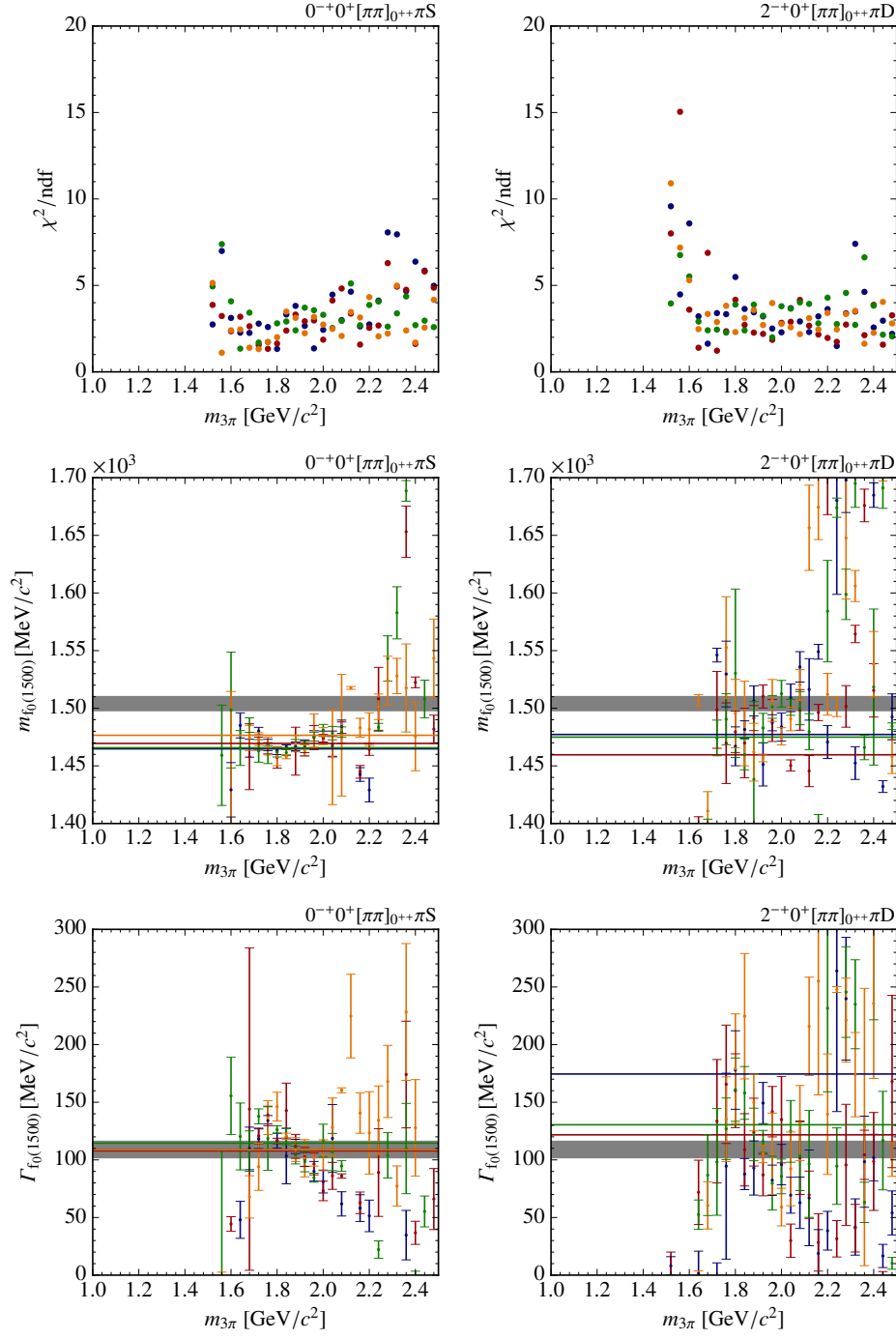
Figure 7.8.: Similar to fig. 7.2, now showing results for the $f_0(1500)$ in the $0^{-+}0^+$ $[\pi\pi]_{0^{++}}\pi$S and the $2^{-+}0^+$ $[\pi\pi]_{0^{++}}\pi$P waves, with the $m_{2\pi}$ fit range restricted from 1.25 to 1.72 GeV/c^2.

is also consistent over all t' bins. A two-dimensional Gaussian fit to the distribution the resonance parameters yields the following parameters[e]:

$$
\begin{aligned}
\mu_{m_{\rho_3}} &= 1670 \, \text{MeV}/c^2, & \sigma_{m_{\rho_3}} &= 74 \, \text{MeV}/c^2, \\
\mu_{\Gamma_{\rho_3}} &= 199 \, \text{MeV}/c^2, & \sigma_{\Gamma_{\rho_3}} &= 39 \, \text{MeV}/c^2, & (7.5) \\
\varrho_{m_{\rho_3}\Gamma_{\rho_3}} &= 0.205. &&
\end{aligned}
$$

The systematic uncertainties on the resonance parameters are higher than in the cases of the $\rho(770)$ or the $f_2(1270)$ resonances (see sections 7.0.8 and 7.0.9). These higher systematic uncertainties and the larger correlation coefficient might be caused by the fact, that the biggest signal for the $\rho_3(1690)$ is heavily influenced by the opening phase space, as can be seen in fig. 6.35. However, within these uncertainties, the central values for m_{ρ_3} and Γ_{ρ_3} are consistent with the values given by the PDG [2].

7.0.13. Resonance parameters of ρ'

In addition to the $\rho(770)$ resonance, we see a second loop structure in the Argand diagram for the extracted dynamic isobar amplitudes of the $1^{++}0^+ \, [\pi\pi]_{1^{--}} \pi S$ wave in the high-$m_{3\pi}$ region, which could correspond to a ρ' resonance. Since, the shape is not circular and overlaps with the $\rho(770)$ resonance, we know that a description with a Breit-Wigner is only a crude approximation. However, since we lack a better parameterization, we nevertheless use a Breit-Wigner amplitude to extract estimates for the parameters of a potential excited ρ' resonance. To do so, we first fit the parameters of the $\rho(770)$ in every $m_{3\pi}$ and t' bin the same way we did in section 7.0.8, restricting the $m_{2\pi}$ range to below $1.2 \, \text{GeV}/c^2$. In a second step, we fix the $\rho(770)$ parameters to the values obtained in the first fit, add a second Breit-Wigner amplitude to the model function, and fit its parameters, now using the whole kinematically allowed $m_{2\pi}$ range. An example of the fit of the ρ' is shown in the lower left plot of fig. 7.1. We see, that the model is not able to fully describe the peaks of the $\rho(770)$ and ρ'. We also see, that the Breit-Wigner descriptions of both resonances overlap and the signal of the ρ' resonance is very small compared to the $\rho(770)$.

The results for the ρ' parameters are shown in the right column of fig. 7.9. The χ^2/ndf values of 5 to 10 are in a similar range than for other resonance fits. Compared to the results in fig. 7.3, where the same data is described without a ρ' resonance, we find, that including both resonances results in a better description of the data.

In the sub-threshold region of $m_{3\pi} < 1.4 \, \text{GeV}/c^2$, the ρ' mass $m_{\rho'}$ rises with increasing $m_{3\pi}$ in all four t' bins until $m_{3\pi} \approx 1.4 \, \text{GeV}/c^2$, where the resonance can be on-shell. In the first two t' bins, $m_{\rho'}$ decreases again with increasing $m_{3\pi}$, while in the upper two t' bins, it stays roughly constant. For $m_{3\pi} \gtrsim 2.0 \, \text{GeV}/c^2$, the

---

[e]Similar to section 7.0.8, we restrict the fit results to $1200 < m_{\rho_3} < 2200 \, \text{MeV}/c^2$ and $100 < \Gamma_{\rho_3} < 300 \, \text{MeV}/c^2$.
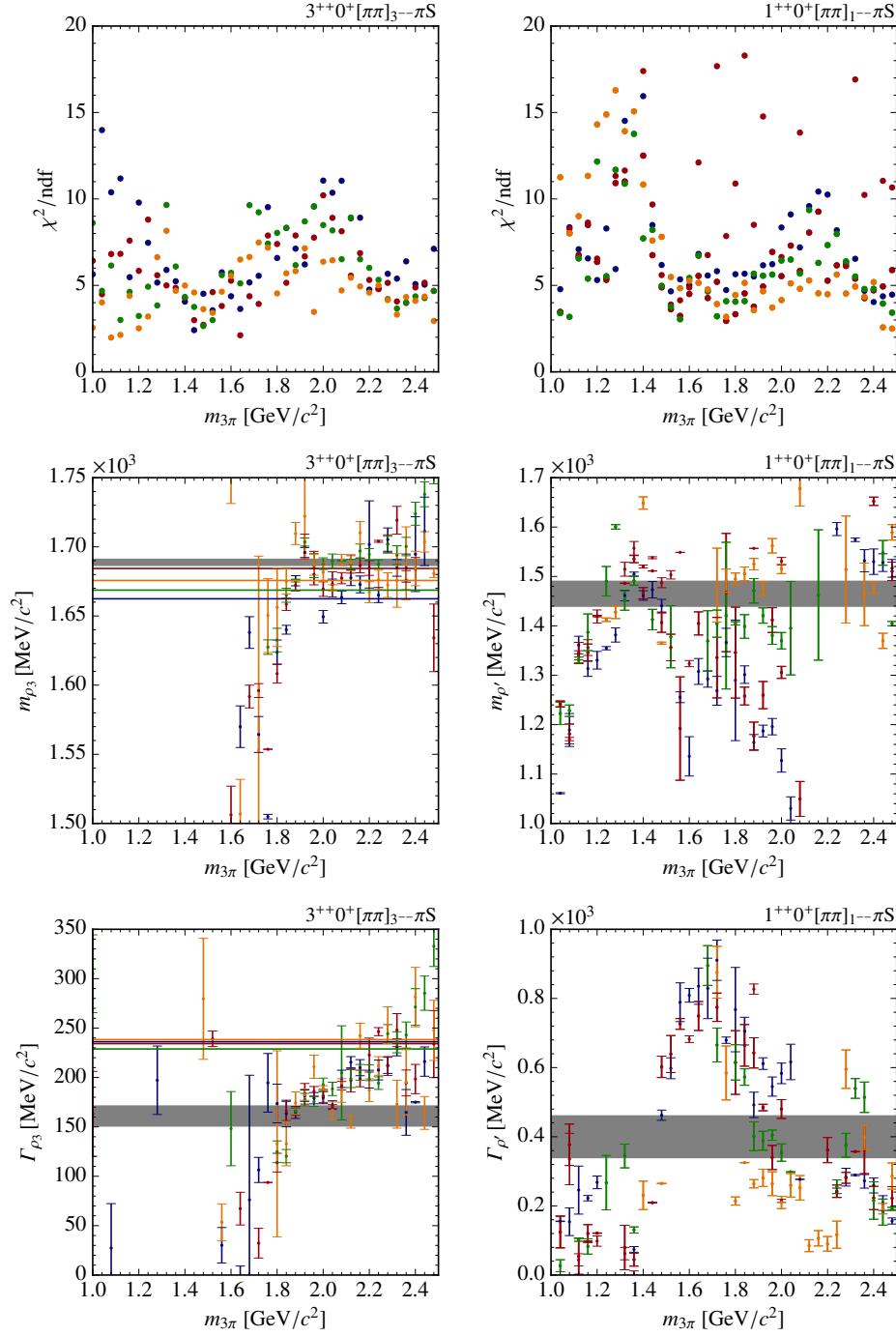
Figure 7.9.: Similar to fig. 7.2, now showing results for the $3^{++}0^+\,[\pi\pi]_{3^{--}}\,\pi S$ wave from study H with no restrictions on the $m_{2\pi}$ range (left) and for the ρ' fits to the $1^{++}0^+\,[\pi\pi]_{1^{--}}\,\pi S$ wave from study "C" (right).

results for $m_{\rho'}$ tend to become unstable. The values for the ρ' width $\Gamma_{\rho'}$ tend to scatter, but are consistent over the different t' bins.

To get an estimate for the ρ' resonance parameters and their systematic uncertainties, we performed a two-dimensional Gaussian likelihood fit to the distribution of the ρ' parameters like in section 7.0.8.

The resulting Gaussian parameters are[f]:

$$
\begin{aligned}
\mu_{m_{\rho'}} \quad &= 1390\,\mathrm{MeV}/c^2, \quad \sigma_{m_{\rho'}} = \quad 145\,\mathrm{MeV}/c^2, \\
\mu_{\Gamma_{\rho'}} \quad &= 421\,\mathrm{MeV}/c^2, \qquad \sigma_{\Gamma_{\rho'}} = \quad 230\,\mathrm{MeV}/c^2, \\
\varrho_{m_{\rho'}\Gamma_{\rho'}} \quad &= -0.273.
\end{aligned}
\tag{7.6}
$$

The central value for the mass is lower, that the value for the $\rho'(1450)$ given by the PDG [2], but both values agree within the uncertainties. The central value for $\Gamma_{\rho'}$ agrees with the value given by the PDG [2].

7.0.14. Interpretation of fit results

The results for the extracted isobar resonance parameters are summarized and compared to the PDG values in ref. [2] in table 7.1. We use the Gaussian standard deviation of our fits as uncertainties on the parameters, which is caused by the simplicity of our Breit-Wigner model for the dynamic isobar amplitudes. These uncertainties are large and we see from figs. 7.2 to 7.4 and 7.6 to 7.9, that the isobar resonance parameters could be determined with much higher accuracy, if the underlying physical effects, causing their dependence on $m_{3\pi}$, were understood. However, since we do not have a model for these effects at the moment, we can only include them as systematic uncertainties. We also see, that the central values we obtain are closer to the PDG values given in ref. [2] than our uncertainty estimates suggest.

---

[f]Similar to section 7.0.8, we restrict the fit results to $1000 < m_{\rho'} < 2000\,\mathrm{MeV}/c^2$ and $100 < \Gamma_{\rho'} < 1000\,\mathrm{MeV}/c^2$.

Table 7.1.: Fit results for the isobar resonance parameters obtained with Gaussian fits to the distributions obtained from the fits in $(m_{3\pi}, t')$ bins. The systematic uncertainties are given by the widths of the respective Gaussian distributions. The parameters $g_{\pi,\mathrm{K}}$ are given in units of $\left(\mathrm{GeV}/c^2\right)^2$, all others in MeV/c^2.

Parameter	Fit			PDG [2]		
$m_{\mathrm{f_0(980)}}$	980	$\pm$	12			
g_π	0.067	$\pm$	0.029			
g_K	0.071	$\pm$	0.131			
$m_{\mathrm{f_0(1500)}}$	1494	$\pm$	68	1504	$\pm$	6
$\Gamma_{\mathrm{f_0(1500)}}$	109	$\pm$	30	109	$\pm$	7
$m_{\rho(770)}$	770	$\pm$	17	775.25	$\pm$	0.26
$\Gamma_{\rho(770)}$	146	$\pm$	28	149.1	$\pm$	0.8
$m_{\rho'}$	1390	$\pm$	145	1465	$\pm$	25
$\Gamma_{\rho'}$	421	$\pm$	230	400	$\pm$	60
$m_{\mathrm{f_2(1270)}}$	1256	$\pm$	50	1275.7	$\pm$	0.8
$\Gamma_{\mathrm{f_2(1270)}}$	178	$\pm$	51	186.7	$^+_-$	$^{2.2}_{2.5}$
$m_{\rho_3(1690)}$	1670	$\pm$	74	1688.8	$\pm$	2.1
$\Gamma_{\rho_3(1690)}$	199	$\pm$	39	161	$\pm$	10

Chapter 8.

Conclusions and Outlook

In this thesis, we have extended the freed-isobar method, used for simple applications for example in refs. [10–12], to an arbitrary number of freed waves with step-like dynamic isobar amplitudes, by identifying and resolving appearing mathematical ambiguities. Since we were not only reducing the model dependence of our PWA this way, but could extract the dynamic isobar amplitudes for 24 waves directly from the data, we were able to extract resonance parameters for the appearing isobar resonances from these results and obtain an unprecedented insight in the interplay of the dynamics of the 2π and 3π subsystems in the process $\pi^- p \to \pi^- \pi^+ \pi^- p$.

8.1. The freed-isobar method

To circumvent the necessity for fixed dynamic isobar amplitudes in a three body PWA, we introduced the freed-isobar method in chapter 5, where these fixed parameterizations are replaced by piece-wise constant functions. This approach allows us to infer binned approximations to the dynamic isobar amplitudes from the data, using the same functional form of the likelihood as in the conventional analyses with fixed dynamic isobar amplitudes, like the one introduced in chapter 4. This allows to use the same software packages for both types of analyses, which in turn makes it easy to directly compare both approaches, and to make use of the same computational benefits: the pre-calculation of normalization integrals and partial-wave decay amplitudes.

Due to the high number of degrees of freedom in freed-isobar analysis models, continuous mathematical ambiguities, called zero modes, appear, which are represented by complex-valued coefficients. We first showed the analytic origin of these ambiguities, which are complete cancellations between partial-wave amplitudes and their Bose symmetrized counterparts. We also showed that these cancellations are present in a fully covariant as well as in a non-relativistic formulation of the PWA model, and can also appear in other processes, that do not necessarily have to be Bose symmetrized. The complexity of these analytic calculations increases drastically with increasing particle spins and with the number of freed-isobar waves. We therefore developed a numerical method that allows to identify zero modes in a freed-isobar model using an eigenvalue decomposition of the phase-space integral matrix of the decay amplitudes. We developed a method using the knowledge on

the m_ξ dependence of the zero modes to resolve the corresponding ambiguities. We verified this method on a Monte Carlo data set and demonstrated the validity of the freed-isobar method. The Monte Carlo studies in sections 5.3 and 6.2 showed that the freed-isobar method is a powerful tool to infer dynamic isobar amplitudes directly from the data. The method allows to extract much more information about the appearing partial waves than the conventional PWA method, if the appearing ambiguities are identified and resolved. The freed-isobar approach makes less assumptions on the dynamic isobar amplitudes and is therefore less model dependent, than the fixed-isobar approach.

Even though the developed methods to resolve the zero-mode ambiguities yielded consistent results, not all methods worked equally well. Especially resolving ambiguities by requiring smoothness over neighboring $m_{3\pi}$ bins yielded results that were inconsistent with other methods, which use additional knowledge on the appearing 2π isobar resonances. However, this can be explained by the fact, that the smoothest solution does not necessarily have to be correct, since for example appearing 3π resonances lead to a considerable change with $m_{3\pi}$. In our case, the knowledge on isobar resonances was enough to resolve all appearing ambiguities, but in different channels and applications it may become necessary to develop new approaches, for example if the prior knowledge on the corresponding dynamic isobar amplitudes is not sufficient.

8.2. Freed-isobar analysis of Compass data

In chapter 6 we applied the freed-isobar method to the data set for the process $\pi^- p \to \pi^- \pi^+ \pi^- p$ collected by the COMPASS experiment, for various intermediary 3π states X, as well as for four different combinations of isobar J_ξ^{PC} quantum numbers: 0^{++}, 1^{--}, 2^{++}, and 3^{--}. All together we used a total of 24 freed waves in 9 studies, all based on a freed-isobar wave set consisting of the eleven waves with the highest relative intensities in the fixed-isobar PWA. We performed these studies in $40\,\mathrm{MeV}$ wide bins in $m_{3\pi}$ in the range from 0.5 to $2.5\,\mathrm{GeV}/c^2$ and in four non-equidistant bins in the squared four-momentum transfer t' in the range from 0.1 to $1.0\,(\mathrm{GeV}/c)^2$. We resolved the appearing ambiguities in the dynamic isobar amplitudes of these freed-isobar waves using several different approaches, for example using the parameterizations from the fixed-isobar analysis or Breit-Wigner amplitudes with floating mass and width as constraints. In general, we find a good qualitative agreement between the results of the freed-isobar and those of the fixed-isobar approach. However, some details differ between both approaches, indicating that the fixed-isobar approach is a good approximation to the physical dynamic isobar amplitudes, but minor features are still unaccounted for. On the one hand, this justifies the results of the fixed-isobar approach, since both approaches match reasonably well, while on the other hand it shows the need for improved parameterizations for the dynamic isobar amplitudes, to be able to describe these smaller features of the data that were unaccounted for in the fixed-isobar approach, like signals from excited resonances like the ρ'.

In a next step, we determined the parameters of the appearing isobar resonances, using Breit-Wigner and Flatté parameterizations, from the dynamic isobar amplitudes extracted by the freed-isobar PWA. We performed this analysis independently for every $m_{3\pi}$ and t' bin, and for every wave. This way, we were able to study the systematic dependences of the isobar resonance parameters on these quantities. We find a strong dependence on the mother wave and $m_{3\pi}$, but only a weak dependence on t'. This is in accordance with the expectation that the production kinematics of X influence the dynamic isobar amplitudes only weakly. Finally, we combine the fit results for the parameters of each resonance in each wave and all $m_{3\pi}$ and t' bins in a Gaussian fit, to determine their central values and estimate their systematic uncertainties. We estimate the systematic uncertainties stemming from the simplicity of our model, which does not take into account rescattering or non-resonant effects, using the standard deviations of our fitted Gaussian distributions. These contributions to the uncertainties are rather high and could be drastically decreased, if we were able to understand the $m_{3\pi}$ dependence of the isobar parameters. To do this, models for the dynamic isobar amplitudes are necessary, that go beyond simple Breit-Wigner parameterizations. However, all our extracted isobar parameters agree within our estimates for the systematic uncertainties with the corresponding world averages given by the PDG in ref. [2].

8.3. Future prospects

Based on the results of this thesis further studies of dynamic isobar resonances become possible. The extracted dynamic isobar amplitudes allow to analyze the 2π dynamics with unprecedented detail and advanced models to describe the dynamic isobar amplitudes can easily be tested. This is impossible within the fixed-isobar approach, since free parameters in the dynamic isobar amplitudes are unfeasible, and there is no good criterion to judge the goodness of a fit. However, using the result of the freed-isobar analysis, simple χ^2 fits of the dynamic isobar amplitudes are possible. This way models describing the amplitudes in an advanced way can be applied and adjusted. This includes models for a unitary description of overlapping resonances, like the $\rho(770)$ and the ρ', models for the deformation of dynamic isobar amplitudes due to rescattering effects with the bachelor pion, and models for the shapes of dynamic isobar amplitudes from non-resonant contributions like the Deck effect. Resulting parameterizations can in turn be used in further analyses, for example the PWA of multi-particles decays, where they can improve the parameterizations of the decay amplitudes.

Going one step further, two- or three-dimensional fits of the extracted dynamic isobar amplitudes are possible, where not only the $m_{2\pi}$ dynamic of the process is modeled, but also the $m_{3\pi}$ and the t' dependence and their respective interplay. This helps to develop theoretical descriptions of the process, that do not only fulfill two-body unitarity, but also allow the inclusion of three-body unitarity.

To gain further understanding of the 3π channel, the freed-isobar method can also be combined with automated model selection algorithms, to determine proper wave sets for this channel, as well as for other channels, independent of a fixed parameterization of the dynamic isobar amplitudes. One automated model selection method is described in refs. [9, 13, 14], where a biggest conceivable model method with Cauchy priors is used to determine an appropriate wave set. Combining this approach with the freed-isobar method, using a prior on the total intensity of the freed-isobar waves, allows to select a wave set without specifying parameterizations for the dynamic isobar amplitudes.

The freed-isobar method is not limited to three-pion final states, but can be applied to any three-particle final state, for which a large enough data set exists. A first example for such a process could be the diffractive production of a $K^-\pi^+\pi^-$ final state. We have already shown that in this process, a freed-isobar approach would also suffer from zero modes that are not caused by Bose symmetrization, but by simultaneously freeing $[\pi\pi]_{0^{++}}$ and the $[K\pi]_{0^{++}}$ waves.

Besides diffractive processes, the freed-isobar method is applicable to all partial-wave analyses of three-particle final states, for example analyses of heavy meson decays recorded at B factories, like BELLE or LHCb. Depending on the channel, and physics goal, the freed-isobar method can be used to study a variety of quantities. Besides the more detailed study of appearing isobar resonances, the freed-isobar method can for example be used to identify excited D mesons in the Dalitz plot decays of B mesons and determine their J^{PC} quantum numbers. In addition, application of the freed-isobar method to B and D decays, and the CP conjugated processes, can help to exactly pin down the possible sources for CP violation resolved in the J^{PC} quantum numbers and invariant mass of the isobar.

Another possibility to use the freed-isobar approach is, to replace the dynamic isobar amplitudes by step-like functions not only in resonant partial waves, but also in non-resonant amplitudes in the model, like the Deck amplitude introduced in appendix B. This allows to study effects of non-resonant contributions in more detail and to develop a satisfying model for this kind of contribution to the process.

The application of the freed isobar method to final states with more than three particles is also an interesting possibility to be explored. Since for every additional final-state particle, an additional isobar appears in the decay amplitude, the extension of the freed-isobar method can be done in several different ways. The most general one is to free the dynamic amplitudes of all appearing isobars simultaneously, which results in a two-dimensional binning in the invariant isobar masses and therefore in an even larger number of free parameters. This approach is only applicable to very large data-sets. Another possibility is to only free a single isobar per wave, which does not give total freedom to the model, but still allows to study part of the dynamic isobar amplitudes. In such an approach, less known isobars, for example $(\pi\pi)_S$ waves, can be freed while better known isobars, like the $\rho(770)$, remain with fixed dynamic isobar amplitudes. The choice of the method depends on the analyzed channel, the size of the data set, and the over all goal of the analysis. These approaches can improve the partial-wave analyses of multi-particle final states, where the fixed-isobar approach did not yield convincing results so far.

In principle, the freed-isobar method can be used in any PWA, that is based on the isobar model, to validate, improve, or study the parameterization of the appearing dynamic isobar amplitudes, which were pure model assumptions up to now. Using the methods developed in this work, the freed-isobar approach is not limited to a single or very few waves, but can accommodate an arbitrary number of them. The sole requirement for this approach to be applicable is a large size of the data set, to obtain reasonably small statistical uncertainties. Since a number of recent experiments, like COMPASS, BELLE, LHCb, BES, and GlueX, have collected or will collect such large data sets, the freed-isobar method will be able to yield a valuable contribution to the improvement of PWA models and a detailed insight into the dynamics of various hadronic decay processes.

116

Appendix A.

Introduction to tensor formalisms

According to the Noether theorem, the conservation of angular momentum is related to the invariance of physical processes under rotations in space. Rotations in space can be described as elements of the special orthogonal group $\mathfrak{SO}(3)$, which is a subgroup of the Lorentz group. The corresponding transformations $\Lambda^\mu{}_\nu$ are given in the matrix representation as:

$$\Lambda^0{}_0 = 1; \quad \Lambda^0{}_i = \Lambda^i{}_0 = 0; \quad \Lambda^i{}_j = \mathbf{O}_{ij}, \tag{A.1}$$

where Greek indices are Lorentz indices, running from 0 to 3, with 0 representing the time component, and roman indices denote spatial indices, running from 1 to 3. $\mathbf{O}_{ij}$ is an element of the $\mathfrak{SO}(3)$ rotation group in the fundamental representation[a]. In this chapter, we indicate elements of the $\mathfrak{SO}(3)$ group by bold characters.

Since rotations do not commute with Lorentz boosts, the block diagonal form in eq. (A.1) relies on the choice of a reference system. To describe the angular momentum of particles, this is the rest frame of these particles.

Since, rotations are described by the $\mathfrak{SO}(3)$ subgroup of the Lorentz group, we have to study the structure of this group to learn about the transformation behavior of four-vectors and tensors under rotations. In the following chapter we give a short summary of these considerations, which can be found in more detail in refs. [19, 39–42].

A.1. The group structure of $\mathfrak{SO}(3)$

Since the rotation group $\mathfrak{SO}(3)$ is a Lie group, the most fundamental quantity to specify is the Lie algebra of its generators $\mathbf{K}_i$:

$$[\mathbf{K}_i, \mathbf{K}_j] = \epsilon_{ijk}\mathbf{K}_k, \tag{A.2}$$

where the square brackets denote the commutator, $\mathbf{K}_i$ are the generators of the $\mathfrak{SO}(3)$, and ϵ_{ijk} is the Levi-Civita total antisymmetric tensor:

$$\epsilon_{ijk} = -\epsilon_{jik} = -\epsilon_{kji} = -\epsilon_{ikj}; \quad \epsilon_{123} = 1. \tag{A.3}$$

---

[a]The fundamental representation of a Lie group is the representation, in which the generators carry the same kind of indices as the group elements.

Appendix A. Introduction to tensor formalisms

Note, that in this chapter we will use the Einstein sum convention also for spatial indices. To determine the irreducible representations of the $\mathfrak{SO}(3)$[b], it is convenient to introduce the Hermitian operators $\mathbf{J}_i = -i\mathbf{K}_i$. These have the commutation relations:

$$[\mathbf{J}_i, \mathbf{J}_j] = i\epsilon_{ijk}\mathbf{J}_k. \tag{A.4}$$

Combining the $\mathbf{J}_i$ into a vector $\vec{\mathbf{J}}$, rotations about an axis $\vec{n}$ by an angle φ can be written as:

$$\mathbf{O} = \left[\exp\left(i\varphi\vec{n}\cdot\vec{\mathbf{J}}\right)\right]. \tag{A.5}$$

The product $\vec{n}\cdot\vec{\mathbf{J}}$ is a linear combination of the three generators, and can be interpreted as the generator of a rotation around the chosen axis $\vec{n}$. If we multiply it by the angle φ and exponentiate it, we obtain the corresponding elements of the rotation group $\mathfrak{SO}(3)$.

We now want to look at the irreducible representations of $\mathfrak{SO}(3)$. To do this, we define the common ladder operators:

$$\mathbf{J}_\pm = \frac{1}{\sqrt{2}}\left(\mathbf{J}_x \pm i\mathbf{J}_y\right). \tag{A.6}$$

With these definitions and eq. (A.4), it is easy to see, that the ladder operators obey the following commutation relations:

$$[\mathbf{J}_z, \mathbf{J}_\pm] = \pm\mathbf{J}_\pm; \quad [\mathbf{J}_+, \mathbf{J}_-] = \mathbf{J}_z. \tag{A.7}$$

Additionally, we define the Casimir operator:

$$\mathbf{J}^2 = \mathbf{J}_x^2 + \mathbf{J}_y^2 + \mathbf{J}_z^2, \tag{A.8}$$

which commutes with all $\mathbf{J}_i$ and therefore also with $\mathbf{J}_\pm$.

Since we want to study the properties of irreducible representations of $\mathfrak{SO}(3)$, we need a way to label the objects that transform under this representation. We do this, by using the eigenbasis of $\mathbf{J}^2$ and $\mathbf{J}_z$ and label the object transforming under a specifit representation of the rotation group $|\iota, j_x\rangle$ with the corresponding eigenvalues:

$$\begin{aligned}\mathbf{J}^2|\iota, j_z\rangle &= \iota|\iota, j_z\rangle \\ \mathbf{J}_z|\iota, j_z\rangle &= j_z|\iota, j_z\rangle.\end{aligned} \tag{A.9}$$

We can do this, since the operators $\mathbf{J}^2$ and $\mathbf{J}_z$ commute[c]. Since we cannot find a third operator that commutes with the previous two, we cannot diagonalize further. However, the choice to diagonalize with respect to $\mathbf{J}_z$ and not one of the other components of the angular momentum operator is convention. We use this

---

[b]An irreducible representation is a representation, in which all degrees of freedom, that parameterize elements in this representation can mix under group transformations, while they do not mix with the elements of different irreducible representations.

[c] This works analogous to quantum mechanical considerations.

basis to determine the properties of the irreducible representations, especially the number of degrees of freedom, or dimension, of such a representation. This is the number of possible combinations of the eigenvalues ι and j_z. For the considerations made here, we will assume finite-dimensional representations, but one can show, that all representations of $\mathfrak{SO}(3)$ are finite dimensional [39].

Using the commutation relations in eq. (A.7), we can study, how the objects transforming under the $\mathfrak{SO}(3)$ relate to each other:

$$\mathbf{J}_z \mathbf{J}_\pm \left| \iota, j_z \right\rangle = \left(\mathbf{J}_\pm \mathbf{J}_z \pm \mathbf{J}_\pm \right) \left| \iota, j_z \right\rangle = \left(j_z \pm 1 \right) \mathbf{J}_\pm \left| \iota, j_z \right\rangle. \tag{A.10}$$

The ladder operators transform an eigenstate of $\mathbf{J}_z$ with eigenvalue j_z into another eigenstate, with an eigenvalue of $j_z \pm 1$. Since $\mathbf{J}^2$ commutes with the ladder operators, the transformed state is still an eigenstate of $\mathbf{J}^2$ with the same eigenvalue.

Since we assumed a finite dimensional representation, there has to be a maximum and a minimum value for j_z. This can be achieved, by requiring:

$$\mathbf{J}_+ \left| \iota, j_z^{\mathrm{max}} \right\rangle = 0; \quad \mathbf{J}_- \left| \iota, j_z^{\mathrm{min}} \right\rangle = 0. \tag{A.11}$$

If we use the identity:

$$\mathbf{J}_\pm \mathbf{J}_\mp = \mathbf{J}^2 - \mathbf{J}_z^2 \pm \mathbf{J}_z, \tag{A.12}$$

and apply $\mathbf{J}_\pm$ to eq. (A.11), we find:

$$\begin{aligned} \mathbf{J}_- \mathbf{J}_+ \left| \iota, j_z^{\mathrm{max}} \right\rangle = & \left(\iota - j_z^{\mathrm{max}} \left(j_z^{\mathrm{max}} + 1 \right) \right) \left| \iota, j_z^{\mathrm{max}} \right\rangle = 0 \\ \mathbf{J}_+ \mathbf{J}_- \left| \iota, j_z^{\mathrm{min}} \right\rangle = & \left(\iota - j_z^{\mathrm{min}} \left(j_z^{\mathrm{min}} - 1 \right) \right) \left| \iota, j_z^{\mathrm{min}} \right\rangle = 0. \end{aligned} \tag{A.13}$$

From these conditions, we find:

$$\begin{aligned} \iota - j_z^{\mathrm{max}} \left(j_z^{\mathrm{max}} + 1 \right) &= 0, \\ \iota - j_z^{\mathrm{min}} \left(j_z^{\mathrm{min}} - 1 \right) &= 0, \\ j_z^{\mathrm{max}} \left(j_z^{\mathrm{max}} + 1 \right) &= j_z^{\mathrm{min}} \left(j_z^{\mathrm{min}} - 1 \right). \end{aligned} \tag{A.14}$$

The two solutions to this equation are:

$$j_z^{\mathrm{max}} = j_z^{\mathrm{min}} - 1 \tag{A.15}$$

$$j_z^{\mathrm{max}} = -j_z^{\mathrm{min}}. \tag{A.16}$$

The solution in eq. (A.15) is contradictory, since the maximum value is smaller than the minimum value, so the solution of eq. (A.16) is the correct one. The requirement for an integer distance between the eigenvalues j_z in eq. (A.10) and the relation in eq. (A.16) can only be achieved, if:

$$j_z^{\mathrm{max}} = \frac{n}{2}, \tag{A.17}$$

for some integer n. Inserting this into eq. (A.14), we find:

$$\iota = j_z^{\mathrm{max}} \left(j_z^{\mathrm{max}} + 1 \right) = j_z^{\mathrm{min}} \left(j_z^{\mathrm{min}} - 1 \right) = j \left(j + 1 \right). \tag{A.18}$$

Appendix A. Introduction to tensor formalisms

We have shown, that a linear combination of the operators $\mathbf{J}_x$ and $\mathbf{J}_z$ can transform an eigenstate $|\iota, j_z\rangle$ into a state with any allowed value for j_z, while no such transformation is able to change ι. Therefore, we have identified irreducible representations, which we label with j. Counting the number of allowed values for j_z for a given j, we find that a representation has $2j + 1$ degrees of freedom. We can identify j with the total angular momentum of a system.

A.2. Representation of particles with spin by tensor objects

With this knowledge about the representations of the underlying $\mathfrak{SO}\,(3)$, we want to construct tensors, that represent objects of a certain spin. Note, that we restrict this discussion to objects with integer spin. For an object with zero spin, the representation is trivial, since here we can use a scalar which has one degree of freedom.

For a spin-one object, the representation becomes already non-trivial. A first guess would be a four-vector A_1^μ, but its four degrees of freedom do not match the required number of three. While the four-vector is an irreducible representation of the full Lorentz group, it turns out to be reducible in the $\mathfrak{SO}\,(3)$ subgroup that describes spatial rotations, as can be seen from eq. (A.1), since the corresponding transformations for a vector Λ^μ_{ν} take block diagonal form. Thus, a spin-one object is represented only by the spatial components of a four-vector, which now has the right number of degrees of freedom, while the time component describes a scalar. We write this as:

$$A_1^\mu = \mathbf{0} \oplus \mathbf{1}, \tag{A.19}$$

where representations of a certain spin are represented by bold numbers. The lower index indicates the rank of the tensor.

For a spin two quantity, our first guess is to add a second Lorentz index to the object to get a rank-two tensor. However, the sixteen degrees of freedom of the most general tensor largely exceed the five degrees of freedom of a spin-two representation. In terms of representations, we can write:

$$T_2^{\mu\nu} = (\mathbf{0} \oplus \mathbf{1}) \otimes (\mathbf{0} \oplus \mathbf{1}) = \mathbf{0} \oplus \mathbf{1} \oplus \mathbf{1} \oplus (\mathbf{0} \oplus \mathbf{1} \oplus \mathbf{2}), \tag{A.20}$$

where we have made use of [39]:

$$\mathbf{n} \otimes \mathbf{m} = |\mathbf{m} - \mathbf{n}| \oplus \ldots \oplus (\mathbf{m} + \mathbf{n}). \tag{A.21}$$

From eq. (A.20), we can already see, that the spin-two quantity will be described by the $\mathbf{2}$ representation, but we still have to identify, which parts of the tensor transform under this representation. To do so, it is useful, to split the general tensor $T_2^{\mu\nu}$ in a symmetric part $S_2^{\mu\nu}$ and an antisymmetric part $A_2^{\mu\nu}$ with respect to the exchange of the two Lorentz indices:

$$S_2^{\mu\nu} = \frac{1}{2}\left(T_2^{\mu\nu} + T_2^{\nu\mu}\right); \quad A_2^{\mu\nu} = \frac{1}{2}\left(T_2^{\mu\nu} - T_2^{\nu\mu}\right). \tag{A.22}$$

It is easy, to show, that $S_2^{\mu\nu}$ and $A_2^{\mu\nu}$ do not mix under Lorentz transformations:

$$
\begin{aligned}
S_2'^{\mu\nu} &= \Lambda^\mu{}_{\mu'}\Lambda^\nu{}_{\nu'}S_2^{\mu'\nu'} = \Lambda^\nu{}_{\nu'}\Lambda^\mu{}_{\mu'}S_2^{\nu'\mu'} = S_2'^{\nu\mu}, \\
A_2'^{\mu\nu} &= \Lambda^\mu{}_{\mu'}\Lambda^\nu{}_{\nu'}A_2^{\mu'\nu'} = -\Lambda^\nu{}_{\nu'}\Lambda^\mu{}_{\mu'}A_2^{\nu'\mu'} = -A_2'^{\nu\mu},
\end{aligned}
\tag{A.23}
$$

and therefore, we already have reduced the representation of the rank-two tensors. However, since the numbers of degrees of freedom of ten for $S_2^{\mu\nu}$ and six for $A_2^{\mu\nu}$ do not match any of the irreducible representations of the $\mathfrak{SO}\,(3)$, we have to reduce them further.

To do this, we look at the antisymmetric part $A_2^{\mu\nu}$ and see, that the quantity A_2^{0i} transforms as a three-vector under $\mathfrak{SO}\,(3)$, since time components transform trivially under transformations given in eq. (A.1); the elements A_2^{i0} are then fixed by antisymmetry. We label this representation $\mathbf{1}_A$. A second quantity, that transforms as a three-vector is:

$$
\epsilon_{ijk}A_2^{jk}.
\tag{A.24}
$$

This can be seen, if we compare eq. (A.24) with the known cross-product of two vectors $\vec{v}$ and $\vec{w}$:

$$
(\vec{v}\times\vec{w})_i = \epsilon_{ijk}v_j w_k,
\tag{A.25}
$$

which also transforms as a three-vector under $\mathfrak{SO}\,(3)^{[d]}$. We label this second three-vector in $A_2^{\mu\nu}$ as $\mathbf{1}_A'$. We have identified two quantities within the antisymmetric tensor, that transform as three-vectors and are therefore irreducible representations of $\mathfrak{SO}\,(3)$.

If we look at the symmetric part $S_2^{\mu\nu}$ of the tensor, we immediately find, that the component S_2^{00} is not affected by transformations of the type defined in eq. (A.1) and therefore represents a scalar, which we label $\mathbf{0}_S$. A second quantity that transforms as a scalar can be identified as the trace of the symmetric spatial tensor, since:

$$
S_2'^{ii} = \mathbf{O}^{ij}\mathbf{O}^{ki}S_2^{jk} = S_2^{ii},
\tag{A.26}
$$

where we have used, that the elements of $\mathfrak{SO}\,(3)$ are orthogonal: $\mathbf{OO}^T = \mathbb{1}$. We label the scalar corresponding to the trace as $\mathbf{0}_S'$. Therefore, we have identified two scalar quantities in the symmetric tensor. There are no corresponding quantities in $A_2^{\mu\nu}$, since all its diagonal elements are zero. Similar to the antisymmetric case, we can identify an additional vector representation as S_2^{0i}, which we label $\mathbf{1}_S$. A second vector, analogue to the one defined in eq. (A.25), is not present here, since it vanishes due to the symmetry of $S_2^{\mu\nu}$.

Taking all this together, we have identified two scalar and three vector representations in $T_2^{\mu\nu}$. If we compare this to eq. (A.20), we find, that the remaining five degrees of freedom have to belong to the spin-two representation, which we label as $\mathbf{2}_S$. This can be identified to be a symmetric, traceless rank-two tensor with only spatial components, since the trace transforms as spin-zero object, as shown

---

[d]Strictly speaking, it transforms as a pseudo-vector, which does not matter in our case, since all elements of $\mathfrak{SO}\,(3)$ conserve parity (in contrast to $\mathfrak{O}\,(3)$).

in eq. (A.26). The number of degrees of freedom of such an object—five—matches the number required for a spin-two object. Putting this together, we can parameterize an arbitrary tensor $T_2^{\mu\nu}$ explicitly with degrees of freedom of the single representations:

$$
T_2^{\mu\nu} = \begin{pmatrix}
\mathbf{0}_S & \mathbf{1}_S^1 + \mathbf{1}_A^1 & \mathbf{1}_S^2 + \mathbf{1}_A^2 & \mathbf{1}_S^3 + \mathbf{1}_A^3 \\
\mathbf{1}_S^1 - \mathbf{1}_A^1 & \mathbf{2}_S^{11} & \mathbf{2}_S^{12} + \mathbf{1}_A'^{12} & \mathbf{2}_S^{13} + \mathbf{1}_A'^{13} \\
\mathbf{1}_S^2 - \mathbf{1}_A^2 & \mathbf{2}_S^{12} - \mathbf{1}_A'^{12} & \mathbf{2}_S^{22} & \mathbf{2}_S^{23} + \mathbf{1}_A'^{23} \\
\mathbf{1}_S^3 - \mathbf{1}_A^3 & \mathbf{2}_S^{13} - \mathbf{1}_A'^{13} & \mathbf{2}_S^{23} - \mathbf{1}_A'^{23} & \mathbf{0}_S' - \mathbf{2}_S^{11} - \mathbf{2}_S^{22}
\end{pmatrix}.
\tag{A.27}
$$

Note, that for simplicity, we label the components of the $\mathbf{1}_A'$ representation with two indices, even though it transforms as a three-vector. The connection to the parameterization of a vector is shown in eq. (A.24). If we count the number of independent elements in eq. (A.27), we recover the 16 degrees of freedom of an arbitrary rank-two tensor[e].

To generalize this to objects of arbitrary spin, we use complete induction. With the explicit example of the spin-two tensor, we already have a starting point. To make an induction step, we assume, that an object of spin j, that transforms under the $\mathbf{j}$ representation, is described by a symmetric, traceless, spatial tensor of rank j:

$$
\tilde{T}_j^{\mu_1\dots\mu_j}.
\tag{A.28}
$$

Since this tensor is fully symmetric, an exchange of any two indices does not change the object; since it is traceless, the contraction of any two indices gives a tensor of rank $j - 2$, of which every component is zero; and since it is spatial, every component, where any of the indices is zero vanishes.

For spin $j + 1$, we again add another Lorentz index, and use eq. (A.21) to determine, which representations this new object will consist of:

$$
\mathbf{j} \otimes (\mathbf{0} \oplus \mathbf{1}) = \mathbf{j} \oplus \left[(\mathbf{j} - \mathbf{1}) \oplus \mathbf{j} \oplus (\mathbf{j} + \mathbf{1}) \right].
\tag{A.29}
$$

To identify the individual representations, we denote the resulting rank-$(j + 1)$ tensor by:

$$
T_{j+1}^{\mu_1\dots\mu_j,\nu},
\tag{A.30}
$$

where the indices μ_i are the indices corresponding to the symmetric, traceless, spatial rank-j tensor of the $\mathbf{j}$ representation, and the index ν corresponds to the index of the additional $(\mathbf{0} \oplus \mathbf{1})$ representation. $T_{j+1}^{\mu_1\dots\mu_j,\nu}$ therefore consist of four symmetric, traceless, spatial rank-j tensors, which are labeled with the additional index ν. However, these four tensors do not have to be identical.

With this definition, we can see, that the first $\mathbf{j}$ representation in eq. (A.29) corresponds to the quantity $T_{j+1}^{\mu_1\dots\mu_j,0}$ and the $(\mathbf{j} - \mathbf{1})$ representation corresponds to the trace:

$$
T_{j+1}^{\mu_1\dots\mu_j,\nu} g_{\mu_j\nu}.
\tag{A.31}
$$

---

[e]The choice, which diagonal element of the $\mathbf{2}_S$ representation is not present, due to the requirement of tracelessness, is left to convention.

Since the **j** representation is symmetric, it does not matter, which μ_i we contract with ν and since it is traceless, all contractions of two indices μ_n and μ_m vanish by definition. We now construct a traceless, spatial tensor $\tilde{T}_{j+1}^{\mu_1\dots\mu_j,\nu}$, where the two representations we have already identified are removed. According to eq. (A.29), this tensor has to be reducible in a **j** and a $(\mathbf{j+1})$ representation, since the other two representations in eq. (A.29) have been already identified and removed. We can then split $\tilde{T}_{j+1}^{\mu_1\dots\mu_j,\nu}$ in a symmetric and an antisymmetric part:

$$
\begin{aligned}
\tilde{S}_{j+1}^{\mu_1\dots\mu_j,\nu} &= \frac{1}{2j}\sum_{i=1}^{j}\left(\tilde{T}_{j+1}^{\mu_1\dots\mu_i\dots\mu_j,\nu} + \tilde{T}_{j+1}^{\mu_1\dots\nu\dots\mu_j,\mu_i}\right) \\
\tilde{A}_{j+1}^{\mu_1\dots\mu_j,\nu} &= \frac{1}{2j}\sum_{i=1}^{j}\left(\tilde{T}_{j+1}^{\mu_1\dots\mu_i\dots\mu_j,\nu} - \tilde{T}_{j+1}^{\mu_1\dots\nu\dots\mu_j,\mu_i}\right).
\end{aligned}
\tag{A.32}
$$

The symmetric tensor is symmetric in all indices, including ν, and the antisymmetric tensor is symmetric in the first j indices and antisymmetric under an exchange of the last index ν with any of the other. Analogue to eq. (A.23) we see that both tensors do not mix under $\mathfrak{SO}(3)$ and are therefore reduce the $\mathfrak{SO}(3)$ representation. If we count the degrees of freedom of the symmetric tensor, which is by definition spatial and traceless, since $\tilde{T}_{j+1}^{\mu_1\dots\mu_j,\nu}$ is spatial and traceless, we find that it has $2(j+1)+1$ degrees of freedom[f] and we can identify it with the $(\mathbf{j+1})$ representation. This concludes our induction step and we have shown, that we can describe an object of arbitrary integer spin j with a symmetric, traceless, spatial tensor of rank j, since it transforms under the correct representation of $\mathfrak{SO}(3)$.

A.3. Construction of spin amplitudes

We now want to construct the corresponding tensor structures for a particle X decaying into two particles, a and b, with relative orbital angular momentum L. In the previous chapter, we have seen, that this is achieved by constructing a symmetric, traceless, spatial tensor of rank L. The spins of all particles involved are arbitrary, since we only have to construct the spatial wave functions, only taking into account orbital angular momenta.

Since the resulting tensors have Lorentz indices, they must be constructed out of four-vectors. The only two four-vectors we have available, are the two four-momenta of the daughter particles p_a^μ and p_b^μ. Since in the previous chapter, we discussed everything in the rest frame of X, the two four-momenta must satisfy:

$$
P_X^\mu = \begin{pmatrix} m_X \\ 0 \\ 0 \\ 0 \end{pmatrix} = p_a^\mu + p_b^\mu,
\tag{A.33}
$$

---

[f] A symmetric spatial tensor of rank n has $\frac{n^2}{2}+\frac{3n}{2}+1$ degrees of freedom and the tracelessness imposes $\frac{n^2-n}{2}$ additional conditions.

where P_X^μ is the four-momentum of the decaying particle. To get a spatial tensor, we must project out the spatial component of all Lorentz structures. This is done by a diagonal projection operator $g_\perp^{\mu\nu}$ with:

$$g_\perp^{00} = 0; \quad g_\perp^{ii} = 1, \tag{A.34}$$

in the rest frame of the decaying particle. Since we want to construct a fully covariant formalism, we compose this projection operator of covariant objects. We find, that eq. (A.34) is fulfilled by:

$$g_\perp^{\mu\nu} = g^{\mu\nu} - \frac{P_X^\mu P_X^\nu}{m_X^2}. \tag{A.35}$$

This operator fulfills the requirement in the rest frame of the decaying particle, but can be used in any reference system with the formulation in eq. (A.35). The following relation is always fulfilled:

$$g_{\perp\nu}^\mu P^\mu = 0. \tag{A.36}$$

If we define:

$$K^\mu = \frac{1}{2} \left(p_a^\mu - p_b^\mu \right), \tag{A.37}$$

we can rewrite:

$$p_a^\mu = P_X^\mu + 2K^\mu; \quad p_b^\mu = P_X^\mu - 2K^\mu, \tag{A.38}$$

and find, that due to eq. (A.36), the only purely spatial four-vector available is $K_\perp^\mu$:

$$\begin{aligned} g_{\perp\nu}^\mu p_a^\nu &= 2g_{\perp\nu}^\mu K^\nu \equiv 2K_\perp^\nu \\ g_{\perp\nu}^\mu p_b^\nu &= - 2g_{\perp\nu}^\mu K^\nu \equiv -2K_\perp^\nu. \end{aligned} \tag{A.39}$$

This makes sense, since a and b are produced "back-to-back" in the rest-frame of X, and are therefore described by a single linear independent three-vector, due to momentum conservation. We now can easily write the tensor structures for decays with $L = 0$ and $L = 1$:

$$X_0 = 1; \quad X_1^\mu = K_\perp^\mu. \tag{A.40}$$

The spin-zero case is trivial and for the spin-one case, we can easily check, that $K_\perp^\mu$ fulfills all requirements for the tensor.

For the spin-two case, the simplest guess is, to use $K_\perp^\mu K_\perp^\nu$, which is symmetric and spatial, but not traceless. To fulfill all requirements, the correct tensor structure is:

$$X_2^{\mu\nu} = \frac{3}{2} K_\perp^\mu K_\perp^\nu - \frac{1}{2} g_\perp^{\mu\nu} K_\perp^\rho K_{\perp\rho}, \tag{A.41}$$

which can be shown to be symmetric, spatial, and traceless, since $g_{\perp\mu}^\mu = 3$.

For a general tensor of rank L, we can formulate the following recursion relation taken from ref. [19]:

$$
X_L^{\mu_1\cdots\mu_L} = \frac{1}{L^2}\left[(2L-1)\sum_{n=1}^{L} K_\perp^{\mu_n} X_{L-1}^{\mu_1\cdots\not\mu_n\cdots\mu_L} \right.
$$
$$
\left. -2K_\perp^\rho K_{\perp\rho} \sum_{n=1}^{L}\sum_{m=1}^{n-1} g_\perp^{\mu_n\mu_m} X_{L-2}^{\mu_1\cdots\not\mu_n\cdots\not\mu_m\cdots\mu_L} \right],
$$

(A.42)

since the appearing sums run over all L indices, the crossed out indices on the tensors indicate, which index is left out of the full list from 1 to L. These indices are then added externally via $K_\perp^\mu$ or $g_\perp^{\mu\nu}$.

With these prerequisites, we now want to describe the decay of an initial-state particle with spin J into an isobar ξ with spin j and a pseudo-scalar particle c, in a relative orbital angular momentum L. The isobar subsequently decays into two pseudo-scalars, a and b. In this process two decays with given orbital angular momentum appear, so we can formulate the corresponding tensors according to eq. (A.42). The decay of X into ξ and c can be described by $X_L^{\mu_1\cdots\mu_L}$ and the decay of the isobar can be described $X_j^{\mu_1\cdots\mu_j}$, since a and b are pseudoscalar particles, the spin j of ξ must be identical to the relative orbital angular momentum of a and b.

Note, that these two tensor structures were initially defined in different rest frames. However, since the whole formalism is fully covariant, this does not pose any problem. The condition that tensors must only have spatial components then translates into the condition of the tensors being transversal to the four-momentum P^μ of a moving decaying particle:

$$
X_n^{\mu_1\cdots\mu_i\cdots\mu_n} P_{\mu_i} = 0 \;\forall\; i \in [1,n].
$$

(A.43)

We now want to construct a tensor $T_J^{\mu_1\cdots\mu_J}$ of rank J to describe the decaying particle X out of the two tensors $X_L^{\mu_1\cdots\mu_L}$ and $X_j^{\mu_1\cdots\mu_j}$. From the basic rules of the coupling of angular momenta we know, that the appearing angular momenta must fulfill:

$$
|L-j| \le J \le L+j.
$$

(A.44)

Starting at the maximum value $J = L+j$, the only way to construct a tensor of the appropriate rank is [19]:

$$
R_J^{\mu_1\cdots\mu_J} = X_L^{\mu_1\cdots\mu_L} X_j^{\mu_{L+1}\cdots\mu_{L+j}}.
$$

(A.45)

For tensors of lower rank, we can contract k pairs of indices to obtain a tensor of rank $J = L+j-2k$ [19]:

$$
R_J^{\mu_1\cdots\mu_J} = X_L^{\nu_1\cdots\nu_k\mu_1\cdots\mu_l} X_{j\nu_1\cdots\nu_k}^{\mu_{l+1}\cdots\mu_J},
$$

(A.46)

where $l = L-k$ is chosen such, that the numbers of indices match. Since the tensors are symmetric, it does not matter, which indices we contract. However,

since the tensors are traceless, contractions of two indices on the same tensor are zero. With this formula, we only can describe particles with spin J that differs by a multiple of two from the maximum value $L + j$ down to $|L - j|$. For lower spins, contractions of two indices on the same tensor become necessary and the resulting tensor would therefore vanish. For states with $J = L + j - 2k - 1$, we use the following formula [19]:

$$R_J^{\mu_1 \dots \mu_J} = \epsilon_{\rho\sigma\tau}^{\mu_1} P^\rho X_L^{\nu_1 \dots \nu_k \sigma \mu_2 \dots \mu_l} X_{j\nu_1 \dots \nu_k}^{\tau \mu_{l+1} \dots \mu_J}. \tag{A.47}$$

The expressions in eqs. (A.45) to (A.47) are only valid, if at least one of the particles involved in the decay, ξ or c, is spinless. If both carry spin, the tensors for ξ and c are coupled to a tensor describing the total spin first, which then is be coupled with $X_L^{\mu_1 \dots \mu_L}$ to form $R_J^{\mu_1 \dots \mu_J}$.

We can easily see, that the resulting tensors $R_J^{\mu_1 \dots \mu_J}$ do not yet fulfill the requirements for a **J** representation, since they are obviously not symmetric and traceless. Therefore, we have to project the resulting tensor:

$$X_J^{\mu_1 \dots \mu_J} = O_{\nu_1 \dots \nu_J}^{\mu_1 \dots \mu_J} R_J^{\nu_1 \dots \nu_J}, \tag{A.48}$$

with an operator $O_{\nu_1 \dots \nu_J}^{\mu_1 \dots \mu_J}$, that fulfills the defining condition of a projection operator:

$$O_{\rho_1 \dots \rho_J}^{\mu_1 \dots \mu_J} = O_{\nu_1 \dots \nu_J}^{\mu_1 \dots \mu_J} O_{\rho_1 \dots \rho_J}^{\nu_1 \dots \nu_J}, \tag{A.49}$$

and is symmetric and traceless in its upper and lower indices. The projector for spin one is given by:

$$O^\mu_{\ \nu} = g^\mu_{\perp \nu}, \tag{A.50}$$

and the projector for spin J is constructed as:

$$O_{\nu_1 \dots \nu_J}^{\mu_1 \dots \mu_J} = \left(\frac{1}{J!} \right)^2 \sum_{P(\mu_i)} \sum_{P(\nu_i)} \hat{O}_{P(\nu_i)}^{P(\mu_i)}, \tag{A.51}$$

where the sum runs over all possible permutations $P(\mu_i)$ of the respective indices. The unsymmetrized $\hat{O}_{\nu_1 \dots \nu_J}^{\mu_1 \dots \mu_J}$ projectors are constructed from the spin-one projector in eq. (A.50) [40]:

$$\hat{O}_{\nu_1 \dots \nu_J}^{\mu_1 \dots \mu_J} = \prod_{i=1}^J O_{\nu_i}^{\mu_i} + a_1 \, O_{\nu_1 \nu_2} O^{\mu_1 \mu_2} \prod_{i=3}^J O_{\nu_i}^{\mu_i} + \dots$$

$$\dots + \begin{cases} a_{J/2} \, O_{\nu_1 \nu_2} O^{\mu_1 \mu_2} \dots O_{\nu_{J-1} \nu_J} O^{\mu_{J-1} \mu_J} & \text{if J even,} \\[2mm] a_{(J-1)/2} \, O_{\nu_1 \nu_2} O^{\mu_1 \mu_2} \dots O_{\nu_{J-2} \nu_{J-1}} O^{\mu_{J-2} \mu_{J-1}} O_{\nu_J}^{\mu_J} & \text{if J odd.} \end{cases} \tag{A.52}$$

The coefficients a_i are:

$$a_i = \left(-\frac{1}{2} \right)^i \frac{J!}{i! \, (J - 2i)!} \frac{1}{(2J - 1)(2J - 3) \dots (2J - 2i + 1)}. \tag{A.53}$$

With this, we can calculate the rank-J tensor, as defined in eq. (A.48), which has $2J+1$ degrees of freedom. If we want to obtain the spin amplitude $\Psi_J^{J_z}\left(p_a^\mu, p_b^\mu, p_c^\mu\right)$ for certain values of J_z, we have to contract this tensor with the appropriate polarization tensor $\Phi_{\mu_1\ldots\mu_J}^{J,J_z}$:

$$\Psi_J^{J_z}\left(p_a^\mu, p_b^\mu, p_c^\mu\right) = \Phi_{\mu_1\ldots\mu_J}^{J,J_z} X_J^{\mu_1\ldots\mu_J}\left(p_a^\mu, p_b^\mu, p_c^\mu\right). \tag{A.54}$$

The polarization vectors for a spin one object in its rest frame are:

$$\Phi_\mu^{1,-1} = \frac{1}{\sqrt{2}}\begin{pmatrix} 0 \\ -1 \\ i \\ 0 \end{pmatrix}; \quad \Phi_\mu^{1,0} = \begin{pmatrix} 0 \\ 0 \\ 0 \\ 1 \end{pmatrix}; \quad \Phi_\mu^{1,+1} = \frac{1}{\sqrt{2}}\begin{pmatrix} 0 \\ 1 \\ i \\ 0 \end{pmatrix}. \tag{A.55}$$

The polarization tensors in the rest frame of X for objects with higher spin J and spin projection J_z can be constructed recursively using the appropriate Clebsch-Gordan coefficients [41]:

$$\Phi_{\mu_1\ldots\mu_J}^{J,J_z} = \sum_{M=-(J-1)}^{J-1} \sum_{n=-1}^{1} \left(J-1, M, 1, n | J, J_z\right) \Phi_{\mu_1\ldots\mu_{J-1}}^{J-1,M} \Phi_{\mu_J}^{1,n}. \tag{A.56}$$

With these definitions, we can formulate all required amplitudes for our analysis in the covariant tensor formalism. If in a different process, one of the final state particles has non-zero spin, the corresponding tensor $X_j^{\mu_1\ldots\mu_j}$ is replaced by the appropriate spin wave function of eq. (A.56).

A.4. The non-relativistic tensor formalism

A related formalism is the non-relativistic tensor formalism [20, 21]. Here, the tensors for objects with spin J are constructed again as symmetric, traceless, spatial tensors of rank J. This is always done in the rest frame of the decaying particle. In contrast to the covariant tensor formalism, the tensors are not constructed in a way, that the condition to be spatial in the rest frame of the object translates in being transversal to the total four-momentum of the decaying particle. They are constructed each in its own rest-frame as tensors of dimension three. The contraction and projection of the tensors, are done as for example in eq. (A.46) and in eq. (A.54). However, in the rest frame of the decaying particle, the tensors in the non-relativistic formalism are identical to the spacial components of the tenors in the covariant formalism.

This alternative tensor formalism can be viewed as a non-relativistic version of the covariant tensor formalism. It has been checked numerically to be equivalent to the helicity formalism by D. Ryabchikov, discussed in section 4.1.3. The helicity formalism in turn has been shown in ref. [42] to differ only by factors of the Lorentz factor $\gamma = E/m_0$ from the covariant amplitudes; E is the energy of the decaying particle and m_0 its rest mass.

128

Appendix B.

The Deck effect

For the process $\pi^- p \to \pi^- \pi^+ \pi^- p$ introduced in section 2.1, we assumed that resonant production of the three-pion final state shown in fig. B.1 (left), is the dominant process. However, 3π production may also occur without any intermediary three-pion resonance. An example for such a process is the so-called Deck effect schematically depicted in the right diagram of fig. B.1 [43].

An amplitude describing the Deck process is not orthogonal to resonant partial-wave amplitudes, i.e. the off-diagonal elements of the phase-space integral matrix as given in eq. (3.13) do not vanish. Therefore, Deck-like effects may leak into partial waves. A model for the Deck effect based on ACCMOR [44] was studied by F. Haas in ref. [8], by generating Monte Carlo data according to the model and analyzing these data with the 88-wave fixed-isobar model. In this fixed-isobar PWA of Monte Carlo data, the intensity distributions of many of the 88 waves in the model, predominantly those with high spin of X, turned out to be similar to those from the fixed-isobar PWA on real data.

Following ref. [44], the Deck amplitude without Bose-symmetrization was modeled as the product of two vertex amplitudes and a pion propagator:

$$\hat{\mathcal{A}}_{\mathrm{Deck}}\left(\vec{\tau}\right) = \mathcal{N}_{\mathrm{Deck}}\hat{\mathcal{A}}_{\pi\pi}\left(s_{\pi_1\pi_2}\right)\hat{\mathcal{A}}_{\pi p}\left(s_{\pi_3 p}, t\right)\frac{\exp\left[-b_2\left(m_\pi^2 - t_\pi\right)\right]}{m_\pi^2 - t_\pi}, \qquad (\mathrm{B.1})$$

where π_1^- and π_2^+ form the intermediary 2π resonance.
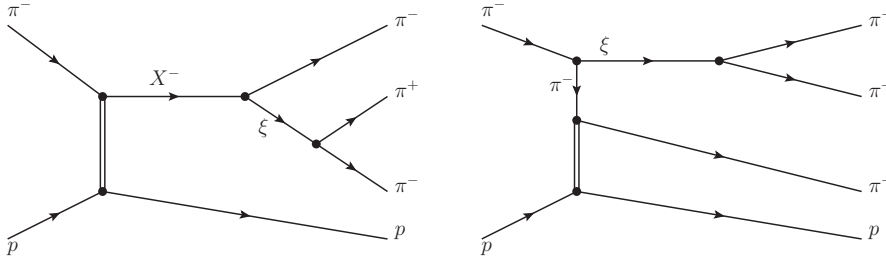
Figure B.1.: Resonant 3π production (left) and Deck effect (right).

Appendix B. The Deck effect

The kinematic variables are:

$$s_{\pi_1 \pi_2} = \left(p_{\pi_1}^\mu + p_{\pi_2}^\mu\right)^2, \quad s_{\pi_3 p} = \left(p_{\pi_3}^\mu + p_{p_{\text{recoil}}}^\mu\right)^2, \quad t_\pi = \left(p_{\pi_1}^\mu + p_{\pi_2}^\mu - p_{p_{\text{recoil}}}^\mu\right)^2,$$

(B.2)

and t as defined in section 2.1. The $\pi\pi$ vertex amplitude $\hat{\mathcal{A}}_{\pi\pi}\left(s_{\pi_1 \pi_2}\right)$ was taken from ref. [45] and the πp vertex amplitude was modeled as:

$$\hat{\mathcal{A}}_{\pi p}\left(s_{\pi p}, t\right) = s_{\pi p} \exp\left(-b_1 t\right).$$

(B.3)

The normalization factor $\mathcal{N}_{\text{Deck}}$ is given by the normalization condition in eq. (3.14). The two "slope parameters" are $b_1 = 8 \left(\text{GeV}/c\right)^{-2}$ and $b_2 = 0.45 \left(\text{GeV}/c\right)^{-2}$.

Inspired by the Deck study of ref. [8], we performed a study, in which the Deck amplitude, parameterized as in eq. (B.1), was used as an additional coherent partial wave, added to the 88-wave model listed in table 6.1. With this model, we performed a fixed-isobar PWA analogous to the analysis in ref. [8], with 100 $m_{3\pi}$ bins and 11 non-equidistant t' bins. If the model for the Deck amplitude was able to describe all non-resonant contributions, the results are expected to fulfill the following criteria:

1. the intensity distribution for the Deck amplitude matches the theoretical prediction,

2. the results for partial waves that are dominated by pure resonances, like the $2^{++}1^+ \rho(770)\,\pi\text{D}$ wave, do not change,

3. resonant peaks, that move with t' due to interference with non-resonant contributions like the $a_1(1260)$ in the $1^{++}0^+ \rho(770)\,\pi\text{S}$ wave, stop moving, and

4. the intensities for waves with high spins and without resonances, like $4^{-+}0^+ \rho(770)\,\pi\text{F}$ and $6^{-+}0^+ \rho(770)\,\pi\text{H}$, vanish.

Some results for the first study of this kind are shown in fig. B.2. On the upper left plot we see the comparison of the intensity distribution of the Deck partial wave with its theoretical prediction. The gross trend matches, but both shapes do not agree on a quantitative level. Event though criterion 1 is therefore not fulfilled on a quantitative level, this nevertheless indicates, that Deck-like non-resonant effects play a role in diffractive 3π production. The right plot in the middle row of fig. B.2 shows the comparison of the intensity distribution of the $2^{++}1^+ \rho(770)\,\pi\text{D}$ wave with and without the Deck amplitude in the model. Here we see a good qualitative agreement, therefore criterion 2 is fulfilled in this wave. For the $1^{++}0^+ \rho(770)\,\pi\text{S}$ wave, shown in the middle left of fig. B.2, we do not find such an agreement, since the intensity in the $a_1(1260)$ peak region strongly decreases. The Deck study in ref. [8] already found a significant contribution of the Deck amplitude in this wave. In the upper right plot of fig. B.2, the intensity distributions, obtained with the 88 waves + Deck model, for this wave are shown for lowest and highest t' bin. Since

the peak position still moves significantly, the Deck amplitude does not suffice to describe all non-resonant contributions and criterion 3 is not fulfilled. The lower row of fig. B.2 shows the intensity distributions for the two high spin waves $4^{-+}0^+\rho(770)\,\pi F$ and the $6^{-+}0^+\rho(770)\,\pi H$. For both waves, we see a significant drop of intensity for both waves and therefore criterion 4 is fulfilled by the Deck amplitude, also indicating that the intensities of these two waves are mostly caused by non-resonant effects.

While the overall findings of including a coherent Deck amplitude in the PWA model look promising, it is also evident that the Deck amplitude given in eq. (B.1) does not fulfill all criteria for a convincing description of non-resonant contributions. We performed several similar studies with severely modified Deck amplitudes, for example using a different parameterization for the pion propagator, or separating the different intermediate 2π resonances that appear combined in $\hat{\mathcal{A}}_{\pi\pi}\left(s_{\pi_1\pi_2}\right)$ of ref. [45]. The latter results in several different Deck amplitudes describing for example only the contribution of the $\rho(770)$ or the $f_2(1270)$ resonance. Since none of the studied parameterizations fulfilled all criteria for a convincing description of the non-resonant contributions, we left out his amplitude from our freed-isobar analyses. More dedicated studies are required in order to find a more realistic model for the non-resonant contributions.
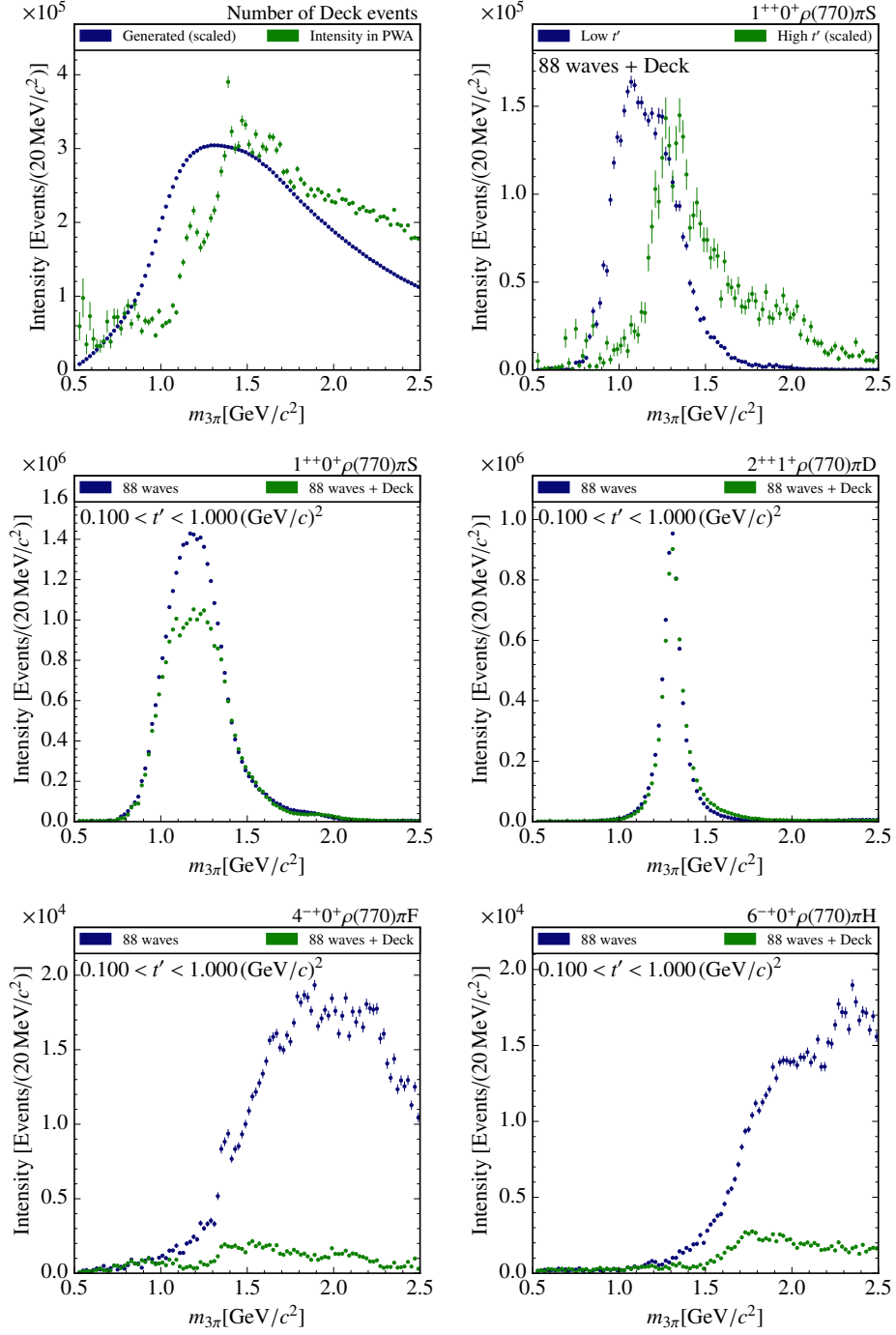
Figure B.2.: Upper left: Comparison of the intensity distribution for the Deck wave as extracted by the PWA with the theoretical predictions. Upper right: Intensity of the $1^{++}0^{+}\rho(770)\,\pi\mathrm{S}$ wave for the highest and lowest t' bin for the 88 wave + Deck model. Middle and lower row: Comparison of intensity distributions of selected partial waves for the 88 wave model and the 88 wave + Deck model.

Appendix C.

Projections of the covariance matrix

In plots similar to fig. 5.2, several directions in the space of production amplitudes may appear, that do not, or only slightly, alter the total intensity. Examples are the direction of a global phase rotation, leaving the intensity perfectly unchanged, or the direction of a zero mode. Therefore, the uncertainties, given by the diagonal elements of the covariance matrix of the fitting parameters obtained by a fitting algorithm, are large. However, since we have understood the underlying reasons for these huge uncertainties we want to remove them from the covariance matrix, to obtain more meaningful uncertainty estimations by removing the high correlations between the single points.

For illustration, we first consider the two-dimensional problem of a single complex number $g = |g| \exp(i\varphi)$, whose real and imaginary part have the covariance matrix $\mathbf{C}$.

Assuming, that the uncertainty $\Delta\varphi$ on the complex phase φ of g is large, as for example as depicted in fig. C.1, but of minor interest, we want to remove the effect of $\Delta\varphi$ from $\mathbf{C}$. However, since the basis of $\mathbf{C}$ are real and imaginary part, we cannot simply remove the corresponding entries from $\mathbf{C}$. We therefore determine the direction $\vec{v}$ in the complex plane corresponding to a change of phase φ:

$$\vec{v} = \frac{\vec{w}}{|\vec{w}|} = \begin{pmatrix} -\sin\varphi \\ \cos\varphi \end{pmatrix}, \tag{C.1}$$

where $\vec{w}$ is the directional derivative with respect to φ:

$$\vec{w} = \begin{pmatrix} \frac{\mathrm{d}\Re g}{\mathrm{d}\varphi} \\ \frac{\mathrm{d}\Im g}{\mathrm{d}\varphi} \end{pmatrix} = |g| \begin{pmatrix} -\sin\varphi \\ \cos\varphi \end{pmatrix}. \tag{C.2}$$

To remove the effect of $\Delta\varphi$ from $\mathbf{C}$, we define the projection operator $\mathbf{P}$:

$$\mathbf{P}_{ij} = \delta_{ij} - \vec{v}_i\vec{v}_j = \begin{pmatrix} 1 - \sin^2\varphi & \sin\varphi\cos\varphi \\ \sin\varphi\cos\varphi & 1 - \cos^2\varphi \end{pmatrix}. \tag{C.3}$$

With this, we can construct a modified covariance matrix $\tilde{\mathbf{C}}$, where the variance in the direction of $\vec{v}$ is zero[a]:

$$\tilde{\mathbf{C}} = \mathbf{P} \cdot \mathbf{C} \cdot \mathbf{P}. \tag{C.4}$$

---

[a]Since the variance in one particular direction is set to zero from $\mathbf{C}$, the corresponding eigenvalue
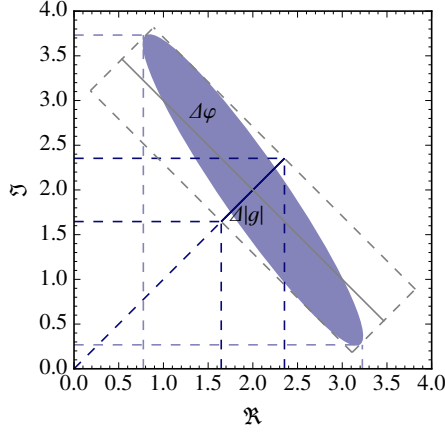
Figure C.1.: Example for the removal of the phase direction. The error ellipse and uncertainties on real and imaginary part are shown in light blue before and blue after the projection. In the latter case, the error ellipse is degenerated into a line corresponding to $\Delta|g|$. $\Delta\varphi$ is shown as gray line.

The effect of such a projection can also be seen in fig. C.1, where the two-dimensional error ellipse degenerates into a one-dimensional line.

We now can extend this procedure to higher dimensions, for example to the set of production amplitudes $\vec{\mathcal{T}}$ obtained by a maximum likelihood fit like in section 6.3. The direction to remove could be the direction of a zero mode: $v_i = \mathcal{T}_i^0$, as in eq. (5.61), where the i is again a combined index, as defined in eq. (5.66), encoding different properties of the single waves. Note, that in this case, the normalization condition $|\vec{v}| = 1$ is automatically fulfilled, since $\vec{\mathcal{T}}^0$ is an eigenvector of the phase-space integral matrix. The direction $\vec{v}$ could also encode the rotation of a global phase φ for all production amplitudes $\vec{\mathcal{T}}$ simultaneously. In this case, $\vec{v}$ is:

$$\vec{v}_i = \frac{\vec{w}}{|\vec{w}|}, \tag{C.5}$$

where $\vec{w}$ is the directional derivative in φ direction:

$$w_i = \frac{\mathrm{d}\mathcal{T}_i}{\mathrm{d}\varphi}. \tag{C.6}$$

With the direction $\vec{v}$, we can define a projection operator:

$$\mathbf{P}_{ij} = \delta_{ij} - \vec{v}_i\vec{v}_j, \tag{C.7}$$

---

vanishes and $\mathbf{C}$ it is no longer invertible. To use it in χ^2 functions, the pseudo-inverse has to be used instead, which also ensures that the direction in which the variance was set to zero does not contribute to the value of χ^2. In this work however, we use the full $\mathbf{C}$ in the χ^2 functions, given in eq. (5.65), and only manipulate $\mathbf{C}$ for plotting.

and use eq. (C.4) to obtain a modified covariance matrix $\tilde{\mathbf{C}}$. This projected covariance matrix now has zero variance in the direction of $\vec{v}$, while the behavior in all directions orthogonal to $\vec{v}$ remains unchanged:

$$\vec{v} \cdot \tilde{\mathbf{C}} \cdot \vec{v} = 0, \tag{C.8}$$

and for all $\vec{q}$ with $\vec{q} \cdot \vec{v} = 0$;

$$\vec{q} \cdot \tilde{\mathbf{C}} \cdot \vec{q} = \vec{q} \cdot \mathbf{C} \cdot \vec{q}. \tag{C.9}$$

136

Appendix D.

Effects from integration over $m_{2\pi}$ bins

In the Monte Carlo study in sections 6.2.3 to 6.2.5 find, that the values for the $\rho(770)$ resonance parameters determined by the "fit$_\rho$" method do not agree with the input values within their uncertainties.

To study the underlying reasons for this effect, we use a simple model case with only a single wave. For this wave, we use a fixed-width Breit-Wigner amplitude, as defined in eq. (3.26) with $m_0 = 770\,\mathrm{MeV}/c^2$ and $\Gamma_0 = 110\,\mathrm{MeV}/c^2$. According to the intensity distribution of this dynamic isobar amplitude, we generate a data set of 10^5 events in the $m_{2\pi}$ range from 0.5 to $1.5\,\mathrm{GeV}/c^2$ and bin the events in 25 bins each with $40\,\mathrm{MeV}/c^2$ width.

We then fit the resulting distributions again with the same fixed-width Breit-Wigner amplitude using three methods:

1. integrating the intensity distribution of the Breit-Wigner amplitude over each of the $m_{2\pi}$ bins,

2. integrating the Breit-Wigner amplitude over each of the $m_{2\pi}$ bins, and

3. evaluating the Breit-Wigner amplitude at the corresponding $m_{2\pi}$ bin centers.

For all three methods, we determine the pull distributions of m_0 and Γ_0 for $2.5 \cdot 10^5$ of such pseudo experiments (see fig. D.1).

We observe, that method 1—integration over the intensity—yields a pull distribution centered at zero. A likelihood fit of a two-dimensional gaussian to the pull distribution yields standard deviations of 1.07 and 1.59 for the gaussian width of the m_0 and Γ_0, respectively. The distributions for both quantities are not correlated. Except the too large standard deviation of the pull distribution of the width, the results of this fit are in accordance with expectations.

For method 2—integration of the amplitude—a two-dimensional gaussian fit yields central values for the pull distributions of mass and width of -0.66 and 4.75, giving a bias to too big values of the width. The standard deviations for both distributions are 1.07 and 2.02, which is similar to the integration of the intensity. The pull distributions of mass and width are correlated with a correlation coefficient of -0.07.

Performing a fit of a two-dimensional gaussian to the pull distribution obtained with method 3—evaluation at the $m_{2\pi}$ bin center—we find central values for the pulls of mass and width of -0.52 and -5.69, giving a bias on the width to smaller values. The standard deviations are 1.10 and 2.07 and the correlation coefficient is -0.06.
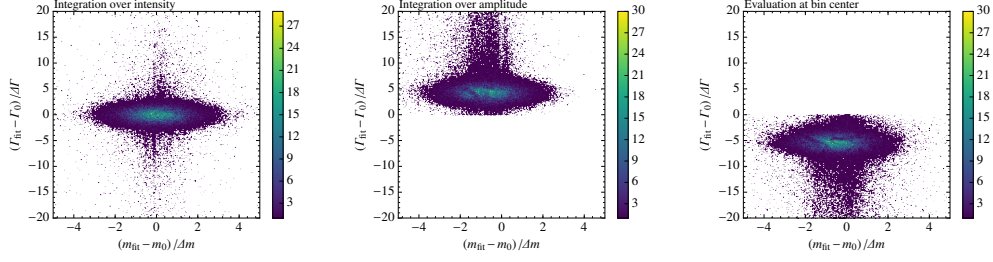
Figure D.1.: Pull distributions for fitted resonance mass m_0 and width Γ_0, obtained by integration of the intensity (left), integration of the amplitude (center) and evaluation at the $m_{2\pi}$ bin center (right).

We see, that evaluation at the $m_{2\pi}$ bin center and the integration over the amplitudes are several standard deviations away from the input values, while the integration over the intensity gives an average pull of around one standard deviation, as expected. In this example, there is only one wave and we are therefore able to integrate the intensity. However, in the more complex applications in sections 6.2.3 to 6.2.5, such an integration is not possible, since the interference with other waves has to be taken into account, giving a small bias on the resulting resonance parameters. Since methods 2 and 3 yield biases of similar size, we use the evaluation at the bin center for our applications, since it is computationally less expensive.

List of Figures

List of Tables

Bibliography

[1] W. Celmaster and R. J. Gonsalves, "The Renormalization Prescription Dependence of the QCD Coupling Constant," *Phys. Rev.* **D20** (1979) 1420.

[2] **Particle Data Group** Collaboration, C. Patrignani *et al.*, "Review of Particle Physics," *Chin. Phys.* **C40** no. 10, (2016) 100001.

[3] S. U. Chung *et al.*, "Exotic and q anti-q resonances in the $\pi^+\pi^-\pi^-$ system produced in π^-p collisions at 18 GeV/c," *Phys. Rev.* **D65** (2002) 072001.

[4] A. R. Dzierba *et al.*, "A Partial wave analysis of the π^- π^+ π^- and π^- π^0 π^0 systems and the search for a $J^{PC} = 1^{-+}$ meson," *Phys. Rev.* **D73** (2006) 072001, `arXiv:hep-ex/0510068 [hep-ex]`.

[5] **VES** Collaboration, A. Zaitsev, "Study of exotic resonances in diffractive reactions," *Nucl. Phys.* **A675** (2000) 155C–160C.

[6] **Compass** Collaboration, M. Alekseev *et al.*, "Observation of a $J^{PC} = 1^{-+}$ exotic resonance in diffractive dissociation of 190 GeV/c π^- into $\pi^-\pi^-\pi^+$," *Phys. Rev. Lett.* **104** (2010) 241803, `arXiv:0910.5842 [hep-ex]`.

[7] **COMPASS** Collaboration, C. Adolph *et al.*, "Odd and even partial waves of $Peta\pi^-$ and $\eta'\pi^-$ in $\pi^-p \to \eta^{(')}\pi^-p$ at 191 GeV/c," *Phys. Lett.* **B740** (2015) 303–311, `arXiv:1408.4286 [hep-ex]`.

[8] F. Haas, *Two-Dimensional Partial-Wave Analysis of Exclusive* $190\,\text{GeV}$ π^-p *Scattering into the* $\pi^-\pi^-\pi^+$ *Final State at* Compass *(CERN)*. PhD thesis, Technische Universität München, 2014.

[9] F. Kaspar, "Application and verification of model-selection techniques for diffractively produced three-pion final states," Master's thesis, Technische Universität München, 2017.

[10] **E791** Collaboration, E. M. Aitala *et al.*, "Model independent measurement of S-wave K^- π^+ systems using $D^+ \to K\pi\pi$ decays from Fermilab E791," *Phys. Rev.* **D73** (2006) 032004, `arXiv:hep-ex/0507099 [hep-ex]`. [Erratum: Phys. Rev.D74,059901(2006)].

[11] **LHCb** Collaboration, R. Aaij *et al.*, "Observation of $J/\psi p$ Resonances Consistent with Pentaquark States in $\Lambda_b^0 \to J/\psi K^- p$ Decays," *Phys. Rev. Lett.* **115** (2015) 072001, `arXiv:1507.03414 [hep-ex]`.

[12] **COMPASS** Collaboration, C. Adolph *et al.*, "Resonance Production and $\pi\pi$ S-wave in $\pi^- + p \to \pi^-\pi^-\pi^+ + p_{recoil}$ at 190 GeV/c," *Phys. Rev.* **D95** no. 3, (2017) 032004, arXiv:1509.00992 [hep-ex].

[13] K. Bicker, *Model Selection for and Partial-Wave Analysis of a Five-Pion Final State at the COMPASS Experiment at CERN.* PhD thesis, Technische Universität München, 2016. https://inspirehep.net/record/1503584/files/\protect$\relax\protect\unhbox\voidb@x\hbox{CERN}$\protect\let\futurelet\@let@token\let-THESIS-2016-102.pdf.

[14] O. Drotleff, "Model Selection for Partial-Wave Analysis of $\pi^- p \to \pi^-\pi^+\pi^- p$ at the COMPASS Experiment at CERN," Master's thesis, Technische Universität München, 2015.

[15] **COMPASS** Collaboration, P. Abbon *et al.*, "The COMPASS Setup for Physics with Hadron Beams," *Nucl. Instrum. Meth.* **A779** (2015) 69–115, arXiv:1410.1797 [physics.ins-det].

[16] **COMPASS** Collaboration, P. Abbon *et al.*, "The COMPASS experiment at CERN," *Nucl. Instrum. Meth.* **A577** (2007) 455–518, arXiv:hep-ex/0703049 [hep-ex].

[17] S. U. Chung and T. L. Trueman, "Positivity Conditions on the Spin Density Matrix: A Simple Parametrization," *Phys. Rev.* **D11** (1975) 633.

[18] V. Filippini, A. Fontana, and A. Rotondi, "Covariant spin tensors in meson spectroscopy," *Phys. Rev.* **D51** (1995) 2247–2261.

[19] A. V. Anisovich, V. V. Anisovich, V. N. Markov, M. A. Matveev, and A. V. Sarantsev, "Moment operator expansion for the two meson, two photon and fermion anti-fermion states," *J. Phys.* **G28** (2002) 15–32, arXiv:hep-ph/0105330 [hep-ph].

[20] C. Zemach, "Determination of the Spins and Parities of Resonances," *Phys. Rev.* **140** (1965) B109–B124.

[21] C. Zemach, "Use of angular momentum tensors," *Phys. Rev.* **140** (1965) B97–B108.

[22] M. Jacob and G. C. Wick, "On the general theory of collisions for particles with spin," *Annals Phys.* **7** (1959) 404–428. [Annals Phys.281,774(2000)].

[23] S. U. Chung, "Spin Formalisms,".

[24] F. Von Hippel and C. Quigg, "Centrifugal-barrier effects in resonance partial decay widths, shapes, and production amplitudes," *Phys. Rev.* **D5** (1972) 624–638.

[25] S. U. Chung, J. Brose, R. Hackmann, E. Klempt, S. Spanier, and C. Strassburger, "Partial wave analysis in K matrix formalism," *Annalen Phys.* **4** (1995) 404–430.

[26] K. Gottfried and J. D. Jackson, "On the Connection between production mechanism and decay of resonances at high-energies," *Nuovo Cim.* **33** (1964) 309–330.

[27] J. D. Richman, "An Experimenter's Guide to the Helicity Formalism,".

[28] E. Wigner, "Einige Folgerungen aus der Schrödingerschen Theorie für die Termstrukturen," *Z. Phys.* **43** (1927) 624–652.

[29] G. Breit and E. Wigner, "Capture of Slow Neutrons," *Phys. Rev.* **49** (1936) 519–531.

[30] **BES** Collaboration, M. Ablikim *et al.*, "Resonances in $J/\psi \to \phi\pi^+\pi^-$ and ϕK^+K^-," *Phys. Lett.* **B607** (2005) 243–253, `arXiv:hep-ex/0411001 [hep-ex]`.

[31] S. M. Flatté, "On the Nature of 0^+ Mesons," *Phys. Lett.* **63B** (1976) 228–230.

[32] K. L. Au, D. Morgan, and M. R. Pennington, "Meson Dynamics Beyond the Quark Model: A Study of Final State Interactions," *Phys. Rev.* **D35** (1987) 1633.

[33] P. Guo, R. Mitchell, M. Shepherd, and A. P. Szczepaniak, "Amplitudes for the analysis of the decay $J/\psi \to K^+K^-\pi^0$," *Phys. Rev.* **D85** (2012) 056003, `arXiv:1112.3284 [hep-ph]`.

[34] S. Schmeing, "Resonance Extraction in Diffractive 3π Production using 190 GeV/c π^- at the Compass Experiment (CERN)," Master's thesis, Technische Universität München, 2014. `http://wwwcompass.cern.ch/compass/publications/theses/2014_dpl_schmeing.pdf`.

[35] S. Wallner, "Extraction of Resonance Parameters of Light Meson Resonances in the Charged Three-Pion Final State at the Compass Experiment (CERN)," Master's thesis, Technische Universität München, 2015. `http://wwwcompass.cern.ch/compass/publications/theses/2015_dpl_wallner.pdf`.

[36] F. Krinner, D. Greenwald, D. Ryabchikov, B. Grube, and S. Paul, "Ambiguities in model-independent partial-wave analysis," `arXiv:1710.09849 [hep-ph]`.

[37] **Compass** Collaboration, C. Adolph *et al.*, "Observation of a New Narrow Axial-Vector Meson a$_1$ (1420)," *Phys. Rev. Lett.* **115** no. 8, (2015) 082001, `arXiv:1501.05732 [hep-ex]`.

[38] **Compass** Collaboration, "Light isovector resonances in
$\pi^- p \to \pi^- \pi^+ \pi^- p_{\text{recoil}}$ at 190 GeV/c," *publication in preparation* (2018) .

[39] M. Maggiore, *A Modern Introduction to Quantum Field Theory.* Oxford
Master Series in Physics. OUP Oxford, 2004.
`https://books.google.de/books?id=Uln-zfVUBKsC`.

[40] R. E. Behrends and C. Fronsdal, "Fermi decay of higher spin particles,"
Phys. Rev. **106** (Apr, 1957) 345–353.
`https://link.aps.org/doi/10.1103/PhysRev.106.345`.

[41] P. R. Auvil and J. J. Brehm, "Wave Functions for Particles of Higher Spin,"
Phys. Rev. **145** no. 4, (1966) 1152.

[42] S.-U. Chung and J. Friedrich, "Covariant helicity-coupling amplitudes: A
New formulation," *Phys. Rev.* **D78** (2008) 074027, `arXiv:0711.3143`
`[hep-ph]`.

[43] R. T. Deck, "Kinematical interpretation of the first π–ρ resonance," *Phys.
Rev. Lett.* **13** (1964) 169–173.

[44] **ACCMOR** Collaboration, C. Daum *et al.*, "Diffractive Production of 3π
States at 63 GeV and 94 GeV," *Nucl. Phys.* **B182** (1981) 269–336.

[45] B. Hyams *et al.*, "$\pi\pi$ Phase Shift Analysis from 600 MeV to 1900 MeV,"
Nucl. Phys. **B64** (1973) 134–162.

Own Contributions

Based on the idea of replacing fixed dynamic isobar amplitudes by step like functions in three-body partial-wave analyses, first introduced in ref. [10] and applied to COMPASS data by D. Ryabchikov, I extended this approach in this work to an arbitrary number of freed waves. Doing so, I encountered continuous ambiguities in the resulting fit models, stemming from complete cancellations between different terms of the amplitude description. I was able to show the analytic origin of these cancellations using covariant and non-relativistic formalisms. In turn, I developed a method to find such cancellations numerically and resolve them with additional constraints. I was able to show the validity of these methods on Monte Carlo data sets. Together with D. Greenwald, B. Grube, S. Paul, and D. Ryabchikov, I wrote a paper on this method, currently in the review process of Phys. Rev. D [36].

I applied my developed methods on the data set for the process $\pi^- p \to \pi^- \pi^+ \pi^- p$, collected by the COMPASS experiment in 2008. Hereby, I used the same event selection and Monte Carlo data, as developed by F. Haas for refs. [8, 12]. I used the same set of partial waves for my analysis, with the difference that several of these waves now employ freed dynamic isobar amplitudes to extract them directly from the data. I freed 24 different partial waves and was able to resolve their dynamics in t', $m_{3\pi}$, and $m_{2\pi}$, after fixing arising ambiguities with the developed methods.

I fitted the extracted dynamic isobar amplitudes with simple Breit-Wigner models, to extract the parameters of the appearing isobar resonances. I did this in every $m_{3\pi}$ bin, t' bin and partial wave separately and was able to get an unprecedented insight into the interplay of (2π) and (3π) dynamics in the analyzed channel.

In addition to the work on freed-isobar PWA, I performed studies of the Deck effect by including a corresponding amplitude in the PWA model. Even though first results looked promising, I did not include this amplitude in my main analysis, since none of the parameterizations of the Deck effect yielded fully convincing results.

Besides the work described in this thesis, I was involved in the development of the `rootpwa` partial-wave analysis framework, to which K. Bicker, O. Drotleff, B. Grube, S. Neubert, S. Uhl, and S. Wallner were main contributors. Together with D. Ryabchikov and S. Schmeing, I worked on implementing a method to use the full covariance matrix information in resonance model fits like in refs. [34, 35, 38]. In addition, I presented the results of my work on meetings within the COMPASS collaboration, on numerous national and international conferences, and in the corresponding proceedings. I also took part in the annual COMPASS data taking campaigns from 2014 to 2017.

Danksagung − Acknowledgments

Zuerst möchte ich Prof. Stephan Paul dafür danken, dass der mir ermöglicht hat, meine Dissertation zu diesem sehr interessanten und neuartigen Thema an seinem Lehrstuhl anzufertigen, dabei eigene Ideen verfolgen zu können und die Ergebnisse auf zahlreichen nationalen und internationalen Konferenzen präsentieren zu dürfen; zudem für sein immerwährendes Interesse am Fortschritt meiner Arbeit.

Besonders danken möchte ich Boris Grube, der über die Jahre allzeit bereit war, mit bei der Lösung von Problemen, physikalischer, statistischer und organisatorischer Natur zu helfen. Zudem hat er diese gesamte Arbeit korrekturgelesen, die somit zweifelsohne ein deutlich besseres Resultat abgibt.

Ferner möchte ich meinen Kollegen bei E18 danken, die meinen Arbeitsalltag deutlich erleichtert und angenehmer gestaltet haben. Allen voran Karin Frank für ihre beständige Unterstützung bei allen organisatorischen Fragen. Ebenso Sebastian Uhl für seine stetige Unterstützung und seinen reichen Erfahrungsschatz, Stefan Wallner für seine Hilfe in allen Computerfragen, Florian Kaspar für die Diskussionen über verschiedenste, meist statistikrelatierte Themen, Christian Dreisbach, Jan Friedrich und Stefan Huber.

Большое спасибо Дмитрию Рябчикову. Он положил основу для диссертации с его первым анализом и с тех пор помогал мне словами и делами. Я также благодарю его за рекомендации о пиве, квасе и водке перед поездкой в Россию. Спасибо Дмитрию Левит за исправление моего русского языка.

Zusätzlich danke ich zahlreichen Kollegen, die mittlerweile nicht mehr, oder nur noch sehr selten am Lehrstuhl sind: Sverre Dørheim, Florian Haas, Markus Krämer, sowie Karl Bicker, den ich bereits am ersten Tag meines Studiums in seiner damaligen Funktion als Tutor im Mathematikvorkurs kennenlernen durfte; «s'Läbe isch es Chruezli!».

I also want to thank all E18 members whom I didn't mention explicitly for the great time the last five years and the interesting discussions on physical and nonphysical topics.

There are numerous colleagues from outside of Munich and the E18 group, who contributed to this work. First I want to thank Suh-Urk Chung for sharing his great experience in hadron physics with me. In addition, I want to thank the people

I also want to thank:

for	fruitful discussions	trusting in me as tutor for the Bavarian dialect	YAP	suggesting this table
Daniel Greenwald	✓	✓		✓